Fundamental Characteristics of Turbulent Opposed Impinging Jets

By

Gheorghe Stan

A thesis
presented to the University of Waterloo
in fulfillment of the
thesis requirement for the degree of
Master of Applied Science
in
Mechanical Engineering

Waterloo, Ontario, Canada, 2000

I hereby declare that I am the sole author of this thesis. This is a true copy of the thesis, including any required final revisions, as accepted by my examiners.

I understand that my thesis may be made electronically available to the public.

Gheorghe Stan

Abstract

A fundamental study of two turbulent directly opposed impinging jets in a stagnant ambient fluid, unconfined or uninfluenced by walls is presented. By experimental investigation and numerical modeling, the main characteristics of direct impingement of two turbulent axisymmetric round jets under seven different geometrical and flow rate configurations ($L^* = \frac{L}{d} = \{5, 10, 20\}$, where L is nozzle to nozzle separation distance and d is nozzle diameter, and $\mathrm{Re} = \frac{\rho U_0 d}{\mu} = \{1500, 4500, 7500, 11000\}$ where ρ is fluid density, μ is dynamic viscosity of fluid and U_0 is average initial velocity of fluid) are discussed. Flow visualization and velocity measurements performed using various laser based techniques have revealed the effects of Reynolds number,Re, and nozzle to nozzle separation,L^*, on the complex flow structure. Although locally valid, the classical analysis of turbulence is found unable to provide reliable results within the highly unstable and unsteady impingement region. When used to simulate the present flow, the assessment of the performance of three distinct $k - \varepsilon$ turbulence models showed little disagreement between computed and experimental mean velocities and poor predictions as far as turbulence parameters are concerned.

Acknowledgements

I am deeply grateful to my supervisor, Professor David A. Johnson, whose advice and encouragement have guided me throughout the past two years. He first suggested the topic as a direct link to my aerospace background. I am also thankful for the prolific discussions I have had with Professor Gord Stubley, Professor Al Strong and Professor Elizabeth J. Weckman.

I wish to thank Mr. Al Hodgson and Mr. Gord Hitchman, for their technical support and assistance in various matters. To my colleagues I am thankful for their friendship. Special thanks to Stephen Reuss and Frank Ham for computer support.

This research has been supported financially by the Natural Sciences and Engineering Research Council of Canada, in the form of a graduate scholarship and a research assistantship. Their support is gratefully acknowledged.

To my wife Nicoletta, I wish to express my sincere appreciation for love and support throughout my studies.

Contents

Figures

Tables

Nomenclature

Latin Letters

a_1	slope coefficient in curve fit equation
a_2	coefficient in curve fit equation
b	half width of the jet $[m]$
c_p	specific heat at constant pressure $[J/kgK]$
c_v	specific heat at constant volume $[J/kgK]$
C_{scat}	scattering cross section area of a particle $\left[m^2\right]$
d	nozzle diameter $[m]$
$d_{e^{-2}}$	diameter of laser beam focal waist $[m]$
$D_{e^{-2}}$	diameter of laser beam $[m]$
d_m	diameter of measurement control volume $[m]$
d_{pixel}	pixel pitch $[\mu m]$
d_p	particle diameter $[\mu m]$
D_{ij}	mean strain rate (deformation) tensor
f	focal length $[m]$
f_D	Doppler frequency $[Hz]$
f_i	impingement region oscillation frequency $[Hz]$
f_r	radial jet periphery oscillation frequency $[Hz]$
f_μ, f_ε	wall damping functions
f, g	functions that describe light intensity
F, G	Fourier transforms of f, g
h	transfer function
I_0	light intensity incident on the particle $\left[W/m^2\right]$
I	CFD turbulence intensity "guess" value $\left[m^2/s^2\right]$
k	turbulent kinetic energy $\left[m^2/s^2\right]$

l	nozzle length $[m]$
L	nozzle to nozzle separation distance $[m]$
L_{ii}	integral length scale $[m]$
l_k	Kolmogorov length scale $[m]$
l_m	length of measurement control volume $[m]$
m, n	image coordinates $[pixels]$
N	number of velocity samples
N_{fr}	number of fringes
n	coordinate normal to the wall $[m]$
p	pressure $\left[N/m^2\right]$
P_k	production of turbulent kinetic energy $\left[m^2/s^3\right]$
P_s	scattered power $[W]$
Q	flow rate $\left[m^3/s\right]$
R_{fg}	cross-correlation function
R_{ii}	correlation coefficient
Re	Reynolds number based on nozzle wetted diameter
$\mathrm{Re}_{\lambda_\mathrm{g}}$	experimental turbulent Reynolds number
Re_t	numerical turbulent Reynolds number
S	object - image scale factor
Δs	mean local displacement $[m]$
S_{ui}	momentum equation source term $\left[N/m^3\right]$
T	period of averaging $[s]$
t	time $[s]$
t_0	time origin $[s]$
$T_{E_{\mathrm{ii}}}$	integral time scale $[s]$
t_k	Kolmogorov dissipation time scale $[s]$
Δt	illumination interval $[s]$
$u_{i,}\ u_j$	spatial velocity vector (tensor notation) $[m/s]$
u_{rms}	longitudinal turbulent intensity $[m/s]$
u_m	centerline (maximum) longitudinal velocity $[m/s]$
U_0	average initial velocity $[m/s]$
u_s	settling or sedimentation velocity $[m/s]$
$U_\perp$	velocity perpendicular to the fringes $[m/s]$
u, v	velocity components $[m/s]$
v_{rms}	transverse turbulent intensity $[m/s]$
V_H	instantaneous velocity of a particle relative to the fluid $[m/s]$
$x_{i,}\ x_j$	spatial coordinate (tensor notation) $[m]$
x, y	space coordinates $[m]$
Δx	fringe spacing $[m]$

Greek Letters

α	slope $[^\circ]$
β	RNG model - constant
δ_{ij}	Kronecker-Delta tensor
ε	dissipation of turbulent kinetic energy $\left[m^2/s^3\right]$
η	dimensionless strain rate (RNG model)
η_0	asymptotic dimensionless strain rate in 2D plane homogeneous turbulence
κ	wave number $[rad/m]$
λ	laser beam wave length $[m]$
λ_f	longitudinal microscale for length $[m]$
λ_g	transverse microscale for length $[m]$
μ	dynamic viscosity of fluid $\left[Ns/m^2\right]$
ν	kinematic viscosity of fluid $\left[m^2/s\right]$
ρ	density of fluid $\left[kg/m^3\right]$
σ_{ij}	stress tensor in momentum equation $\left[N/m^2\right]$
τ_{ij}	viscous stress tensor
$\tau_{E_{\mathtt{ii}}}$	Taylor microscale for time $[s]$
φ	half angle intersection of laser beams $[^\circ]$

Subscripts

f	fluid
fr	fringe
n	normal component
p	particle
t	turbulent
w	wall component
τ	shear component
11	longitudinal component
22	transverse component

Superscripts

$\overline{()}$	mean value
$'$	fluctuation component
*	dimensionless
$^+$	dimensionless

Introduction

Motivation

Turbulence is one of the key phenomena in fluid dynamics. A major challenge in propulsion and mixing design is to provide the theory with highly accurate experimental data and rigorous turbulence models used in computational fluid dynamics (CFD) simulations. Jet to jet impingement is an engineering field which pertains to the research, development, and design of propulsion systems and various systems demanding a dynamic mixing of two or several jet flows in order to achieve their intended purpose. The system may be a side dump combustor of a Vertical Short Take-Off and Landing (V/STOL) aircraft, a combustion chamber of an Internal Combustion (IC) engine, the Environmental Control System (ECS) of a civilian airplane, the mix head for Reaction Injection Molding (RIM), etc., which are of great industrial significance. In such configurations, the mixing or combustion processes take place within the impingement region of the jets, therefore the flow must maintain certain conditions to ensure the best efficiency and stability.

A quantitative description of mixing requires understanding of the fundamental processes that govern formation and evolution of jet to jet impingement structures. Even the simplest case of jet to jet impingement that undergo reaction can be regarded as a combination of four nonlinear, coupled, spatially and temporally distributed processes: convection, stretching, diffusion and pressure interaction; chemical reaction or phase transform takes place instantaneously within the impingement region or follows the impingement process. Convection moves portions of fluid from one location to another, promoting global uniformity by redistributing in time and space initially separated jets. Stretching transforms portions of fluid into elongated parcels, increasing the amount of contact area. Diffusion, which is generated by the thermal and kinetic energy of individual molecules, induces locally isotropic and homogeneous turbulence at small scales. Energy is transferred from the largest to the smallest scales via diffusional processes, vortex stretching, pressure interactions, etc. These processes typically generate partially mixed structures. When mixing is inadequate, desired reactions are slowed and even stopped before reaction is complete.

The jet to jet impingement problem has usually been studied in the context of a particular application such as the side dump combustor or the mix head for RIM, where the two

opposed impinging jets are wall-bounded and the interaction between an inner layer and an outer boundary layer is crucial, however fundamental aspects of that complex flow have never been clearly discussed.

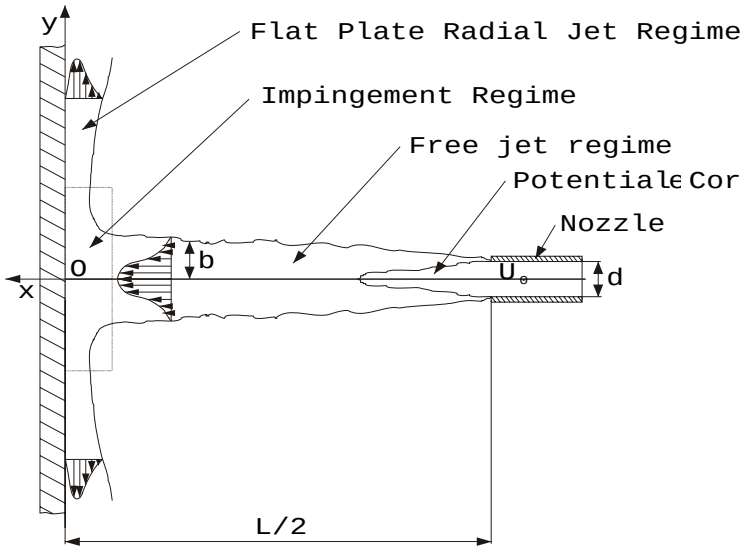

Figure I.1: Impinging Jet on a Flat Plate - MIC

Moreover the traditional approach is guided mainly by the " mirror image concept" (MIC). The concept indicates that the impinging of two jets separated by a distance L is theoretically equivalent to a single jet impinging on a flat plate at a distance $L/2$ downstream (Figure I.1). Even though the concept seems plausible when applied to the impingement of laminar jets, instabilities associated with the " free jets" before impingement induce justified doubts on the validity of the concept in a turbulent flow field.

The motivation for the current work is the observation that understanding the fundamental characteristics associated with jet to jet impingement dynamics is essential in treating its derivative applications. Understanding the mechanism governing the turbulence structure and the instabilities associated with jet to jet impingement dynamics in an unconfined case is essential for determining mixing and entrainment characteristics present within more complex configurations. Consequently, it makes sense to start the study with the general configuration of two opposed impinging jets in a stagnant ambient fluid, unconfined or uninfluenced by walls.

The resulting approach, followed both experimentally and computationally in this research, is termed the " free radial jet concept" (FRJC). According to this theory the two opposed jets initially separated by a distance L, impinge on each other at a station situated at about $L/2$ downstream and spread out radially creating a three dimensional free radial jet (Figure I.2).

In this study two identical cylindrical nozzles of inside diameter, d, and long enough to ensure a fully developed flow at their outlets were used. To avoid exterior perturbations and wall effects, they were isolated (stationary) within a very large tank in comparison with the distance between nozzles, L, and nozzle diameter, d.

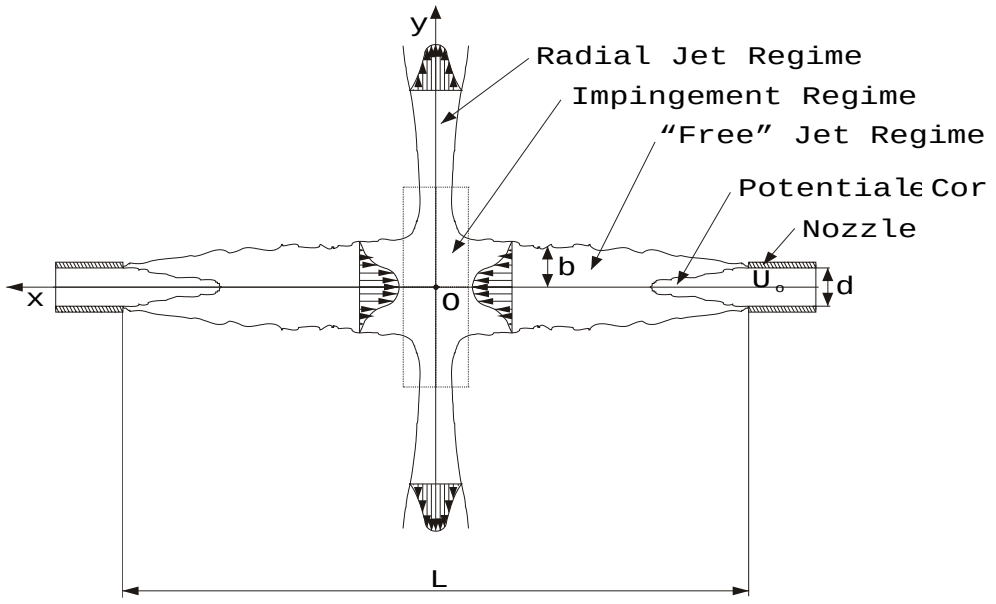

Figure I.2: Opposed impinging jets - FRJC

Three geometrical configurations with respect to nozzle to nozzle specific distance, $L^* = L/d$, and four flow rates with respect to dimensionless parameter, Reynolds number, $\mathrm{Re} = \frac{\rho U_0 d}{\mu}$, are used to characterize the impingement of isothermal turbulent opposed impinging jets. In this thesis, only the incompressible case is considered both experimentally and computationally.

Objectives

The primary objectives of this thesis are to demonstrate the viability of the ” radial jet concept” by investigating experimentally and computationally the complex flow field characteristics of two turbulent (relative high speed) directly opposed impinging jets in a stagnant and isothermal ambient fluid and to determine the effects of geometrical configuration (through the nozzle separation distance, L) and flow rate through its dimensionless parameter, Re, on the flow structure. These will be performed by considering several smaller objectives.

1. The work is built around qualitative flow visualization and velocity measurements by laser based techniques which are compared with model results obtained by CFD means. The first objective is to develop a complete data bank of flow visualization images (i.e. covering the entire spectrum of geometry and flow rate configurations) able to provide good support for future velocity measurements and CFD simulations. Moreover flow visualization is used to provide a general idea of the complicated, unstable and unsteady flow field.

2. A second objective of this work is the application of the Laser Doppler Anemometry (LDA) technique to obtain a reliable base case velocity distribution within the flow field, which will be used to validate the application of the Particle Image Velocimetry (PIV) technique to this complex flow.

3. Even though the technique is in the development phase, PIV is recognized for its high density data output and an accuracy comparable with that of LDA data. Another objective is to extend the application of PIV technique to all remaining cases of study proposed. It is also regarded as a reliable means upon which CFD solutions can be checked.

4. The last objective is to develop a CFD simulation able to provide credible solutions, which then would be compared with the above mentioned measurement results.

For the effectiveness of this work and due to availability, our attention will be restricted to the incompressible flow of constant-property fluids in one or two spatial dimensions. The unconfined jet to jet impingement arrangement would require additional effort to extend it to flow cases involving non-coaxial jets, compressible fluids, non-isothermal flow conditions (including phase transforms) and induced dynamic perturbations.

Outline

The thesis is mainly divided into five chapters. The first chapter presents the differential equations describing fluid flow together with the principal aspects of turbulent jet flow and a review of the relevant literature. Chapter 2 deals with the experimental aspects of this work; here the experimental equipment and the experimental laser based techniques involved are discussed. The third chapter presents the description of CFD numerical models and techniques used. Chapter 4 contains the experimental results pertaining to the proposed flow configurations and the methods of investigation used. By direct comparisons with the experimental data, numerical simulation results obtained using a CFD code (TASCflow) are also discussed. Some conclusions and recommendations for further study are given in the final part, Chapter 5.

Chapter 1

Background

Given the fundamental approach followed here and in order to place the unconfined jet to jet impingement flow into context, it is important to develop a sense of existing theory. First, the physics of fluid flow, as described by the continuity and Navier-Stokes equations, will be reviewed. Free turbulent jet theory is the closest link to unconfined jet to jet impingement, thus the theory of turbulent submerged jets of incompressible fluid will then be summarized. This chapter will conclude with a review of the theoretical and numerical work directly related to turbulent opposed impinging jets.

1.1 Fluid Dynamics Basic Theory

1.1.1 Mathematical Basis

Fluid dynamics is described by a coupled set of equations representing the mathematical statement of the conservation laws of physics. These include the equations representing conservation of momentum together with the assumption of a linear stress-strain rate relationship (named the *Navier-Stokes equations* after the two $19th$ century scientists who derived them independently), continuity and conservation of energy equations. Experience shows that the Navier-Stokes equations describe the flow of a Newtonian fluid accurately. In most cases, even the simplified equations cannot be solved analytically, one must use numerical methods introducing errors. Only the simplified case of incompressible flow with constant property fields is considered. This condition renders the energy equation redundant. Turbulent (unsteady) flow is also assumed. Then using Cartesian tensor notation, the instantaneous continuity equation in the conservative form is,

$$\frac{\partial u_i}{\partial x_i} = 0 \tag{1.1}$$

and the momentum equation is,

$$\frac{\partial(\rho u_i)}{\partial t} + \frac{\partial(\rho u_j u_i)}{\partial x_j} = \frac{\partial}{\partial x_i}\sigma_{ji} + F_i \tag{1.2}$$

where u_i is the velocity in the x_i-direction, t is time, ρ is the fluid density, F_i is an external (body) force/unit volume in $[N/m^3]$, and σ_{ji} is the stress tensor which for a Newtonian fluid is,

$$\sigma_{ji} = -p\delta_{ij} + \mu\left(\frac{\partial u_j}{\partial x_i} + \frac{\partial u_i}{\partial x_j}\right) \tag{1.3}$$

where p is the pressure and μ is the dynamic viscosity. Liquids and gases flowing at low speeds behave as incompressible fluids. Without density variations there is no linkage between the energy equation and the mass conservation and momentum equations. The flow field can often be solved by considering continuity and momentum equations only. The energy equation only needs to be solved simultaneously if the problem involves heat transfer.

In the derivation of these equations the fluid has been regarded as a continuum. Activity at microscopic length scales exists in liquids and gases, however, for the analysis of fluid dynamics at macroscopic length scales (1 μm and larger) the molecular structure of matter and molecular motions are ignored. A fluid particle or point in a fluid is then the smallest possible element of fluid whose macroscopic properties are not influenced by individual molecules. Thus, the behavior of the fluid is usually described in terms of macroscopic properties, such as velocity, pressure, density and temperature and their space and time derivatives. These may be thought of as averages over a suitably large number of molecules. These conventions are followed here.

1.1.2 Physical Behavior

Based on their evolution in time, physical phenomena are divided into two principal categories of behavior [53]:

- Equilibrium processes
- Marching processes

The processes in the first category are steady state situations (e.g. the irrotational flow of an incompressible fluid) and mathematically they are governed by elliptic equations. In this case the information is considered to travel in space only, being constant in time. An important feature of elliptic problems, and this concerns both the physical and the mathematical behavior, is that a disturbance in the interior of the flow domain, changes the solution everywhere else. Disturbance signals travel in all directions through the interior solution. Therefore, to ensure that information propagates in all directions, the numerical techniques for elliptic problems must allow events at each point to be influenced by all its neighbors.

All unsteady flows, transient heat transfer and wave phenomena fall into the second category, the marching or propagation processes. Mathematically these problems are governed by parabolic or hyperbolic equations. In these cases the flow direction acts as a time-like coordinate along which marching is possible. Parabolic equations describe time-dependent flows which involve a significant amount of dissipation such as unsteady viscous flows. A disturbance at a point in the interior of the flow domain can only influence events at later times. The solutions of these equations move forward in time and diffuse in space. The steady state is reached as the time $t \to \infty$ and is elliptic. Time dependent processes with negligible amount of dissipation are governed by hyperbolic equations (wave equations). However, it is possible for a single flow to exhibit two types of physical behavior described mathematically by the associ-

ated equations. Such an example is the impinging jets flow discussed in this thesis where the elliptic behavior of the impingement region comes to add up to the " strongly parabolic" [46] behavior manifested by the free jet flows.

1.2 Onset of Turbulence

Turbulence is the most common state of fluid flow in a wide range of engineering applications and natural conditions. Since the critical Reynolds number has only a modest value, being of the order of 10 when referred to a transverse thickness [55], it follows that laminar flows are the exception rather than the rule in most engineering situations. A turbulent flow field is characterized by rapid fluctuations, a fact which probably led Boussinesq to reject deterministic models for the phenomenon, indicating the use of stochastic formulation [45]. He claimed that such a field is far too complicated to be known in complete detail. The present day literature is mostly restricted to the study of homogeneous, isotropic turbulence as an incompressible flow. The chaotic nature of turbulent motion could lead one to consider it as a counterpart of laminar motion. It is the Reynolds number ($\mathrm{Re} = \overline{u}l/\nu$), which gives a measure of the relative importance of inertia forces (associated with convective effects) and viscous forces, that people use to categorize different flows. Usually, a transition flow field is required for a laminar flow regime, characterized by an ordered displacement of adjacent layers of fluid and a lower Re, to emerge as a turbulent flow characterized by a random behavior and a higher Re number.

In general, a turbulent flow is characterized by the mean values of flow properties ($\overline{u}$, $\overline{v}$, $\overline{w}$, $\overline{p}$, etc.) and the statistical properties of their fluctuations (u', v', w', p', etc.).

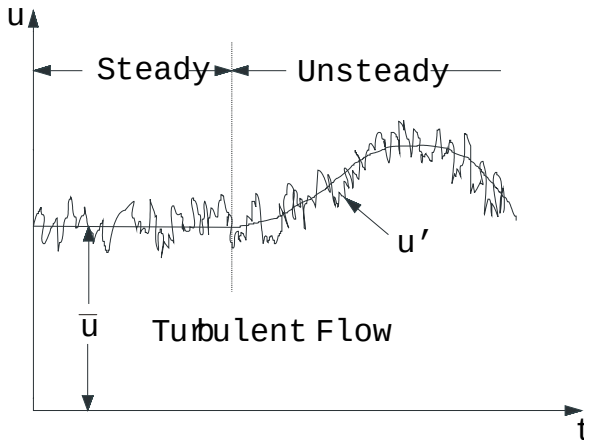

Figure 1.1: Steady and unsteady turbulent flow [55]

Thus, following the decomposition proposed by Reynolds, the randomly changing flow variables are replaced by mean values plus fluctuations about the average. In a Cartesian system and using tensor notations the velocity in Figure 1.1 becomes:

$$u_i\left(x_i,t\right)=\overline{u_i}\left(x_i\right)+u_i'\left(x_i,t\right) \qquad [m/s] \tag{1.4}$$

This rule together with the definition of time averaging of the mean value,

$$\overline{u_i}=\lim_{T\to\infty}\left[\frac{1}{T}\int_{t_0}^{t_0+T}u_i dt\right] \qquad [m/s] \tag{1.5}$$

are used appropriately for stationary turbulence (i.e. $\overline{u_i}$ does not vary with time). Therefore, the period T of the variation of mean value must be large compared to the relevant period of the fluctuations. Instead, if $\overline{u_i}$ has an observable variation with time, then as Figure 1.1 shows, we speak of this case as an unsteady flow.

Even in flows where the mean velocities and pressures vary in only one or two space dimensions, turbulence fluctuations have a tridimensional spatial character. Moreover, visualization of turbulent flows reveal rotational flow structures (i.e. turbulent eddies) with a wide range of length scales. Particles of fluid which are initially segregated can be brought together by the eddying motions in turbulent flows. As a consequence, heat, mass and momentum are very effectively exchanged yielding effective mixing. The largest turbulent eddies interact with and extract energy from the mean flow through the process called vortex stretching. The stretching work done by the mean flow on the large eddies provides the energy which maintains the turbulence. Smaller eddies are stretched strongly by somewhat larger eddies and more weakly by the mean flow. Through this " energy cascade" the kinetic energy is transmitted down from large eddies to progressively smaller and smaller eddies. All the fluctuating properties of a turbulent flow contain energy across a wide range of frequencies or wave numbers $\kappa=\frac{2\pi}{\lambda}$, where λ is the wave length [46]. The smallest scale of motion which can occur in a turbulent flow is dictated by viscosity. At these scales (on the order of 10 to 100 μm) and relative high frequency (about 5 to 10 kHz, in typical engineering flows) [53] viscous effects become important. The action of viscous stresses is partially counteracted by the work performed by eddies, so that the energy associated with the eddy motions is dissipated and converted into thermal energy. Therefore, through the dissipation process the energy losses associated with turbulent flow increase. The diffusive action of viscosity tends to overwhelm directionality at small scales. Thus, at high mean flow Re numbers the smallest eddies in a turbulent flow are isotropic (i.e. non-directional). However, the structure of the largest eddies is highly anisotropic (i.e. directional) and flow dependent due to their strong interaction with the mean flow.

1.3 Free Axisymmetric Submerged Turbulent Jets - Fundamental Concepts

In many cases of motion of a liquid or gas, tangential separation surfaces (thin flow zones separating one stream from the other) arise; the flow of fluid on either side of this surface is termed a jet. The jets may move in the same direction or in opposite directions and at different speeds. Even though the distribution of static pressure proves continuous (constant) throughout the flow, except for turbulent fluctuations within the layer, the other flow parameters such as velocity, temperature, etc. exhibit variations due to the tangential separation [2].

The term *" free turbulent flows"* describes turbulent motions that are not affected by the presence of a solid boundary. Some examples of free turbulent flows are an axisymmetric (round

or circular) submerged jet (Figure 1.2), a plane submerged jet and the flow in the wake of an immersed body, etc.

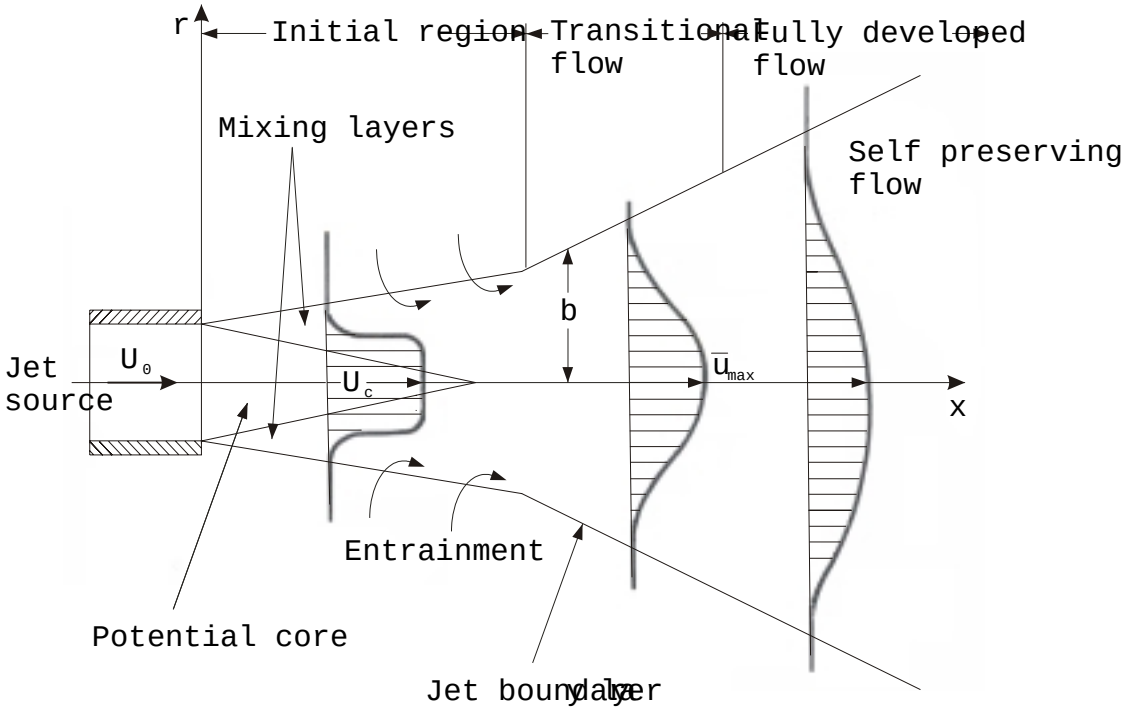

Figure 1.2: Schematic of an axisymmetric free submerged jet [55].

Figure 1.2 presents a sketch of the development of the mean velocity distribution in the streamwise direction for an axisymmetric free jet assuming a stagnant ambient fluid. The figure is valid for submerged jets only (e.g. air into air or water into water). A typical turbulent jet issues from the nozzle with a nearly uniform, fully turbulent velocity profile. The evolution of the jet starts with an almost inviscid flow termed *potential core* within which the centerline velocity, U_c, remains constant, and the *mixing layer* formed at the edge of the nozzle and growing between the stagnant ambient and the potential core. The potential core vanishes at a distance of about one diameter from the exit and there the velocity profile loses its mixing layer flat core shape [55]. Beyond the limit of the potential core, transition to turbulence occurs and the turbulence causes vigorous mixing of adjacent fluid layers and rapid widening of the region; this is the developing flow region. Velocity changes take place and Gaussian type velocity profiles where the maximum velocity, $\overline{u_{max}}$ is less than the exit centerline velocity are found. At about 20 diameters downstream of the nozzle and greater, the velocity profile exhibits a *self-preserving shape* [55],

$$\frac{\overline{u}}{\overline{u}_{\max}} = f\left(\frac{y}{b}\right) \tag{1.6}$$

where y is the radial direction and b is the *half width* of the jet (or $y_{\frac{1}{2}}$, the distance between jet axis and the point at which the velocity is equal to half the maximum axial velocity [2]). The

literature suggests that it would take longer for the turbulence components to fully develop. Self similar behavior is observed at about 50 diameters downstream for the axial turbulence component u' (rms value) and 70 diameters downstream for the transverse components v' (rms value) [55] in the case of a round jet.

$$\frac{u'}{\overline{u_{\max}}} = f_1\left(\frac{y}{b}\right), \quad \frac{v'}{\overline{u_{\max}}} = f_2\left(\frac{y}{b}\right) \tag{1.7}$$

Prandtl [34] showed that the instability of the tangential separation surface of a jet creates eddies on it, which move in a disorderly fashion both across and along the stream. This random process brings about an exchange of matter, a transverse transfer of momentum, heat and constituents between neighboring jets. Because of *entrainment,* the volume rate of the flow past any section in the jet increases in the x direction and the mean speed of the jet at its centerline decreases. The region of finite thickness which forms on the boundary of the two jets is termed the *turbulent jet boundary layer* and is characterized by a continuous distribution of velocity, temperature and constituents [2]. In the vicinity of the jet boundary layer large velocity gradients are present and so the terminology *" shear flow"* can be used [53]. Characteristically, free shear layer flows, and therefore free jets, are highly unstable.

For this type of flow the largest values of u', v' and the Reynolds stress $\overline{-u'v'}$ are found in the region where the mean gradient $\frac{\partial \overline{u}}{\partial y}$ is largest emphasizing the intimate connection between turbulence production and sheared mean flow. The component u' causes the largest of the normal stresses creating a discrepancy amongst fluctuating velocity magnitudes, which imply an anisotropic structure of the turbulence. Usually higher levels of turbulence (30%) are present in comparison with wall boundary layer flows. As $\left|\frac{y}{b}\right|$ increases, the mean velocity gradient tends to zero and therefore no shear exists; as a consequence turbulence cannot be sustained in this region. Also, the mean velocity gradient is zero at the centerline of the jet and hence no turbulence is produced here. However, the values of u' and v' do not decrease significantly because strong eddy mixing transports fluid from nearby regions of high turbulence production towards and across the centerline. By symmetry the value of $\overline{-u'v'}$ has to be zero at the centerline of the jet since the shear stress must change sign.

Most of the theory of turbulent flow and its modeling was initially developed by examination of the turbulence structure of thin shear layers. The free turbulent motion of a jet has an important property in common with boundary-layer (zero pressure gradient) motion , the width of the jet, b, is small relative to x, and the velocity gradient in the radial direction is large relative to the x direction $\left(\frac{\partial v}{\partial y} \gg \frac{\partial u}{\partial x}\right)$. Therefore, a boundary layer type of approximation applies. However, in free shear turbulent flows, viscous shear stresses can be neglected in comparison with turbulent stresses throughout the entire flow field. In wall bounded flows, the wall damps the turbulence (i.e. there are no turbulent eddying motions close to the wall), and therefore the fluid flow closest to the wall is dominated by viscous shear stresses. Since this laminar (viscous) sublayer is very thin, the shear stress can be considered constant and equal to the wall shear stress τ_w.

Complex flows such as the opposed impinging jets have in addition of the production of turbulence via shear (flow near nozzles) mechanisms attributable to pressure gradient forces (flow in the impingement region, i.e. imposed curved flow). In the impingement region, the usual production of turbulence by shear is absent being replaced by production due to normal stresses.

1.4 Opposed Turbulent Impinging Jets

Due to its important applications and also its physical complexity, the opposing jet problem is regarded with serious interest by numerous researchers in various fields. However, most of the studies refer to some particular applications such as the side dump combustor [27] and the mix head for RIM [57], where the two opposed impinging jets are wall-bounded, or, the studies pertain to combustion and flame investigations [56], which makes separation and assessment of the nonreacting opposed jets flow field difficult. Consequently a sparse amount of literature exists on free opposed turbulent impinging jet flows. Various differences between the geometrical and flow configurations used in the existing works do not allow a direct comparison among these studies. The only way they can be classified would be based on the nature of the work itself, experimental and/or computational, leaving their specific treatment of the problem to be individually discussed. However, no literature was found concerning the fundamental constituency of the flow field produced by axisymmetric opposed jets and under such flow conditions and geometric configurations as those considered in the present thesis. With the range of Reynolds number between 1500 to 11000 the flow falls in the fully turbulent category. Moreover a combined experimental-computational treatment is presented. As parameters of interest the mean and turbulent velocities pertaining to different regions in the flow, nozzle to nozzle spacing, extent of the different flow regions in the opposed impinging jet flow, initial frequency of the flow and frequency of oscillation of the impinging region can be mentioned.

1.4.1 Experimental Studies

Chronologically, three Russian scientists, Denshchikov, Kondrat'ev and Romashov [16], were the first to conduct free opposed impinging jet experimentations, following the model of the local hurricane winds (boras) based on the interaction between two opposing air currents proposed by Academician M.A. Lavrent'ev. This work outlines the oscillatory character of the interaction between two identical planar submerged water jets.

To preserve the two-dimensional character of flow they used two slit nozzles ($100 \times 80 \times 7$ mm) " in the form of plane boxes" [16] immersed in a water-filled transparent tank; the x and z dimensions of the tank ($1 \times 1 \times 0.23$ m) were huge in comparison with same nozzle dimensions, however the third dimension of the tank was just about three times greater than nozzle's same dimension (y). The velocity of the water issuing the nozzles was varied in the range of $2 - 20$ cm/s and the distance between nozzles was varied from 5 to 25 cm. Experiments were carried out with nozzles of width $\delta = 0.4$ and 0.7 cm.

They observed that at jet exit velocities, u, of the order of 10 cm/s, and a transverse nozzle size, δ, of 0.7 cm, the Reynolds number $\mathrm{Re} \simeq 700$, indicates that the jet is turbulent. Also, use of a single nozzle led to the formation of a characteristic jet in which motion was damped with distance and the jet had a stable position with respect to the symmetry plane. When adding a second opposed jet, " both jets begin to oscillate in the direction perpendicular" [16] to the symmetry plane. However, the results of these experiments are only of qualitative nature in the form of flow visualization. Even though the method of determining the period of the oscillations and the apparatus used are not revealed, photographs of the two opposed impinging water-jets colored with ordinary inks were taken at successive ordered times (i.e. $t = 0$, $T/4$ and $T/2$, where T is the oscillation period) [16].

For the above setup at constant flow Denshchikov et al. [16] observed that the amplitude and period of the oscillations are determined by the system itself. This is the reason why system's oscillations are then termed self-oscillations or auto-oscillations. For constant fluid properties (i.e. liquid density and viscosity), they considered the determining parameters of

the system the distance between the nozzles, L, and the characteristic jet-flow velocity, u (the velocity of a single jet at $L/2$ from the nozzle outlet). For given values of L and u, they reported periods varying between 2 and 30 s. Also, the period of oscillation remained constant within approximately $10 - 15$ %. Based on these experiments they presented an empirical formula $T = \frac{6L}{u}$.

In 1983, Denshchikov et al. issued a second paper on the same topic as mentioned above [17]. This experiment was an upgraded version of the first one using tap water as the working fluid. Laser Doppler measurements of the velocity profile issuing from a single nozzle with $\delta = 0.3$ cm revealed a rectangular profile of the mean velocity within 5 % accurate, also the pulsating components of the velocity did not exceed 2 % of the mean value; however they report 7 % rms error. This time the velocity at nozzle exit based on the flow rate of the water, was varied from " a few cm/s to 100 cm/s" [17].

Using the mechanical similarity and dimensional arguments they assumed the period of oscillation as being a function of jet velocity out of the nozzles, u_1, u_2, transverse dimensions of the nozzles, δ_1, δ_2, distance between nozzles, L, density of working fluid, ρ, and dynamic viscosity of the fluid, η (i.e. $T = T(u_1, u_2, \delta_1, \delta_2, L, \rho)$). Following the π theorem they found,

$$\frac{T}{T^*} = f\left(\mathrm{Re}_1, \mathrm{Re}_2, \frac{\delta_1}{L}, \frac{\delta_2}{L}\right) \tag{1.8}$$

where the dependence $T^* = \frac{\rho L^2}{\eta}$ was found experimentally. They observed that the period, T/T^*, of the auto-oscillations took maximal values when the lengths l_1 and l_2 of the two jets encountering on the symmetry axis were approximately equal. Based on their experiments the following formula was introduced for the case of equal jets,

$$\frac{T}{T^*} = 0.34\left(\frac{\rho L I}{\eta^2}\right)^{-0.5} \tag{1.9}$$

where, $I = I_1 = I_2 = \rho\delta u^2$ is the impulse of the jet.

In their findings, for $\mathrm{Re} < 90 - 100$ oscillations are absent for any value of the parameter δ/L and the flow can be assumed laminar; for $100 \leq \mathrm{Re} \leq 4800$ (the upper limit of Re in their study) the presence or absence of auto-oscillations depends on the value of δ/L. They noticed that the transition value of δ/L lays in the interval $0.16 - 0.24$. Also, for $\delta/L = 0.2$ and $\mathrm{Re} \leq 100$ the flow was considered laminar; the transition regime to turbulence was reported to be between $100 \leq \mathrm{Re} \leq 550$ and the fully turbulent regime for $\mathrm{Re} \geq 550$ [17].

Two years later Ogawa and Maki performed studies on opposed turbulent jets being mainly concerned about " influences of a body on the axis of opposed turbulent jets" [28]. In this experiment the authors attempted to establish the location of the impinging surface by velocity measurements taken with a hot wire anemometer. Once the natural impinging surface was found, their goal was to replace that with an impinging flat plate and then to insert a slender bar on the turbulent jet axis in order to determine its effects over the neighboring flow. Axisymmetric nozzles placed in the same symmetry plane were used with air as the working fluid. They mentioned an interior nozzle diameter of 28.2 mm and the existence of some kind of settling chambers before the nozzle exits. Even though reference to the nozzles' separation to nozzle diameter ratio is made, the limits of this ratio, the exact position and the geometry of the settling chambers are never specified (Figure 1.3).

There is no clear statement about the magnitude of fluid velocity used in these experiments. The lack of clarity and consistency in this work made the extraction of the main results and conclusions a difficult task. In this manner, observations valid for the existence of a solid

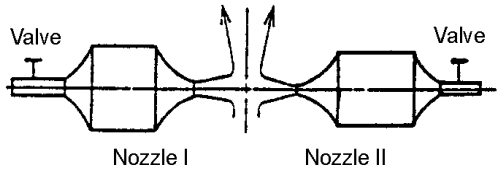

Figure 1.3: Nozzle setup [28]

impinging flat plate are commented as though a liquid impinging surface had been present and vice-versa.

Considering the opposed impinging jets case, they state that the impinging surface should be located where the respective total pressures in the flow issuing from the two opposed nozzles are equal [28]. Thus, the variation of total pressure on the jet axis between one nozzle and the impinging flat plate is measured instead using a " semi-conductor pressure transducer" [28].

Even though the article is abundant in graphical representations and values, the conclusions drawn here are more qualitative than quantitative. Thus, " the location of the impinging surface in the opposed turbulent jets is not only determined by the nozzle exit momentums, but is influenced significantly by the fluctuation in the flow fields" [28]. Also, turbulent intensities at nozzle outlets, on average, strongly influence the location of the impinging surface.

When the slender body is introduced on the jet axis, contrary to what one would expect as a conclusion of the well established turbulence theory, they conclude that, " since the mean flow distributions in the turbulent jet flow fields become as shown in Figure 1.4, it is considered that kinetic energy is locally transferred from the fluctuant to the mean components" [28].

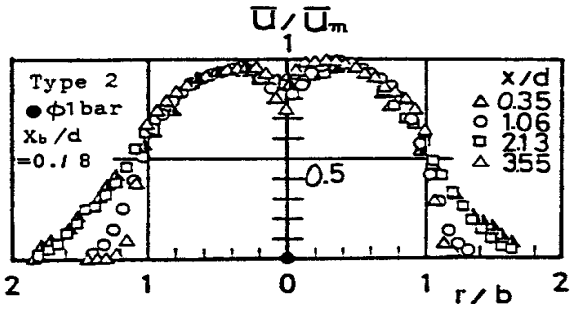

Figure 1.4: Transverse velocity profiles [28]

A possible explanation to their observation could be given by the appearance of a turbulent boundary layer along the slender body, turbulence which will influence the flow field upstream in the initial jet.

In 1992, the same research group, conducted a new set of experiments on opposed turbulent jets; the main interest this time was in establishing the impact position and the magnitude of the " turbulent component" in the jet center when two different grids were used to generate an uniform turbulent field [29]. A similar geometry configuration of the axisymmetric nozzles and " mass flow rates nearly equal" were employed. Even though some of the dimensions involved

are mentioned, there is no objective explanation of the reason for which two settling chambers of different volumes were used. Measurements of the impact position were performed by means of velocity measurements using a hot-wire anemometer set at 20 mm from the jet center and moved parallel to it [29]. During experimentation two grids of different aspect ratio (1 = fine grid, 2 = coarse grid) were interchanged at about 30 mm away from nozzle 1 exit.

In these experiments the point corresponding to maximum output of the anemometer was defined as the impact position of the two jets. Their results showed that in the case of $\mathrm{Re} = 5.61 \times 10^4$ and $L/D = 4.3$ (where L is the impact length and $D = 35$ mm is the nozzle diameter) the mean axial velocity of both nozzles are nearly constant when measured in the core region. Decrease in the mean axial velocity corresponding to nozzle 2 was observed when either one of the two above mentioned grids were introduced in the available slots of nozzle 1 (Figure 1.5 - a). Due to the difference in the characteristics of the settling chambers the magnitude of turbulence intensity associated with nozzle 2 was observed to be larger than that of nozzle 1 when no grid was inserted. The same flow and geometric features generated a greater turbulence magnitude in the vicinity of nozzle 1 when either grid was used (Figure 1.5 - b). As expected, a higher Re number flow (8.58×10^4) generated larger turbulent intensities, however the influence of Re number on the mean velocity profiles is insignificant [29].

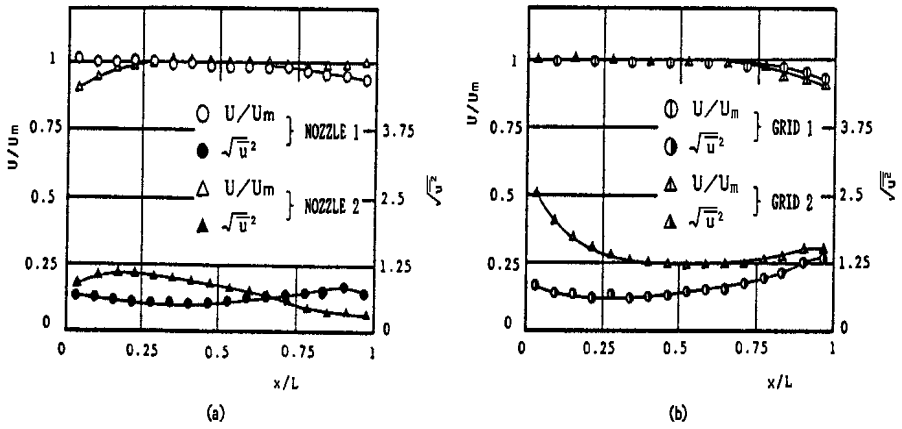

Figure 1.5: Axial mean velocity and turbulence intensity profiles: $L/D = 4.3$, Re = 56100 [29]

As figures 1.5 a, b show, instantaneous axial velocities and turbulent quantities were captured as if they represented the two initial free jets or two jets impinging on a flat plate, instead of two opposed jets colliding at a certain point or within a region situated between the two nozzles. The possibility of discerning the two initial jets (i.e. their characteristic parameters: velocities, turbulent values, etc.) in the neighborhood of the impingement region (i.e. within the same impact length, L, as if they were impinging on a fix flat plate) is hardly questioned.

Experiments carried out for larger nozzle to nozzle spacing ($L/D = 8.57$) revealed a substantial decrease of the mean axial velocity in the development region of the two jets for any of the Re numbers. Strong turbulence is observed everywhere except in the potential core region [29].

Mean transverse velocity (i.e. mean velocity profiles in the r direction) and turbulent intensity profiles showed a slight decrease in mean velocity at $x/D = 3.57$ and an increasing

turbulence intensity near the nozzle 1 exit (i.e. at location $x/D = 0.18$) when grid 1 was employed. Since at location $x/D = 3.57$ the turbulence magnitude did not show considerable changes, the authors concluded that the production of turbulence due to the shear layer dominates the initial grid turbulence [29].

Further, based on $U_1/U_2 = f(x_s/L)$ representations, where x_s is the impact coordinate and U_1, U_2 are mean velocities at nozzle exits, they divide the flow field into three regions: I - the region where the impact position is moved widely according to slight changes of U_1/U_2, II - the region near the nozzle 1 exit and III - the region near the nozzle 2 exit [29]. Specific length intervals (L/D) are given for different Re numbers, nozzle to nozzle spacing (L) and grid aspect ratio. Finally they affirmed that the impact position of two turbulent opposed jets " varies according to the magnitude of turbulence in the center of one side of the jet" [29]. It is also implied that in the case of $L/D = 4.3$, the two opposed jets impinge within the potential core region, however, in the case of $L/D = 8.5$, the impact takes place outside the potential core region.

In the same year, Shevtsov and Galin examined the effect of flowrate fluctuations on the turbulence characteristics of countercurrent coaxial jets [40]. Their work was part of a study of the effect of heat flux fluctuation in boiler furnaces on the temperature conditions of waterwall tube metal. The turbulence characteristics of steady (i.e. the flowrate is constant with time) and pulsating opposed impinging jets were investigated; comparison with the flow field created by a single jet impinging on a flat plate situated at $H/2$ downstream was performed. The experiments involved two countercurrent coaxial planar jets with constant and pulsed flows of $\mathrm{Re} = 2 \times 10^4$ situated at a distance of 200 mm (i.e. $H = 20h$, where h is the height of the nozzle). Due to a honeycomb and a fine mesh installed in the channels, the initial degree of turbulence of each steady stream was low (about 0.45%). In the experiments with pulsating jets, before issuing from the nozzles the air was passed through a pulsator so that the flow was pulsated in single phase ($\Delta\varphi = 0$) and in antiphase ($\Delta\varphi = \pi$).

Their setup provided an almost constant frequency distribution in velocity at the nozzle outlet and the velocity profiles differed by no more than 3%. The data obtained by Shevtsov and Galin showed that the resulting flow of two countercurrent coaxial jets with a steady flowrate differs substantially from the structure of a jet impinging onto a flat plate located at a distance $H/2$ from the plane of discharge. A summary of the outlined differences that may apply to this configuration are:

- the profiles of average velocity in the transverse cross-sections of countercurrent jets suggest a fully developed jet flow;
- the degree of turbulence at the nozzle outlet is twice as high (i.e. $2 - 2.2\%$);
- at station $x = (5 - 7)\,h$ the velocity fluctuations reached peak relative values and the degree of turbulence exceeds 50%;
- in the impact region of the two opposed jets (i.e. at about $H/2$) the averaged velocity was observed to drop by $24 - 27\%$ with respect to the maximum;
- analysis of the spectra revealed that fluctuations in velocity are strongly displaced towards the low frequency region ($0 - 40\ Hz$). The amplitude is considerably higher than corresponding fluctuations in the case of an impinging jet onto a flat plate ($1.7 - 2$ times higher).

Their findings concerning the differences in opposed pulsating jets from countercurrent steady jets are as follow:

- the turbulent intensities relative to the mean velocity in pulsating jets is $10 - 40\%$ higher;

- the turbulent velocity spectra for the pulsating jets contain harmonics which are multiples of the excitation frequency;

Comparing the influence of the phase of pulsation on the resulting flow field of two opposed jets the researchers observed that with flow pulsating in antiphase ($\Delta\varphi = \pi$), the energy of turbulent velocity fluctuations is higher than with ($\Delta\varphi = 0$). Also, the energy of the axial turbulent velocities with antiphase velocity pulsation corresponding to a certain excitation frequency is lower than that with flow pulsations in one phase.

Regarding the experimental model as a simplified model of a furnace chamber, from the point of view of the effect of the spectrum of heat flux fluctuations on the temperature conditions of the metal, they concluded with the recommendation that it would be better to locate the burners on one waterwall, rather than in an opposed jet arrangement on opposite walls.

1.4.2 Numerical Studies

The present study also involves the numerical modeling of one of the turbulent opposed impinging jet configurations. A complete description of the techniques used in the numerical simulation is given in Chapter 3 and the CFD results are presented in Chapter 4. This section includes the review of the only numerical paper found in the literature that studied turbulent opposed impinging jets.

In 1993, Champion and Libby published a numerical study involving two closely spaced turbulent jets flowing counter to one another, for both two-dimensional and axisymmetric configurations [10]. By closely spaced they indicated that the diameter of the jets is large compared to their separation distance, therefore the option of two widely separated jets where large-mixing with the surrounding ambient occurs, is excluded. They consider the flow associated with closely spaced, opposed jets consisting of an outer region between the jet exit and the neighborhood of the plane containing the stagnation line or point, termed the stagnation plane, and a thin layer centered about that plane in which adjustments to various quantities on each side take place. The absence of a wall in the vicinity of the opposed jet flow is also mentioned; thus, the lack of a viscous sublayer in these flows made it suitable for application of a high Re number version of the Reynolds stress equations. In this study, the asymptotic analysis, coupled with a Reynolds stress approach, is used to determine the turbulence characteristics in a known mean velocity field. The implication is that in a Reynolds stress formulation in which there is no direct connection between the velocity gradient and the mean shear stress, the fundamental conditions at the plane of symmetry are the vanishing of the mean normal velocity and the Reynolds shear stress. The schematic of the opposed jet flow modeled in this paper is shown in Figure 1.6.

With the appropriate interpretation of the coordinate systems and thus the velocity components, this representation was used to simulate both two-dimensional and axisymmetric configurations. It has to be mentioned that grid or baffle generated turbulence was implied. Based on the grid geometry, the scale of the turbulence was determined and found to be small compared with the jet spacing $2d$. The assumptions of a small integral scale of the turbulence compared with half the separation distance of the jets and a low intensity of the turbulence issuing from the jets form the basis of an asymptotic analysis. Consequently, excepting the thin layer centered about the stagnation plane and within which " the discontinuities in the flow from each jet are adjusted" [10], the mean velocity components are given by the mean Euler equations.

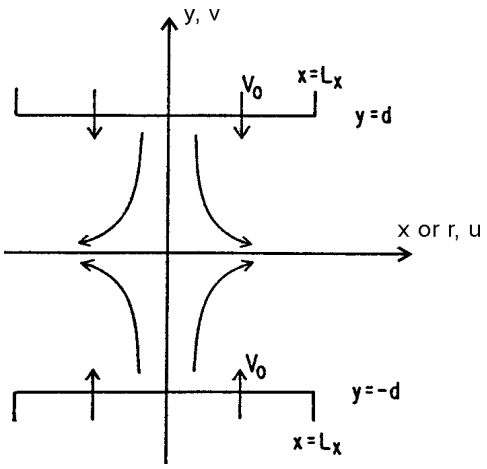

Figure 1.6: Schematic of opposed jet flow [10]

The analysis is divided into two parts, the planar case and the axisymmetric case. For each of these cases the outer region and the inner region receive individual treatment. Neglecting molecular conduction, the temperature characteristics are also discussed. Even though they considered that the velocity field is doubly symmetric (i.e. symmetric about both the $x = 0$ plane, termed the plane of symmetry, and the $y = 0$ plane, termed the stagnation plane), a different geometry and adjustments for both the Reynolds shear stress and temperature variables were performed in the axisymmetric case.

Comparisons amongst the two different geometric configurations (i.e. two-dimensional and axisymmetric) revealed close values for the mean axial velocity component and mean axial pressure distributions. However, the mean radial velocity (relative to initial velocity V_0) distributions (Figure 1.7) and the turbulent quantities as $y/d \rightarrow 0$ exhibit significant differences in the two flows. Also, in axisymmetric flows, the gradient of the Reynolds shear stress increases continuously from its imposed initial value of zero in contrast with an initial increase but subsequent decrease to zero in two-dimensional flows.

Besides the above mentioned general results, the authors performed a comparison with the experimental data provided by a previous study of Kostiuk [10]. The experimental data was compared to opposed circular jets with air as the working fluid. Similar to the experiment, the simulation test conditions were as follows: the two jets of diameter $d = 35\ mm$ were spaced at $2d$ apart and the mean velocity at the exit plane of each jet was $9\ m/s$. Perforated plates with holes having diameter of $3\ mm$ and a blockage ratio of 50% were installed in each jet slightly upstream of the exit plane.

For the authors, a comparison with the original experimental data proved impossible due to their asymmetric character (i.e. the stagnation plane is not equidistant from the two jets). However, when both jets were considered symmetric about the stagnation plane in the sense of the smaller value of the initial stagnation plane - nozzle spacing, good agreement was found amongst mean axial velocities from both sides of the jet. Finally, even though the authors consider the agreement to be satisfactory, due to the scatter of the experimental data, the available plots show that the numerical model overpredicts the experimental Reynolds stress distributions.

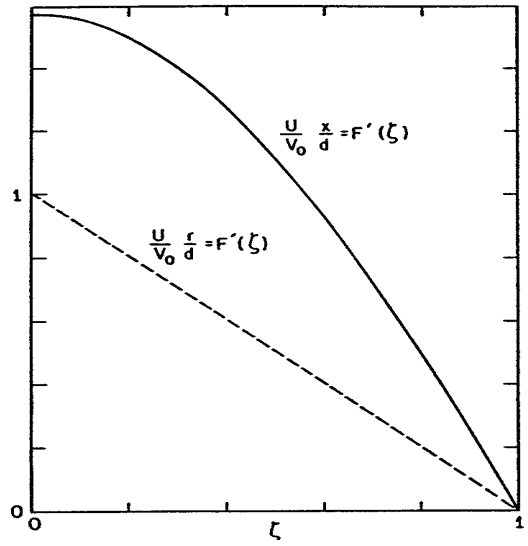

Figure 1.7: Mean radial velocity profiles for axisymmetric (——) and two-dimensional (- - -) flows [10]

Chapter 2

The Experiment

In this chapter, the experimental setup, the apparatus used to obtain experimental data and the associated techniques are described. Several interconnected tasks must be addressed: opposed jets configuration, flow visualization, theory and practice of Laser Doppler Anemometry (LDA), theory and practice of Particle Image Velocimetry (PIV), data analysis, and measurement noise and accuracy. Each of these components will be considered in turn.

2.1 Experimental Arrangement

2.1.1 Opposed-Jets Configuration

Given the fundamental aspect of the present research, the purpose is to establish a valid set of data for a particular geometrical model (i.e. axisymmetric nozzles) satisfying the general characteristics of the flow involved and which can subsequently be extended to derivative geometries. All the experiments were conducted in the Turbulent Flow Laboratory at the University of Waterloo. The principal components of the experimental configuration are the two axisymmetric nozzle models mounted in an opposed jets configuration. Three sets of nozzle pairs of different length (see Table 2.1) have been designed and manufactured out of aluminum tubing with an inner diameter, $d = 12.7\ mm$ and a wall thickness of $1.587\ mm$. The spacing between nozzles and the length of the nozzles were established based on the following reasons:

- To achieve the proposed nozzle to nozzle spacing, L, the length of the nozzles must vary.
- To study unconfined and uninfluenced opposed impinging jets, the tank dimensions must be large in comparison with the dimensions of the flow field developed between the two nozzles in order to avoid exterior perturbations and wall effects. Therefore the tank dimensions are multiples of nozzle to nozzle spacing, L, and implicitly depend on the spacing parameter $L^* = L/d$.

- The nozzles have to be long enough to ensure a fully developed flow at nozzle outlets, i.e. nozzle length, $l \gg 10 \cdot d$.

Water proof connections were achieved through a pair of intermediate adapters with the roles of facilitating the interchangeability of different length nozzles and fastening the nozzles to the tank wall. In the present case of axisymmetric nozzles, intermediate adapters of circular cross section have been used. The two opposed nozzles have been properly rigged and aligned by means of a 5 mW Helium Neon laser beam. Without considering the intermediate adaptors and the wall connectors, the length of the nozzles and the nozzle to nozzle spacing involved in our case of study are summarized in Table 2.1 below.

Table 2.1: Configurations of opposed nozzles

$Configuration$	I	II	III
$L\ [mm]$	250	127	63.5
$L^* = L/d$	20	10	5
$l\ [mm]$	270	332	363

Free jets are described in the literature [2] as flows that are very susceptible to disturbances in the surroundings. As it will be discussed later (Chapter 4), this characteristic has proven true in the case of opposed impinging jets too and more pronounced at small velocities. Small perturbations of any kind in the background environment can greatly affect the flow field and make repeatable measurements difficult to obtain. Moreover, these flows are very difficult to visualize and to seed properly, which becomes important for the use of the laser based measurement techniques chosen herein. For some techniques (e.g. PIV) proper seeding and the use of particles that follow the true flow is essential. For these reasons, even though flow visualization was performed using both air and water as the working fluids, water ($\rho = 998\ kg/m^3$, $\mu = 1.0 \times 10^{-3}\ kg/(m \cdot s)$) was used for instantaneous velocity measurements. According to Reynolds similarity principle, comparable experiments accomplished in different fluid mediums will provide the same flow characteristics, on the condition that the flows are geometrically similar, if the Re number for the two flows is the same and the flows are incompressible. Thus, extending the results obtained in a water based case to incompressible air flows (i.e. small speeds, subsonic) is possible.

Four sets of experiments were conducted for each nozzle to nozzle spacing parameter. The Re number of the respective flows is the product of the wetted diameter and the associated volumetric flow rate of the nozzle which gives the initial average velocity U_0. These values are given in Table 2.2.

Table 2.2: Kinematic flow parameters

Re	1500	4500	7500	11000
$Q\ [m^3/s]$	$1.507 \cdot 10^{-5}$	$4.510 \cdot 10^{-5}$	$7.512 \cdot 10^{-5}$	$1.101 \cdot 10^{-4}$
$U_0\ [m/s]$	0.119	0.356	0.593	0.869

Air or water were supplied to the nozzles by means of equal lengths flexible tubing, wall connectors and intermediate adaptors so that the two resultant jets impinge upon each other. Providing that the two nozzles are opposite each other, the spacing parameter, L^*, is constant,

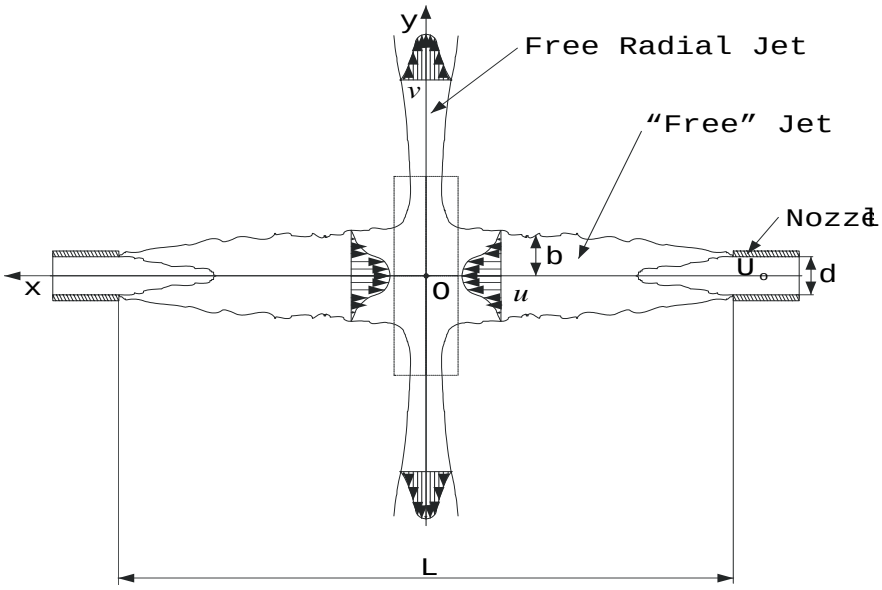

Figure 2.1: Opposed jets configuration

the fluid is supplied to the nozzles at the same flow rates and the environment is identical with the fluid issuing from the nozzles (i.e. submerged jets), the two jets impinge on each other in a region situated at about $L/2$ downstream and spread radially outwards resembling a free radial jet. Figure 2.1 shows a schematic of the flow field for the opposed jets configuration used in these experiments.

2.1.2 Apparatus and Instrumentation

The general opposing jet system which, with some small modifications, has also been used for the impinging jet on a flat plate and free jet investigations, includes a large main tank made of transparent acrylic where the submerged nozzles are located, two volumetric flow-meters, a centrifugal submersible pump, a reservoir and a few valves needed to thoroughly control the flow. The overall setup of the opposing jet system is displayed in Figure 2.2.

Given its large working dimensions in comparison with nozzle's diameter, i.e. length $\times$ width $\times$ height $= 1193.8 \times 584.2 \times 584.2$ mm, the main tank provided the unconfined (or uninfluenced by wall) flow environment required by this study. All measurements were taken while the level of water in the tank was constantly maintained at 525 mm from the bottom surface, which ensured a stagnant three dimensional medium into which the opposing jets issued. Flow visualization, as well as velocity measurements, will demonstrate the validity of these conditions. The tank's transparent walls allowed optical access to the measuring points so that velocity measurements could be obtained.

Water was supplied to the nozzles through a submersible centrifugal pump providing a flow-rate up to 75 l/min at a height of 1.2 m.

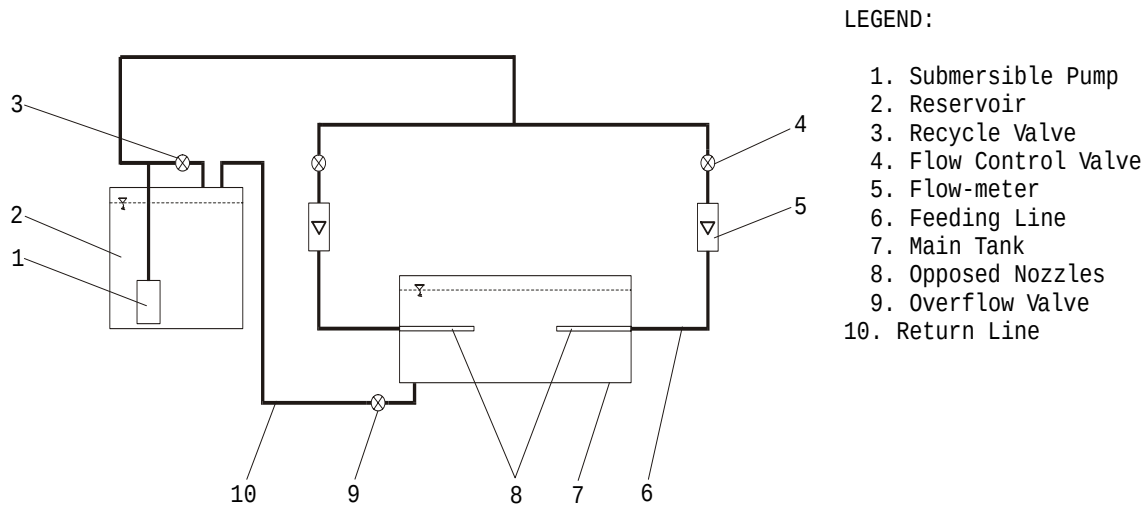

Figure 2.2: Overall sketch of the flow system (not to scale)

The overflow valve placed near the bottom of the main tank, made it possible to maintain a constant level in the main tank by recirculating the water to the reservoir. Two SK Instruments flowmeters (tube no. 4-HCFB, float 44-J STN. STL.) were employed to ensure identical volumetric flow rates, Q through both nozzles (see Table 2.2). By means of a pressurized air supply and corresponding flow meters, air was supplied to the nozzles for the air based visualization case.

2.2 Flow Visualization Technique

Flow visualization methods are integral to experimental fluid dynamics and can always reveal important characteristics of the flow field. They can also provide information regarding how and where velocity measurements should be undertaken. A variety of flow visualization techniques have been reviewed by Merzkirch and others [24], [30]. There are several methods of time line visualization (i.e. velocity profile) such as the photochromic dye tracing method and the laser induced fluorescence or phosphorescence (LIF or LIP) which can provide limited quantitative information [30]. However, conventional visualization methods for a liquid flow, such as the dye injection method and other tracer injection methods, can only give qualitative information about the flow field; special attention has to be paid in choosing a neutrally buoyant dye which would truly follow the flow. Buoyancy differences between the marker and the fluid are difficult to interpret. Thus, to fully understand the flow field characteristics, detailed information such as mean and turbulent velocities are required. These quantities can be measured using a velocity measurement technique such as laser Doppler anemometry (LDA) and/or particle image velocimetry (PIV). The theory and practice associated with these are discussed in section 2.3.

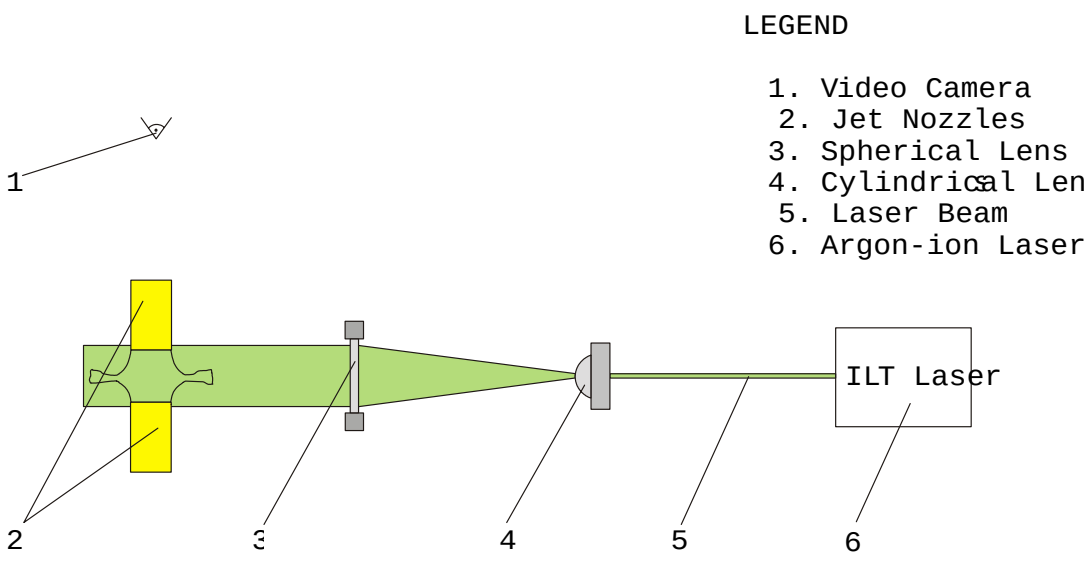

Figure 2.3: Flow visualization setup (LIF technique)

2.2.1 Flow Visualization Setup - LIF Technique

The LIF technique was used to visualize the flow field created in the imaginary horizontal plane containing the centerline of the two nozzles. This was accomplished by illuminating the respective cross-sectional plane with a collimated laser light sheet while soluble fluorescent dye was injected into the flow going to one of the two nozzles (see Figure 2.3).

A collimated planar laser beam, wide enough to cover the range of nozzle to nozzle spacings mentioned in Table 2.1 has been obtained by passing the coherent light beam of a 500 mW argon ion laser ($\lambda = 514.5\ nm$) through a succession of cylindrical (to obtain a planar light cone) and spherical (to get a collimated planar light sheet) lenses.

It is well known that fluorescent dye provides enhanced visibility when illuminated by a laser light beam, however it is not well observed under normal lighting conditions. Since dye injection is a partially invasive technique, Fluorescein dye has been injected far upstream into the flow of one of the two nozzles in order to obtain an uniform distribution of dye concentration and to avoid disturbing the flow. Thus, the green radiation emitted when the Fluorescein dye was excited by the argon ion laser revealed the flow field generated by the opposed impinging jets. A video camera placed normal to the laser sheet acquired a successive set of images of the flow field for a period of 3 to 5 minutes. Further, the PIV technique also permitted interactive flow visualization with image saving while velocity measurements were collected.

The only differences in flow visualization technique consisted of using polypropylene (50 to 150 μm diameter) or Titanium Dioxide (TiO_2, 0.3 to 2 μm diameter) particles and a high energy Nd:YAG pulsed laser instead of soluble dye as means of revealing the flow pattern. Thus, similar flow visualization images were obtained for all opposing jets flow configurations. For the air based case, flow visualization was undertaken using smoke generated tracer particles.

Flow visualization images and an insight into the physical process observed by visual inspection will be presented in Chapter 4.

2.3 Velocity Measurement Procedures

Standard techniques for measuring local instantaneous velocity such as hot wire anemometry and pressure measurement (Pitot-static) rely on the insertion of a probe into the flow. These are usually categorized as invasive techniques and can cause flow disturbances and are sensitive to the particulate content of the flow.

" Non-invasive" techniques usually rely on optical methods to separate the measurement device from the fluid, however, the fluid must be often " seeded" with some form of tracer particles, which themselves interact with the flow.

For measurements of the kinematics of turbulent opposed impinging jets, a measurement technique with at least the following characteristics would be required:

- Given the instability of free and impinging jets, a " non-invasive" technique would be essential, since the effect of any probe in the flow would be significant.
- The supposed " similar" character of the flow as well as its unsteady (oscillatory) behavior make a time history of the flow at one point as well as instantaneous spatial velocity maps important.
- Since the flow field generated in the case of two axisymmetric turbulent impinging jets is considered to be axisymmetric in the average, a two dimensional measurement technique will suffice.
- As many experiments were planned, a method capable of automated analysis would be beneficial.
- Accurate velocity information is always desired.

Given the large amount of data that had to be collected, two " non-invasive" techniques that satisfy the above criteria have been used to measure the instantaneous velocities and therefore mean and turbulent velocities in the present investigations, LDA and PIV. Due to its recognized quantifiable precision, LDA has been employed to create a reference case which will then be used to evaluate the application of the PIV technique to this particular flow. Moreover, PIV was preferred for its high density planar data output. However, to get true data both methods require knowledge of the range of velocities being measured.

2.3.1 Laser Doppler Anemometry Technique

LDA is a non-invasive method that allows measurement of velocity at an isolated point (small volume) in space over a period of time. It provides a time history of the flow, and hence time averaged statistics, at one point.

The underlying measuring principle of LDA is the Doppler shift of light scattered from small (0.1 to 10 μm) particles. A particle moving through the intersection point of two laser beams scatters light at a different frequency than that of the incident laser beams. The difference frequency is known as the Doppler shift and in the case of a dual beam approach it can be detected using a stationary detector. " Differential Doppler" [1] is another term applied to the dual-beam approach of the Doppler effect. There is extensive literature dedicated to the theory and practice of LDA [19], [18], [32], [36].

The single component dual beam approach is the most common optical arrangement used for LDA measurements. Two or even three velocity components could be measured simultaneously if an extension of this configuration is considered. Even though a two-component dual beam forward scatter LDA system has been used in the present experiments, since the operat-

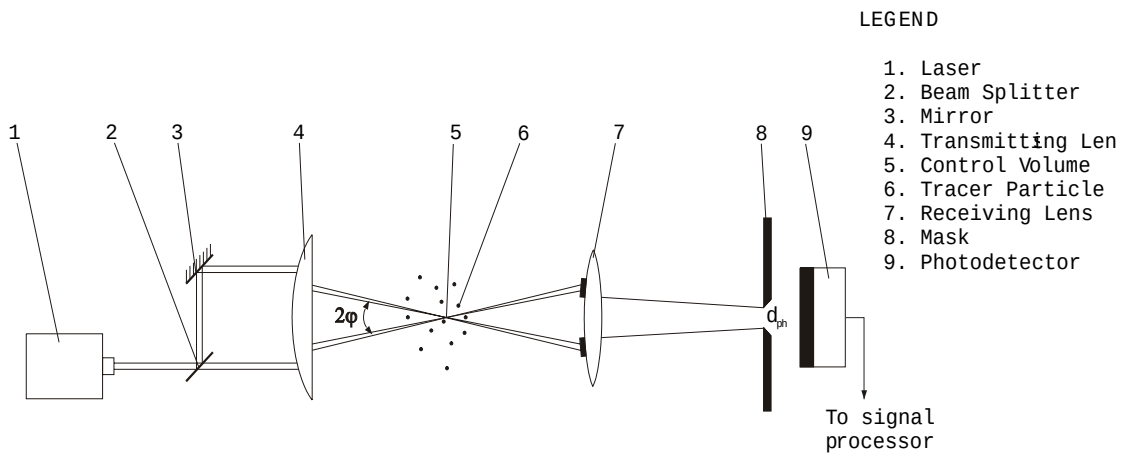

Figure 2.4: LDA - Differential Doppler mode [52]

ing principle is generally the same, a single component dual-beam forward scatter configuration will be discussed here. Figure 2.4 shows the basic components of a LDA system.

The " fringe" model of LDA will be described. The single component dual beam LDA system uses a collimated, coherent light source, a laser, whose beam is passed through a series of optics to transform it into a pair of green (blue or other wavelength light) beams focused at a common point, and to provide the framework for fluid flow velocity measurements. A beam splitter separates the initial laser beam into two beams of equal intensities. At this point, usually a frequency shift of one of the beams is introduced. The frequency shift in velocity measurements in reversing flows, high turbulence and fluctuating flows with zero mean velocity is used to resolve flow directional ambiguity. Intersecting a frequency shifted laser beam with an unshifted one, results in a fringe pattern that moves from the beam of higher to that of lower frequency. The direction of positive velocity is opposite to the movement of the fringes. In a certain flow, a particle in the control volume could be stationary and then the Doppler shift is the " frequency" difference between the two interfering beams, can move with the fringes and the Doppler shift will be lower or it can move against fringes and the Doppler shift will be higher [12], [13]. Furthermore, frequency shifting allows a better signal to noise ratio. Then, a transmitting lens will focus the two beams to a common intersection point where an ellipsoidal measuring control volume (mcv) is created (Figure 2.5).

Moire fringes can be used to explain the basic characteristics of an LDA system [52]. As Figure 2.5 shows, when two beams with the same frequency intersect, it is assumed that a stationary interference fringe pattern forms in the measured control volume. The fringe spacing, Δx, is independent of the properties of the fluid. It depends on the laser wavelength, λ, and half of the angle between the intersecting beams, φ, [52]

$$\Delta x = \frac{\lambda}{2 \sin \varphi} \qquad [mm] \tag{2.1}$$

When the fringe model is combined with the Gaussian behavior of the interfering beams, an ellipsoidal surface on which the amplitude of the fringes is $1/e^2$ of the maximum intensity is obtained at the intersection point. In three dimensional coordinates, this surface generates the above ellipsoidal control volume.

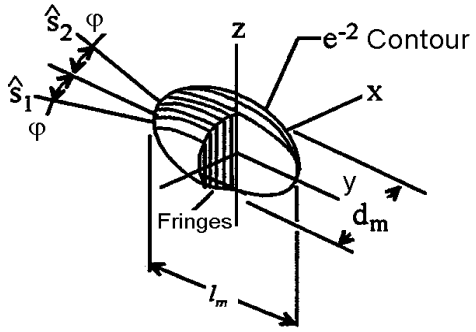

Figure 2.5: LDA measuring control volume [52]

The mcv dimensions (i.e. the ellipsoid axes, in this case denoted as the diameter and the length of mcv) can be calculated using the following relationships [52]:

$$d_m = \frac{d_{e^{-2}}}{\cos\varphi} \qquad [mm]\,, \qquad l_m = \frac{d_{e^{-2}}}{\sin\varphi} \qquad [mm] \tag{2.2}$$

where $d_{e^{-2}}$ is the diameter of the focused Gaussian laser beam (or the focal waist) measured at $1/e^2$ of the centerline intensity and at the focal spot. The focal waist is calculated as a function of the beam waist measured at a focal length before the transmitting lens, $D_{e^{-2}}$, the focal length, f, of the transmitting lens, and the laser wavelength, λ, [52].

$$d_{e^{-2}} = \frac{4f\lambda}{\pi D_{e^{-2}}} \qquad [mm] \tag{2.3}$$

The resultant number of fringes would be [52],

$$N_{fr} = \frac{d_m}{\Delta x} = \frac{1.27d}{D_{e^{-2}}} \tag{2.4}$$

where d is the beam separation before transmitting lens.

Light scattered by tracer particles passing through the measuring control volume is collected by the receiving lens and focused onto a mask in front of the photodetector. A pin-hole is used to localize the collected light from the measuring volume. The effective mcv is the volume imaged onto the pinhole of the photodetector. The resultant " beating" light signals are detected by a photodetector which transforms them into electrical signals proportional to the intensity of the scattered light, making it possible with subsequent processing by appropriate electronic means to yield a certain instantaneous velocity vector component. The relationship between the component of the velocity perpendicular to the fringes, $U_\perp$, and the frequency of the photodetector signal, f_D, is linear [52],

$$U_\perp = f_D \Delta x \qquad [m/s] \tag{2.5}$$

where the Doppler frequency is given by the difference between light scattered from the two beams, $f_D = f_{s_1} - f_{s_2}$.

Receiving optics for the dual beam system can be placed at any angle, however, the forward and the back scatter arrangement are the most used due to the highest scattered light intensity. In a back scatter configuration, the photodetector and the collecting optics are usually mounted on the same module with the transmitting optics. The advantage of this arrangement is that the receiving optics move simultaneously with the transmitting optics, and thus they are always aligned. In a forward scatter configuration, the receiving optics and the photodetector are positioned separately from the transmitting optics, beyond the mcv and looking forward to it. In either arrangement, the resulting signal from the receiving system will still give the same frequency. However, signal quality and intensity will vary greatly. Due to the fact that the intensity of light scattered by a particle depends on scattering angle (see section 2.4) [52], for a given LDA system, the signal intensity is several orders of magnitude larger in forward scatter.

To optimize a LDA measurement, particles that follow the flow may be added to it and a photodetector that provides an optimum signal-to-noise-ratio at the photodetector output should be used. Due to its high amplification and low noise output, in most applications the photodetector is the most suitable. A signal processor that extracts the maximum information from the signal, and accurate data processing techniques that provide the needed flow parameters from the output of the signal processor, are also needed.

2.3.2 LDA Implementation

The LDA system employed in the present experiments is a two-component dual-beam forward scatter system. It consists of a laser, optics, two photomultipliers (PMs), two counter processors, a frequency shifter, a digital oscilloscope and a computer and interfacing hardware. An overall schematic of the LDA experimental setup is provided in Figure 2.6. A complete description of the hardware and operation of the Dantec LDA modules is given in the manufacturer's manuals [12], [13], [14] or/and [22].

The laser and optics are mounted on a computer controlled three perpendicular axis traversing rig so that accurate displacements can be achieved. 1 mm displacement of the LDA in any of the three directions corresponds to 160 steps in the stepper motor. All stepper motors are controlled by the main data acquisition computer via a subroutine integrated into the processing software and a parallel printer port. The PM module is separated and attached to a mobile tripod placed on the other side of the main tank and aligned with the LDA optics in the forward scatter configuration. Given the available equipment, even though a back scatter arrangement could also have been used, the forward scatter configuration is preferred for the above mentioned reasons. The same nozzle configurations and experimental arrangement as those described in section 2.1 and employed for flow visualization were used to obtain LDA measurements. The traversing rig system made it possible a rigorous (within 1.5 % error, the deviation of the laser system displacement with respect to the measurement plane was observed to be about 1.5 mm in 100 mm displacement) alignment of the mcv with the desired measurement plane (the imaginary horizontal plane containing the centerline of the two nozzles).

A low power argon-ion laser, ILT model 5500A, provides the collimated, coherent light source needed in these experiments. The generated light is dominant at 488 and 514.5 nm wavelengths. In LDA measurements, enough laser power to satisfy the light scattering condition that ensures a good PM input signal is required. Even though the maximum output power of this laser can be adjusted up to 500 mW, power in the range of $200-250$ mW provided sufficient power for the required measurements.

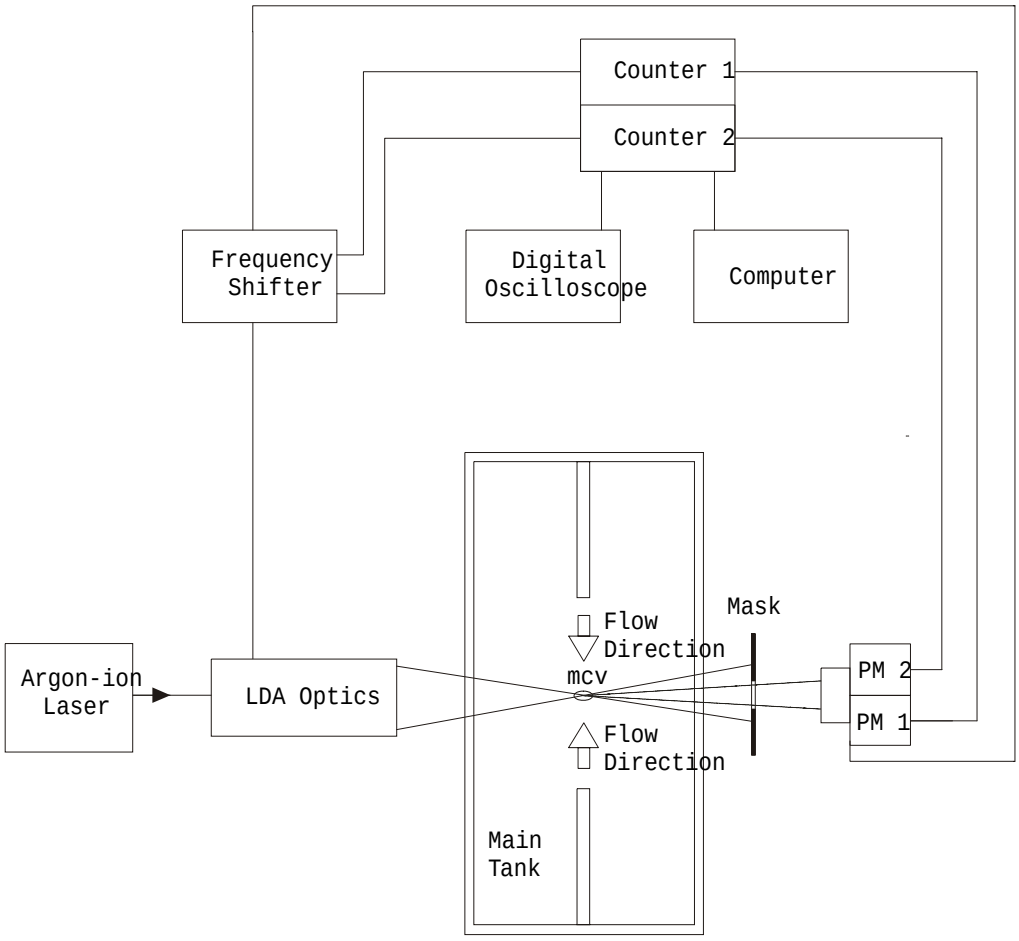

Figure 2.6: Schematic of the LDA Experimental Arrangement

The Dantec 55X Modular Optics follows the argon-ion laser in the present LDA system. It consists of a series of integrated components such as a beam waist adjuster, beam splitters, Bragg cell, back scatter module for mounting the PM optics if the forward scatter arrangement is not practical, and a front lens. The beam waist adjuster allows the beam waist to be located within the mcv in order to optimize the fringe pattern quality. Upon entering the LDA optics and then the beam waist, the initial cyan laser beam is split into two beams of equal intensity by a neutral beam splitter. The 55N10 frequency shifter provides a 40 MHz signal that controls a Bragg cell used to optically shift one of the beams by 40 MHz. This is to avoid directional ambiguity and to improve the signal to noise ratio. The frequency shifted beam is then passed through a splitter and color separation module generating one green beam at 488 nm and one blue beam at 514.5 nm, with either a positive or negative 40 MHz shift with respect to the unshifted beam. The same splitting and color separation are applied to the unshifted beam. A beam translator is then used to set the separation distance, $d = 39$ mm (and thus the intersection angle) at which the beam pairs leave the optics. The last components of the optics

module are a beam expander and a 600 mm focusing lens that focuses the four beams to a common intersection point, the mcv.

After leaving the transmitting optics the four laser beams pass through the acrylic side wall of the main tank and create the mcv at their intersection point.

For the above mentioned arrangement two PMs are employed to detect and convert the optical information to electrical output signals. The signal reaching the PMs consists of the Doppler frequency representing both the 40 MHz frequency shift and the particle frequency. To achieve optimum resolution and noise filtering in the signal analysis equipment, the PM output signal is downshifted electrically by means of a mixer block within the frequency shifter module. Based on the velocity range of interest, the effective shift of the Doppler frequency may by selected in the range of 10 KHz to 9 MHz. In the present experiments, the maximum fluid velocity has not exceeded 1.5 m/s so the shift of the Doppler frequency has been set to 1 MHz. A mask was placed before the PM to guard it against high light intensities. The PM module used in these experiments incorporates the X34 photomultiplier optics having a focal length of 600 mm and the pin-hole to locate the mcv. To satisfy the high voltage excitation demand of the photosensitive elements of the PMs, they were connected to a high voltage supply module in each of the counters via high voltage coaxial cables. The PM module was located at about 600 mm (including the correction imposed by the refractive index of the acrylic wall) away from the intersection point of the laser beams, on the opposite side of the main tank. During the experimentation, the transmitting optics and the PM module were always aligned. The output signals from the PMs were sent to the LDA counters via the frequency shifter described above.

The Dantec 55L90a LDA counters operating in conjunction with the 55N10 frequency shifter provide a very sophisticated electronic system for analysis of an LDA optical signal. They are timing devices with burst detection and noise rejection circuits to discriminate between Doppler shift frequencies and noise [22]. The signal that corresponds to each particle passing through the control volume is termed a Doppler burst. LDA counters are used to find the frequency of these bursts by measuring the time it takes a particle to cross 8 interference fringes (the time between successive zero crossings is supposed to be relatively constant) and so to determine the Doppler frequency corresponding to that particle. The Doppler signal is initially filtered to remove high and low frequency noise, amplified and then the burst time duration is measured. The signal is validated using the 5/8 comparison scheme described in [14]. This validation process corresponds to the fixed N_f mode of the counters' operation.

The output signal of each counter was monitored on the screen of a high speed digital oscilloscope (LeCROY 9400A). It provided the necessary visual information such as the Doppler burst shape and the presence of noise in the counter output signals, which along with the counter's data rate modules helped to optimize the adjustment of the focus and pin-hole mcv location of the PMs.

The LDA optical-counter processor configuration parameters are summarized in Table 2.3. Due to room temperature variations, the beams are adjusted at the translator so that the four beams overlap perfectly (checked on a millimetric sheet of paper when the intersection point of the four laser beams was passed through a microscopic lens) producing the smallest possible mcv. Thus, the new mcv dimensions were calculated using Equations 2.1, 2.2, and 2.4.

Table 2.3: LDA optical-counter processor parameters

Parameter	Green Beam (Vertical)	Blue Beam (Horizontal)
$\lambda\ [nm]$	514.5	488
$f\ [mm]$	600	600
$2\varphi\ [^\circ]$	6.81779 ± 0.15	6.61166 ± 0.15
$d_m\ [mm]$	0.06032	0.06359
$l_m\ [mm]$	1.01267	1.1009
$\Delta x\ [mm]$	4.32633×10^{-3}	4.23129×10^{-3}
N_{fr}	14	15
Optical Shift Frequency $[MHz]$	40	40
Doppler Shift Frequency $[MHz]$	1	1
Low Pass Filter $[kHz]$	2000	2000
High Pass Filter $[kHz]$	256	256

2.3.3 LDA Data Acquisition and Processing

Prior to performing LDA measurements and in order to identify and limit the most important regions in the flow where measurements had to be taken, a map of the flow field (based on the flow visualization images previously recorded) was created using the ImagePro software package. This preliminary map of the flow field and considerations regarding the number of data points to be collected, led to the generation of an efficient two dimensional measuring grid.

The measuring grid corresponding to these specifications has a 2 mm, uniform grid spacing in the transverse direction and a two way bias spacing with an expansion factor of 1.195 in the longitudinal direction.

LDA measurements were performed mainly with regard to the case $L^* = 20$ and for the opposed impinging jets only. In all experiments, 40960 instantaneous velocity samples were collected at a constant sampling frequency of 250 Hz. As recommended in water flow experiments and a forward scatter LDA configuration, the natural particles occurring in the fluid were adequate seed. In an attempt to determine the oscillatory behavior of the flow field, a limited number of data sets containing 40960 velocity samples have been acquired at 1 kHz or 2 kHz sampling frequency. In these cases, the measurement points were situated within the impingement region of the two opposed jets at positions similar to those for which samples were collected at 250 Hz. A planar coordinate system, xy ($z = 0$), similar to that pictured in Figure 2.1 was used in taking the velocity measurements. The corresponding velocities are u and v.

The LDA system uses a PC 286 AT computer for data acquisition and pre-processing. It runs three DOSTEK FORTRAN programs (subsequently in house modified) which cover the main data acquisition task, the configuration of the laser optical-counter processor system and the pre-processing work. The pre-processing module provides various options regarding sampling frequency, number of data samples to be acquired, filtering, calculation of local mean and turbulence velocities and related parameters. All data processing was performed off line on another computer.

2.3.4 Particle Image Velocimetry Technique

Similar to LDA , the PIV technique allows the measurement of the velocity of a fluid element indirectly by means of the velocity of tracer particles initially added to the flow. A full field method, PIV is an extension of flow visualization techniques, where velocity vectors can be

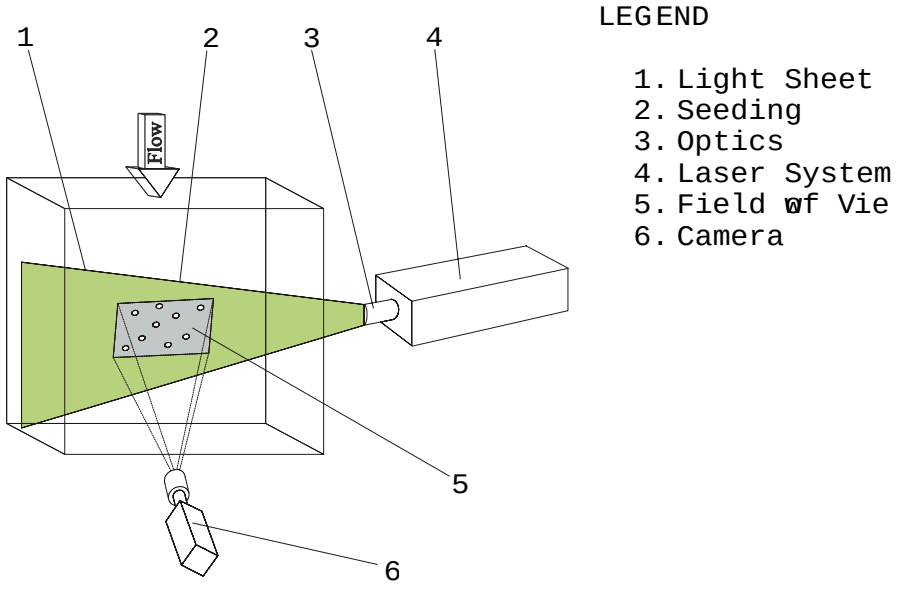

Figure 2.7: Basic principle of PIV [15]

measured simultaneously at thousands of points. With PIV the spatial resolution is high, whereas the temporal resolution may be limited.

PIV is based on measurement of the displacement of particle images in the time between two laser flashes (multiple flashes can also be used) that illuminate a plane within the flow field. Knowledge of the displacement and time between images gives the local particle velocity. Figure 2.7 concisely depicts the configuration of a typical PIV system [15].

Even though PIV was developed from Laser Speckle Velocimetry in the early 1980's [3], the technique is still under development today. As with the LDA [54], some of the uncertainties pertaining to the PIV method have not been well documented yet. The reader is referred to the book by Raffel and Willert [37] for detailed information on PIV, and only a brief description will be given here.

Typically, a PIV system consists of several subsystems (Figure 2.7): tracer particles, a light source (laser) with the associated optics, an image recording device, a programmable time delay and sequence generator, a camera interface, computer and image acquisition/processing software.

This combination allows time continuous velocity measurements by PIV, a process that can be divided into the following steps:

1. The flow is seeded with small neutrally buoyant tracer particles which follow the motion of the fluid. Since, in general, most of the seeding considerations in LDA also apply to PIV, a common treatment of the seeding topic, outlining the distinctive features corresponding to each of the two methods will be sought. Due to this approach and its acknowledged importance within the laser based measurement methods, a separate section, 2.4, is set apart for seeding issues.

2. A measurement plane within the flow is illuminated with a two-dimensional pulsing light sheet.

3. Images are captured to a resolution that will allow an appropriate object - image scale factor S.
4. Images are analysed by dividing the acquired image up into a number of small " interrogation regions" and calculating one velocity vector for each interrogation area.
5. The results are post processed to provide vector maps and to remove systematic errors, noise and erroneous vectors.

Each of these steps will be discussed in turn.

2.3.4.1 Illumination

As previously mentioned, due to the contradiction between the particle size and the demand of high light intensity scattering, in most applications a compromise has to be found. Thus, usually in liquid flows larger particles and a lower power light source are accepted while light sources of high power and tiny tracer particles are required for a good illumination in gas flows. In PIV, the velocity information is extracted by determining the distance travelled by seeding particles between successive illumination pulses, i.e.

$$u\left(x,t\right)=\frac{\Delta s(x,t)}{\Delta t}\qquad [m/s] \tag{2.6}$$

where, $u\left(x,t\right)$ is the local spatial mean velocity (and also the instantaneous velocity at a certain time), and Δs is the local mean displacement over the illumination interval Δt.

Since the seeding and the illumination are strongly interrelated, in addition to the aspects mentioned in the seeding subsection, the illumination interval and the flow velocity range must be such that seeding particles travel in the range of $2-20$ particle diameters between each illumination pulse [7]. The maximum out of plane particle motion should be limited to 30 % of the light sheet thickness. To control this parameter, the light sheet thickness, or the time between laser pulses, should be varied. The time separation between laser pulses, Δt, " is the single most important adjustable variable in a PIV system, as it determines the maximum and minimum velocities that can be measured" [3]. In order to reduce the number of particles leaving the light sheet plane between pulses, the most practical solution is to decrease the time between the laser pulses considerably. The duration of the laser pulse determines the degree to which an image is frozen during the pulse exposure. It is the programmable time delay and sequence generator which is mainly responsible for the synchronization between laser pulse generation and camera performance.

The choice of a light source to generate a pulsing light sheet of sufficient intensity is between pulsed lasers such as Nd:YAG (neodymium: yttrium-aluminum-garnet crystals) which deliver a short time duration intense pulse of light, and continuous wave lasers such as argon-ion whose output must be modulated to create a lower power pulsing illumination. Due to their high output power, the Nd:YAG lasers are preferred for PIV applications.

2.3.4.2 Image Capturing

PIV records the light which is scattered by particles illuminated by a thin laser sheet. PIV images may be captured by conventional photography, videography or by using a charged-coupled device (CCD) camera positioned at right angles to the light sheet. Since the governing parameter in the dynamic range of the PIV system is the spatial resolution, the choice of image capturing method is very important. It is well known that photographic recording achieves

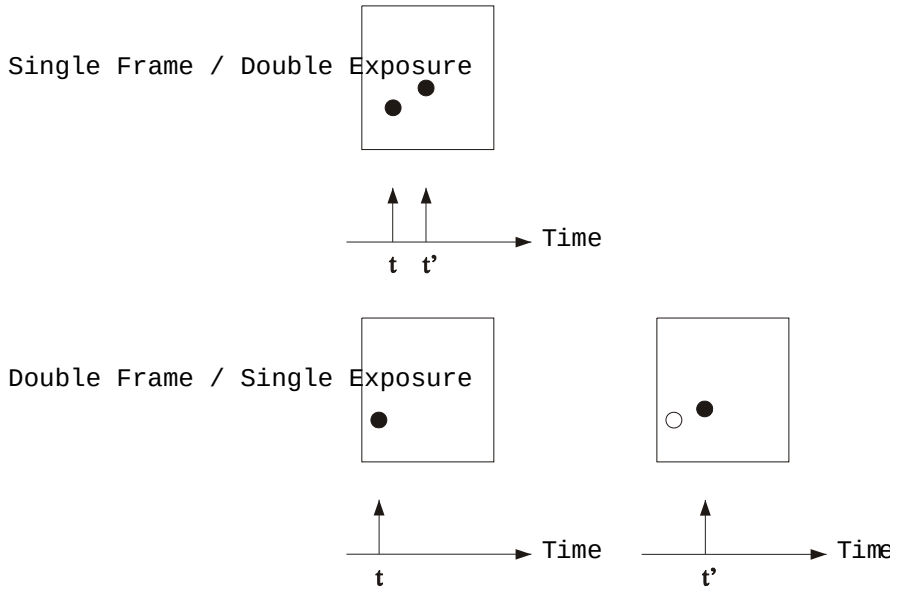

Figure 2.8: Sketch of two PIV recording techniques [37]

a higher spatial resolution than can be obtained with current methods of digital videorecording, especially when using large formats (e.g. standard video tubes offer a resolution of about 500×500 pixels, available high resolution video arrays offer 2048×2048, a standard 35 mm frame of 30 lines per mm Kodak Technical Pan contains 10500×7500 pixels and CCD cameras are available with resolutions up to 4096×4096 pixels [3]). Even though CCD sensors with increasing resolutions are continuously under development, it will take time until digital recording techniques can reach the spatial resolution of present day film material. Thus, at least for PIV applications in high velocity flows with requirements of high spatial resolution, the photographic technique is the method of choice.

The illuminated flow plane can be captured on to a single frame, a method called single frame / multi-exposure PIV or a single illuminated image for each illumination pulse, method referred to as multi-frame / single exposure PIV. The single frame / multi exposure method has the disadvantage that it does not retain information on the temporal order of the illumination pulses, giving rise to a directional ambiguity in the recovered displacement vector. The multi frame / single exposure method inherently preserves the temporal order of the particle images (Figure 2.8) [37].

One major disadvantage of the photographic technique is that it is difficult to record the images of the tracer particles on to different frames, especially for high speed flows where the time separation between laser pulses is extremely small (i.e. a few microseconds). That implies solving the problem of directional ambiguity. Given this problem and the fact that a high quality and reliable focusing device is necessary in order to save time in the alignment of the system (and of course based on availability), the multi-frame / single exposure PIV method as well as a CCD camera would be preferred. If a lower spatial resolution is accepted, the multi-frame / single exposure approach with illumination pulses delivered asynchronously extends PIV recording to provide images even in high speed flows. Nowadays CCD cameras can switch frames fast enough, the pulsing light sheet and the camera are synchronized so that particle

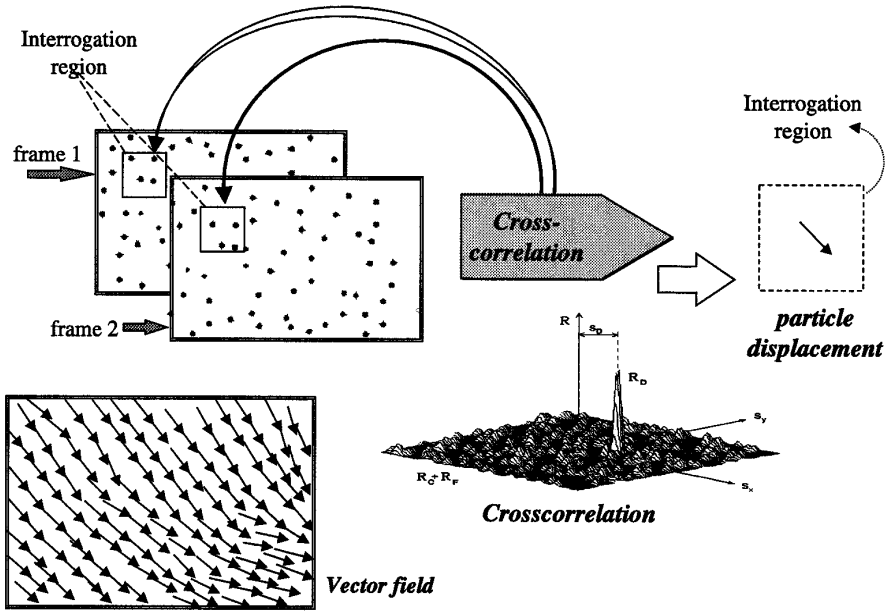

Figure 2.9: PIV image analysis [1]

positions at the instant of laser pulse number 1 are recorded on frame 1 of the camera, and particle positions from pulse number 2 are recorded on frame 2.

2.3.4.3 Image Analysis

This is the most important stage in PIV. Standard (commercial) PIV analysis does not follow the behavior of individual particles. The seeding concentration is too high to resolve individual particles in most PIV applications and therefore a particle tracking method cannot be used to follow the motion of individual particles. Instead, a section-by-section statistical analysis is performed on small rectangular areas of the flow field, creating a grid of velocity information. The small areas are called " interrogation regions" and for each interrogation region the image from the first and the second pulse of the light sheet are correlated to produce an average particle displacement vector. Dividing this by the time between laser pulses, an average velocity vector is computed (Figure 2.9).

Typically, interrogation areas for cross-correlation PIV measure 64×64 pixels on a digitized image of 1024×1024 pixels, yielding a 16×16 vector map, if the interrogation areas do not overlap. Interrogation areas are often overlapped by up to 75 %, but in so-doing care must be taken to avoid registering velocities taken from the same particle pairs in more than one location.

PIV recordings are evaluated by locally cross-correlating two frames of single exposures of the tracer particles ensemble (see Figures 2.8 and 2.11).

The success of image correlation demands that each interrogation region contains several particles. Since PIV is an instantaneous measurement technique, all spatial information is sampled at the same time and therefore a finite statistical probability that there will be regions where there is really no meaningful input exists. The projection of the interrogation regions

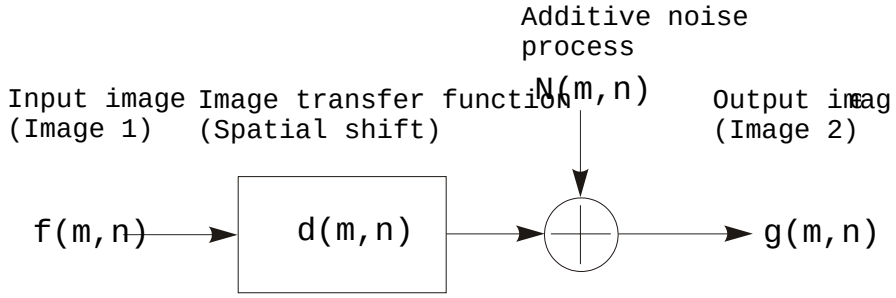

Figure 2.10: Idealized linear digital signal processing model for the double frame /single exposure recording method [37]

into the light sheet would be the interrogation volumes (due to light sheet thickness). The effect of perspective projection, which is a result of seeding particles moving into or out of the interrogation area in the period between the two recordings, is taken into consideration by the PIV analysis technique as a noise function, $N(m,n)$, where m,n are image coordinates measured in pixels [15]. N contains the recording noise, the effect of perspective projection and the most important, the noise contribution due to FFT based correlations.

Considering signal (image) processing, the first image of the pair may be considered the input to a system whose output produces the second image of the pair. Thus, a transfer function d, which converts the input image to the output image exists. In Figure 2.10 the transfer function d takes $f(m,n)$ as input and adding the noise function $N(m,n)$ would output the image function $g(m,n)$. The function $f(m,n)$ describes the light intensity within the interrogation area recorded at time t, and the function $g(m,n)$ describes the light intensity recorded at time $t+\Delta t$ [37].

The target is to estimate the displacement field d, knowing f and g and excluding N. However, the signals (images) are not continuous, i.e. the dark background cannot provide any displacement information, therefore a statistical approach based on localized interrogation areas is used to estimate the displacement. This is accomplished through the use of the discrete spatial cross-correlation function whose integral formulation is given by the Equation 2.7

$$R_{fg} = \sum_{i=-K}^{K} \sum_{j=-L}^{L} f(i,j)g(i+x,j+y) \tag{2.7}$$

where (i,j), (K,L) describe image coordinates in pixels while (x,y) represent the object coordinates measured in mm [37]. A direct calculation of the spatial cross-correlation function implies taking advantage of the theorem which states that the cross-correlation of two functions is equivalent to a complex conjugate multiplication of their Fourier transforms [37]:

$$R_{fg} \Leftrightarrow F \cdot G \tag{2.8}$$

where F and G are the Fourier transforms of the corresponding lower case functions. In practice, the implementation of the Fourier transform is done numerically on a computer by means of the Fast Fourier Transform (FFT) algorithm [8] which reduces considerably the number of computations. Figure 2.11 illustrates the implementation of cross-correlation algorithm using FFT. The two dimensional correlation process of Equation 2.7 is therefore reduced to computing

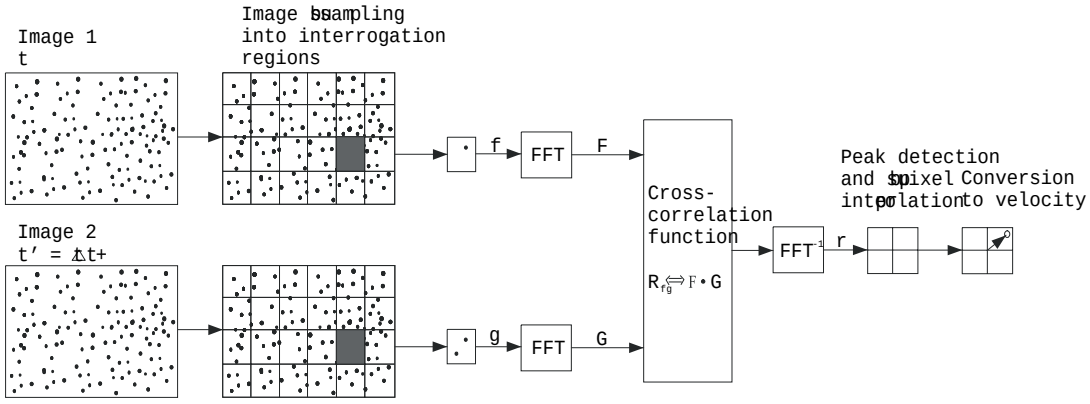

Figure 2.11: Cross-correlation method for PIV image processing [37].

two-dimensional FFTs on equal sized interrogation regions of the images followed by a complex-conjugate multiplication of the resulting Fourier coefficients.

This result is then inversely Fourier transformed to produce the actual cross-correlation plane which has the same spatial dimensions as the input plane. A high cross-correlation value is obtained where many particles match up with their corresponding spatially shifted partners (true correlation) and small cross-correlation peaks may be observed when individual particles match up with other unrelated particles (random correlations). Tracer particles entering or leaving the interrogation region during the period between the recording of the first and the second image will not contribute to the true correlation; however, they decrease the signal to noise ratio through the " loss-of-pairs" effect. The highest correlation peak can be considered to represent the best match between the functions f and g when the number of matching particle pairs is large. The position of the peak in the correlation plane corresponds directly to the average particle displacement within the interrogation area investigated. However, the use of a two-dimensional FFT for the computation of the cross-correlation plane imposes a number of properties whose effects have to be dealt with. These effects are: fixed sample sizes - the most common FFT implementation requires the input data to have a base-2 dimension (e.g. 64×64 pixel samples); periodicity of data - the Fourier transform is an integral (or sum) over an infinite domain $(-\infty, \infty)$ while in this case the integrals are computed over finite domains which is justified assuming the data to be periodic; this assumption leads to a nonuniform weighting of the data in the correlation plane (aliasing) and to a bias displacement vector.

2.3.4.4 Post-Processing

Given the huge amount of data that is usually collected, fast and automated post-processing of the PIV data is desired. PIV analysis is based on a statistical process relying on parameters which are not always under control, such as local seeding concentration and variations in illumination and visibility. Thus, a finite probability of incorrect velocity vectors (" outliers") being returned exists. In order to detect and eliminate these erroneous vectors the raw flow field data have to be validated. Although visual detection is possible, if a great number of recordings has to be evaluated, manual elimination would not be efficient. Different techniques for data vali-

dation have been described in the literature [35], [37], [15]; however, no general solution for the problem of data validation in PIV is offered. These include a global histogram operator, dynamic mean value operator, peak height ratios, and velocity range validation. The purpose of validation is to detect, reject and remove the outliers and using interpolation / extrapolation techniques to possibly substitute other vectors instead of the rejected vectors. The substituted vector is estimated from the surrounding measured vectors. Usually the substitution is done to improve the visual appearance of the vector map and is similar to filtering a signal.

Generally, the validation methods can be classified into:

- Single point validation, which evaluates the validity of every single vector (i.e. checks if the vector is in a certain velocity range), and
- Whole flow field validation, which evaluates all vectors in a map or in a smaller region by comparing each vector with its neighbors and analysing the difference.

Also, chain validation sequences can be applied by combining the above methods. It is recommended that a peak level validation be followed by moving average validation or a single point validation should be applied before a whole field validation. Methods which substitute vectors should be applied last and then only under certain conditions.

2.3.5 PIV Implementation

The same nozzle configurations and experimental arrangement as those employed for the flow visualization and LDA measurements were used to obtain PIV measurements. The PIV system used in these experiments was a Dantec FlowMap PIV 2100 including the following components: a light source (Nd:YAG pulsed laser) with the associated optics, a CCD camera, a programmable time delay and sequence generator, a camera interface, computer and image acquisition/processing software. A complete description and operation of the Dantec PIV system is given in the manufacturer's manual [15]. The experimental setup used in the present results is shown schematically in Figure 2.12.

2.3.5.1 The Seeding

Prior to acquiring any image the flow issuing from the two opposed nozzles was seeded. As recommended in section 2.4 the seeding particles are required to follow the flow passively and faithfully, and scatter light efficiently. In these PIV experiments seeding the flow has proved itself crucial for the success of the measurements.

The most important parameter in determining whether the particles will follow the flow, from the dynamic and buoyancy point of view, is the difference in density between the fluid and the particles. Considering the incompressible character of these flows (i.e. $\rho_{water} = const.$) and the density of water at standard temperature and pressure conditions, $\rho_{water} = 998\ kg/m^3$, a material for which the density of the particles is constant would be preferred. Subject to availability, particles made of two different materials and two size ranges were used independently to seed the opposed jets flow. The first were polypropylene particles (spheres). Besides their physical characteristics summarized in Table 2.4, they are cheap even in large volumes, but with a large spread in particle diameter. Prior to adding seeds into the reserve tank used for recirculating the fluid, they were soaked for several minutes in a small amount of tap water. During the trials performed to evaluate their behavior under the present flow conditions, it was seen that their size, density, and light scattering properties were appropriate for these measurements. To ensure an appropriate particle concentration within the image plane, the fluid has

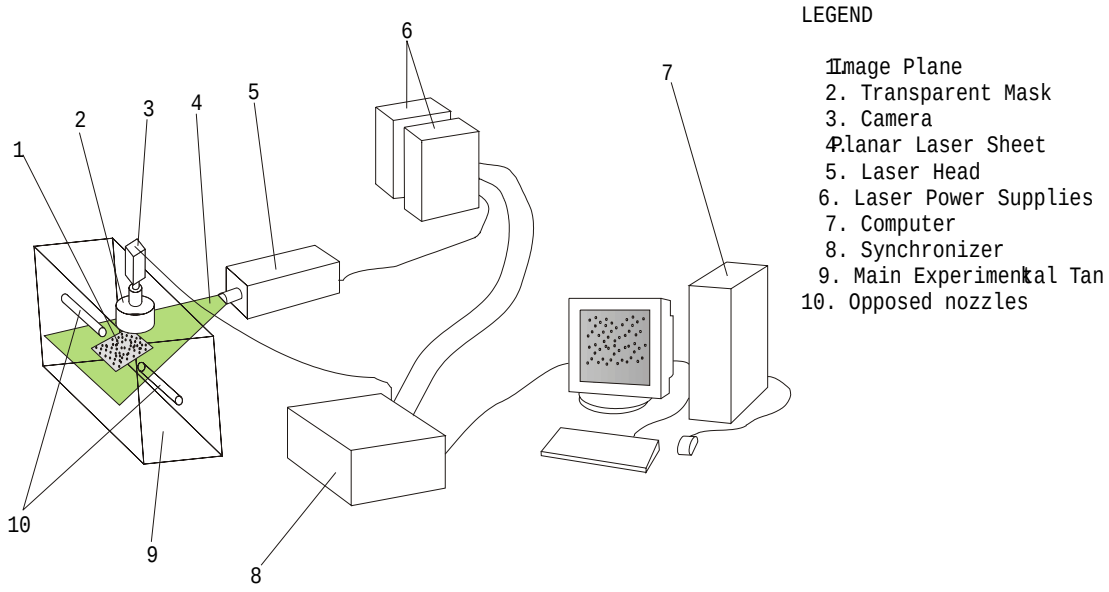

Figure 2.12: PIV Experimental Setup

to be seeded occasionally due to the slow upward rise of the particles in the main and reserve tank volume. This also implied a thorough mixing of the reserve tank prior to acquiring new images. Particles rising from lower levels tended to collect at the free surface of the water leading to some signal loss within the recorded images and resulting in excessive concentration on the mask (described in section 2.3.5.3) surface which often needed clearing. A complete set of, say 250 images has to be made up of three or four image subsets for this reason.

Table 2.4: Properties of tracer particles

Seeding description	Density $[g/cm^3]$	Particle size $[\mu m]$	Purity [%]
Polypropylene	0.94	$50 - 250$	95.0
Titanium Dioxide (TiO_2)	4.26	$0.3 - 2$	94.0

Titanium dioxide particles were the second choice in these experiments. They are more expensive, but can be delivered with a narrow size distribution. Usually, their use is recommended for air based flows, however, after soaking and mixing them in a small amount of water for a few minutes and then adding this compound to the large capacity reserve tank, they manifested good suspension and spreading characteristics in water. Although their properties (see Table 2.4) were different than those of the polypropylene particles, their global behavior was very good. Even though the particles were very small, the light scattering property ensured excellent visibility. Particle concentrations within the acquired images was good, leading to little reseeding of the flow and seldom clearing of the mask.

The errors which arose from seeding are discussed in section 2.6.

2.3.5.2 Illumination

The amount of illumination energy required for PIV is significantly higher than that required for LDA because a plane rather than a point is illuminated at a poor normal scattering angle, since the PIV camera is positioned at 90° to the light sheet rather than 180° (forward scattered) or 0° (back-scattered).

In these experiments, the light sheet was provided by a New Wave Minilaser Nd:YAG illumination system. It contains a dual-cavity, Q switched Nd:YAG laser [15] with $2 \times 120\ mJ$ output. It is able to provide sufficient energy density for obtaining images of seeding particles in the present flow. The light sheet optics have an adjuster for varying the light-sheet thickness and a protective beam obstructor. The dimensions of the delivered light sheet covered the desired flow field completely (i.e. the distance between nozzles by main tank width). The laser is integrated in the setup and the 532 nm wave length laser beam path is shielded from surroundings under normal operating conditions.

The illumination system is mounted on a tripod with possibilities of height adjustment, 360° rotation in the horizontal plane and about 25° rotation in each corresponding vertical plane. This system allowed alignment of the light sheet with the desired measurement plane, in this case the imaginary horizontal plane containing the centerline of the two nozzles and the right angle placement of the camera with respect to the laser sheet. The thickness of the light sheet passing through the flow (cross section of the tank) was set to about $2 - 3\ mm$ by measuring it on the input acrylic wall of the main tank.

The laser has a fixed repetition rate of 15 Hz (the laser is flashing in response to an internal trigger pulse generated at this fixed frequency) and the pulse duration has been set to 10 ns to minimize streaking effects of faster moving particles and yet provide enough light for the recording of images. The laser was pulsed from each cavity at a variable period between pulses depending on the following parameters: velocity being measured (Re number), particle size and type (material) and type of flow (opposed jets). Prior to setting the final time between pulses, a preliminary longest value has been calculated using the following formula [15]:

$$t \leq \frac{8Sd_{pixel}}{U_{\max}} \qquad [\mu s] \tag{2.9}$$

where, $U_{\max}$ is the maximum velocity estimated in the flow field (assumed to be $1.5 \cdot U_0$), S is the object:image scale factor and d_{pixel} is the pixel pitch (i.e. 9 μm for the Kodak ES 1.0 camera). A summary of the illumination periods (i.e. time between pulses) used in these experiments is given in Table 2.5.

Table 2.5: Opposed impinging jets flow - PIV illumination time

		Time between pulses $[ms]$			
Average velocity of the flow as Re $(\times 10^3)$		11	7.5	4.5	1.5
Seeding	Polypropylene (PP powder)	1.5	2.7	4.7	10.5
	TiO_2	1.0	1.6	3.0	9.2

2.3.5.3 Image Acquisition

The image acquisition system consisted of a Kodak Megaplus Digital Camera ES 1.0 through which the signal was quantized at 8 bits per pixel by an image digitizer and processor. Accurate

measurements of the various positions within the planar flow field have been obtained by on-line calibration of (focusing) the CCD camera when a mm graded ruler, submerged into the water, was aligned with the centerline of the nozzles. To optimize the effectiveness of subpixel interpolation so that particle positions can be estimated to subpixel accuracy, it is recommended that the camera is focused so that particle images are greater than 3 pixel pitches in diameter and the peaks in the correlation plane have a width between 3 and 6 pixels [15]. The vertical distance from camera lens to the planar measurement field (i.e. laser sheet) has been varied as a function of particle size, distance between nozzles and the desired real image area. A transparent mask with the eye positioned under the separation surface between the water in the tank and the surrounding air, has assured an almost constant refraction index for all experiments. In this way the sum of the distances between the submerged measurement plane and the mask eye, and that between the camera lens and the eye of the mask, was kept constant.

Digitized images have an active area of 1008 pixels horizontally by 1018 pixels vertically, which, depending on the calibration (i.e. focusing) of the camera for each experiment, corresponds to a field of view between $90.2 - 145$ mm by $91.1 - 147.5$ mm or to the associated scaling factors of 9.946 - 15.98 $pixels/mm$. Since it inherently preserves the temporal order of the particle images, the double frame / single exposure method of recording was used.

The acquired images were written to a computer hard disk capable of storing a few thousand images. Each image pair is about 1.3 MB. In these experiments, due to the relatively high number of cases studied and computer limitations, $250 - 500$ image pairs have been usually stored, excepting the case common to LDA measurements where 1000 image pairs were recorded.

The collected data covers the downstream flow locations 82 mm measured from the edge of each nozzle, the impingement region of the two jets and the resulting radial jet, in the case $L^* = 20$ of opposed jet flow and the whole flow field in the other experimental configurations.

2.3.5.4 PIV Data Processing and Validation

The multiselection choice (of the acquired images) as well as the option of a chain analysis within Dantec's FlowManager software made sequential and automatic processing of the image maps corresponding to each individual experiment possible. Thus, the cross-correlation of image pairs, and the range and peak validations were performed as part of the initial processing of the acquired data.

Due to the high resolution CCD camera which allows complete separation of consecutive camera images by a very small time interval (of the order of μs, therefore avoiding the directional ambiguity of the auto-correlation technique), and the improved dynamic range (by decreasing the number of random correlations), the cross-correlation technique was chosen to determine the displacement between the initial and final particle positions. In this respect, each image was divided into rectangular 64×64 $pixels$ interrogation regions; this proved to give a good compromise between velocity dynamic range ($0.01 - 1.1$ m/s) and spatial resolution (≈ 2 mm). Near interrogation area edges there is an increased risk, that either the initial or the final particle position is outside the interrogation area. Thus, to increase the contribution of the particles near the edges to the velocity calculation the cross-correlation plane was determined for 75 % relative overlapping of the interrogation regions. The maximum acceptable particle displacement was 25 % of the side dimension of the interrogation area. As described in section 2.3.4.4, the correlation plane is determined by FFT processing of the image map. Scanning the correlation plane for the highest correlation peak would reveal the average displacement within the interrogation area investigated. Several trials have been performed for each experimental configuration until at least 5 particles/interrogation region concentration occurred (i.e. decreasing the signal to noise ratio) and therefore reasonable results were achieved.

The resulting raw vector maps were then validated. Two methods of validation were used to detect and reject correlation plane outliers: range validation and peak validation. The range validation validated or rejected individual vectors based on the expected minimum and maximum values of the x and y component of the velocity vector. In the present experiments, the longitudinal component of the instantaneous velocities was ranged $-1.5 \leq u \leq 1.5\ m/s$, and the vertical component $-0.5 \leq v \leq 0.5\ m/s$. Vectors outside these ranges are considered outliers and were rejected.

The peak validation routine validated or rejected individual vectors based on the values of the peak heights in the correlation plane where the vector displacement was measured [15]. In this method, it is assumed that the measured peak is the signal and the second highest peak is noise. The criterion here was to reject any vectors for which the signal to noise ratio is less than a certain threshold. In the present experiments this threshold value was 1.4 (i.e. signal peak / second peak = 1.4). In order to obtain good measurements, the peaks in the correlation plane should have a width of between $3 - 6$ pixels. Narrower or wider peak widths will lead either to insufficient information to make use of subpixel interpolation or to a poorly defined position of the peak center. Thus, a threshold value of 3.5 that accounted for the peak minimum width within the correlation plane accompanied the peak validation threshold. In order to maintain the accuracy and consistency of the results throughout all the experiments, all vectors including substituted vectors (see section 2.3.4.4) were used in the statistics calculation.

Based on a number N_v of vector maps obtained from the acquired image pairs, mean velocity values, standard deviations (rms) and correlation coefficients are determined for each interrogation area. The calculations are automatically done using the formulas given in the PIV user's guide [15]. Further, a two-dimensional vorticity map and the two-dimensional streamlines of the flow can be obtained.

Since velocities measured by PIV are estimated averages over large interrogation regions, the small-scale classical turbulent structures may not be revealed. In order to correct this discrepancy the dimensions of the interrogation regions should be smaller than the turbulent length scales of the flow field. This is a reason why, at least these quantities, may not be identical with those measured by LDA means.

2.4 Principles of Seeding Selection

In LDA as well as in PIV it is not the velocity of the flow that is measured, but the velocity of particles suspended in the flow. Thus, in most applications, artificial tracer particles have to be added to the flow. The need to employ tracer particles for the measurement of the flow velocity requires a careful checking for each particular experiment whether the particles will faithfully and passively follow the motion of the fluid. Particles employed to simulate the motion of a fluid continuum should satisfy the following requirements: be able to follow the flow and be good light scatterers. In order to satisfy the safety requirements and allow ease of use, the particles should be non-abrasive, non-volatile, chemically inactive, clean, non-toxic, non-corrosive and cheap [19].

In general, the motion of tracer particles suspended in a fluid is influenced by fluid dynamic behavior, physical properties of the particles such as particle shape and size, relative density of the particle with respect to that of the fluid, concentration of particles in a specific volume of fluid, and the effect of body forces on the particles.

For most liquid flows, seeding can be done by suspending solid particles in the fluid and mixing them in order to get a homogeneous distribution. Depending on the magnitude of the velocity being measured, LDA measurements can be straightforward in water flows when naturally occurring particles provide acceptable seeding. Unless the flow under investigation involves phase transformation, where creation of new particles is part of the process itself, most flows require artificial seeding prior to PIV measurements.

The shape of the seeding particles influences the drag exerted on the particle by the surrounding fluid. The size of the particles together with their relative density affect their response to velocity changes in the surrounding fluid. Usually, smaller particles, neutrally buoyant and of a similar density to the fluid, track the flow more accurately and will avoid velocity lag [37]. In many flows, however, the neutrally buoyant character of the particle is a secondary consideration. In general, the maximum allowable particle size decreases with increasing flow velocity, turbulence and velocity gradients. It is clear that LDA efficiency depends on signals from particles suspended in the flow rather than from the fluid itself. Physically speaking, the light scattered by tracer particles is a function of the refractive index of the particles relative to that of the surrounding fluid, the particle size and its orientation. Usually, larger particles with a high relative refractive index and scattering light paraxially (i.e. at 0° or 180°) provide the best scattering efficiency [37]. In a short review of light scattering from molecules and atoms, trying to reveal the size range of particles needed to provide valuable LDA measurements, Durst et. al. [19] defined the scattering cross-section, C_{scat} $\left[m^2\right]$, of a particle as:

$$C_{scat} = \frac{P_s}{I_0} \qquad \left[m^2\right] \tag{2.10}$$

where P_s is the power scattered in all directions, in $[W]$, and I_0 is the light intensity incident on the particle, in $\left[W/m^2\right]$. Evaluating C_{scat} for particles of diameter near the order of the wave length of scattered light, they found that it is several orders of magnitude greater than the Rayleigh scattering cross-section for molecules and atoms. This review indicates that larger particles should be preferred as scatterers. In PIV, it is implied that the seeding particles must scatter sufficient light so that distinct particle images can be detected and image analysis more accurate. Since larger particles provide better light scattering efficiency, this is in contradiction to the demand of having as small particles as possible in order that they follow the flow accurately.

Thus, in both methods, due to the contradiction between the particle size and the demand of high light scattering intensity, a compromise has to be found in most applications. Another limitation, namely the fringe spacing in the control volume simplifies the problem in the LDA case. Careful matching of particle size and fringe spacing is desirable to obtain optimum signal to noise ratio. Experience [19] has shown that the ratio of the mean particle size to the fringe spacing should be of the order of one quarter (1/4). Usually, depending on the application and considerations mentioned in sections 2.3.4.2 and 2.3.5.3, particles used in PIV include aluminum oxide, glass spheres, polystyrene, oil droplets, oxygen bubbles and granules for synthetic coatings. Typical sizes range from 2 μm for aluminum, to about 1000 μm for oxygen bubbles [37]. In both LDA and PIV, however, the full turbulent flow field would be revealed only if the tracer particles have sizes much smaller than the smallest turbulence scales involved in the flow.

The concentration of particles influences particle motion through the interaction between different particles. In LDA, a concentration sufficient to maintain at least one particle in the scattering volume most of the time is ideal. Agglomeration of more particles in the tiny control volume will lead to light attenuation and signal interference and therefore a deteriorated photomultiplier signal, and damping of turbulence. A minimum particle concentration is established

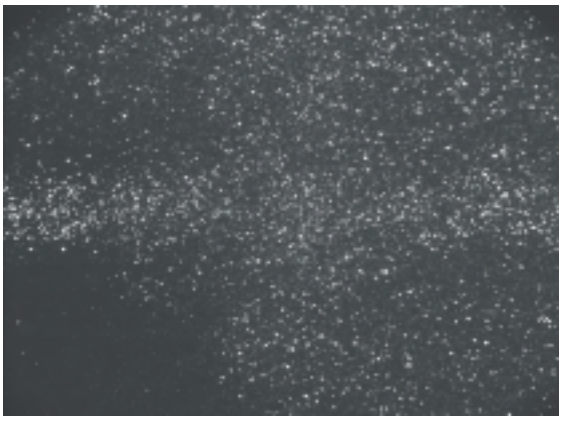

Figure 2.13: Medium image density (Turbulent opposed impinging jets - Re = 11000, $L^* = 20$; TiO_2 particles, image 1008×1018 pixels)

by the minimum allowable measurement rate with counters [19]. In practice, a relatively low concentration will ensure separations between particles of the order of several particle diameters and particle interaction can usually be neglected [19]. In PIV, a low concentration of particles in the recorded images will make it difficult or even impossible to achieve the minimum number of particles per interrogation region required to minimize the " signal" dropout, while a high density of particles in the images generates a decreased signal to noise ratio due to the impossibility of detecting individual particles. A homogeneous distribution and medium density of tracer particles is always desired for high quality PIV in order to obtain optimal evaluation. Figure 2.13 shows a medium image density as it should be for reliable PIV measurements.

Excepting very slow flows, where buoyancy of the tracer particles may be important, body forces such as gravity can normally be neglected.

In order to reveal the exact size and type of the particles that should be used in laser based measurements to accurately follow a certain fluid flow, particle motion relative to a viscous fluid has to be analysed.

Stokes described particle dynamics based on the free falling of a solid spherical particle of diameter d_p in a stationary fluid. As a result the following equation was derived [25]:

$$u_s = \frac{d_p^2 \left(\rho_p - \rho_f\right) g}{18\mu} \qquad [m/s] \tag{2.11}$$

where subscript p refers to particle and f to fluid respectively. Since this is the velocity that the particle reaches at the end of a free fall, u_s was termed the " terminal settling velocity". A simple mathematical manipulation of this equation (i.e. dividing both the numerator and the denominator with ρ_f) without a meaning change, allowed Merzkirch [24] to call u_s, the sedimentation velocity. He considered that a particle is neutrally buoyant if its sedimentation velocity is 0. Even though it simulates the viscous motion in steady flow past a sphere, Equation 2.11 could at most describe the particle dynamics for the laminar range, therefore an assessment of particle dynamics for the turbulent range of flow would fail.

It was Basset who first studied the complex particle motion for the particular case of a sphere in an infinite fluid. In 1888 he derived the following equation describing the motion of a sphere relative to a stagnant fluid [19], [21]:

$$\frac{\pi}{6}d_p^3\rho_p\frac{d\widehat{U}_p}{dt} = -3\pi\mu d_p\widehat{V} + \frac{\pi}{6}d_p^3\rho_f\frac{d\widehat{U}_f}{dt} \tag{2.12}$$

$$-\frac{\pi}{12}d_p^3\rho_f\frac{d\widehat{V}}{dt} - \frac{3}{2}d_p^2\sqrt{\pi\mu\rho_f}\int_{t_0}^{t}\frac{d\widehat{V}}{d\xi}\frac{d\xi}{\sqrt{1-\xi}} \tag{2.13}$$

where ξ is a parameter describing the time history of the flow, $\widehat{U}_p$ is the mean velocity of the particle, $\widehat{V}$ is the mean vertical velocity of the particle and $\widehat{U}_f$ is the mean velocity of the fluid relative to the particle. The term on the left side represents the force required to accelerate the sphere and the first term on the right side describes the viscous drag as given by Stokes law. The pressure gradient developed in the vicinity of the particle as a consequence of the induced acceleration of the particle is defined by the second term. The third term is the reaction of an inviscid fluid to acceleration of the sphere and is given by potential flow theory. The last term represents the drag force originating from an unsteady motion. This equation is subject to certain conditions such as: homogeneous, steady turbulence, particle diameter is smaller than turbulence length scales, particle is surrounded by the same fluid molecules, there are no interactions between particles, Stokes drag law applies and external forces are neglected. Even though experience shows that the shape of the particle affects its drag, it is assumed that the results of this analysis apply qualitatively to particles of an irregular shape.

Seventy years later, Hinze [21] expanded this equation to a moving fluid, considering the instantaneous velocity of the particle relative to the fluid a relationship of the form, $V_H \equiv U_p - U_f$.

Based on analyses developed by Stokes and Basset it has been shown that the optimum size range of tracer particles used in LDA measurements is between $0.8-16\ \mu m$ [19]. Typically, depending on the nature of the flow, seeding particle diameters used for PIV measurements range from 0.1 to 50 μm.

2.5 Data Analysis

This section provides an overview of the analysis techniques used in this thesis to evaluate the experimental data collected using both LDA and PIV. In most flows, turbulent motions contribute significantly to the transport of momentum and mass and therefore have an important influence on the velocity distribution and species concentration within the flow field. Thus, analysis of the current data is performed with the intention of revealing the mean and turbulent features of the flow and its oscillatory behavior. In the present flow, turbulence production is attributed to a combination of turbulence production via shear manifested in the vicinity of the nozzles and turbulence production via pressure gradient (flow curvature) occurring in the impinging region of the two jets. Therefore opposed jets impingement flow is a complex turbulent flow. At the smallest scales, it can be assumed that the flow is quasi-isotropic, but its global homogeneous and stationary turbulence characteristics are questionable. Even though the impingement region may be hard to characterize, to a lesser extent it can be supposed that the flow is inhomogeneous but partially stationary. This supposition would make time averaging an appropriate method for the present flow analysis. If instead, at least the impingement region is considered unsteady and inhomogeneous, then a combined approach such as time averaging and phase averaging (if the flow is periodic) or spatial filtering (as in LES) [46] must be considered. In light of the above comments, classical analysis techniques based on a

statistical description of turbulence which focuses mainly on isotropic-inhomogeneous and stationary turbulence is utilized here [46]. In this respect, the use and definition of measurable turbulence statistics such as time averaged functions, turbulence intensity, signal correlations, spectral functions, etc., will provide valuable information with regard to the energy distribution (dominant frequencies of the flow), length and time scales, etc.

To determine the distribution of a stationary signal in space and time, its descriptive properties can be categorized into two classes [9]: amplitude-domain statistics which describe the variation in signal amplitude, and time-domain statistics that give information regarding signal distribution with respect to time. In general, the most important of these in the context of importance in estimating the present flow structure are the mean and turbulent (rms) velocities and probability density functions (PDF) as amplitude descriptors and the autocorrelation function in time, turbulence length and time scales and energy spectra as time-domain descriptors. Calculation of each of these is discussed below.

2.5.1 Mean and rms Velocities

Even though the expressions for the mean and rms velocities can be directly derived from the definition of the probability density function (PDF), these quantities are the first to be addressed due to their prime importance in determining the flow structure. As briefly mentioned in section 1.2, in classical turbulent flow analysis, the instantaneous velocity is decomposed into a mean velocity and a fluctuating component. In a Cartesian coordinate system and using tensor notation we have:

$$u_i\left(x_i,t\right)=\overline{u_i}\left(x_i\right)+u_i^{'}\left(x_i,t\right) \qquad [m/s] \tag{2.14}$$

This rule together with the definition for time averaging gives,

$$\overline{u_i}=\lim_{T\to\infty}\left[\frac{1}{T}\int_{t_0}^{t_0+T}u_i dt\right] \qquad [m/s] \tag{2.15}$$

which is appropriately used for analysis of stationary turbulence (i.e. $\overline{u}$ does not vary with time, or $\frac{\partial\overline{u}}{\partial t}=0$). The period T of the variation of mean value must be large compared to the relevant period of the fluctuations. If on the contrary, u has an observable variation with time, then as Figure 1.1 shows, we speak of this case as an unsteady flow.

In this work, ensemble averaging was used to approximate the theoretical time average since it is the most general and effective way for processing experimental data. The average of the acquired discrete signal sampled at a regular frequency of 250 Hz is then:

$$\overline{u_i}=\frac{1}{N}\sum_{n=1}^{N}\left(u_i\right)_n \qquad [m/s] \tag{2.16}$$

where N is the total number of samples used in calculations. The fluctuating component of the instantaneous signal is defined as:

$$u_i^{'}\left(x_i,t\right)=u_i\left(x_i,t\right)-\overline{u_i\left(x_i\right)} \qquad [m/s] \tag{2.17}$$

and its average value is identically zero $\left(\overline{u_i'}=0\right)$.

Even though the turbulence intensities can be derived via probability density functions, it is more common to define them as the *rms* normal stress components (no summation) [46]:

$$(u_i)_{rms} = \sqrt{\overline{u_i' u_i'}} = \left\{ \frac{1}{N} \sum_{n=0}^{N} \left[(u_i)_n - \overline{u_i} \right]^2 \right\}^{1/2} \qquad [m/s] \tag{2.18}$$

Usually, in graphical representations the average velocities and turbulence intensities are normalized by either $\overline{u_i}$ or the maximum velocity present in a certain section of the flow, $(U_i)_{\max}$.

2.5.2 Turbulent Kinetic Energy, Production and Dissipation [/unit mass]

Turbulent kinetic energy per unit mass is defined as [46]:

$$k = \frac{\overline{u_i' u_i'}}{2} = \frac{\overline{u_i'^2}}{2} \qquad \left[m^2/s^2 \right] \tag{2.19}$$

Due to the axisymmetric character of the present flow and a lack of measurements in the third dimension, symmetry is assumed in the transverse plane, i.e. $u_2 = u_3$ and therefore the turbulent kinetic energy equation becomes [46]:

$$k = \frac{\overline{u_1'^2} + 2\left(\overline{u_2'^2}\right)}{2} \qquad \left[m^2/s^2 \right] \tag{2.20}$$

where u_1 is the velocity in the dominant direction of the flow. Given the complex flow under investigation, the principal direction of the flow is a function of position within the flow field and therefore the weight of each velocity in the turbulent kinetic energy formula changes accordingly. In other words, as denoted in the opposed jets co-ordinate system (Figure 2.1), $u_1 = u$, is the principal flow direction when the fluid flows along the x axis and so $u_2 = v = u_3 = w$ in that region. The same procedure is used when the fluid flows along the y axis where v becomes the principal flow direction.

The specific production rate (i.e. production rate per unit mass) of turbulent kinetic energy is estimated using the equation which respects the pipe or boundary layer flow models [46]:

$$P = -\overline{u'v'} \frac{\partial \overline{u}}{\partial y} \qquad \left[m^2/s^3 \right] \tag{2.21}$$

where $\overline{u'v'}$ is the mean Reynolds shear stress and the velocity gradient is calculated by fitting a decay function to the mean longitudinal velocity profile across the jet. Fitting functions corresponding to different locations in the flow will be determined and discussed in Chapter 4.

The rate at which the energy produced at the largest scales is dissipated to heat at the smallest scales (molecular diffusion) is defined by the dissipation rate per unit mass relationship [46]:

$$\varepsilon = \nu \overline{\frac{\partial u_i'}{\partial x_j} \frac{\partial u_i'}{\partial x_j}} \qquad \left[m^2/s^3 \right] \tag{2.22}$$

Usually the dissipation of turbulent kinetic energy is approximated by the following formula [46]:

$$\varepsilon = \frac{10k^{3/2}}{\mathrm{Re}_{\lambda_g}\,\lambda_g} \qquad \left[m^2/s^3\right] \tag{2.23}$$

where Re_{λ_g} is the turbulent Reynolds number evaluated from the turbulent kinetic energy, k, transverse microscale for length (defined below), λ_g, and kinematic viscosity of the working fluid ν:

$$\mathrm{Re}_{\lambda_g} = \frac{k^{1/2}\lambda_g}{\nu} \tag{2.24}$$

2.5.3 Probability Density Function

The experimental turbulent velocity signal represents the digital (continuous by quantization) distribution of a random variable u in a fixed time interval t. By definition, for a stationary signal $u(t)$, the probability density function, $P\,(u_k)$, shows the number of times one particular value u_k of the random variable u occurs. At any time there is a probability $\mathcal{P}$ that the signal amplitude falls between u_k and $(u_k + \Delta u_k)$. Therefore, if t_k is the amount of time out of the total recording time t, within which $u(t)$ lies in the interval $[u_k,\ \ (u_k + \Delta u_k)]$,

$$\mathcal{P}(u_k) = \lim_{t\to\infty} \frac{t_k}{t} \tag{2.25}$$

For a small Δu_k and t approaching infinity, the PDF is defined by [9]:

$$P(u_k) = \lim_{t\to\infty}\left[\lim_{\Delta u_k\to 0} \frac{t_k}{t\Delta u_k}\right] \tag{2.26}$$

As the LDA signal was acquired in blocks of 1024 samples, calculation of the PDF requires first finding the maximum and minimum of the signal amplitudes and then dividing this amplitude interval in a certain number of windows, n. Summing the number of data values that fall in each window, N_n, and dividing by the product of the total number of samples, N, and the width of the window, Δu_k, gives the probability density function:

$$P(u_k) = \frac{N_n}{N\Delta u_k} \tag{2.27}$$

The real signal is almost always limited to a certain amplitude range, and the PDF indicates the domain where the amplitude of the signal is within limits and the domain where the signal is out of range or sparse.

2.5.4 Autocorrelation

In a statistically steady situation, and we considered the present flow as being stationary on certain portions of the flow field, the origin of time is irrelevant, so that the correlation between $u_i(t)$ and $u_i(t+\tau)$ (i.e. the autocorrelation), should depend only on the time difference, τ. Thus, the normalized time correlation coefficients with respect to τ are calculated as [46]:

$$R_{ii} = \frac{\overline{u_i'(x,t)u_i'(x,t+\tau)}}{\overline{u_i'^2}} \tag{2.28}$$

where $i = 1, 2$. The integral of the time correlation between the signal and itself was calculated using the ensemble average procedure:

$$\begin{aligned} \overline{u_i'(x,t)u_i'(x,t+\tau)} &= \frac{1}{T}\int_t^{t+T} u_i'(x,t)u_i'(x,t+\tau)dt \\ &= \frac{1}{N}\sum_{n=1}^{N} u_i'(x,t)u_i'(x,t+\tau) \qquad \left[m^2/s^2\right] \end{aligned} \tag{2.29}$$

where N is the number of the samples collected at station x.

Usually, based on the direction of correlation separation with regard to the velocity components, a simplified denomination is used. In this respect, R_{11} is termed the longitudinal correlation and R_{22} the transverse correlation. The time separating array, τ, was calculated as $\tau = \frac{n}{f}$, where $n = 0, 1, 2, ...N$ and $f_s = 250\ Hz$ is the sampling frequency. Since in turbulence, it is always assumed that the integral time scale, T_E, is finite [21], and its value is a rough measure of the interval over which $u_i(t)$ is correlating with itself, the integration was stopped at the first zero crossing of the autocorrelation.

2.5.5 Characteristic Scales of Turbulence

Among the information that " measured" correlations reveal, the length and time scales of turbulence are perhaps the most important. The integral time scale may be related to the average size of the largest eddies present in the flow, while the integral length scale can be associated with the geometric scales of the flow geometry [46]. The integral length scale can be used as a " guess" value for starting the CFD simulation. The Taylor microscale for time is a measure of the most rapid changes that occur in the fluctuations of u_i while the microscale for length provides information regarding the isotropic character of the flow. Finally, Kolmogorov's length and time scales for dissipation give an estimation about the turbulence equilibrium state.

The integral time scale, T_E, and the Taylor microscale for time, τ_E, are defined from the aforementioned autocorrelation coefficients. The integral time scales were calculated using a second order trapezoidal formula on the interval $(0,\ \tau_{ii\text{crossing}})$:

$$T_E = \int_0^{\tau_{ii\text{crossing}}} R_{ii}(\tau)\, d\tau \qquad [s] \tag{2.30}$$

where $i = 1, 2$ and no summation is in effect.

Assuming that the turbulence process is partially homogeneous-isotropic, the estimation of the Taylor microscales for time requires approximation of the normalized autocorrelation second derivative at $\tau = 0\ s$. These values have been approximated by the first derivative of the signal fluctuations:

$$\tau_{E_{\mathrm{ii}}} = \sqrt{\frac{2\overline{u_i'^2}}{\left(\frac{\partial u_i'}{\partial t}\right)^2}} \qquad [s] \tag{2.31}$$

which in the code was carried out by a finite difference formula.

The integral length scale, L, was defined based on a spatial correlation which in turn is derived from normalized time autocorrelations assuming Taylor's " frozen hypothesis".

$$L_{ii} = \int_0^\infty R\left(r_i\right) dr_i \qquad [m] \tag{2.32}$$

where r is the separation between measurement stations with data collected simultaneously at all stations. For $i = 1, 2$ longitudinal and transversal length scales are obtained.

Taylor supposed that spatial separation is obtained from the product of time separating and the mean convecting velocity, i.e. $dr_1 = \overline{u} d\tau$. However, this assumption is valid only for homogeneous-isotropic turbulence, i.e. in regions where [46]

$$\frac{u_i'}{\overline{u_i}} \equiv \frac{\sqrt{\overline{u_i'^2}}}{\overline{u_i}} < 0.10 \tag{2.33}$$

By using all the above definitions, derivation of longitudinal and transverse integral scales, L, as well as micro-length scales, λ, become obvious:

$$L_{ii}\left(r_i\right) = \overline{u} T_{E_{\mathrm{ii}}} \qquad [m] \tag{2.34}$$

$$\lambda_f = \overline{u} \tau_{E_{11}} \qquad [m] \tag{2.35}$$

$$\lambda_g = \overline{u} \tau_{E_{22}} \qquad [m] \tag{2.36}$$

where $\overline{u}$ is the dominant mean velocity and $i = 1, 2$ without summation. A proof that the local turbulence is isotropic is implied by the ratio λ_f / λ_g whose magnitude should not exceed $\sqrt{2}$ [46].

The analysis continues with the estimation of the Kolmogorov length and time scales, which according to Kolmogorov's " universal equilibrium theory" [46] are based on the dissipation per unit mass and the kinematic viscosity ν as in:

$$l_k = \left(\frac{\nu^3}{\varepsilon}\right)^{1/4} \qquad [m], \qquad t_k = \frac{l_k}{\left(\nu\varepsilon\right)^{1/4}} \qquad [s] \tag{2.37}$$

2.5.6 Turbulence Spectra

Turbulence may be represented as a superposition of periodic waves characterized by different time and length scales which can in turn be decomposed [46]. Thus, the random turbulent signal at a point in a flow would exhibit a turbulence energy spectrum (power spectral density) that in fact represents the distribution of energy amongst the component frequencies. Given the fact that much of the turbulence structural information is lost through time averaging, the energy spectrum calculation could provide an overall understanding of generation, diffusion

and destruction of turbulence. In the present case, the power spectral density of the velocity fluctuations (with mean velocity component removed) was calculated using [22]

$$\widehat{P}_x\left(f_k\right) = \frac{2\Delta t}{n_d N} \sum_{i=1}^{n_\mathrm{d}} \left|\chi_{ik}\right|^2 \qquad \left[m^2/s\right] \tag{2.38}$$

which represents power normalized by the frequency resolution, Δf. In this equation, x is the signal to be analysed, χ_{ik} represents the discrete Fourier transform of the real signal, f_k are the discrete frequencies that constitute the signal, N is the total number of acquired samples, n_d is the number of data blocks used in the calculation and Δt is the sampling time interval which is constant. Since the frequencies involved in the signal are symmetric about the Nyquist frequency, $k = 0, 1, 2, ..., N/2$.

The power spectral density function of a turbulence signal is expected to reveal the range of frequencies containing most of the signal energy, noise components, frequency of any important resonance and the largest or smallest frequency in the signal.

The preprocessing subroutine included in the program that runs the LDA acquisition system provided local mean and turbulent velocities. A Fortran code was written with the purpose of reading, sorting and organizing the above mean velocity and turbulent intensity values and doing so their global distributions within the flow field were mapped. Calculation of all the other quantities mentioned in the " Data Analysis" section was coded in MatLab version 5.2.

2.6 Noise and Measurement Accuracy

Due to the large variety of relevant parameters, an estimation of the measurement uncertainty for a complex device such as the LDA or PIV system is not trivial. In general two types of methods can be used: the statistical method based on a simulated system through the use of numerically generated LDA time series or PIV recordings, and the direct method which estimates the uncertainty from real LDA time series or PIV recordings provided the fluid flow is known and well defined. The second method is applied here. Previous works on LDA uncertainty [33], [32], provide background regarding the errors involved in LDA measurements. However, due to the unknown character of the flow under investigation and the sparse literature existent on uncertainty, estimation of the errors affecting PIV measurements will become an important task.

Usually an error is defined as the difference between the true value and the calculated value in the case of a numerical simulation, or the difference between the true value and the measured value in a measurement [26]. The uncertainty is regarded as the maximum error which may plausibly appear in a parameter being measured or as a result of its computation from measured data. The overall measurement accuracy in LDA or PIV is a combination of a variety of aspects extending from the physical measuring process itself to the methods of evaluation of the collected data. This section is devoted to summarizing the principal types of errors that lead to experimental uncertainty while a detailed error analysis will be placed in Appendix A.

Multiple-sample experiments are those in which sufficient data sets are collected at each measurement point that a statistical interpretation of the result and the associated random errors is possible. Both experiments satisfy this criterion: LDA through the 40960 data samples collected at one point in the flow domain, and PIV through the several images (250 to 1000)

recorded for the whole or partial flow field. In this case, the absolute measurement error, ε_{tot}, can be decomposed into a group of systematic errors which can be eliminated, ε_{sys}, (e.g. using an adequate analysis method), and a group of residual errors that remain in the form of a measurement uncertainty, ε_{resid} [37]:

$$\epsilon_{tot} = \varepsilon_{sys} + \varepsilon_{resid} \tag{2.39}$$

In practice, it is not always possible to separate the systematic errors from the residual errors, so that the total error or the experimental uncertainty is usually expressed as a function of a bias error, B, and a random or precision error, S, [26], [54]:

$$\epsilon_{0.95} = \pm\sqrt{B^2 + (t_{95}S)^2} \tag{2.40}$$

where t_{95} is a multiplier for a 95% confidence interval. For a sample number greater than 30, $t_{95} \simeq 2$ [33].

Any error that remains constant during an experiment and passes along unaltered from one experiment to another is termed a bias or fixed error. These are systematic errors and arise from tolerances of the instruments, calibration, data acquisition and data reduction processes, etc. The overall bias limit of a certain measurement is defined as the root sum-square combination of all the fixed error components [54]:

$$B = \sqrt{\sum_{i=1}^{n} B_i^2} \tag{2.41}$$

S is more often called the precision index of a measurement [26], and it represents a measure of the measurement random error. This can be estimated from the measured data only and is equal to its standard deviation. The multiplier t accounts for the number of degrees of freedom represented by S and the confidence interval considered. In a complex situation, other variations in the measured value appear amongst repeated measurements. The precision index is calculated as:

$$S = \sqrt{\sum_{i=1}^{n} S_i^2} \tag{2.42}$$

Sources of these variations would involve calibration, acquisition and data reduction.

Based on these observations an error analysis was performed. The analysis is in Appendix A and results are summarized in Table 2.6.

Table 2.6: Summary of total uncertainty in LDA mean and turbulent longitudinal velocities as calculated in Appendix A

Error	Error in $\overline{u}$	Error in u_{rms}
B [%]	±4.25	±14.7
S [%]	6.1	0.6847
$\epsilon_{0.95}$ [%]	±13.1	±14.76

Although both types of errors, bias and precision have the same weight in the case of mean longitudinal velocity uncertainty ($4-6$ %), the fluctuating component of the longitudinal velocity is mainly affected by bias errors due to mcv positioning (14.7 %). Summarizing, the total uncertainty is about 13 % for the mean velocity and 14.7 % for the *rms* velocity.

It has been observed that the signal resulting from laser based measurements is often contaminated with an unwanted background or induced signal which is not included in the known errors and adds more influence on measurement accuracy. In an LDA signal, noise arises from at least four sources: seeding, optical sources, photodetection effects, and electronic sources.

Optical noise usually accounts for noise introduced in the generation and transmission of the laser beam and could be a measure of the beam perturbations of a diffractive and refractive nature, coherence degradation, light dispersion from lenses and medium, optics angular misalignment (which also introduces a fixed error), etc. [18].

The current obtained from a photomultiplier output is dependent upon the number of photons incident on its surface per unit time (i.e. the amount of scattered light). Since there is only a finite number of photon emissions per second, high frequency fluctuations will always exist. These fluctuations are termed " shot noise". The other important noise that affects the photomultiplier's output is the dark current. The dark current noise is the current created by incident particles other than the laser photons. Related to the photomultiplier noise is the noise caused by seeding concentration, particle shape and size, and the particle's capability of light scattering. Since all of these could improve or degrade the signal to noise ratio, the use of an opaque mask in front of the photomultiplier (see Figure 2.6) in order to avoid unwanted light striking the photomultiplier and special care when seeding the flow are recommended (see section 2.4).

Other electronic noise is associated with the counter processor hardware and the network background noise.

The influence of the different noise sources can be summed and represented as a single additive noise component, $n(t)$, on the Doppler signal $x\,(t)$:

$$X(t) = x(t) + n(t) \tag{2.43}$$

where $X(t)$ is the real (altered) photodetected signal. Due to the independent nature of its sources this noise can be termed " white" or Gaussian noise [18]. Usually this noise is partially eliminated from the real signal using appropriate bandpass filters to remove low-frequency components and frequencies that do not contain Doppler information prior to any frequency detection. Further, the noise introduced by the counter processors can be partially removed by filtering the acquired data prior to computing statistics of the flow. These steps were followed in the present experiments. In this case, the bandpass filter frequencies were set to the values mentioned in Table 2.3 while the acquired data was filtered based on the mean and standard deviation values for the entire time series. An evaluation of the difference between filtered and unfiltered LDA data is presented in section 2.7.

As mentioned in subsection 2.3.4, in PIV the additive noise N is a component of the transfer function that converts the input image to the output image. N contains the recording noise, the effect of perspective projection and the most important, the noise contribution due to FFT based correlations. The recording noise includes CCD sensor noise which is generated in the same manner as the LDA photodetection noise and seeding related noise. A careful optimization of the CCD electronics as well as cooling of the sensor plus an efficient seeding could limit the recording noise. Improvement of the signal to noise ratio can also be obtained by using advanced interrogation and peak detection techniques such as offsetting the interrogation windows, and reducing the effect of out-of-plane motion using methods to compensate for the out-of-plane

motion such as reducing the pulse delay between recordings, thicken the laser light sheet for a given pulse delay and using a parallel offset of the light sheet between the illumination pulses in the direction of the flow.

2.7 Testing and Measurement Validation

In general, the purpose of these experiments is to provide a better understanding of a physical or a different natural phenomenon. Fluid dynamics and especially turbulence fall in the category of physical phenomena where the understanding of what you see is revealed by a series of hidden flow properties whose measurement is often a very complex task. Due to this, and considering the fact that measurements must provide reliable information concerning the flow under investigation, the experimental data has to satisfy certain conditions in order to prove its validity. The following represents a series of tests the LDA and PIV data have been exposed to, in order to confirm their validation.

2.7.1 The " Zero" Test

Frequency shifting is essential for two dimensional LDA applications encountered in fluid dynamics. In order to evaluate the joint operation of the PMs, Bragg cell, frequency shifter and counters a zero velocity test was performed. This test would indicate if the PM is responding properly to 40 MHz frequency shifting and if the shift of the Doppler frequency is in the correct range (i.e. a measure of the level of noise existing in the LDA data).

This was accomplished by placing the measuring control volume on the stationary transparent acrylic of the tank wall which was thick enough (12.7 mm) to contain the entire mcv. The data rate on the counters, which is in fact the output from the PM should read 40 MHz, while the magnitude of mean and rms velocities should be zero. This will also prove correct settings on the frequency shifter and counters. Table 2.7 presents a summary of the zero test results for two sampling frequencies and laser beams passing through air or water after the acrylic wall.

Table 2.7: Summary of zero test results (40960 velocity samples)

Fluid	Sampling	$\overline{u}$	u_{rms}	$\overline{v}$	v_{rms}
medium	frequency $[Hz]$	$[m/s]$	$[m/s]$	$[m/s]$	$[m/s]$
air	250	0.002380	0.005320	0.001797	0.012600
	1000	0.002389	0.005468	0.001860	0.012070
water	250	0.002212	0.009530	0.000935	0.017340
	1000	0.003620	0.009359	0.000622	0.015421

Even though the data rate at the time of measurements was fluctuating about 40 MHz (i.e. the correct frequency shifting value) and the validation rate was varying in the range of $900 - 999$ $^0/_{00}$, the data shows mean velocities in the range of $0.6 - 2.6$ mm/s and rms values fluctuating in the interval $5.3 - 17.3$ mm/s. There is no clear variation of mean and rms zero velocities with the sampling frequency, however, rms values manifest a slight increase when the laser beams pass through the water. It is the refractive index of the water which

triggers modifications in the geometry of the laser beams intersection point. Zero velocity tests performed at various times of the day and for different days revealed variations in the background noise which were probably associated with the power supply loading at a certain instant. The velocity values corresponding to this noise appeared to be roughly included in the above intervals. Compared with the magnitude of initial mean velocities in the experiments, i.e. $U_0 \in [0.119, 0.869]$ $[m/s]$, the mean zero velocities would represent a maximum 3% of these values. In the case of rms zero velocities the maximum percentage is approximately 14.5%. Considering these observations, careful filtering of the signal is advised so as not to eliminate important turbulent information.

2.7.2 LDA Signal Filtering

As mentioned, there is a certain noise associated with the LDA counter operation, especially with the validation process. This noise appears in the LDA time series as overshooting the general fluctuation of the signal about the mean velocity. Elimination of the corrupted data is achieved through a simple filtering technique. This consists of replacing any data that is above or below the mean value by 3 times the standard deviation with the previous data value in the time series [22]. If the first data value of the acquired set is corrupted, it is replaced by the mean value. The filtering limits are determined by the initial mean and standard deviation (i.e. including the bad data). Figures 2.14 a), b) show the filtered and unfiltered mean and rms distributions for a typical velocity profile at station $x = 63.5$ mm downstream of the left nozzle (see Figures 2.1 and 4.1 for reference).

It can be seen that the filtering procedure has no effect on either mean velocity nor on the longitudinal rms velocity (u_{rms}). Little effect is observed on the transverse turbulent intensity, the magnitude of which decreased by about 1% after filtering. The general shape of the rms profile is conserved. Data analysis revealed that no more than 2% of 40960 samples, the total number of data samples for an individual measurement, was ever filtered. Consequently, we do not expect changes of mean velocity throughout the flow field and for any Re number and geometry configuration, after the filtering process. Little influence on the rms values without removing turbulence information, especially on the transverse component, is anticipated.

2.7.3 Axisymmetric Test

As mentioned in section 2.1, the opposed jet configurations were geometrically axisymmetric about their imaginary centerline. Consequently, the resulting flow field is expected to be axisymmetric as well. Due to the general experimental arrangement and the limitation of two component LDA and PIV configurations, it was unrealistic to acquire measurements in a constant θ plane (θ is an angle measured within the xy plane), other than 90° or 270°. Therefore, the minimum achievable $\Delta\theta$ between two consecutive measuring planes was 180° in the case of LDA measured velocities. No PIV measurements were performed with the purpose of assessing the axisymmetry of the flow. In this respect, to prove the axisymmetric character of the present flow we could have folded the two radial planes of a single transverse velocity profile about the centerline of the two nozzles. In order to demonstrate the axisymmetric character of the flow issuing from both nozzles, the opposed transverse velocity profiles are represented corresponding to similar measuring stations with respect to each nozzle (i.e. at $x = 4$ mm downstream). Thus, both transverse velocity profiles and transverse turbulent intensity profiles have been plotted for the 90° and 270° planes.

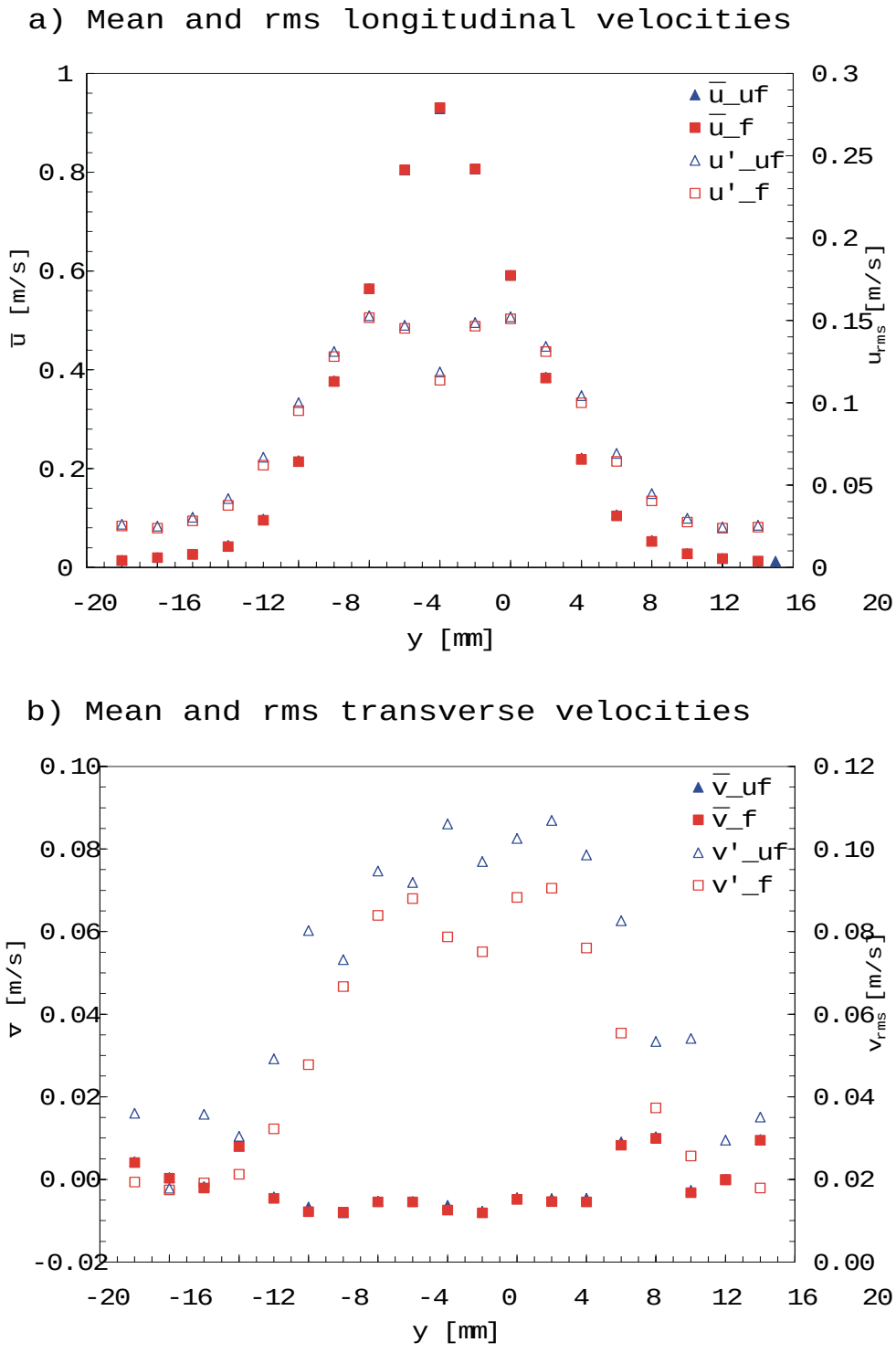

Figure 2.14: Influence of signal filtering on mean and *rms* longitudinal and transverse velocities ($L^* = 20$, Re = 11000, at station $x = 63.5\ mm$ downstream of the nozzle; f = filtered value, uf = unfiltered value, LDA data)

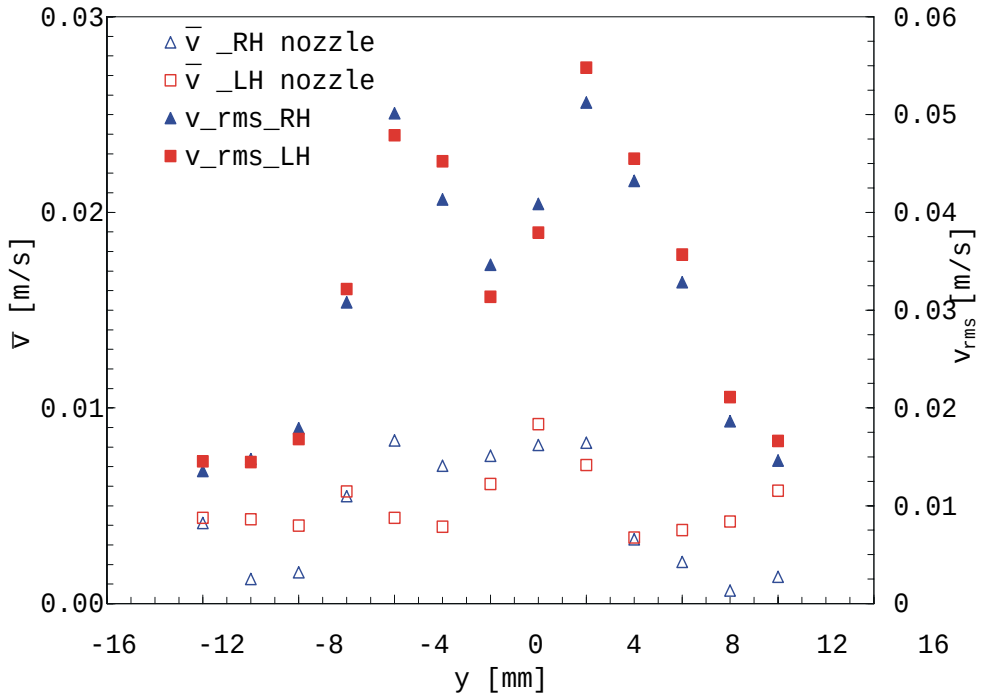

Figure 2.15: Mean and *rms* transverse velocity distributions for different axisymmetric planes ($L^* = 20$, Re $= 11000$, at $x = 4$ *mm* downstream of the nozzle; RH = right nozzle, LH = left nozzle, LDA data)

From Figure 2.15, it is clear that there is some difference between the two measurements. Quantifying this discrepancy presents a maximum level of 9.5 % for the *rms* velocity and an average of 20 % as far as the mean transverse velocity is concerned. It is the level of uncertainty and perhaps the random noise present in the measurements as well as the unsteadiness and instability of the flow, which are responsible for this difference. As a result, we can consider the assumption of axisymmetric flow satisfactory and reduce considerably the number of measurements to be taken.

2.7.4 Conservation of Mass

As in all flows, the fluid must obey the law of conservation of mass. The integral form of the mass conservation equation (continuity) for Newtonian, steady, incompressible flows, whether steady or unsteady, can be written as:

$$\int_{CS} \left(\overrightarrow{V} \cdot \overrightarrow{n} \right) dA = 0 \tag{2.44}$$

where CS is the control volume surface, $\overrightarrow{V}$ is the fluid velocity vector and $\overrightarrow{n}$ is the unit vector orthogonal to the CS. In general, conservation of mass starting from experimental data taken

in an axisymmetric geometrical configuration implies approximating the above integral with the volume generated by rotating a certain velocity profile about its symmetry axis. In turn this volume is approximated by the sum of cylindrical shells or washers, depending on the dominant dimension of the velocity profile, the spatial distribution (i.e. radius) or velocity. The method is easily derived as an application of definite integrals and can be found in any calculus book [50].

In the present case, CS is the cross-sectional area of the nozzle outlet when applying the mass conservation law at the nozzle exit or the cross sectional area of the flow field inside the impingement region for the radial jet (see Figure 2.1). Axial velocity was considered as the dominant direction in the case of the nozzle outlet velocity profile so that the generated volume is approximated by a cumulative series of annular discs (washers), while the radius to the measurement locations (with respect to nozzles centerline) was taken as the dominant direction for the radial jet and therefore a shell type approximation of the generated volume is implied. Thus, the calculation of the volume of fluid per unit time (volumetric flow rate) Q in each of the two cases becomes:

$$Q_{aj} \approx \sum_{k=1}^{m} u_k A_k \qquad Q_{rj} = \sum_{k=1}^{m} A_k v_k \tag{2.45}$$

where the indices aj and rj denote the axial and the radial jets, u and v are the longitudinal and transverse discrete velocities, and A is the area generated by the radius corresponding to u and v measurement stations and m indicates the total number of shells or washers used in calculations.

In order to evaluate the entrainment level, several volumetric flow rates were calculated for both jets at different x measurement stations before impingement and y sections after impingement. Also, experimental data obtained from both LDA and PIV measurements was used. Integrating across the longitudinal velocity profiles associated with the two opposed nozzle outlets (i.e. 2 mm away from the nozzle) and configuration $L^* = 20$, Re = 11000, gave LDA measured flow rates of about $1.1039 \cdot 10^{-4}\ m^3/s$ for the right nozzle and $1.111 \cdot 10^{-4}\ m^3/s$ for the left nozzle, which are close to the initial flow rate of $1.101 \cdot 10^{-4}\ m^3/s$ used in the experimental setup for this configuration. The PIV measured flow rate, when TiO_2 seeding was employed indicated $1.15 \cdot 10^{-4}\ m^3/s$; it has to be mentioned that the PIV flow rate has been calculated for the same number of data points as the LDA ones (less data than available). A summary of the estimated volumetric flow rates corresponding to the same experimental configuration and different measurement locations is given in Tables 2.8 and 2.9.

Table 2.8: Estimated flow rates of the axial jet (left side) at x/d before impingement

	$L^* = 20$	Re = 11000
x/d	$Q_{LDA}\ [m^3/s]$	$Q_{PIV}\ [m^3/s]$
7	4.05×10^{-4}	5.078×10^{-4}
8	4.466×10^{-4}	6.652×10^{-4}
9	5.1569×10^{-4}	6.142×10^{-4}
10	6.498×10^{-4}	5.473×10^{-4}

The above data indicates a high level of entrainment of the surrounding fluid into the axial jet flow. It is observed that the magnitude of the entrainment increases in the flow direction. This should correspond with an increasing rate of jet spread at the same time with a decrease

Table 2.9: Estimated flow rates of the radial jet at y/d after impingement

	$L^* = 20$	Re = 11000
y/d	Q_{LDA} $[m^3/s]$	Q_{PIV} $[m^3/s]$
1	5.299×10^{-4}	5.583×10^{-4}

in the mean speed of the jet at its centerline. A disagreement between the PIV calculated flow rate and the LDA one does exist and would represent a maximum difference of about 20%. It is the high data density PIV can provide (contrary to sparse LDA data) and due to this feature the higher entrainment rate predicted which are responsible for this disagreement.

$x/d = 10$ represents the symmetry axis of the opposed impinging jets; on average, one would expect the axial flow rate to decrease there due to the adverse pressure gradient present as a consequence of the impact between the two jets. Even though the PIV data may suggests this tendency, however, it does not take into account the three dimensional character of the flow field.

There is little difference between the LDA and PIV data with respect to the radial jet flow rate at one nozzle diameter away from jets' centerline. Also, there is a high entrainment rate of surrounding fluid in the radial jet whose flow rate indicates a magnitude almost $4 - 5$ times the magnitude of the initial axial flow rate.

2.7.5 Repeatability Test

Given the considerable amount of LDA data that had to be collected and to ensure the validity of the results, a standard measurement test was run prior to starting every new session of measurements. This test consisted of measuring the velocity at the same designated locations in the flow field. In the present experiments, these locations were two points on the centerline of the two nozzles situated at 4 mm away from each of the two nozzles. Consistent results of this test assured reliable data acquisition and the desired balance of the flow rates issuing from each nozzle.

Furthermore, in order to prove the repeatability of the acquired data, two successive data sets separated by a time period of 10 to 15 minutes were collected at a limited number of measurement points. An example of the results is presented in Figures 2.16 a), b) which show the longitudinal and transverse mean and turbulent velocity distributions at a time t_0 and 15 minutes later at $t_1 = t_0 + 15\ min$.

As can be seen, the difference between the two sets of data is insignificant. A careful analysis of the numerical values reveals a maximum difference of 3 % between the magnitudes of the two groups of data. This conclusion is valid for PIV data as well. Therefore, on average, the characteristics of the flow field created by the two opposed impinging jets are repeatable.

2.7.6 Estimation of the Influence of Number of Samples on LDA and PIV Data

In order to perform a rigorous and accurate data analysis, a correct estimation of the number of data samples needed in the calculation is always advised. Moreover, the computational effort and the amount of associated time required are two other issues that have to be addressed in the same context.

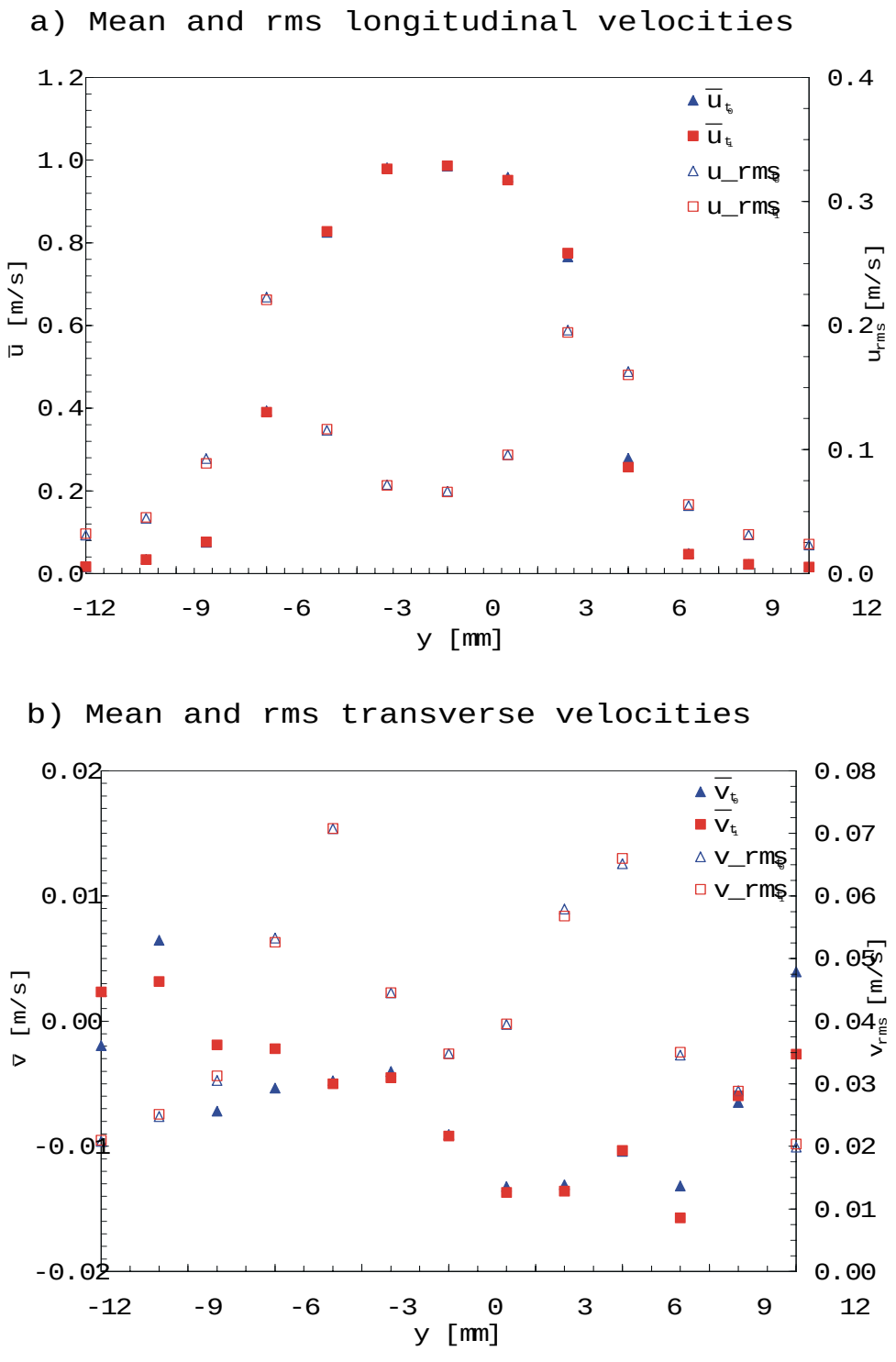

Figure 2.16: Repeatability test - Mean and *rms* longitudinal and transverse velocities ($L^* = 20$, Re $= 11000$, at station $x = 15$ *mm* downstream of the nozzle, LDA data)

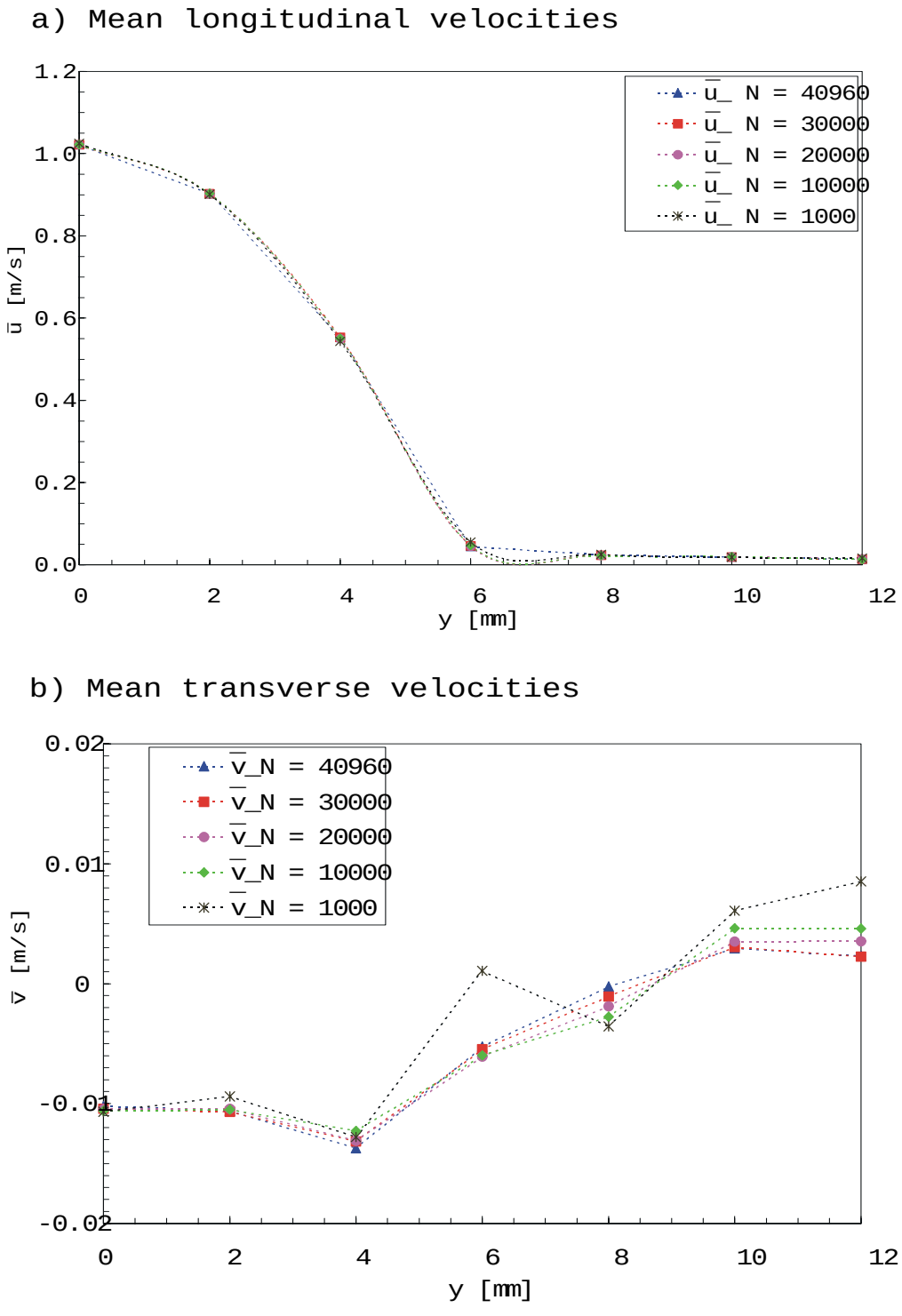

Figure 2.17: Variation of mean longitudinal and transverse velocities with number of samples ($L^* = 20$, Re = 11000, at station $x = 4$ mm downstream of the nozzle, N = samples number, - - - suggested trend for visual purposes only, LDA data)

An examination of the ensemble averaged velocity components at seven locations representing half of the velocity profile at $x = 2\ mm$ ($L^* = 20$, Re = 11000) away from the nozzle and for several sizes of the data block (i.e. 1000, 10000, 20000, 30000, and 40960), have revealed that at least 30000 samples would be necessary to acquire a good accuracy in the full analysis (see Figures 2.17 a, b). Since this involves almost the same computational effort as the entire data set would, the complete sample size (i.e. 40960 samples) is used in all calculations. In this case, using less than 30000 samples in the analysis would lead to important differences in calculated mean value for the v, transverse velocity, component.

Similar to the number of samples in the LDA technique is the number of images one should record to obtain accurate PIV predictions. Since images are large ($\approx 2\ MB$), the issue of computational effort and the time associated with image processing are of greater importance. To illustrate this idea and also the repeatable character of the results, three time independent sets of data have been acquired for the same region of the $L^* = 20$, Re = 11000 opposed jets configuration. The sets consist of 50, 250 and 1000 image pairs, collected as described in section 2.3.5. Processing of these three data sets was performed in the same manner, i.e. using 64×64 pixels interrogation regions and the same correlation and validation schemes. The conclusions of this trial are illustrated in Figures 2.18 a), b).

Little or no difference is observed between the mean and turbulent velocity distributions generated when using 1000 and 250 image pairs, however a pronounced disagreement is shown when the results are compared with those obtained when only 50 image pairs were processed. The flow characteristics (entrainment phenomenon and the vicinity of a strong pressure gradient) probably cause asymmetries in the mean and turbulent transverse velocities even when 1000 image pairs are considered. Based on the above considerations, and the somewhat limited storage memory, 250 image pairs were determined to provide a reasonable accuracy for each experimental configuration in this study.

2.7.7 Effect of Particle Size and Type on PIV Data

As discussed earlier, optimum seeding is crucial to PIV measurements. In general, seeding particles should be chosen as large as possible in order to scatter light, however large particles will not track the flow properly. In this respect, the availability of Titanium Dioxide (TiO_2) particles during the final experimental stages made it possible to evaluate the flow behavior when two different classes of particles were used. Given their physical properties (see Table 2.4), the polypropylene (PP) and TiO_2 particles are situated at opposite ends of seeding limits, a fact that make them suitable for such a comparison. Figures 2.19 a), b) depict the mean and turbulent velocity distributions obtained when 250 image pairs were collected for each seeding case and the processing parameters are maintained as in 2.3.5.

Contrary to what one would expect, mean velocities obtained using the smaller TiO_2 particles were of similar magnitude to those obtained with PP seeding. However, measured turbulent intensities were lower. The camera images of the TiO_2 particles were in the range of $2-3$ pixels / particle while the PP seeding led to particle images at least two times larger (i.e. $5-7$ pixels). This allowed consideration of an enlarged field of view, which also increases the resolution of the technique. From the same pictures, deciding which particles would be more suitable for seeding the present flow is not easy. Experience showed that, due to their size and the lower refractive index of air, TiO_2 particles are more appropriate for air flows. For the above reasons, most of the seeding in these experiments used PP tracer particles.

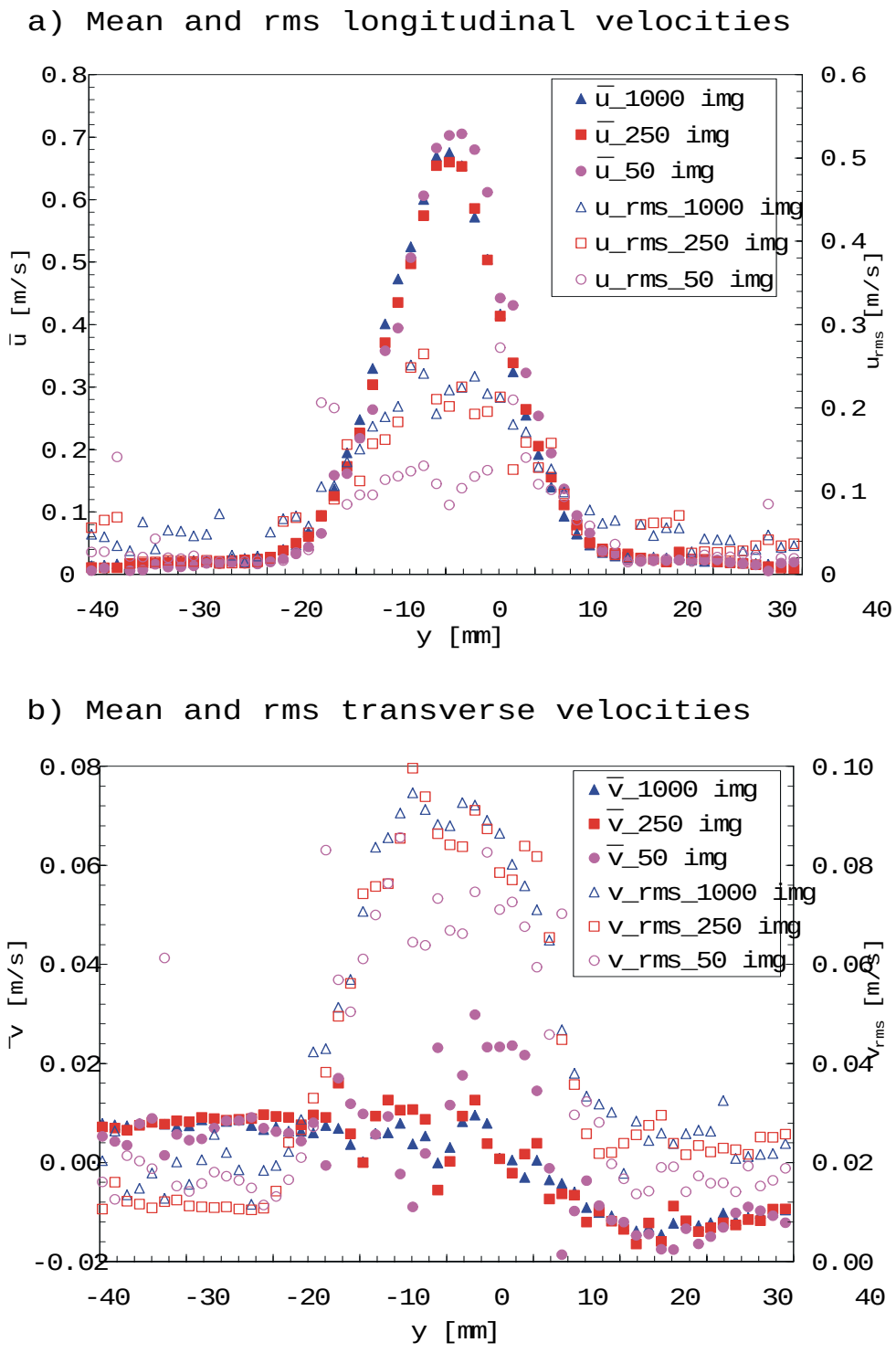

Figure 2.18: Effect of number of PIV images on calculated mean and turbulent velocities ($L^* = 20$, Re = 11000, at station $x/d = 7$ downstream of the nozzle, img = number of images)

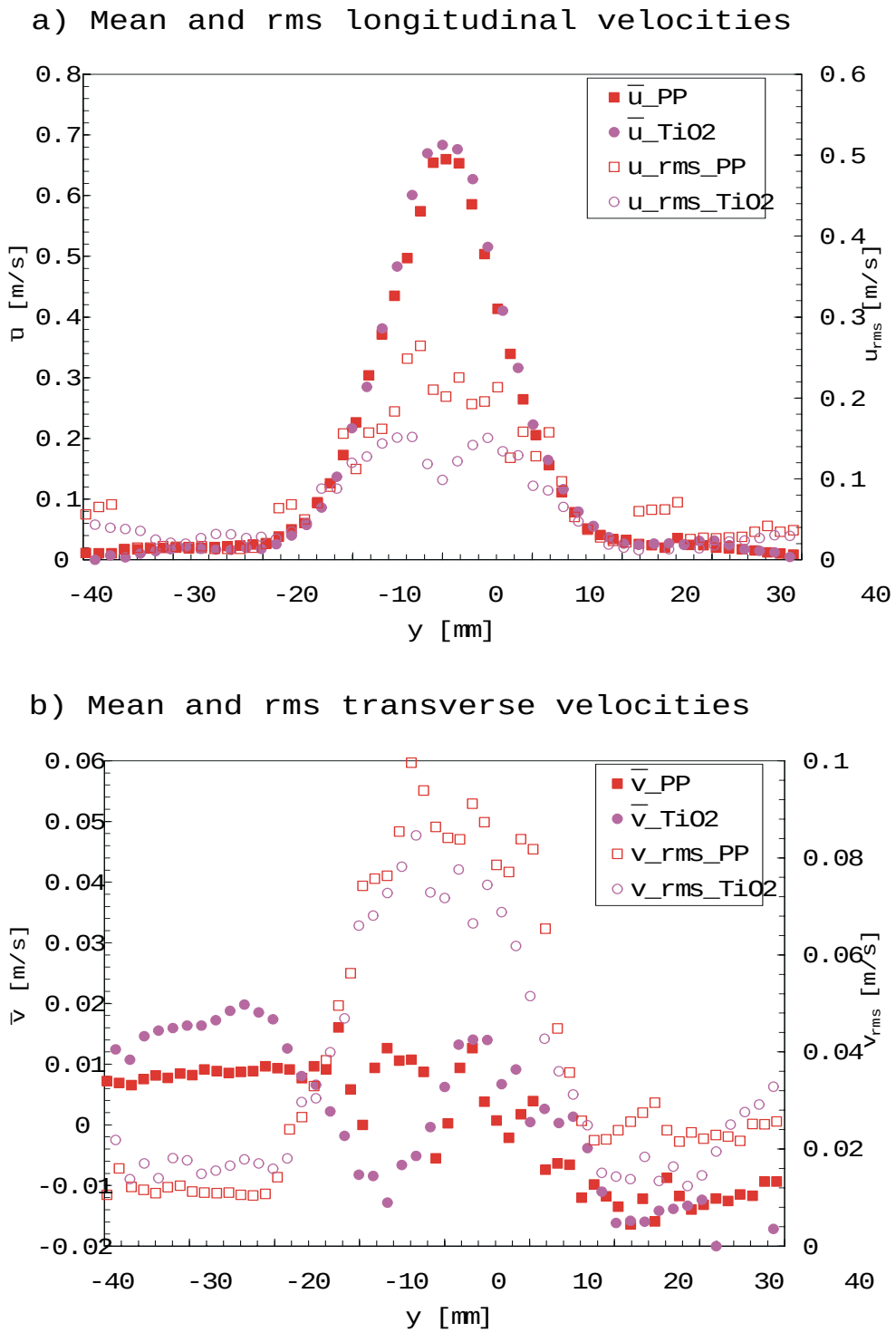

Figure 2.19: Seeding effect on mean and turbulent velocity distributions ($L^* = 20$, $Re = 11000$, at $x/d = 7$ downstream of the nozzle; PP = polypropylene, TiO_2 = Titanium Dioxide, PIV data)

2.7.8 Influence of Interrogation Area Size on PIV Results

The spatial resolution of the smallest velocity structures in PIV is determined by the size of the perspective projection of the interrogation area. This factor is determined by the image to object scale factor, S, the size of the interrogation area on the image plane (in pixels) and the pixel pitch (i.e. the distance between adjacent pixels on the CCD chip) [15]. Since S is a setup parameter and the pixel pitch is a fixed property of the camera, the only variable remaining to be adjusted is the size of the interrogation area on the image plane. A rough idea about choosing the interrogation area size is given by the spatial scales involved in the flow (which we do not know entirely), and the dynamic range of measured velocities. Thus, the size of the interrogation region should be small enough to pick up the small scales present in the flow and yet large enough to get the largest possible dynamic range. An evaluation of the best suitable size of the interrogation area for the opposed jets flow is achieved in Figures 2.20 a), b) and 2.21 a), b) where the performance of 16×16, 32×32, 64×64, and 128×128 *pixels* interrogation areas is tested on the same 250 images (all the other processing parameters are held constant and defined as in section 2.3.5).

These representations show close mean velocity distributions for interrogation areas of 32×32, 64×64, and 128×128 *pixels*. However, great discrepancies are observed for all turbulent intensity profiles and exaggerated magnitudes are provided by interrogation areas of 16×16 *pixels*, which seem to capture much of the noise present. Finally, based on considerations such as smoother velocity distributions (i.e. a good signal to noise ratio), computational effort and processing time, the issue of maximizing the number of vectors in the output vector map as well as satisfying both the requirements of a large dynamic range and a good spatial resolution, interrogation areas of 64×64 *pixels* were used to process the acquired PIV images.

2.7.9 Filtering of PIV Data

As mentioned in section 2.6, the cyclic noise generated by using Fast Fourier Transforms to calculate the correlation plane accounts for the largest share of the additive noise function N in the PIV data. Overlapping the interrogation regions is one solution to reduce this noise and to use some of the information available near the edges of the interrogation regions (i.e. some particle pairs). Overlapping the interrogation areas increases the probability that most of the particle pairs in each image are within at least one of the interrogation areas and, as a consequence, the number of displacement vectors will increase (although it may also increase the number of " false" vectors). Figures 2.22 a) and b) indicate the use of the overlapping option.

Surprisingly, the only significant difference between the three overlapping options (i.e. 0%, 25% and 75%) is the number of the resulting displacement vectors (i.e. the corresponding data points). Thus, even though the 0% overlapping of the interrogation areas produces the smallest number of displacement vectors, the predicted magnitude of the velocity field is situated in the right range. Mainly due to the larger number of resultant displacement vectors and therefore a more even distribution of the graph points, 75% overlapping has been used to process all PIV data sets.

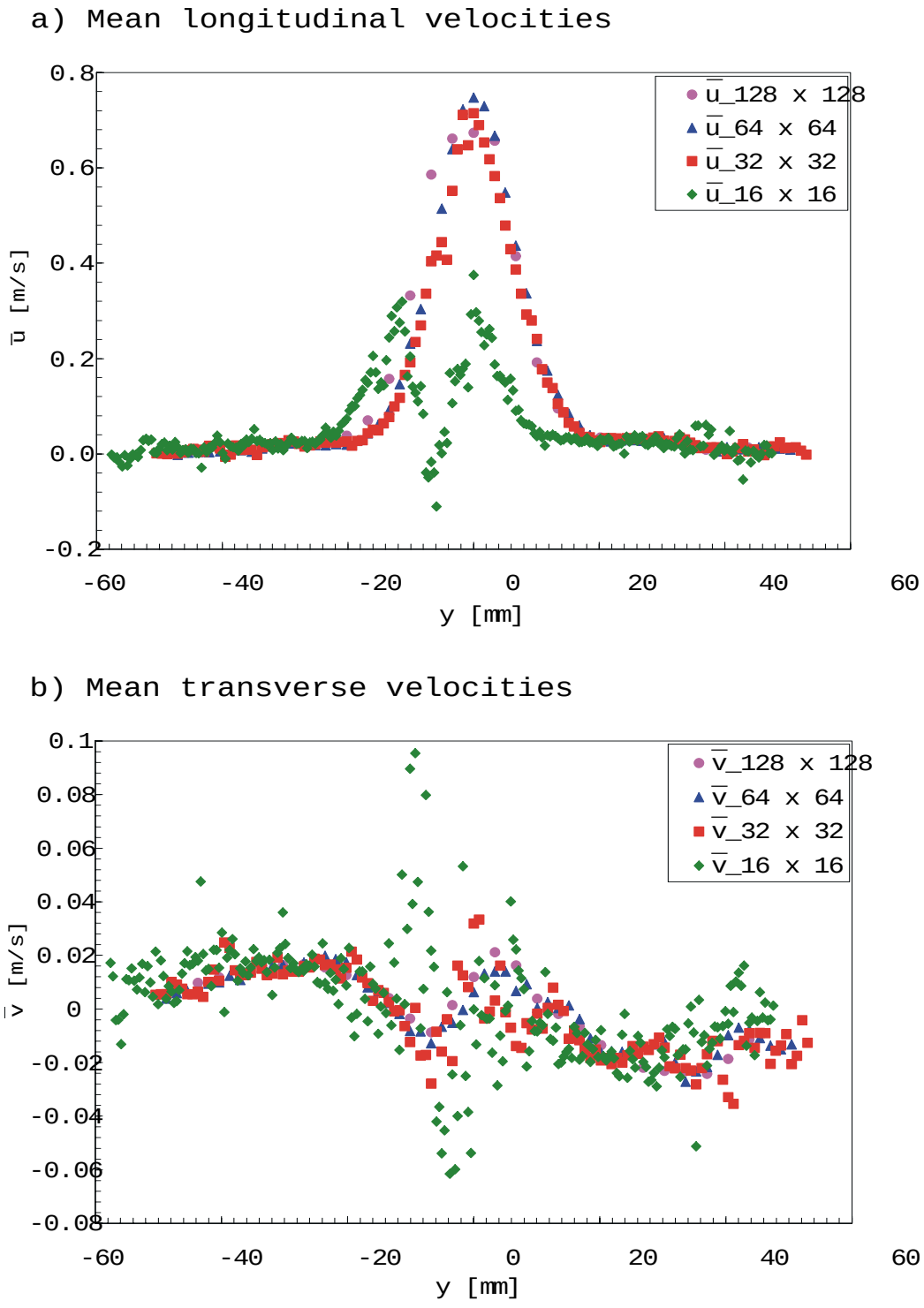

Figure 2.20: Evaluation of optimum interrogation area size - Mean velocity profiles ($L^* = 20$, $Re = 11000$, at $x/d = 7$ downstream of the nozzle, PIV data)

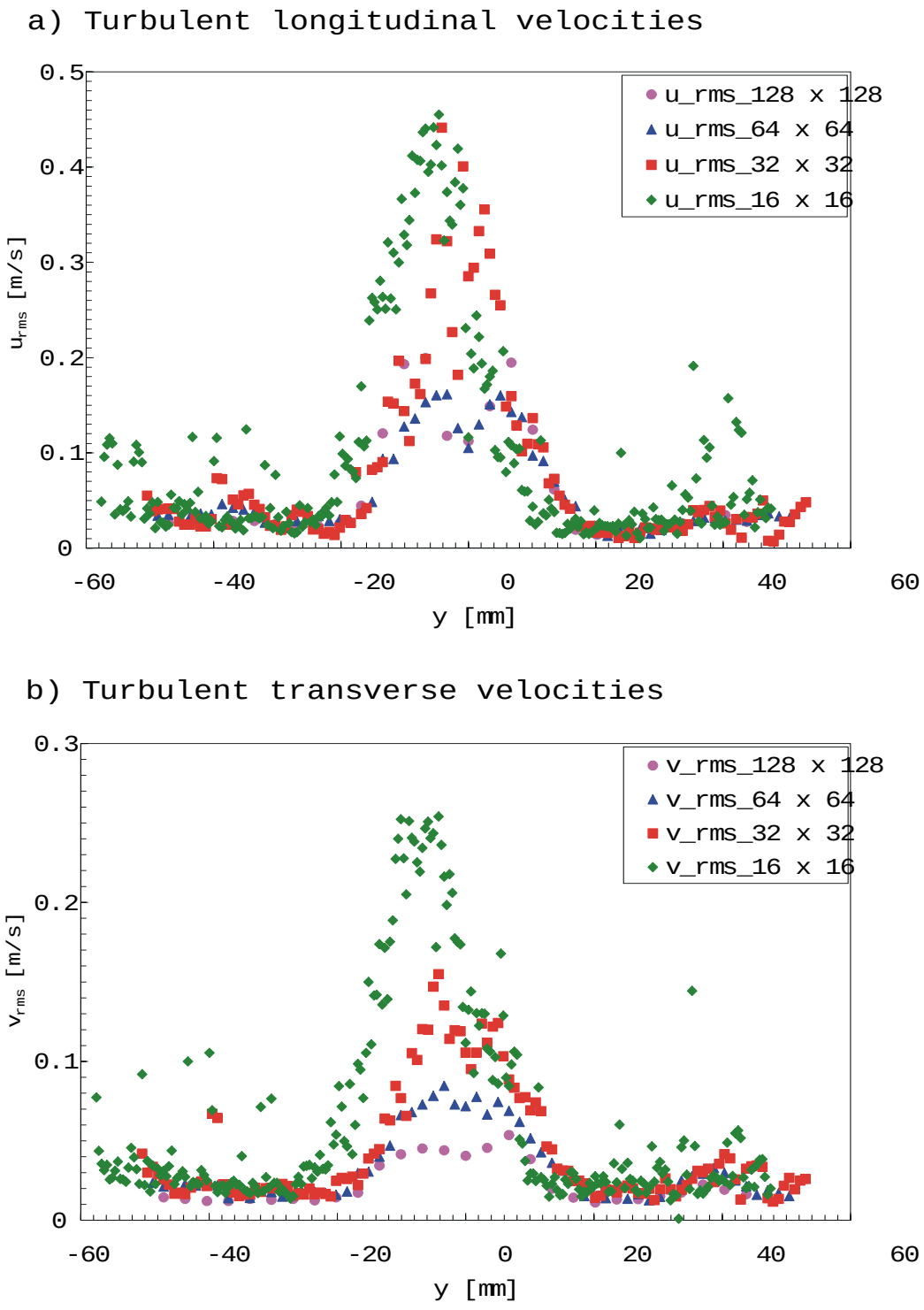

Figure 2.21: Evaluation of optimum interrogation area size - Turbulent velocity profiles ($L^* = 20$, $Re = 11000$, at $x/d = 7$ downstream of the nozzle, PIV data)

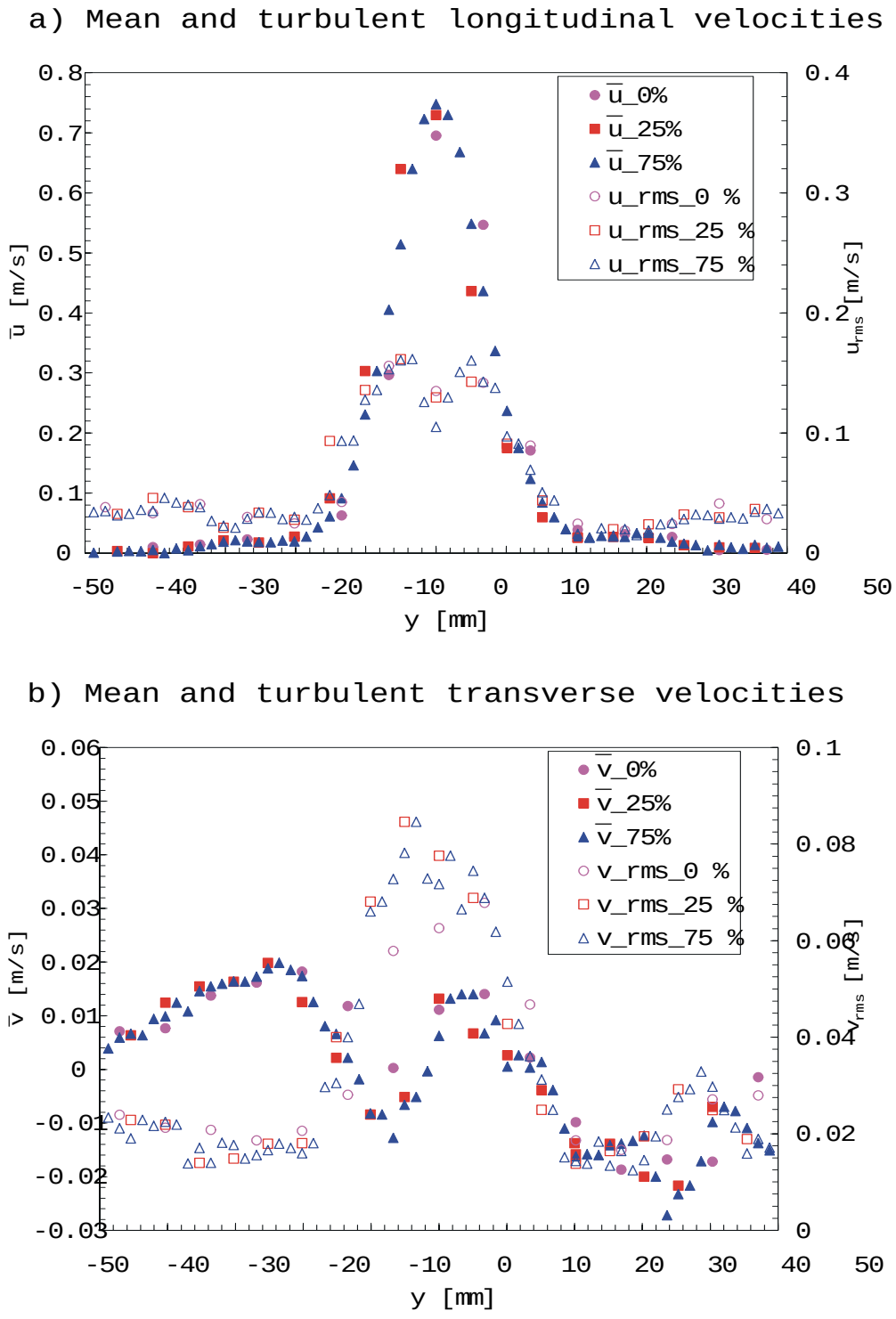

Figure 2.22: Filtering the cyclic noise by overlapping of interrogation regions - Mean and turbulent velocity distributions ($L^* = 20$, $Re = 11000$, at $x/d = 7$ downstream of the nozzle, PIV data)

Chapter 3

Numerical Computation

Computational Fluid Dynamics (CFD) can be described as the ability of replacing the governing partial differential equations of fluid flow with algebraic equations which can be more easily solved and advancing their solutions in time and/or space to obtain a discrete numerical description of the flow field of interest. In recent times, CFD has become the third instrument of study in fluid dynamics, of equal stature and importance to experiment and theory. It is now a permanent presence in all aspects of fluid dynamics, from basic research to engineering design. The high speed digital computer has led to tremendous advances in CFD. Therefore, the progress in CFD is directly and strongly related to advances in computer hardware, particularly in regard to execution speed and storage.

What CFD offers in conjunction with an experimental approach is a substantial reduction of lead time and cost of new designs. These always imply running a good quality code and having knowledge of the flow field under investigation. However, it can be affirmed that CFD cannot be utilized adequately without continued reference to experimental data and validation studies. It is impossible to assess the validity of the models of physics implemented in a CFD code or the accuracy of its final results by means other than experimental work.

This chapter will describe the computation of the turbulent opposed impinging jets flow examined in the experiments using LDA and PIV. In this respect, the theory behind the numerical fluid flow calculation package (TASCflow) [4] used to model the present flow, is presented. The flow was considered statistically stationary, three dimensional, incompressible and with constant fluid properties. The treatment starts with the governing partial differential equations of fluid flow in Cartesian tensor notation. Following that, the turbulence models used in the present simulations and their limitations will be discussed. Some issues related to mesh generation and boundary conditions as applied to this study will then be addressed, and the chapter will conclude with a discussion of the convergence of the solution and its refinement.

3.1 Governing Equations of Fluid Flow

As mentioned in Chapter I, the three dimensional motion of a Newtonian fluid is described by a coupled system of five non-linear partial differential equations: mass conservation (continuity), 3 momentum equations (Navier-Stokes equations) and the energy equation. Low speed liquid and gas flows are usually treated as incompressible flows, and if the problem does not involve heat transfer, the flow field can be solved by considering the continuity and Navier Stokes equations only. Since heat transfer is not of interest here, the reduced system (i.e. equations of mass conservation, x, y and z momentum) is further discussed in this section. It is well known that is impossible to obtain a direct analytical solution to this system of equations. Direct numerical solutions of the system have been obtained for some very simple low Reynolds number flows such as open channel flow, using Direct Numerical Simulation (DNS) techniques and parallel computing [20]. It assumed that on a fine enough scale, all turbulent flows obey the Navier-Stokes equations and for a correspondingly large number of grid points, both fine and large scale aspects of turbulence can be calculated. However, it will take more time until computer hardware will be able to provide sufficient computational power to directly solve more complex flows.

The common approach to solution of the Navier-Stokes equation set, is based on simplifying the equations as much as possible, then introducing turbulence models to approximate the real physics of the flow and using advanced numerical techniques to discretize and transform the initial differential equations into algebraic equations that can be solved by computers. Therefore all CFD solutions of turbulent flows involve physical approximations even though reasonable calculations have been obtained for some situations.

One of the most popular techniques for numerically representing the system of the fluid flow equations, and used by TASCFlow [4], is the finite volume method. It is based on the physical conservation laws and is physically intuitive. According to this method the computational domain is discretized into a grid, which is used to define storage locations for each variable of the system. Finite control volumes are then created around each of these locations, and the governing equations are integrated over each control volume. The fluid flow equations that are directly obtained by applying the fundamental physical principles (i.e. mass is conserved, Newton's second law, and when heat transfer is involved, energy is conserved) to a finite control volume are in integral form. By applying Gauss' divergence theorem, the surface integrals can be transformed into volume integrals. Then, considering a infinitesimally small control volume, the equations containing volume integrals are transformed into partial differential equations [6]. If the finite control volume is fixed in space, the governing equations in any of the above forms are called conservative. The instantaneous conservation equations for mass and momentum, expressed in tensor notation are given by equations 1.1 and 1.2 in section 1.1 of Chapter I.

As previously discussed in sections 1.2 and 2.5.1, in turbulent flows the instantaneous value of any quantity is expressed as a mean and fluctuating component through a process of time-averaging called Reynolds-Stress decomposition. In TASCflow, the fluctuating components are not determined directly, instead time-averaged equations are solved. Therefore, the initial conservation equations 1.1 and 1.2 for an incompressible, Newtonian and isothermal flow, written in terms of time-averaged quantities, become [4]
continuity:

$$\frac{\partial \overline{u_i}}{\partial x_i} = 0 \tag{3.1}$$

and the momentum equation is,

$$\rho \frac{\partial \overline{u_i}}{\partial t} + \rho \frac{\partial \left(\overline{u_j u_i}\right)}{\partial x_j} = -\frac{\partial \overline{p}}{\partial x_i} + \frac{\partial}{\partial x_j}\left(\overline{\tau_{ij}} - \rho \overline{u_i' u_j'}\right) + \overline{S_{ui}} \tag{3.2}$$

where

$$\overline{\tau_{ij}} = \mu D_{ij} = \mu \left(\frac{\partial \overline{u_i}}{\partial x_j} + \frac{\partial \overline{u_j}}{\partial x_i} \right) \qquad \left[N/m^2 \right] \tag{3.3}$$

is the mean viscous stress tensor, μ is the dynamic viscosity and $\overline{S_{ui}}$ are additional source terms. D_{ij} is the viscous stress tensor and is usually termed the rate of deformation of fluid elements or the mean strain rate tensor. The new term, $-\rho\overline{u_i' u_j'}$ is often referred to as the Reynolds Stresses term and it cannot be expressed as a function of the mean flow variables. Besides pressure, $\overline{p}$, and the three velocity components, $\overline{u_i}$, the Reynolds Stresses introduce another six unknowns to the above system of equations, since $\overline{u_2' u_1'} = \overline{u_1' u_2'}$, $\overline{u_3' u_1'} = \overline{u_1' u_3'}$ and $\overline{u_3' u_2'} = \overline{u_2' u_3'}$. These terms must be related to known quantities through a " turbulence model", before a closed solution of the above equation system becomes possible.

3.2 Turbulence Models

Beyond the fact that it is intended to model the physics of the flow, a turbulence model is a computational procedure which allows closure of the system of mean flow equations so that a variety of flow problems can be calculated. A large array of turbulence models exist including classical models based on Reynolds Stress decomposition such as mixing length model, $k - \varepsilon$ model, Reynolds stress equation model and the algebraic stress model, and large eddy simulation based on space filtered equations [53]. Of the classical models, including mixing length theory, the $k - \varepsilon$ model is by far the most widely used and validated. These two models are based on the Boussinesq eddy-viscosity concept which assumes that Reynolds (turbulent) stresses act in a way analogous to the viscous stresses in laminar flows, and therefore the turbulent stresses are proportional to the mean velocity gradient. Experience shows that turbulence decays unless there is shear stress in isothermal incompressible flows [53]. Also, turbulent stresses are found to increase as the mean strain rate increases [53].

The initial eddy-viscosity concept may be expressed as:

$$-\rho\overline{u_i' u_j'} = \mu_t \left(\frac{\partial \overline{u_i}}{\partial x_j} + \frac{\partial \overline{u_j}}{\partial x_i} \right) \qquad \left[N/m^2 \right] \tag{3.4}$$

Boussinesq's relationship, Equation 3.4, is analogous to the mean viscous stress tensor in equation 3.3, excepting for the inclusion of turbulent or eddy viscosity μ_t. The mixing length and $k - \varepsilon$ models assume that the turbulent viscosity is isotropic, therefore the ratio between Reynolds stress and mean strain rate is the same in all directions.

Given the complex character of the flow under investigation and due to the lack of TASCFlow documentation regarding the usage of the implemented turbulence models, the $k - \varepsilon$ model under three distinct formulations (Standard $k - \varepsilon$ model for high Re number flows, Kato-Launder $k - \varepsilon$ model for low Re number flows and the RNG $k - \varepsilon$ model) was used to simulate the opposed impinging jets flow in this study. This section continues with a short description of each of the three models while an assessment of their performance in prediction of opposed jets flow is presented later.

3.2.1 The Standard $k-\varepsilon$ Model

Unlike the mixing length models which describe the stresses by means of simple algebraic formulae for μ_t, the $k-\varepsilon$ model is a more sophisticated and general description of turbulence. It models the effects of transport of turbulence properties by the mean flow and diffusion, as well as for production and destruction of turbulence. The $k-\varepsilon$ model uses an extended Boussinesq relationship, namely the gradient diffusion hypothesis [46], to relate the Reynolds stresses to the mean velocity gradients and the turbulent viscosity:

$$-\rho\overline{u_i'u_j'} = \mu_t\left(\frac{\partial\overline{u_i}}{\partial x_j}+\frac{\partial\overline{u_j}}{\partial x_i}\right)-\frac{2}{3}\rho k\delta_{ij} \tag{3.5}$$

where k is the turbulent kinetic energy as defined in Equation 2.19 and δ_{ij} is the Kronecker-Delta tensor. As proposed by Prandtl and Kolmogorov [46], the turbulent viscosity μ_t (or the turbulent kinematic viscosity ν_t) is modeled as the product of a turbulent velocity V_t and a dissipation length scale l_t, which then becomes a relationship between turbulent kinetic energy k and the turbulent dissipation rate ε based on Kolmogorov's observation that $\varepsilon = \frac{k^{3/2}}{l_t}$ [4]:

$$\mu_t = \rho C_\mu l_t V_t = \rho C_\mu \frac{k^2}{\varepsilon} \qquad \left[Ns/m^2\right] \qquad or \qquad \nu_t = C_\mu\frac{k^2}{\varepsilon} \qquad \left[m^2/s\right] \tag{3.6}$$

If k and either l_t or ε are known, the turbulent viscosity can be computed using equation 3.6 and the Reynolds stresses can be determined from equation 3.5. The $k-\varepsilon$ model solves two additional partial differential equations, one for the transport of turbulent kinetic energy k and a different one for the rate of dissipation of turbulent kinetic energy ε. The equation of the fluctuating component of kinetic energy (i.e. the turbulent kinetic energy) k is derived by subtracting the mean kinetic energy equation from the time averaged instantaneous kinetic energy equation which in turn is obtained by manipulations of the instantaneous momentum equations [49]:

$$\rho\frac{\partial k}{\partial t}+\rho\overline{u_j}\frac{\partial k}{\partial x_j} = P_k-\rho\varepsilon+\frac{\partial}{\partial x_j}\left(\mu\frac{\partial k}{\partial x_j}-\overline{u_j'\left[p'+\rho\frac{u_i'u_i'}{2}\right]}\right)+\overline{S_{uj}'u_j'} \tag{3.7}$$

where

$$P_k = -\rho\overline{u_i'u_j'}\frac{\partial\overline{u_i}}{\partial x_j} = \text{Production of } k \tag{3.8}$$

$$\varepsilon = \frac{\mu}{\rho}\overline{\left(\frac{\partial u_i'}{\partial x_j}\right)^2} = \text{Dissipation of } k \tag{3.9}$$

Further modeling is required for the correlations $\overline{u_j'\left[p'+\rho\frac{u_i'u_i'}{2}\right]}$ referred to as the pressure-velocity fluctuation term. Using the gradient diffusion hypothesis, this becomes [46]:

$$-\overline{u_j'\left[p'+\rho\frac{u_i'u_i'}{2}\right]} \approx \frac{\mu_t}{\sigma_k}\frac{\partial k}{\partial x_i} \tag{3.10}$$

$\overline{S_{uj}'u_j'}$ in equation 3.7 accounts for externally applied forces S_{uj} (such as gravity and buoyancy) and either is neglected or defined for a particular application.

Derived by several artificial manipulations of the momentum equations, the equation of turbulent kinetic energy dissipation, ε, is given by [46]:

$$\rho\frac{\partial\varepsilon}{\partial t}+\rho\overline{u_j}\frac{\partial\varepsilon}{\partial x_j}=C_{\varepsilon1}\frac{\varepsilon}{k}P_k-C_{\varepsilon2}\rho\frac{\varepsilon^2}{k}+\frac{\partial}{\partial x_j}\left(\mu+\frac{\mu_t}{\sigma_\varepsilon}\frac{\partial\varepsilon}{\partial x_j}\right) \tag{3.11}$$

The above equations contain five adjustable constants: C_μ, $C_{\varepsilon1}$, $C_{\varepsilon2}$, and Prandtl numbers σ_k and σ_ε which connect the diffusiveness of k and ε to the eddy viscosity μ_t. Data fitting procedures employed for a wide range of turbulent flows (mostly free turbulent flows but they can also be used for wall flows) have provided the following values for the constants used in a " standard $k-\varepsilon$" model implementation [38]:

$$C_\mu=0.09,\qquad C_{\varepsilon1}=1.44,\qquad C_{\varepsilon2}=1.92,\qquad \sigma_k=1.00,\qquad \sigma_\varepsilon=1.30 \tag{3.12}$$

As a particular feature of the standard $k-\varepsilon$ model one could mention the close link between production and dissipation of turbulent kinetic energy which is partially triggered by the isotropic assumption for the normal Reynolds stresses. In this respect, an equal third is allocated to each normal stress component to ensure that their sum always has its physical value, $-\rho\left(\overline{u'^2}+\overline{v'^2}+\overline{w'^2}\right)=-2\rho k$. This assumption along with the Kronecker-Delta tensor is needed to make the gradient diffusion hypothesis (equation 3.5) applicable to the normal Reynolds stresses. Thus, equation 3.11 for ε assumes that its production and dissipation terms are proportional to the production and dissipation terms of the k equation (3.7). Therefore, the dissipation rate ε is large where production of k is large. The proportionality factor ε/k in the ε equation (3.11) makes the production and destruction terms dimensionally correct.

Boundary Conditions

Due to the parabolic-elliptic behavior of the model equations for k and ε, the following boundary conditions (Table 3.1) should be employed [4]:

Table 3.1: Two Equation Model - general boundary conditions

Flow region	Boundary condition
Inlet	turbulence intensity and eddy length scale or distributions of k and ε must be given
Outlet or symmetry axis	$\partial k/\partial n=0$ and $\partial\varepsilon/\partial n=0$
Solid walls	(no slip condition) approach depends on Reynolds number

Usually, the boundary condition information required to start the simulation are taken from available experimental data or are calculated by means of empirical approximations related to the mixing length formulae.

At high Re numbers, due to very large gradients in the dependent variables near walls (the boundary layer gets thinner), a large number of grid nodes would be required to fully resolve the flow in those regions. In these cases the standard $k-\varepsilon$ model avoids direct integration to the wall by means of "wall functions" which rely on the existence of a logarithmic region (see Figure 3.1) in the velocity profile [20].

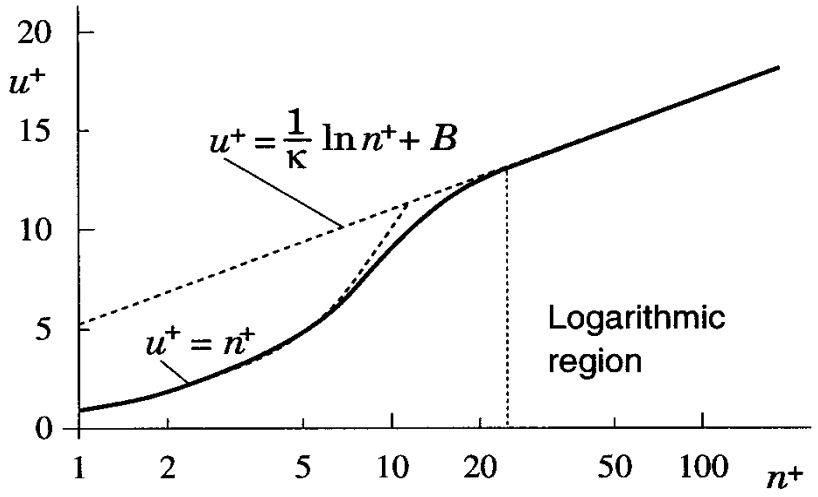

Figure 3.1: Velocity distribution in a turbulent boundary layer near a solid wall (- - - theoretical-numerical data; — experimental data) [20]

In TASCFlow, the wall functions are dependent on the dimensionless distance from the wall n^+,

$$n^+ = \frac{\rho u_\tau n}{\mu}, \qquad where \qquad u_\tau = C_\mu^{1/4}\sqrt{k} \tag{3.13}$$

if local equilibrium is assumed (i.e. the production of turbulence balances the dissipation) and n is the coordinate normal to the wall. Based on the normalized distance from the wall, n^+, the near wall region is divided into three sections corresponding to the viscous sub-layer, the buffer layer and the log-law region, where the associated dimensionless velocity profiles are given by [4]:

$$u^+ = n^+, \qquad n^+ \leq 5 \tag{3.14}$$

$$u^+ = d_1\left(n^+\right)^3 + d_2\left(n^+\right)^2 + d_3 n^+ + d_4, \qquad 5 \leq n^+ \leq 30 \tag{3.15}$$

$$u^+ = \frac{\overline{u_t}}{u_\tau} = \frac{1}{\kappa}\ln\left(n^+\right) + B, \qquad n^+ \geq 30 \tag{3.16}$$

For $5 \leq n^+ \leq 30$, the coefficients are determined such that the u^+ ($\overline{u_t}$ is the mean velocity parallel to the wall) function is continuous and derivable on $n^+ \in [5, 30]$ and their values are as follows [4]: $d_1 = 6.4264 \cdot 10^{-4}$, $d_2 = -5.2113 \cdot 10^{-2}$, $d_3 = 1.4729$, $d_4 = -1.1422$. For the log-law region, the von Karman constant is $\kappa = 0.41$ and B is an empirical constant related to the thickness of the viscous sub-layer ($B = 5.2$ for a flat plate boundary layer [20]). Due to failures of the k and ε equations in the sub-layer region ($n^+ \leq 5$) and of wall function equations beyond $n^+ > 500$, it is recommended that the near wall nodes be placed in the log-law region of $30 \leq n^+ \leq 500$ for smooth walls.

Since the wall boundary condition is of less interest for the present study, appearing as a weak boundary condition in our simulation, the smooth wall will not be further developed and no treatment of rough walls will be presented.

3.2.2 The Low-Reynolds Number $k-\varepsilon$ Model

At low Re numbers, the log-law velocity distribution is not valid so that the above boundary conditions cannot be used. Modifications to the standard $k-\varepsilon$ model have been undertaken to make it suitable for low Re number flows. In this respect, wall damping has to be applied to ensure the transport of turbulent Reynolds stresses to viscous stresses in the viscous sublayer adjacent to solid walls. Thus, for the case of the low Reynolds number $k-\varepsilon$ model, the equations 3.6, 3.7 and 3.11 become [11]:

$$\mu_t = \rho C_\mu f_\mu \frac{k^2}{\widetilde{\varepsilon}} \qquad \left[Ns/m^2\right] \tag{3.17}$$

$$\rho\frac{\partial k}{\partial t} + \rho\overline{u_j}\frac{\partial k}{\partial x_j} = P_k - \rho\varepsilon + \frac{\partial}{\partial x_j}\left(\mu\frac{\partial k}{\partial x_j} - \overline{u_j'\left[p' + \rho\frac{u_i'u_i'}{2}\right]}\right) + \overline{S_{uj}'u_j'} \tag{3.18}$$

$$\begin{aligned}\rho\frac{\partial \widetilde{\varepsilon}}{\partial t} + \rho\overline{u_j}\frac{\partial \widetilde{\varepsilon}}{\partial x_j} \;=\; & C_{\varepsilon 1}\frac{\widetilde{\varepsilon}}{k}P_k - C_{\varepsilon 2}f_\varepsilon\rho\frac{\widetilde{\varepsilon}^2}{k} + 2\mu\mu_t\left(\frac{\partial^2\overline{u_i}}{\partial x_j\partial x_k}\right)^2 \\ & + \frac{\partial}{\partial x_j}\left(\mu + \frac{\mu_t}{\sigma_\varepsilon}\frac{\partial\widetilde{\varepsilon}}{\partial x_j}\right) + Y_c\end{aligned} \tag{3.19}$$

where $\widetilde{\varepsilon}$ is the isotropic dissipation rate of k with

$$\varepsilon = \widetilde{\varepsilon} + 2\mu\left(\frac{\partial k^{1/2}}{\partial x_j}\right)^2 \tag{3.20}$$

and Y_c is a correction term ($C_w = 0.83$, $C_1 = 2.5$) defined as [11],

$$Y_c = C_w\left(\frac{k^{3/2}}{C_1\widetilde{\varepsilon}y} - 1\right)\left(\frac{k^{3/2}}{C_1\widetilde{\varepsilon}y}\right)^2\frac{\widetilde{\varepsilon}^2}{k} \tag{3.21}$$

The most obvious modification, are the addition of a source (sink) term for the dissipation rate including a viscous contribution μ, and multiplication of the constants C_μ, and $C_{\varepsilon 2}$ by wall-damping functions f_μ and f_ε respectively, which are themselves functions of the turbulent Reynolds number $\mathrm{Re}_t = \frac{k^2}{\nu\widetilde{\varepsilon}}$ [49]:

$$f_\mu = \exp\left\{-\frac{3.4}{\left(1 + \frac{\mathrm{Re_t}}{50}\right)^2}\right\} \tag{3.22}$$

$$f_\varepsilon = \left(1 - 0.3\exp\left\{-\mathrm{Re}_t^2\right\}\right) \tag{3.23}$$

In TASCFlow this model is termed the Kato-Launder $k-\varepsilon$ model, using the wall-damping functions.

3.2.3 The Renormalization Group $k-\varepsilon$ Model

The Renormalization Group (RNG) theory constitutes one of the greatest achievements in the field of theoretical physics in the last 30 years. Applications of RNG concepts range from elementary particle physics (quark confinement), to statistical physics (critical phenomena and

pattern formation), and due to the increased understanding and use of RNG theory, it can be applied to evolution of turbulence in fluid dynamics [5].

Since its development in 1970, the $k-\varepsilon$ model has attracted criticism with regard to the lack of strategy and rigorousness in its derivation from the Navier-Stokes equations [43]. To date, there is no analytical solution for exact equations for u, k and ε. As mentioned in section 3.2.1, the standard closure involves an eddy viscosity model as well as model source terms in the k and ε equations. The criticisms are mostly related to the modeling of the source/sink terms in the transport equation for the dissipation rate of turbulent kinetic energy, ε. In the standard $k-\varepsilon$ model, dimensional analysis has been the dominant argument used to derive models of the production/destruction (source/sink) processes and the resulting relationship takes the form [47]:

$$NetSource_{\varepsilon} = C_{\varepsilon 1}\frac{\varepsilon}{k}P_k - C_{\varepsilon 2}\rho\frac{\varepsilon^2}{k} \tag{3.24}$$

where P_k is the shear production of turbulent kinetic energy and $C_{\varepsilon 1}$ and $C_{\varepsilon 2}$ are empirically determined coefficients. Also, for the derivation of the model equation for ε, the source and sink terms of the exact transport equation for ε, which scale as $\mathrm{Re}_t^{1/2}$ ($\mathrm{Re}_t = \frac{k^2}{\nu\varepsilon}$) [49], were assumed to cancel in the limit of large Re_t such that the model source terms are of order one.

Yakhot and Orszag [41] were the first to completely derive a version of the $k-\varepsilon$ model using the scale removing procedure of RNG theory. In this approach, ε is expanded about an equilibrium state with known Gaussian statistics by using the correspondence principle where the effects of mean strains are represented by a random force [43]. At high turbulent Reynolds numbers, the original RNG method neglected several terms in the derivation of the ε transport equation [41], a fact leading to the same form of production and destruction of ε as in equation 3.24 but with different values for $C_{\varepsilon 1}$ and $C_{\varepsilon 2}$ explicitly calculated by the theory. However, a major difference between the standard and the RNG $k-\varepsilon$ models does exist in the near wall treatment. The RNG model can be integrated directly to a solid boundary while the standard model needs empirical wall damping functions to extend its functionality near a solid boundary [43].

Besides the corrections to the constants in the dissipation rate equation made by Yakhot and Smith [43], the latest RNG $k-\varepsilon$ model developed by Yakhot et al. [42] includes a modification of the production of dissipation term to account for non-equilibrium strain rates. A summary of these coefficients is as follows [43]:

$$C_{\mu} = 0.085, \qquad C_{\varepsilon 1} = C_{\varepsilon 1_0} - \frac{\eta\left(1-\frac{\eta}{\eta_0}\right)}{1+\beta\eta^3} \tag{3.25}$$

$$C_{\varepsilon 2} = 1.68, \qquad \sigma_k = 0.7179, \qquad \sigma_{\varepsilon} = 0.7179 \tag{3.26}$$

where $C_{\varepsilon 1_0} = 1.42$, $\eta = Sk/\varepsilon$ is the nondimensional strain rate, and $\eta_0 = 4.38$ is the asymptotic non-dimensional strain rate in 2D plane shear homogeneous turbulence. $S = \left(2\overline{S_{ij}S_{ij}}\right)^{1/2}$ is the norm of the mean rate of strain tensor

$$\overline{S_{ij}} = \frac{1}{2}\left(\frac{\partial\overline{u_i}}{\partial x_j} + \frac{\partial\overline{u_j}}{\partial x_i}\right) \tag{3.27}$$

It has also been shown [47] and [43] that the RNG theory cannot provide a closure for the production of dissipation term in powers of η, so that terms of all orders must be retained to satisfy the weak and strong strain limits. The approximation used to obtain a closed solution for this term led to an undetermined constant $\beta = 0.015$ which was empirically evaluated to

yield the von Karman constant $\kappa = 0.41$. It is well known that the standard $k - \varepsilon$ model underpredicts the reattachment point when applied to a complex shear flow with separation (i.e. turbulent flow over a backward facing step). In turn, the RNG $k - \varepsilon$ model proposed by Yakhot et al. predicts a reattachment point that is extremely close (within 5 %) to the experimental value and a secondary separation bubble below the corner of the step that is even closer to the experimental observations [43]. Aso, when extended to include an anisotropic eddy viscosity this RNG $k - \varepsilon$ model predicts a reattachment point almost identical to the experimental value of 7.1 step heights downstream of the step corner.

This is probably part of the reason why the final RNG $k - \varepsilon$ model of Yakhot et al. which uses values for the coefficients that are consistent with RNG theory, $\{C_\mu, C_{\varepsilon 1_0}, C_{\varepsilon 2}, \sigma_\varepsilon, \beta\} = \{0.085, 1.42, 1.68, 0.77, 0.012\}$ have been recommended by Stubley and implemented in TASCFlow [47].

3.3 Simulation of Turbulent Opposed Impinging Jets Flow

Experience shows that in order to get good computational results it is always advisable to understand the physics prior to starting a numerical simulation. The literature review in Chapter 1 revealed a lack of computational work in the flow under consideration. Consequently, this effort represents more an examination of the application of $k - \varepsilon$ turbulence model to the turbulent opposed impinging jets flow than optimization of a computational solution to this particular flow. As previously mentioned, the $k - \varepsilon$ model under three distinct formulations, standard $k - \varepsilon$ model for high Re number flows, Kato-Launder $k - \varepsilon$ model for low Re number flows and the RNG $k - \varepsilon$ model, was used to simulate the turbulent opposed impinging jets flow in the present study. This section provides a short description of the computational details as they were implemented in TASCFlow in order to obtain a convergent solution of this flow.

3.3.1 The Computational Domain

The opposed impinging jets experimental arrangement described in Chapter 2 (Figures 2.1 and 2.2) has been modelled as a three dimensional block containing half of each of the two opposed nozzles and a parallelepiped with the spacing between nozzles as one of its sides (Figure 3.2).

Due to the axisymmetric configuration of the nozzles and the assumption that, on average, the flow field created by the impingement of the two jets is axisymmetric as well, symmetry conditions were used in simulation of the geometry. This considerably reduced the number of grid points required in the numerical simulation. Symmetry considerations would suggest that just a quarter (or even a finite slice) of the entire computational domain would have sufficed but constraints related to a desirable structured mesh dictated the above shape of the computational domain. A cylindrical computational domain could have generated similar results but similarity with the experimental arrangement was sought.

The model geometry as shown in Figure 3.2 was created in CFX-Build, software package used in conjunction with TASCFlow for the design of appropriate geometries and grid generation for fluid dynamics simulations. The computational model scale emulated the physical (experimental) model dimensions as described in Chapter 2.

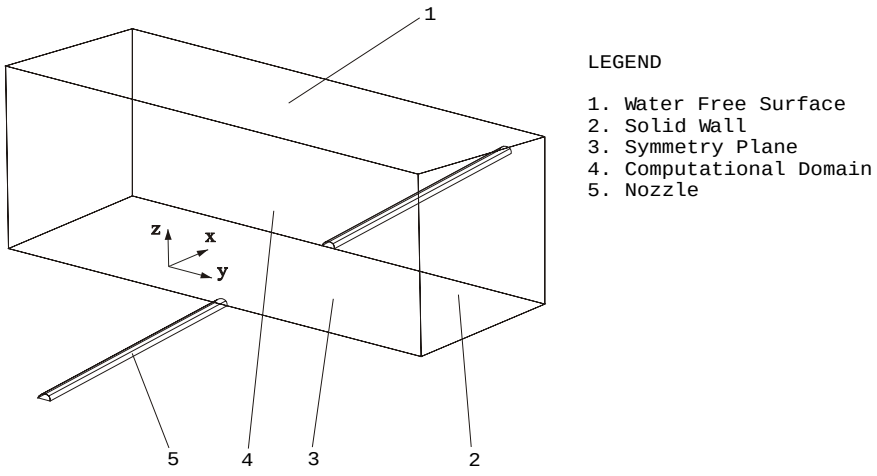

Figure 3.2: The computational domain, 3D view

Grid Generation

Grid generation involves filling the spatial domain with nonoverlapping cells. Structured or unstructured meshes can be selected when solving a flow problem. In the present work a structured mesh is chosen. The choice is based on convenience, since correspondence between measurement locations and placement of numerical grid vertices (nodes) more easily allows for a direct comparison between experimental and simulated data. Usually, the number of mesh vertices depends on the purpose of study, grid aspect ratio, required accuracy and computational power and time available (i.e. cost).

Due to the amount of time and uncertainty involved, it is always recommended [48], [23] to first perform a numerical study on a coarse grid. When the simulation is converged and optimized on that grid subsequent grid refinements are made more efficient. This approach was followed in the present work. Quadrilateral meshes were generated using CFX-Build. It writes data files containing useful data structures that can be imported into TASCFlow, but its speed degrades significantly when the mesh has more than 5000 to 10000 vertices. About 32000 cells have been used in the coarse grid study and 123008 cells were employed in the grid refinement simulation.

Provided that the computational domain was initially divided into two blocks of identical configuration (to be sure that there will be mesh nodes on the impingement line of the two jets) with regard to the number of associated curves and structure of advanced geometrical constraints [4], Figure 3.3 and Table 3.2 give the grid generation details for one half of the solution domain previously discussed.

The fine mesh associated with the horizontal symmetry (xy) plane is shown in Figure 3.4. Since most experimental data was acquired within the area corresponding to the symmetry plane of the computational domain (Figure 3.5) and in order to match the computational power available, the grid refinement procedure was focused on that particular region.

Out of the area pictured in Figure 3.4 it is the region surrounding the centerlines of the axial and radial jets that is given most importance. Therefore the densest grid covers this area.

Assuming that the computational domain is large enough such that the flow created by the two impinging jets is isolated with respect to the solid boundaries, in other words no major

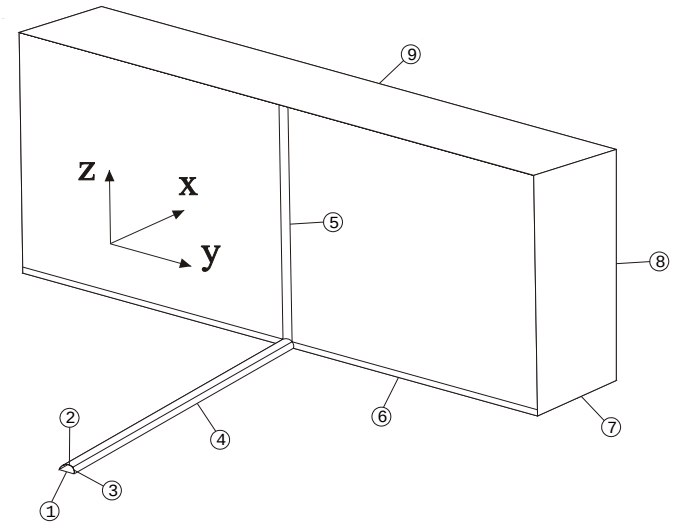

Figure 3.3: Mesh seeding for simulating impinging jets flow (1 to 9 are the independent edges to be seeded with mesh nodes)

velocity gradients are anticipated near walls, a discussion of the placement of grid points in the vicinity of the tank walls is not important for this study. In this respect, even though the assumptions made in the derivation of the first two $k-\varepsilon$ models recommend placement of the near wall grid points in the log-law region, any of the three $k-\varepsilon$ models and wall functions associated is expected to exhibit successful performance near the solid boundary.

Table 3.2: The number of elements, bias, and mesh spacing ratios for the seeding of the 9 independent edges for the fine and coarse opposed impinging jets meshes

Mesh / Edge	1	2	3	4	5
Coarse	4 2-way $L_2/L_1 = 0.9$	4 2-way $L_2/L_1 = 0.9$	2 uniform	16 1-way $L_2/L_1 = 8$	20 1-way $L_2/L_1 = 8$
Fine	6 2-way $L_2/L_1 = 0.9$	6 2-way $L_2/L_1 = 0.9$	2 uniform	16 1-way $L_2/L_1 = 14$	20 1-way $L_2/L_1 = 20$

6	7	8	9
20 1-way $L_2/L_1 = 8$	16 uniform	22 1-way $L_2/L_1 = 12$	44 2-way $L_2/L_1 = 0.25$
40 1-way $L_2/L_1 = 8$	32 uniform	22 1-way $L_2/L_1 = 30$	86 2-way $L_2/L_1 = 0.1$

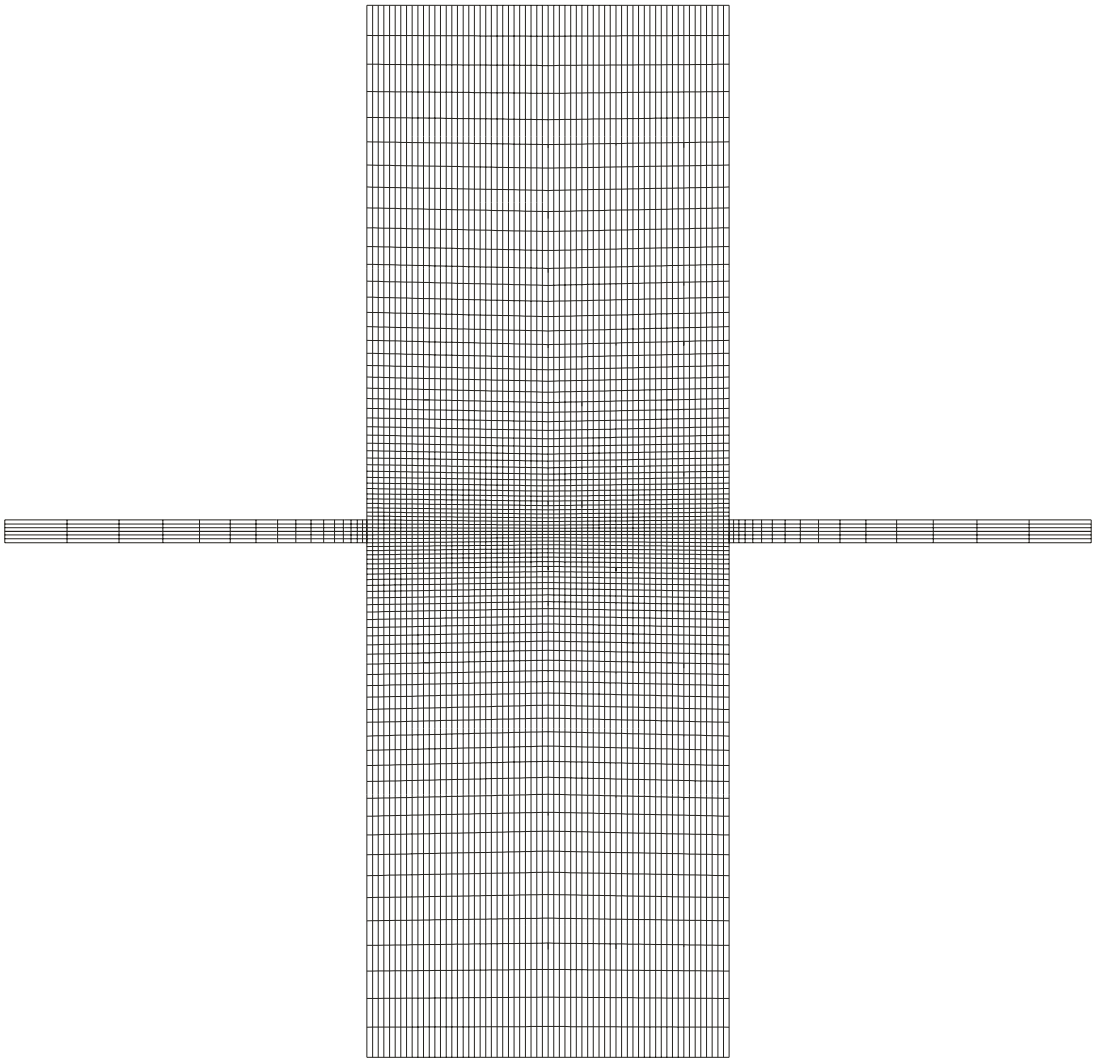

Figure 3.4: The computational mesh - horizontal symmetry (XY) plane

3.3.2 Fluid Properties and Boundary Conditions

Water at standard atmospheric pressure is the working fluid used in these numerical simulations. Its physical properties [4] such as density $\rho = 998.2\ \left[kg/m^3\right]$, dynamic viscosity $\mu = 9.929 \cdot 10^{-4}$ $[Ns/m^2]$, thermal conductivity $k = 0.597\ [W/mK]$, specific heat at constant pressure $c_p = 4182$ $[J/kgK]$, and specific heat at constant volume $c_v = 4182\ [J/kgK]$ match approximately the experimental fluid conditions (water at 15 $°C$).

The boundary conditions used to model the interaction of the surroundings with the solution domain are depicted in Figure 3.5.

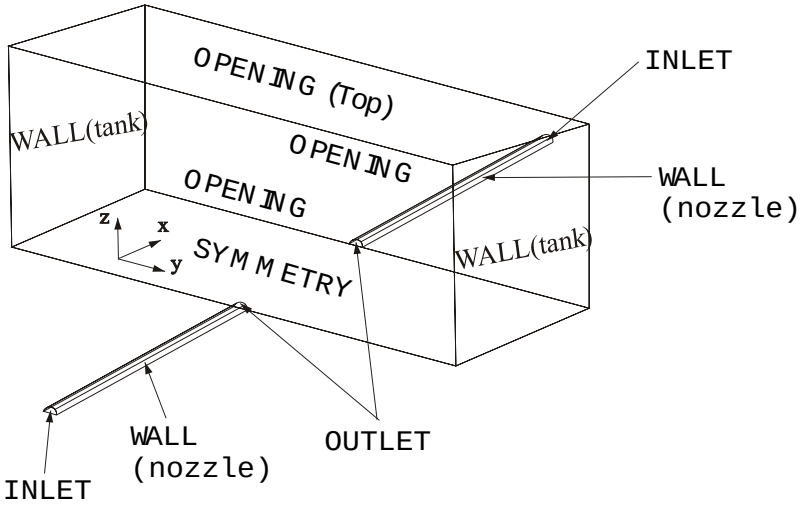

Figure 3.5: Boundary Conditions Placement (3D view)

The inlet boundary conditions were uniform axial velocity and turbulent intensity across the axisymmetric inlets applied normal to the inlet faces and a turbulent length scale of the turbulent eddying motion. Dictated by the geometrical similarity between the computational and experimental models, the axial inlet velocities were the mean velocity values (U_0) used in the experimental investigation; they were given in Table 2.2. A turbulent intensity of $I = 0.08$ $\left[m^2/s^2\right]$, and a turbulent length scale of $L = 0.03\ [m]$ were estimated from the experimental data available using the relationships previously discussed in section 2.5 of Chapter 2 and previous work experience. There is no precise way to determine the optimum magnitudes of I and L to be used in these simulations. However, limitations do exist; they result in very low values for turbulent Reynolds number and turbulent viscosity with catastrophic consequences on the application of $k - \varepsilon$ model within some regions of the flow usually followed by an increase in computational effort (time) and then divergence of the solution. The only guidelines in choosing these values are previous experience and the need to add sufficient turbulence for the simulation to start [48].

The outlet boundary condition was set as a uniform static (gauge) pressure of 0.0 $\left[N/m^2\right]$ magnitude aimed to simulate the constant distribution of static pressure of a fully developed free jet flow (see section 1.3 in Chapter 1). Also, taking into consideration a limited number of options regarding the combination between inlet and outlet boundary conditions, specifying

the static pressure at the outlet is in agreement with the requirements for the inlet boundary condition. Since in incompressible flow it is the pressure difference that is important, a different pressure set up at the outlet would have no influence over the flow field. Therefore the pressure field can be changed by a constant value without changing the results.

Based on the assumptions mentioned in section 3.3.1 of this chapter, a symmetry boundary condition was applied to the computational domain cross section symmetry plane (Figure 3.5) containing the axial cross sections of the two nozzles and the cross section of the parallelepiped between the nozzle outlets. Usually, a symmetry boundary condition implies no flow or scalar flux across the boundary. In its implementation, normal velocities are set to zero at the symmetry boundary and the values of all other properties at the boundary outside the solution domain are equated to their values at the nearest mesh node at the boundary inside the computational domain.

The no-slip condition ($u = v = 0$ $[m/s]$) was the boundary condition applied at the tank and nozzle side walls. Since the flow near the wall is of little interest in the present study, the wall boundary condition appears as a weak boundary condition in this simulation. Moreover, the solid boundaries employed in this computation are assumed to be smooth walls. The implementation of wall boundary conditions in turbulent flows starts with the evaluation of n^+ (see section 3.2.1) and then the wall functions corresponding to smooth walls are employed.

Finally, the side and the top planes of the parallelepiped domain were modelled as opening boundary conditions, which allow for fluid entrainment from the surrounding ambient fluid.

The initial quess information required to start the simulation such as axial mean velocity, turbulent intensity I, and turbulent length scale L took the same values as those used for the inlet boundary conditions.

3.4 Convergence Analysis

The complex and unsteady character of the present problem made it difficult to obtain a converged solution. In the convergence procedure, then, several steps were required: manipulation of the boundary conditions, variation of the magnitude of the turbulence intensity and length scale of the turbulence eddy, variation of the time step, and following a step to step convergence approach (i.e. running the code a few time steps, analyzing the evolution of the residuals, changing some of the above parameters and running it again). Therefore a representation of the degree of convergence would be inappropriate.

The time step was basically calculated as a quarter of the average residence time of a fluid parcel inside the solution domain, i.e. $\Delta t = 0.25\frac{x}{\overline{u}}$ where x is the dimension of solution domain associated with the dominant mean velocity $\overline{u}$. In general the time steps used in these simulations fall in the interval $\Delta t \in [0.1, 1.25]$ $[s]$ for Re $\in [1500, 11000]$ and $L^* = 20$.

In all studied cases, the iterative linear solver (using Multigrid acceleration) attempts to reduce the rms residuals of all the momentum and mass equations as well as residuals of the turbulent kinetic energy and dissipation of turbulent kinetic energy equations down to a point where the maximum residual of 10^{-4} has been reached. In the CFD community this magnitude is considered a "tight" convergence criterion [4]. Given the above convergence path, a total number of 105 to 146 combined iterations (time steps) was needed by the solver to reach the minimum value of the maximum residual allowed. The number of iterations was observed to be a function of several variables involved such as $k - \varepsilon$ model used, Re number, time step value, etc. As far as convergence is concerned the RNG $k - \varepsilon$ model performed the best.

3.5 Accuracy of Numerical Simulation

In general the simulated fields of velocity, pressure and other parameters of interest may differ from the actual fields in any given situation because of several types of errors:

- Physical model errors which include geometry model errors, mesh generation errors, boundary condition modelling, and turbulence model errors.
- Numerical errors which contain two categories: discretization errors such as profile approximations and solver errors such as round off errors and incomplete convergence.

Out of these, the more important issues of grid refinement, discretization errors and turbulence model performance will be individually discussed. The next comparative discussions are built around the LDA experimental results.

3.5.1 Estimation of the Discretization Errors and Choice of Discretization Schemes

The key step of the finite volume method is the integration of the governing equations over each control volume to yield a discretized system of algebraic equations. There are two methods of controlling discretization errors [48]: refining the mesh which will be addressed in section 3.5.2 and improving the profile approximations (interpolation between nodal values).

There are four discretization schemes available in TASCFlow [48], [4]: Upwind Differencing Scheme (UDS), Mass Weighted Scheme (MWS), Modified Linear Profile Scheme (MLPS) and Linear Profile Skew (LPS). Each of these can be coupled with the Pressure Advection Correction (PAC) scheme. UDS is a first order approximation scheme which approximates the value of an integration point as if the flow was one dimensional across each face (linear). MWS provides positive coefficients to the algebraic equations and gives a first order approximation of the advective fluxes. It is more accurate than UDS. MLPS reduces negative coefficients in the discrete equations ensuring that no downstream influence arises due to the linear interpolation. It is considerably more accurate than UDS. LPS approximates the variable on the element face with a two dimensional linear profile between the two face nodes. It addresses the false diffusion that appears when UDS is used. When the grid is sufficiently fine LPS is second order accurate for the advective fluxes. Pressure Advection Correction (PAC) is responsible for the correction of the apparent source of a flux that appears when non-advection processes act on an advected fluid parcel.

Since UDS and LPS are the two schemes situated at opposite ends of the accuracy hierarchy of the discretization schemes [48], their particular performance in solving the flow generated by two turbulent opposed impinging jets is compared. LDA experimental results constitute the basis of this comparison. The analysis is conducted by studying the influence of the chosen discretization schemes on the distributions of dominant mean velocity and turbulent kinetic energy along the centerline of the two jets (Figures 3.6 a, b) and at 63.5 mm (i.e. $L/2$) downstream of the left side nozzle (Figures 3.7 a, b). The better performance and convergence of the RNG version of the $k-\varepsilon$ model prompted its use in this evaluation. The analysis is performed on the finer mesh spacing and for the case $\mathrm{Re} = 11000$ and $L^* = 20$.

The predicted axial distributions of mean velocity and turbulent kinetic energy are shown in Figures 3.6 and 3.7. Similar performance is found for the two discretization schemes. This confirms that both the advection and diffusion phenomena are strongly represented in the second half of the flow domain [i.e. $L^* \in (10, 15)$] containing the impingement region. The slightly better performance observed for the UDS scheme is conferred by the strong oscillatory behavior

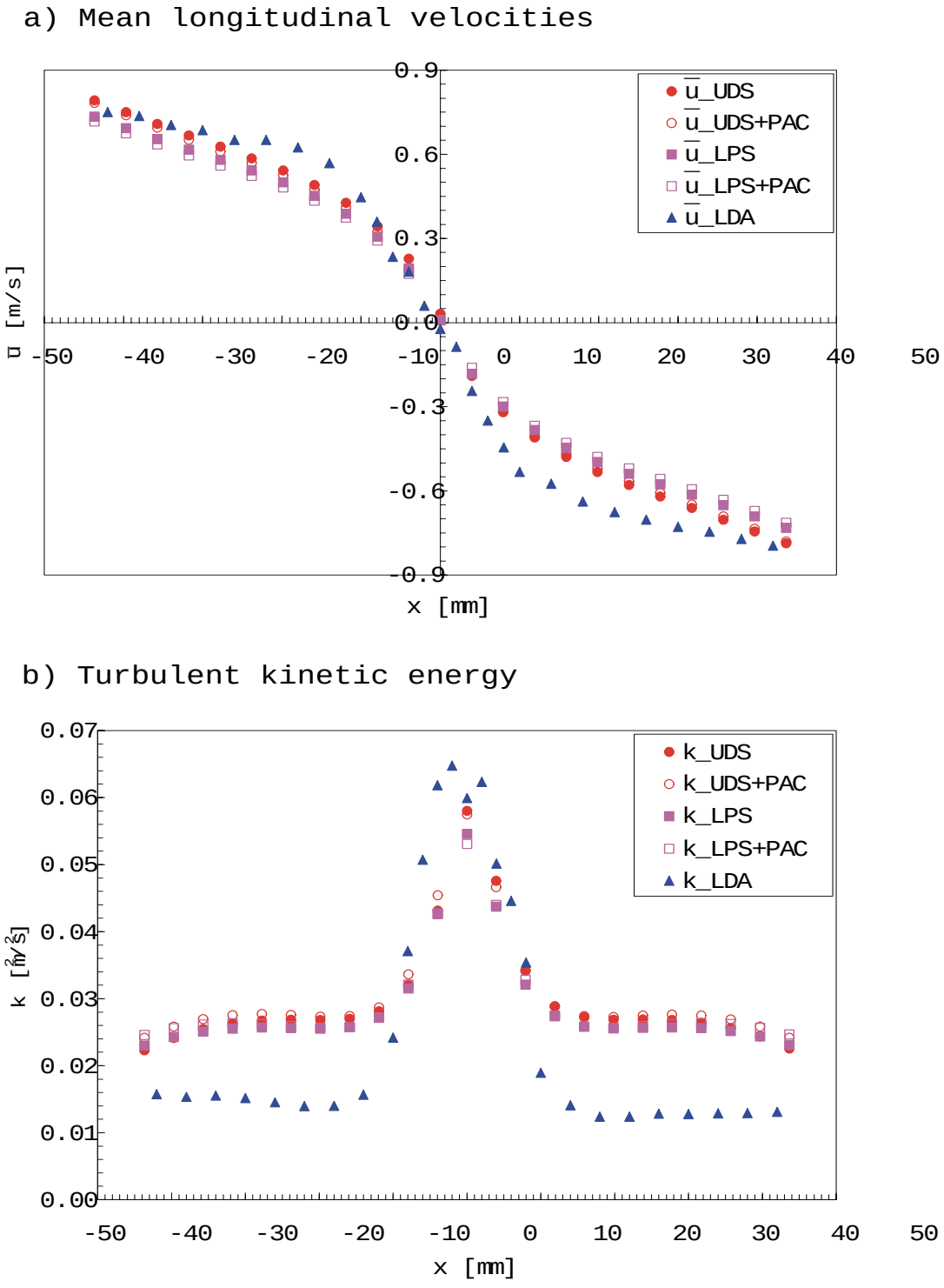

Figure 3.6: Mean longitudinal velocity and turbulent kinetic energy distributions on the jets axis - Comparison between four discretization schemes (RNG $k-\varepsilon$ model, Re = 11000, $L^* = 20$)

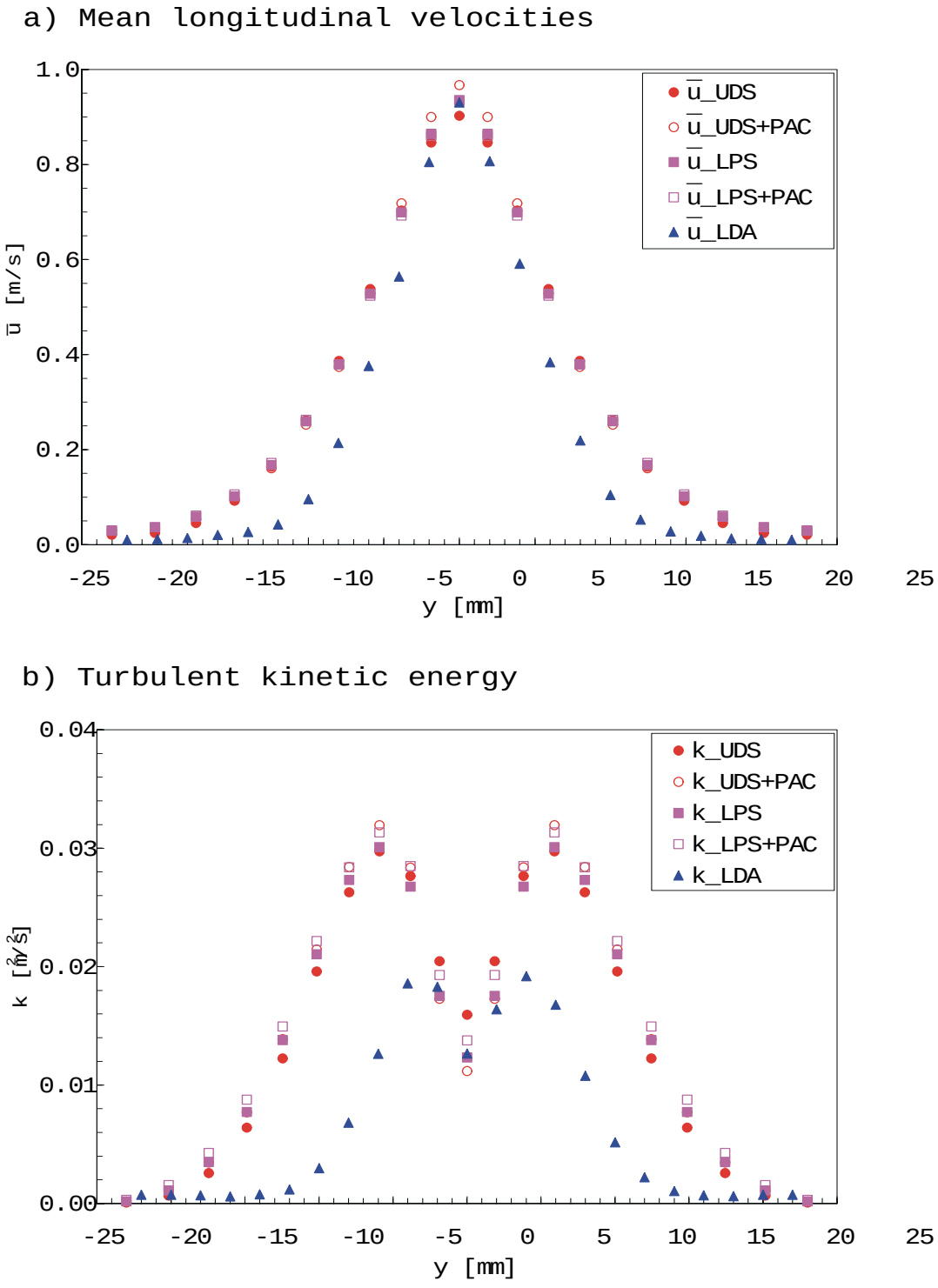

Figure 3.7: Mean longitudinal velocity and turbulent kinetic energy profiles - Comparison between four discretization schemes (RNG $k-\varepsilon$ model, Re = 11000, $L^* = 20$, at station $x = 63.5\ mm$ downstream of the nozzle)

of the flow in the impingement region. As is known [23], the LPS, which is basically a central difference scheme (CDS), does not handle oscillatory flows very well. Since in the first half of the opposed impinging jets flow [i.e. $L^* \in (0, 5)$ or $L^* \in (15, 20)$] the advection is stronger than the diffusive effects slightly better behavior of the LPS scheme (usually recommended for advection dominated flow [48]) is observed in this region. No significant influence of the PAC option is observed. It is also recommended for advection dominated flows.

In conclusion, primarily due to its robustness and better prediction of turbulent kinetic energy in the present flow simulations, the UDS discretization scheme will be preferred in further calculations.

At the end of discretization stage, discrete algebraic equations are formed for each control volume. Then all equations are solved to give estimates of the flow field variables: velocity, pressure, etc. at each node. Usually for more complex situations non-linear effects must also be approximated in a way that the equation are transformed into a linear system of equations that can be solved with some form of matrix equation solver. Based on storage requirements and the number of arithmetic operations that must be carried out to achieve a solution, the algorithms for solving linear matrix equations are [48]: direct solvers such as the simple Gaussian Elimination, semi-direct such as the Conjugate Gradient algorithm and iterative solvers such as Gauss-Seidel Iterative algorithm (GS). It is well known that iterative solvers are preferred to direct algorithms (e.g. they overcome the high cost of inverting large matrixes and they are best suited for non-linear type problems) [48]. Also, the multigrid (MG) acceleration technique is useful for its capability in correcting the stall condition of an iterative solver when low frequency errors are reduced and coefficients of the discrete equation are not isotropic [48]. Furthermore, experience [23] has shown that the MG acceleration with a successive over relaxation (SOR) solver as smoother is overall superior to simple iterative solvers such as GS or SOR (SOR is an accelerated version of GS solver) methods, as far as the convergence rate is concerned. For these reasons the MG solver with SOR as smoother [23] have been chosen in TASCFlow to solve the system of linear equations.

3.5.2 Grid Refinement Test

In the finite volume method, the solution to a flow problem (velocity, pressure, etc.) is defined at vertices inside each control volume (cell). The number of cells in the mesh are critical to the accuracy of a CFD solution. In general, the larger the number of cells (i.e. the better the spatial resolution) the better the solution accuracy. Analysis of the computational errors in a global flow quantity by means of Taylor series would yield [48]:

$$Error \approx C_x \Delta x^{\mathsf{a}\,x} + C_y \Delta y^{\mathsf{a}\,y} + C_z \Delta z^{\mathsf{a}\,z} + C_t \Delta t^{\mathsf{a}\,t} \tag{3.28}$$

where a is the order of error of the discretization scheme and gives information about how the error will be reduced as the grid is refined. Ideally as the grid spacing (Δx, Δy, Δz) is halved, the error will be reduced by a factor of four for a second order scheme or by a factor of two for a first order scheme. This indicator is only valuable when the grid spacing is fine enough for the Taylor series to be applicable [48].

Thus, the optimum grid resolution based on a trade-off between available computer power and regions in the flow that require special attention, is usually established by experimentation. As a guide, when doing a mesh refinement study a systematic increase of resolution should be performed until the changes in the predicted solution become sufficiently small. A uniform grid spacing should be chosen, mesh should be orthogonal and aligned with the flow and the number of nodes should normally be increased in regions of strong gradients.

It is well known that a complete grid refinement procedure involves simultaneously refining the mesh in all directions. However, the already large amount of computational vertices and limited computer power available, have imposed a two dimensional grid refinement in this study. Therefore the fine grid was obtained by halving the previous grid spacing in the x and y directions only (i.e. only the grid corresponding to the horizontal symmetry plane was refined).

Typical results obtained from numerical simulations conducted on the two previously defined grids (see Table 3.2) and using three different versions of $k-\varepsilon$ turbulence model (as in section 3.2) are depicted in Figures 3.8 a), b) and 3.9 a), b) where mean velocity and turbulent kinetic energy distributions along the centerline of the jets and profiles at $x = 63.5\ mm$ downstream of the left side nozzle are represented. Therefore an assessment of the performance of three versions of the $k-\varepsilon$ turbulence model [standard $k-\varepsilon$ model (STD), Kato-Lauder $k-\varepsilon$ model (KL) and RNG $k-\varepsilon$ model] on two different grids is also attained.

As Figures 3.8 and 3.9 show, there is no significant difference in mean velocity between the coarse (32000 cells) and the finer (123008 cells) grids across all the distributions and profiles. It is also implied that the RNG $k-\varepsilon$ model performs better on the same coarse grid than the other two model versions. The results indicate that a mesh independent result has not yet been reached with the finer mesh, but the solutions feature the correct trend toward the experimental solutions. Overall, in the cases studied, the average percent difference in mean velocity between the coarse and finer meshes is about 4 %.

The turbulence kinetic energy distributions and profiles in Figures 3.8 and 3.9 corresponding to the above mentioned velocity representations, exhibit large discrepancies between the coarse and finer grids when same turbulence model is used. Large differences are also observed when the performances of the three turbulence models on the same mesh are compared. Roughly the percent difference in turbulent kinetic energy magnitude averages between 7 and 20 %. These values do suggest that a new grid refinement procedure is required (however, any further grid refinement could not have been achieved due to limited computational power available).

Usually, given their important role in determining the flow field characteristics and the almost empirical turbulence models involved in the estimation of turbulence quantities, mean velocity results are regarded as the most reliable parameters one could calculate. Based on this affirmation along with the previous observations, we can consider that comparisons between experimental results and numerical data computed on the above defined finer grid, are acceptable. Therefore the final mesh used in computations is the grid (87×65 vertices in the symmetry plane) shown in Figure 3.4.

3.5.3 $k-\varepsilon$ Model Assessment of Performance

To date the $k-\varepsilon$ model is the most widely used and validated turbulence model. It is more sophisticated and general than the mixing length model but also more expensive computationally. The model popularity is explained by its recognized performance in confined flows with a wide range of industrial applications where the Reynolds stresses are most important. In spite of this success the $k-\varepsilon$ model shows only moderate agreement with experimental data in unconfined flows [11].

Experience with the model [11], [46], [48] shows poor performance in the prediction of weak shear flows such as mixing layers and far wakes, and severe overpredictions of the spreading rate of axisymmetric jets in stagnant surroundings. In large parts of these flows the rate of production of turbulent kinetic energy is much less than the rate of dissipation of k and vice-versa. This is in contradiction with the balance between dissipation rate ε and production of k that forms a key assumption in the $k-\varepsilon$ model.

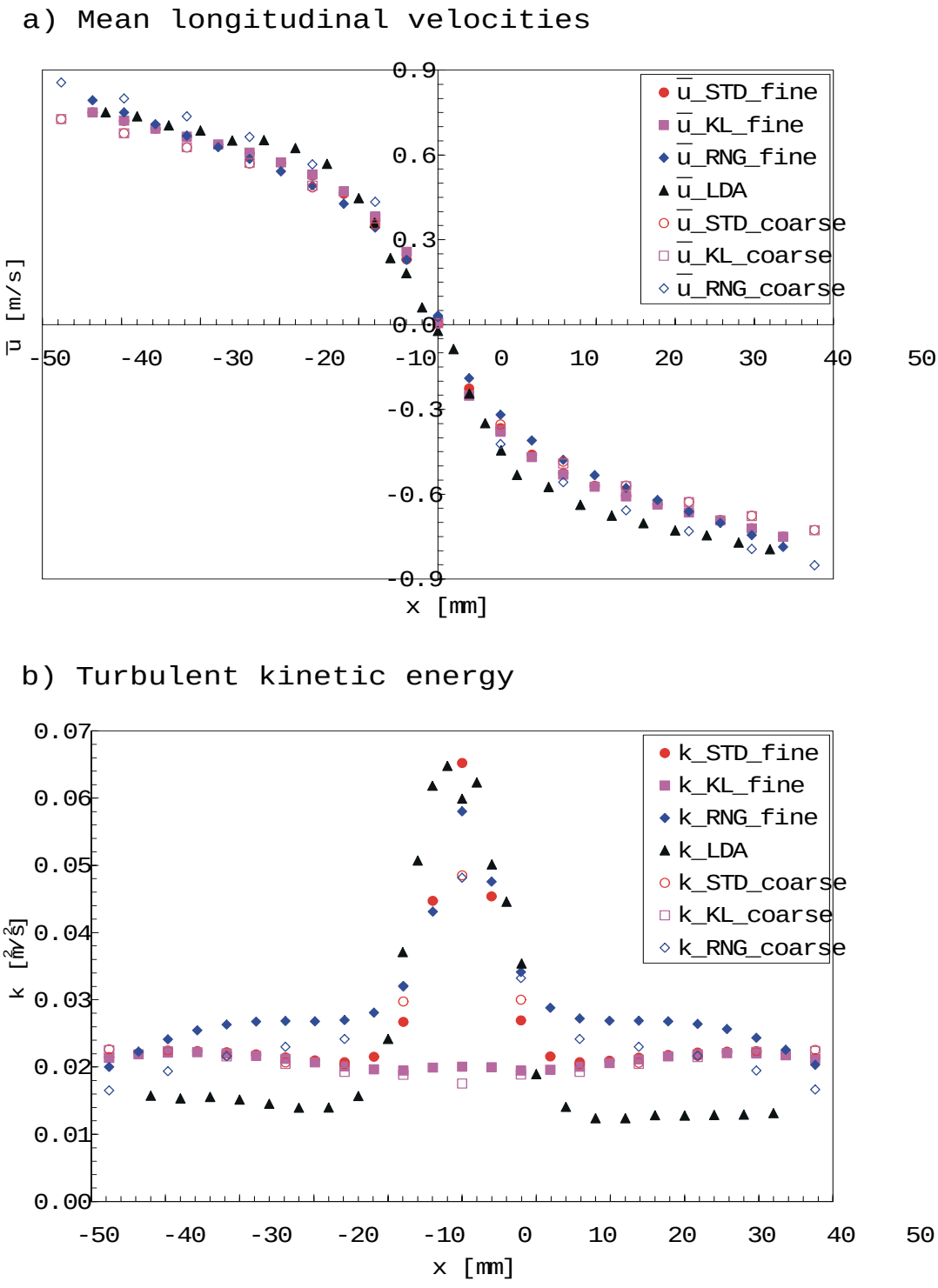

Figure 3.8: Mean longitudinal velocity and turbulent kinetic energy distributions on the jets axis - Dual test: grid refinement and turbulence models assessment on two computational meshes (Re = 11000, $L^* = 20$)

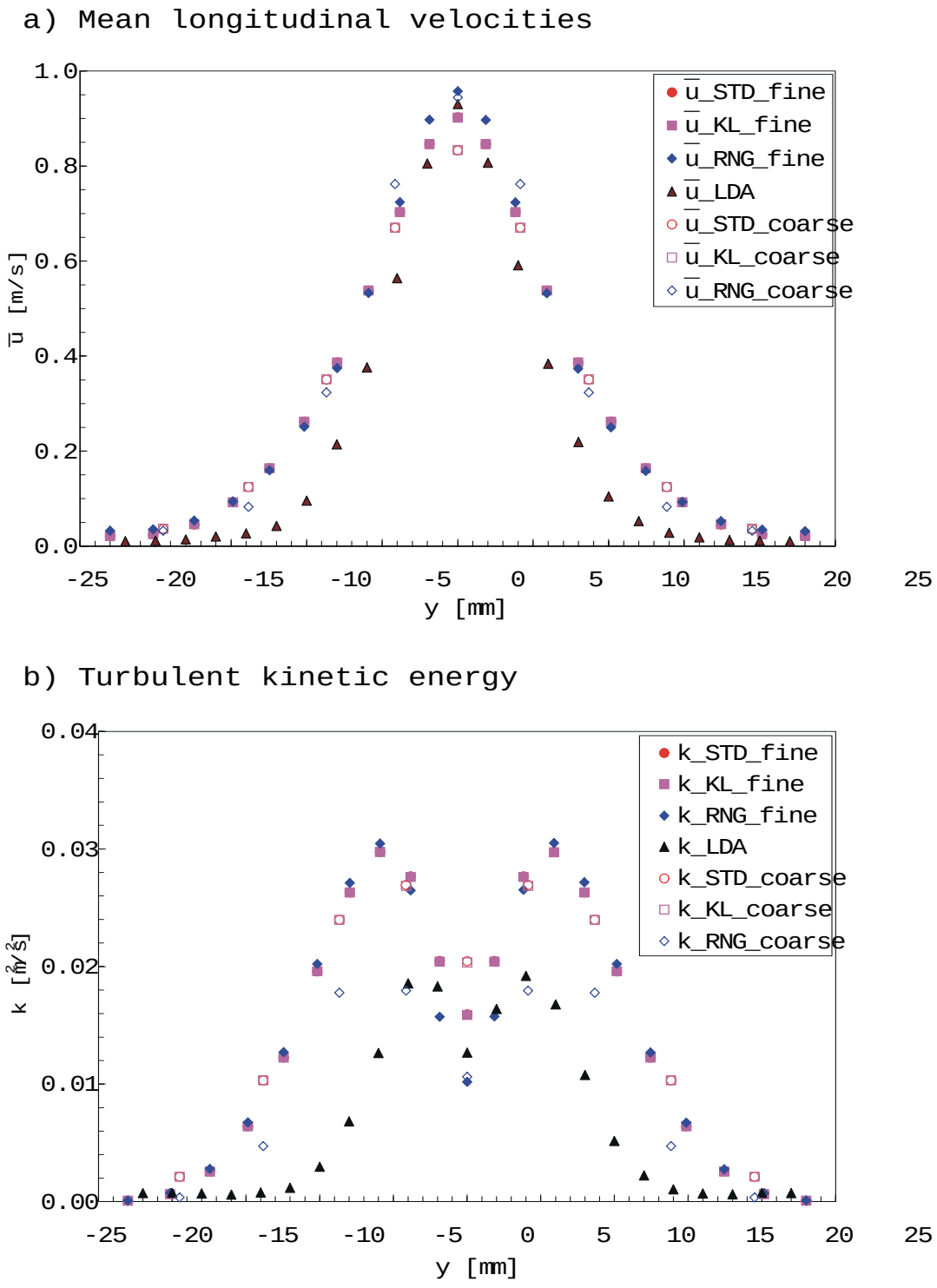

Figure 3.9: Mean longitudinal veloctity and turbulent kinetic energy distributions on the jets axis - Dual test: grid refinement and turbulence models assessment on two computational meshes (Re = 11000, $L^* = 20$, at station $x = 63.5\ mm$ downstream of the nozzle)

As we previously observed (see Chapter 2) it would be appropriate to include the turbulent opposed impinging jets flow in the above category of flows. Therefore a poor performance of the classical $k-\varepsilon$ models in this case will not surprise. In an assessment of the application of several turbulence models to the study of an axisymmetric jet impinging on a flat plate, Craft et al. [11] reported that $k-\varepsilon$ model highly overpredicts the level of turbulent intensity (" turbulence energies") in the vicinity of the stagnation point. They considered the main cause for this behavior the use of a gradient diffusion hypothesis (or the eddy-viscosity stress-strain relationship) to represent normal stresses (equation 3.5). By similarity, assuming that on average the position of the stagnation point is stationary and situated at $L/2$ downstream of the nozzle outlet, one could have the "natural" tendency to extend this conclusion to the opposed impinging jets flow.

Thus, contrary to what one would expect, in previous work [44] it was shown that the stagnation point generated by the dynamic impingement of two turbulent opposed jets exhibits the maximum turbulence intensity level within the entire flow field. As a consequence, the impingement of the two jets would generate a maximum level of turbulent kinetic energy at the stagnation point (Figure 3.8 b). Furthermore, although physically impossible, due to its intrinsic development (i.e. the gradient diffusion hypothesis) the $k-\varepsilon$ model produces negative Reynolds normal stresses ($\overline{u_i' u_i'}$) in regions where the turbulent kinetic energy level is high. While this feature is mentioned in Chapter 4 with regard to the opposed jets impingement flow, for some unknown reason Craft et al. [11] do not report this $k-\varepsilon$ model flaw for the jet impinging on a flat plate flow. The experimental turbulent kinetic energy in these graphs has been calculated using the axisymmetric k formula 2.20, defined in section 2.5 of Chapter 2.

Surprisingly, all three $k-\varepsilon$ model versions predict the axial mean velocity distribution and profiles quite well (Figures 3.8 a, 3.9 a, and 3.10 a) but just two of them (standard and RNG) provide good predictions of the level of k in the vicinity of the stagnation point (Figure 3.8 b). It is probably its particular application for low Reynolds number flows (flow near walls) that led to the catastrophic performance of Kato-Launder $k-\varepsilon$ model with regard to the k prediction. For this reason the Kato-Launder $k-\varepsilon$ model is eliminated from consideration.

As for the other two $k-\varepsilon$ models, the standard version provides a better prediction (in comparison with the experimental results) of k level in the region adjacent to the stagnation point and at the stagnation point, but it fails as the distance from the stagnation point toward upstream is increased over one nozzle diameter (Figure 3.9 b). The RNG version gives a better prediction of k upstream of the impingement point for a portion of half the nozzle diameter either side of the jets centerline, but results in overpredictions at points further from the centerline (Figure 3.8 b). However, both models fail to predict the high level of k corresponding to the shear stress instability zone near the nozzle exits (Figure 3.10 b).

For the standard $k-\varepsilon$ model to overcome the above deficiencies one could simply make ad hoc adjustments to the model constants C_μ, $C_{\varepsilon 1}$, $C_{\varepsilon 2}$. Since it includes a modification of the production of dissipation term to account for non-equilibrium strain rates, the RNG $k-\varepsilon$ model was expected to provide a better performance for the present simulation. Given the above discussion, it probably requires further development or empirical manipulation. As both these models perform poorly within the curved part of the impinging flow field, in order to improve their functionality, specific relationships that will account for the effects of streamline curvature on turbulence have to be incorporated.

Even though it is difficult to decide which of the two $k-\varepsilon$ models is more appropriate to continue the calculations of the present flow field, preference is given to the standard $k-\varepsilon$ model due to its better performance within the impingement region which constitutes the most important zone of interest in this work.

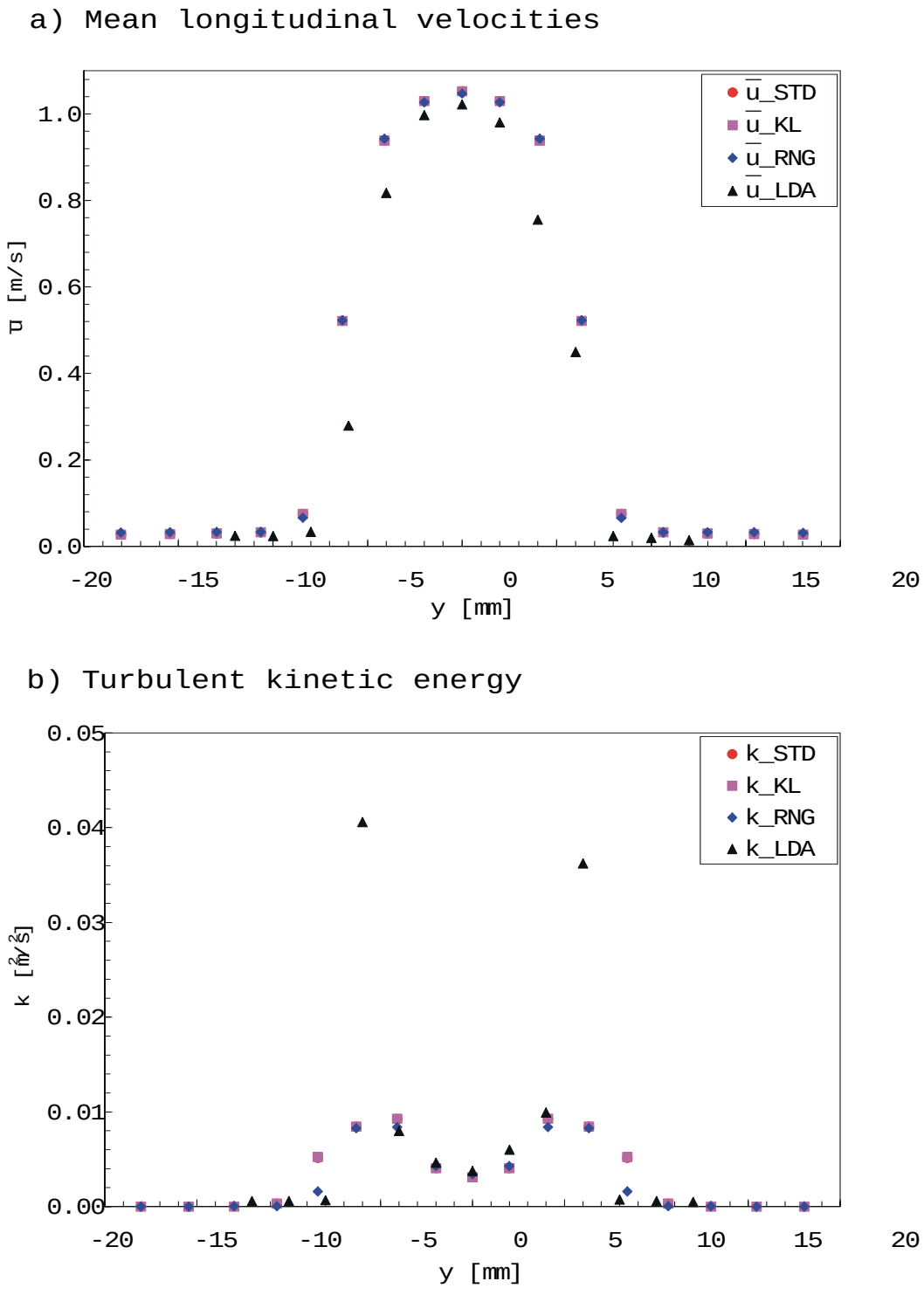

Figure 3.10: Mean longitudinal velocity and turbulent kinetic energy profiles - Turbulence models assessment (Re = 11000, $L^* = 20$, at $x = 4\ mm$ downstream of the nozzle)

Chapter 4

Experimental and Numerical Results - Comments

A great deal of work has been aimed toward exploiting the huge amount of data provided by the strategies and equipment employed in the experimental and numerical study of the flow field generated by two turbulent opposed impinging jets. This chapter is entirely devoted to discussion of the principal results as they were revealed by the experimental data and numerical simulations.

The chapter will begin with a presentation of the visual observations that were extracted from the available flow visualization images. Next, the mean velocity and turbulent intensity (rms) data from LDA and PIV measurements will be detailed. Results obtained from a numerical simulation of the flow corresponding to $\mathrm{Re} \in [1500, 11000]$ and $L^* = 20$ configuration are presented with direct comparisons between experimental and numerical data whenever appropriate. Although CFD is able to provide 3D data values, directional limitations imposed by the measurement equipment have led to confining the discussion of the overall flow field to the 2D horizontal symmetry plane containing the centerline of the two jets. Consequently, the specific sections and points (within the horizontal symmetry plane) where the evolution of the flow is characterized in detail are illustrated in Figure 4.1. The normal distance from the respective section to the nozzle exit plane in the case of axial jets, and to the stagnation point $O(0, 0)$ for the radial jet, is represented by an integer number of nozzle diameters.

Additional turbulence information such as the turbulent time and length scales, the probability density function and the time and spatial correlations are also discussed. Since $L^* = 20$ is the only flow configuration that benefits from an entire array of LDA measurements for $\mathrm{Re} = 11000$ and a limited number of LDA measurements for the other three flow rates $\mathrm{Re} = \{1500, 4500, 7500\}$, the turbulent characteristics of the flow field pertaining to these cases will be mainly discussed. Separate sections will deal with important issues such as self-similarity analysis of turbulent opposed jets and radial jets as well.

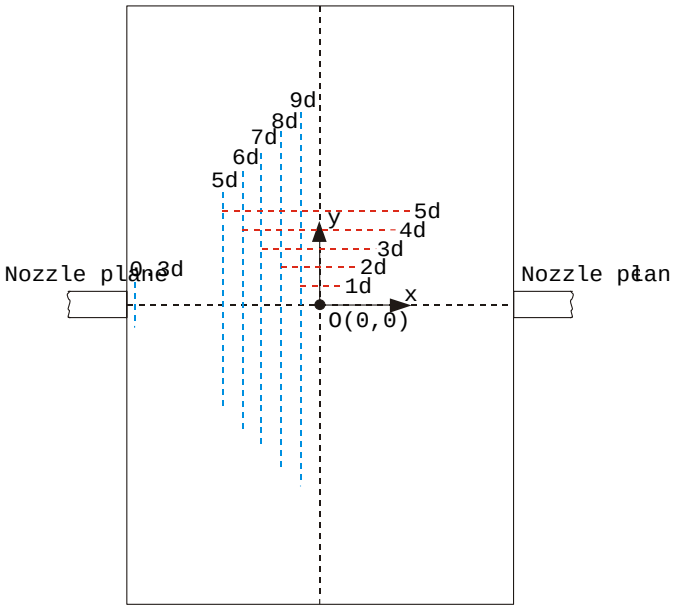

Figure 4.1: Geometry of xy horizontal symmetry plane ($z = 0$). Flow mean and turbulent parameters plotted along the dashed lines (d = nozzle diameter).

4.1 Visual Observations

Two dimensional images acquired through techniques described in Chapter 2 were processed using several chromatic filters available in Corel Photo-Paint so that a good contrast between the impinging flow field and the surrounding medium could be achieved.

Unlike the LDA and PIV experimental setup where tap water used as the working fluid was recirculated, the two jets in the flow visualization experiments were always connected to the water source and just one of them was dyed. Even though the tank was continuously drained in order to maintain a constant fluid level, the background fluid became slightly luminescent. Since one of the jets was transparent water and the other was strongly dyed, it was easier to distinguish between the two jets. In this way the visibility of the entire flow field of interest was obtained.

Figures 4.2, 4.3, 4.4, and 4.5 represent typical flow visualization images collected for each of the four different flow rates $\mathrm{Re} \in [11000, 7500, 4500, 1500]$ and corresponding to the three opposed impinging jet configurations $L^* = \{20, 10, 5\}$. Two additional limit cases with respect to both geometrical and kinematic flow conditions are also presented in Figures 4.6 a) and b).

In general, for all Re numbers and geometrical configurations examined (see Tables 2.1 and 2.2), the flow visualization study showed the formation of a composite flow field characterized by the following distinct regions (see Figure I.2): potential core, a developing jet region (i.e. free jet region), an impingement region and a free radial jet region. The structure (composition) of this complex flow field is observed to be independent of Re number and nozzle to nozzle spacing for the range of $\mathrm{Re} \in [4500, 11000]$ and $L^* \in [5, 20]$. These observations confirm the " free radial jet" approach we have followed in this research.

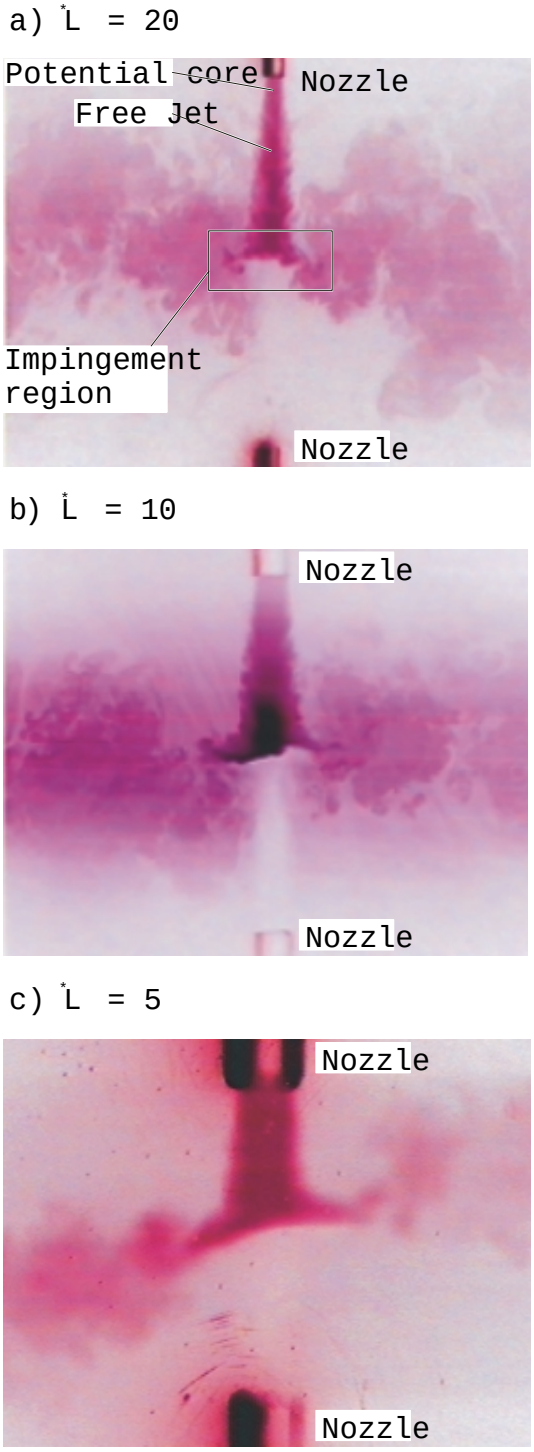

Figure 4.2: Turbulent opposed impinging jets - horizontal XY plane (LIF technique $L^* = L/d$, Re = 11000)

No recirculation phenomena were observed within the impingement region or in the flow field close to the jets for any Re number or L^* (see Figures 4.2, 4.3, 4.4, and 4.5). However, the flow field contained within the impingement zone and a relatively large area surrounding it, manifest a significant alteration. The instantaneous impingement flow field or the radial jet, and these were subsequently shown by instantaneous PIV measurements (Figure 4.7), is not axisymmetric, nor stable and is highly unsteady. With only one jet dyed with fluorescent dye, a strong interaction was observed between the jet fields, with the formation of small toroidal vortices at the end of the radial jet. The impingement surface created at the point of jets impact is better defined and smoother as Re and L^* decrease (Figures 4.2, 4.3, 4.4, and 4.5). For all configurations, the dyed jet is seen to exit the nozzle having a smooth cylindrical surface until small amplitude waves appear on the jet boundary layer due to the entrainment process. This phenomenon becomes more clearly visible when Re number and nozzle separation increase (Figures 4.4, 4.3, 4.2). However, a clear relationship between the entrainment process and the impingement region area cannot be estimated from flow visualization images alone.

At the point of impingement (the stagnation point) the flow turns in the radial direction and clear evidence exists of oscillation at the periphery of the radial jet, in a plane perpendicular to the nozzle centerline (Figures 4.2, 4.3, 4.4, and 4.5). Also, there is evidence of oscillation of the entire impingement region along the nozzle centerline and in the vicinity of the stagnation point. As far as flow visualization data is concerned, the frequency associated with the radial jet periphery (f_r) is a few orders of magnitude higher than that in the impingement region (f_i). They both depend on Re and L^* in the sense that the higher the Re number and the smaller L^*, the higher are the oscillation frequencies. Using sequences of several images digitally separated from the flow visualization recordings, an estimation of the frequencies of oscillation was attempted. When examined on a frame by frame basis (the video camera used in the experiments was able to record 30 $frames/s$) the images revealed non-repeatable and irregular oscillations in the low range of the frequency domain ($1 - 20\ Hz$). Even though these oscillations were observed belonging to a restrictive frequency range, a definitive measure of these frequencies could not be obtained.

Even though the flow field exhibits the general structure of the flow field developed due to opposed jets impingement, special characteristics are observed for Re = 1500 (Figures 4.5, a), b), c)). Up to the point of impingement, the jets have an almost laminar appearance in that their propagation is continuous and parallel to the jet axis, and the spread rate is almost non-existent (minimal). Moreover, the jet bodies appear to shrink as they move toward the impinging point. Although the impingement region is better defined, it is thinner which makes it resemble an impingement surface. No entrainment seems to affect the jet bodies or the impingement region. At Re = 1500 these observations are consistent for all nozzle to nozzle separations L^*, the only difference lies in flow field stability. The smaller the separation distance between nozzles, the more stable the associated flow field.

In order to define the general influence of the variable parameters (Re and L^*) on the opposed jets flow field development, a step by step flow visualization approach has been followed. Figures 4.6 a) and b) show two limit cases found at the opposite ends of the range of variable parameters. Thus, two identical jets issuing from opposed round nozzles of diameter d and separated by a distance $L = 5d$ cease to impinge on each other for Re < 150 (Figure 4.6 b)). Instead, as Figure 4.6 a) shows, the two jets conserve the impingement behavior when they are separated by $L = 20d$ and Re = 142000 (corresponding to maximum flow available). In this case, a few characteristics can be mentioned: the impingement region was observed to become thinner and more stable, the high Re number flow has caused the jets to spread out at a slower rate and consequently smoother jet boundaries are observed. An explanation of this fact could lie in the inability of the recording device to capture eddies at very small scales.

a) $\dot{L} = 20$

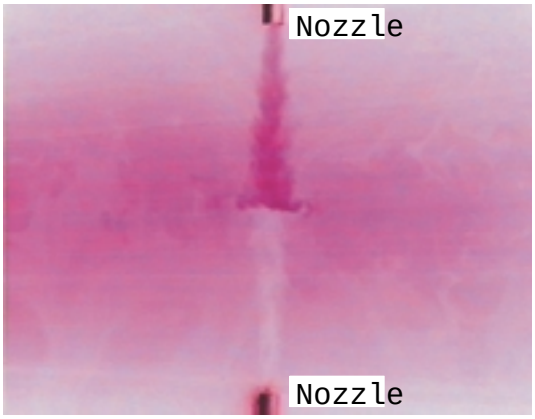

b) $\dot{L} = 10$

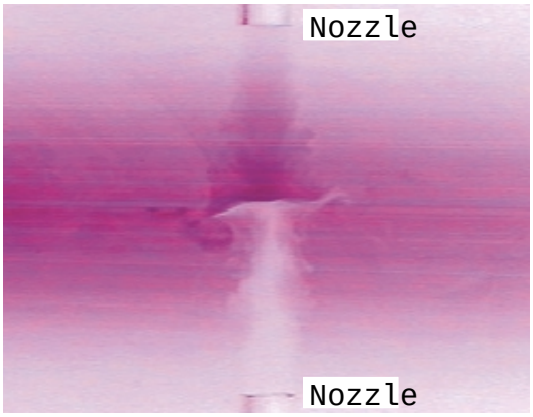

c) $\dot{L} = 5$

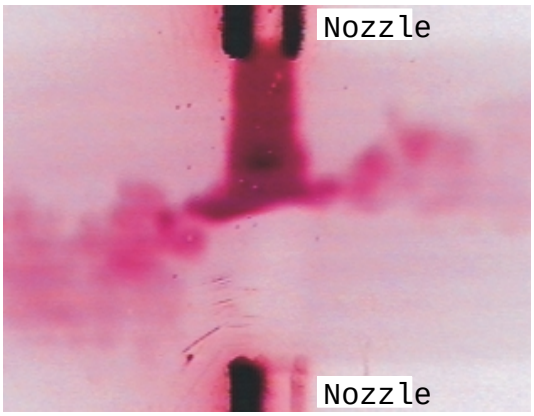

Figure 4.3: Turbulent opposed impinging jets - horizontal XY plane (LIF technique $L^* = L/d$, Re = 7500)

a) $\dot{L}^* = 20$

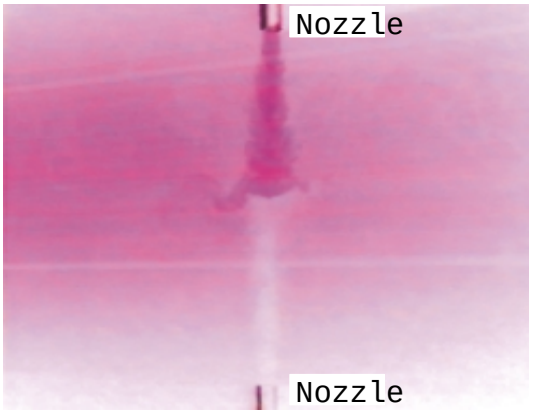

b) $\dot{L} = 10$

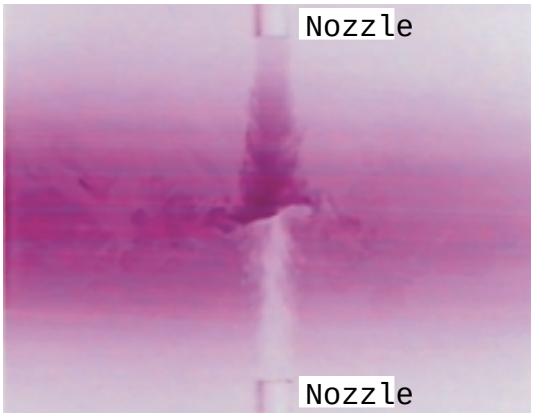

c) $\dot{L}^* = 5$

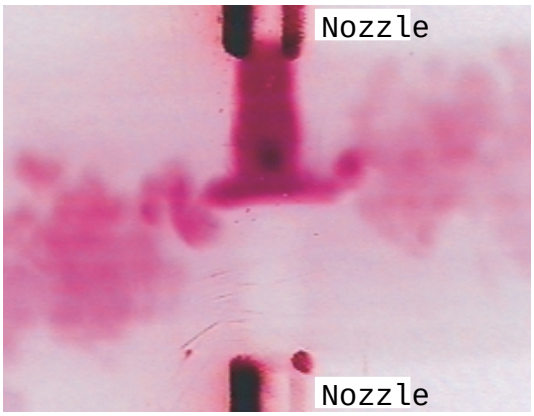

Figure 4.4: Turbulent opposed impinging jets - horizontal XY plane (LIF technique $L^* = L/d$, Re = 4500)

a) $\dot{L} = 20$

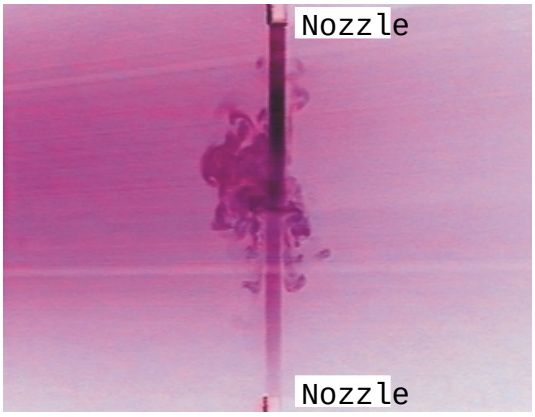

b) $\dot{L} = 10$

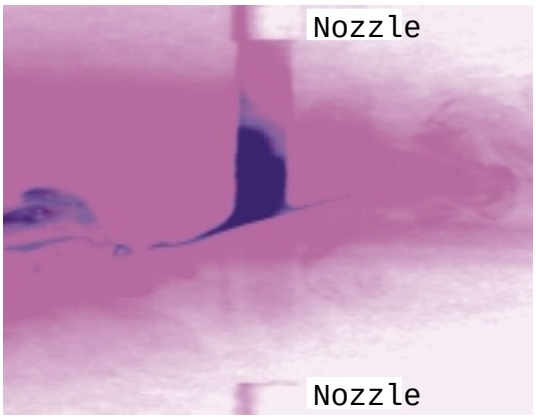

c) $\dot{L} = 5$

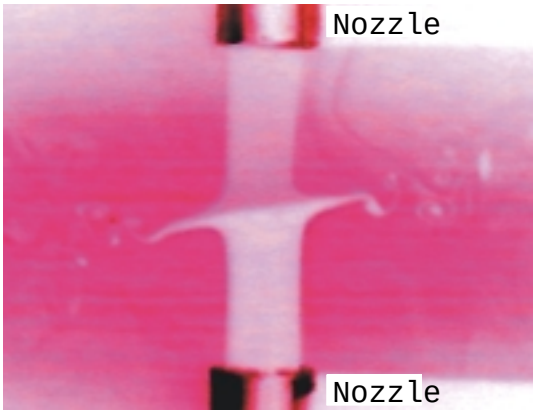

Figure 4.5: Turbulent opposed impinging jets - horizontal XY plane (LIF technique $L^* = L/d$, Re = 1500)

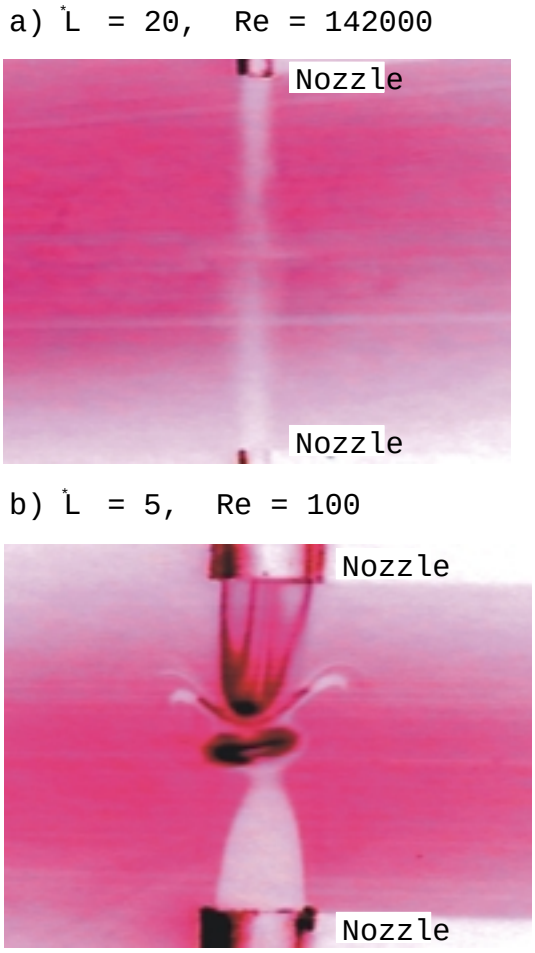

Figure 4.6: Turbulent opposed impinging jets - horizontal XY plane (LIF technique, $L^* = \{5, 20\}$, $\mathrm{Re} = \{100, 142000\}$)

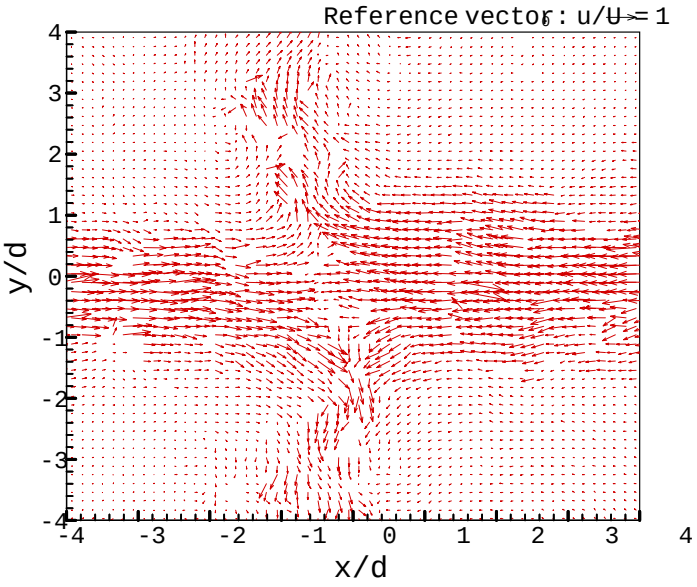

Figure 4.7: Turbulent opposed impinging jets - instantaneous vector plot (Re = 11000, $L^* = 20$, PIV)

Previous conclusions in this section may suggest that optimum Re numbers and L^*, do exist as far as the entrainment magnitude and the impingement area are concerned, since they are the key factors in mixing of the two jets with the surroundings and with one another. In principle, and based on flow visualization considerations, the mechanism that governs the entire jet to jet interaction is complex and is observed to depend on the following parameters: nozzle to nozzle separation L^*, magnitude of Re number, fluctuations of the flow rate feeding the two nozzles and induced vibrations of any kind (fact observed during experiments).

Analysis of the experimental and computed data as they were provided by LDA / PIV measurements and a CFD simulation, is the objective of the following sections. The examination is performed with the intention of revealing some quantitative information regarding the overall flow field development and its particular turbulent features in the case of turbulent opposed impinging jets.

4.2 Mean Velocities

This section contains the analysis of the experimental and computed mean velocity data. Aspects dealing with the general flow field will be emphasized here while more detailed information on the mean velocity profiles along the y axis will be discussed in the similarity analysis section. Even though the phenomena described in the present study are three dimensional and time dependent, for the reasons previously mentioned (section 2.3) a two dimensional approach

is followed here. Thus, the results provided are the output of LDA measurements in the horizontal plane xy for u and the vertical plane xz for v velocity components.

Corresponding to the LDA results are the PIV measured or numerically obtained u and v velocity components within the horizontal xy plane only. Since the axisymmetric assumption has proven to hold on average (see section 2.7), the above correspondence is acceptable. Instantaneous velocities were obtained as described in sections 2.3.3 and 2.3.5.4 while mean velocities were calculated as in section 2.5.1. For $L^* = 20$, the LDA and CFD results refer to the entire flow field in the plane of interest while PIV data mostly refers to a region containing the impingement zone, at least 8 diameters square. For reasons mentioned in section 2.3.5.3, full flow field PIV vector maps were obtained for $L^* = \{5, 10\}$ only.

As previously discussed (section 2.7), a total of 40960 instantaneous velocity samples were used to obtain the LDA ensemble averaged velocities while 250 image pairs were usually processed in the PIV mean velocity calculations (see section 2.7). The time series and the probability density functions (PDF) were continuously monitored during processing of the LDA data for abnormalities. The initial graphic and numeric analysis of the instantaneous measured velocities showed that the overall flow under investigation is approximately stationary, therefore the signal can be decomposed according to Reynolds decomposition, into mean and fluctuating components. This assumption works better for the signal recorded at locations situated closer to the axial and radial symmetry axes of the flow and for the u component. Larger variations about the measured mean velocity are noticed for the locations closer to the external limit of the flow and for the u component as well. The measurement points surrounding the stagnation point and covering an approximately circular region of diameter 1 to 1.5 times the nozzle diameter, i.e. the so called impingement region, is an exception to this rule.

The fine grid and standard $k-\varepsilon$ turbulence model along with UDS as discretization method were used in the numerical simulations (see section 3.5).

Although on average the impingement region is likely a surface and its position coincides with the geometrical symmetry plane of the two nozzles which is also the centerline of the radial jet, instantaneous vector plots show significant alterations of the overall flow field (Figure 4.7). The instantaneous velocity vector plot sample in Figure 4.7 clearly shows the instantaneous radial jet created and the asymmetry of the flow field due to the impact between the two initial jets. By averaging several such instantaneous vector plots a mean velocity vector plot similar to that in figure 4.9 can be obtained. This result would therefore imply the existence of bidirectional oscillations of the impingement region about a symmetry plane situated at $L/2$ downstream of the nozzles and about the centerline of the two jets, and related to this, variations of the entrainment rates.

4.2.1 Mean Velocity Vector Plots

Mean velocity vector plots obtained by mapping the LDA individual mean velocities and from PIV and CFD data processing, for the same configuration case, Re = 11000 and $L^* = 20$, are shown separately for clarity purposes (see Figures 4.8, 4.9 and 4.10). Normalizing the x and y coordinates by nozzle diameter d and $\overline{u}$ and $\overline{v}$ by the initial average velocity U_0, the ratio of vector length to vector magnitude was kept constant. Thus, consistent vector plots were obtained, making possible comparisons between performances of the three techniques (LDA, PIV and CFD) in the impingement jets case. Figure 4.8 shows the mean velocity vector plot obtained by LDA measurements. As we have initially assumed, on average, the symmetry of the two initial jets about their centerline is observed. The LDA vector plot provides a good view of the velocity profiles for the individual jets. It can be seen that these profiles become Gaussian in shape as they advance toward the impingement region (stagnation point). This is

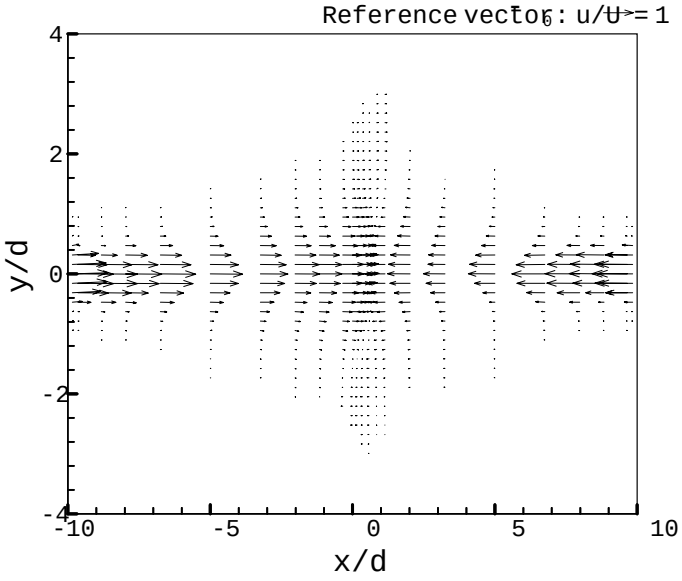

Figure 4.8: Turbulent opposed impinging jets - mean velocity vector plot (Re = 11000, $L^* = 20$, LDA)

analogous to the behaviour expected during evolution of free jet flow [55]. Although the LDA mean velocity vector plot shows a complete view of the flow field, the poor spatial resolution of LDA point measurements could not provide a clear picture of the free radial jet created at the impingement point of the two jets.

As mentioned in section 2.3.4, the PIV technique requires an optimum combination between particle size and its light scattering properties, density of the particles in the flow field of interest, illumination and magnification (i.e. the object - image scale factor) in order to obtain a good signal to noise ratio. Thus, a smaller field of view (about 30 % of the overall flow field in this case, Figure 4.9) is usually characteristic to PIV. This fact along with the constant unity aspect ratio available in PIV makes an overall high data density possible and as a consequence a more dense vector plot output (see Figure 4.9). Thus, the PIV mean velocity vector plot in Figure 4.9 clearly shows the development of the radial jet flow field. Consistently, the high data density available in PIV, made it possible obtaining a radial jet perfectly symmetric about the vertical symmetry plane of the two axial jets.

The CFD generated mean velocity vector plot in Figure 4.10 provides a complete view of the individual development of the two jets as well as a good picture of the free radial jet created at their impingement point. For the mesh used in this simulation, CFD does provide a spatial resolution comparable with that used in PIV measurements (i.e. 2 mm).

Out of the three vector plots displayed here (Figures 4.8, 4.9, and 4.10), although the PIV mean velocity vector plot does not provide a complete view of the flow field under investigation, however, it clearly shows the development of the free radial jet the best. Although all vector plots show a developing co-flow surrounding the two impinging jets, due to its very small magnitude (approximately 0.1 to 1 cm/s for Re = 11000) in comparison with that of the initial jets (1 m/s) and the newly created radial jet (0.3 m/s), it has little influence on the jet behavior.

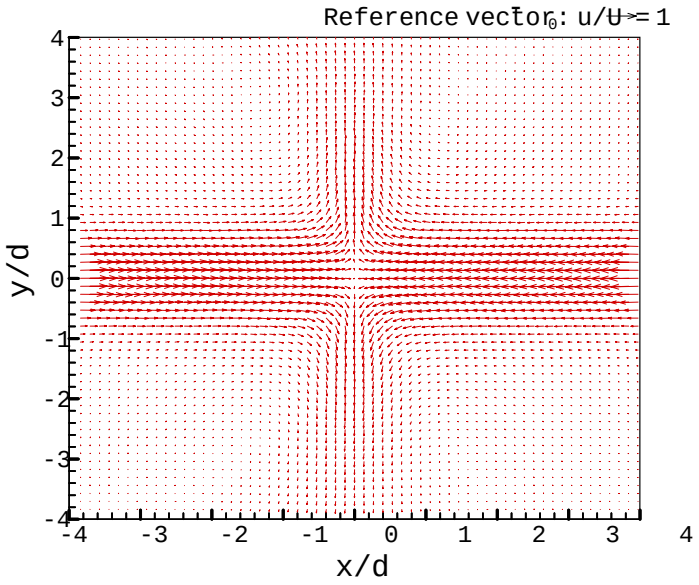

Figure 4.9: Turbulent opposed impinging jets - mean velocity vector plot (Re = 11000, $L^* = 20$, PIV)

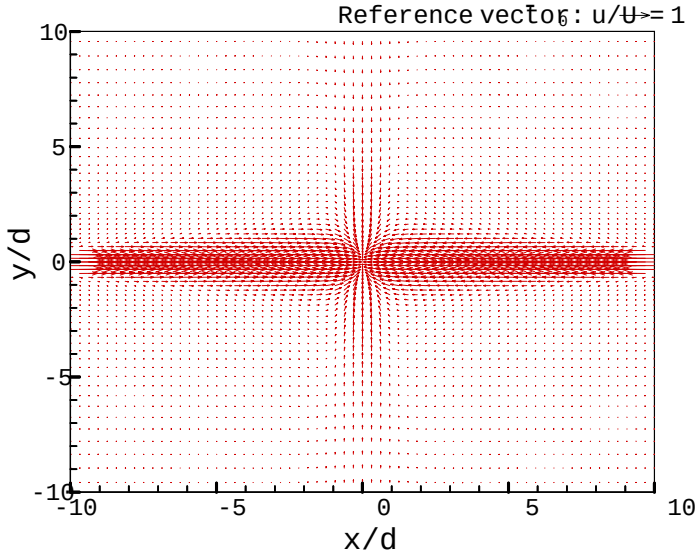

Figure 4.10: Turbulent opposed impinging jets - mean velocity vector plot (Re = 11000, $L^* = 20$, CFD)

It has been proven that based on the same amount of experience gained in dealing with each of the two different measurement techniques (LDA and PIV), PIV would be by far the most efficient in obtaining meaningful results in a certain period of time. CFD will become more efficient when subsequent similar simulations are required only.

4.2.2 Flow Near the Nozzle

Figures 4.11 a) and b) show the variation of mean longitudinal and transverse velocities versus y coordinate at $x/d = 0.3$ away from the exit plane of each of the two nozzles. Only LDA and CFD data are represented. The geometrically and kinematically similar flow conditions are confirmed through the very similar $\frac{\overline{u}}{U_0}$ distributions corresponding to opposed jets. The top portion of the mean longitudinal velocity profiles (Figure 4.11 a) exhibits a nearly flat shape characteristic of turbulent free jet flows (expected through the appropriate geometrical design discussed in section 2.1.1). A flatter variation would have been obtained if both the measurement and the computational grid spacings had been refined. A maximum difference of about 5 % in velocity magnitude is found when the experimental data is compared with the CFD prediction. Acknowledging that the LDA technique does not provide error free measurements (for these measurements LDA induced errors were in the order of 15 %, see section 2.6), then the CFD prediction can be considered acceptable.

The LDA and CFD mean transverse velocity profiles corresponding to the above $\frac{\overline{u}}{U_0}$ distributions are given in Figure 4.11 b. As previously shown (section 2.7) using less than 30000 samples would lead to important differences in the measured mean value for the $\overline{v}$ component, therefore a total of 40960 instantaneous velocity samples were used to obtain the LDA $\overline{v}$ velocity component. As expected, the LDA and CFD results are considerably different mostly within the boundary regions of the jet. Both variations illustrate lower $\frac{\overline{v}}{U_0}$ magnitudes (two to three orders lower) relative to the mean flow and they also exhibit similar symmetry trends. It is the axisymmetric geometry design that is responsible for the symmetry aspects.

While both LDA measurements and CFD simulations show small $\frac{\overline{v}}{U_0}$ values (grouped about $\frac{\overline{v}}{U_0} = 0$) for the jet's lateral boundaries [between $y/d = (0.6, 0.9)$] , which indicates little or no entrainment within this region, numerical simulations show transverse velocities about one order of magnitude higher than their LDA counterpart. The immediate vicinity of the nozzle may explain the low level of entrainment at this stage of the jet development. These conclusions strengthen the idea that the main flow and the turbulence is governed and created by the longitudinal (axial) velocity component, u.

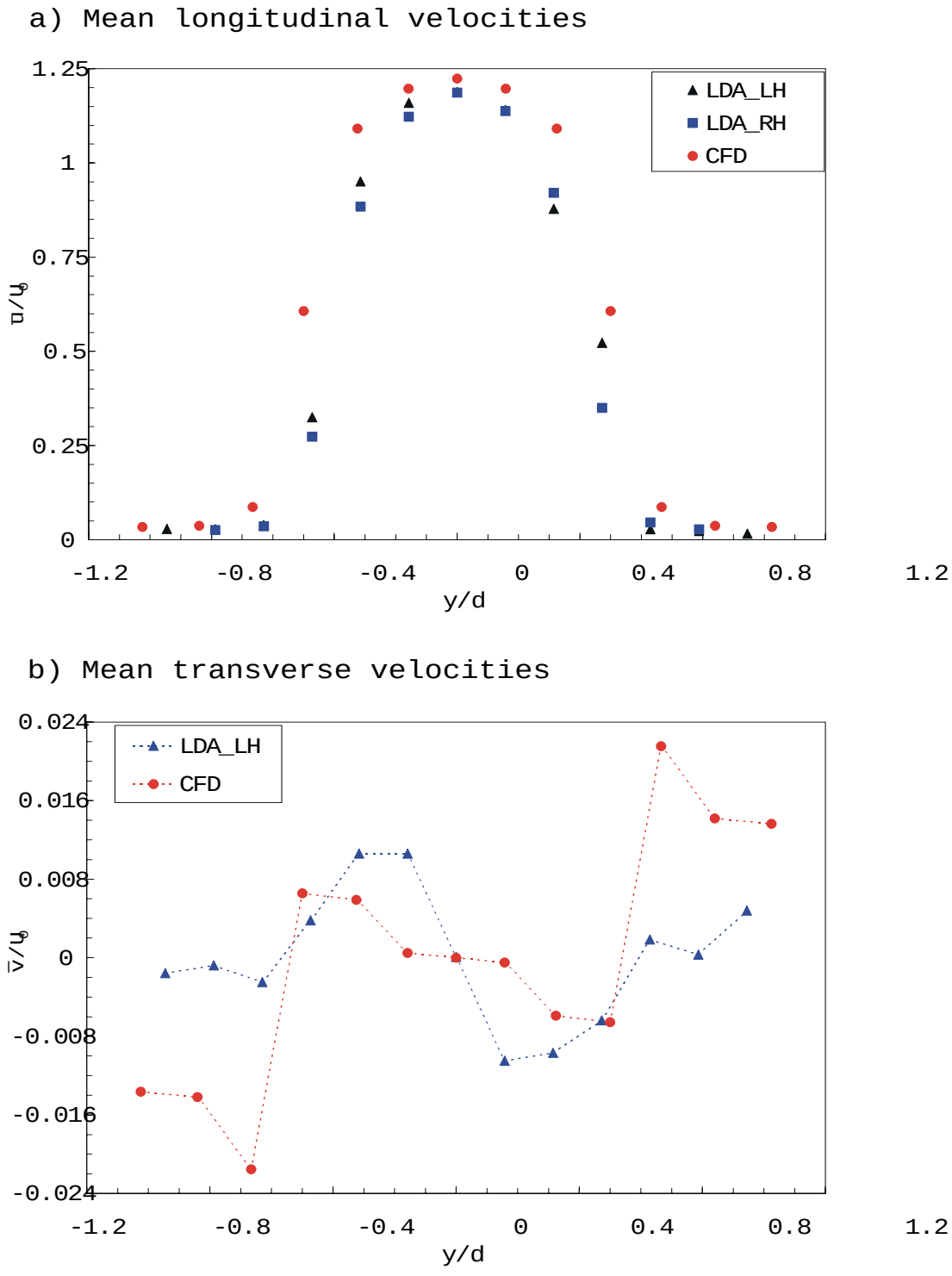

Figure 4.11: Turbulent opposed impinging jets - Mean longitudinal and transverse velocity profiles across the jet (xy horizontal plane, $L^* = 20$, Re $= 11000$, $x/d = 0.3$ downstream of the nozzle exit plane; RH, LH = right and left hand nozzles, - - - suggested trend for visual purposes only)

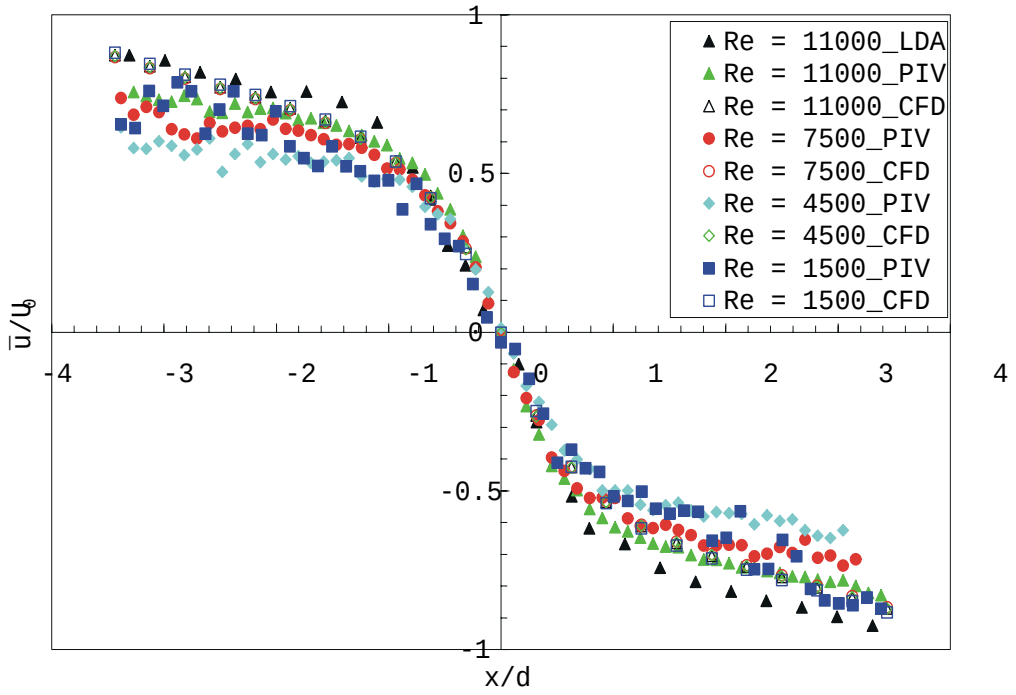

Figure 4.12: Turbulent opposed impinging jets - The effect of Reynolds number on the decay of mean longitudinal velocity on the jet centerline ($L^* = 20$)

4.2.3 Mean Velocities on the Jet Axis

The axial distribution of the mean longitudinal velocity u for various Reynolds numbers and nozzle to nozzle separations is shown in Figures 4.12, 4.13, 4.14, and 4.15.

The mean longitudinal velocity $\overline{u}$ (and $\overline{v}$ component as well) was normalized by the mean velocity at the nozzle outlet, U_0, used to calculate the Reynolds number of the flow, $\mathrm{Re} = \frac{\rho U_0 d}{\mu}$, while the axial coordinate x was normalized by the nozzle wetted diameter d. The point where the x axis is crossed by velocity distributions indicates the stagnation point of the flow for these averaged results and may give information on the flow field stability. Consequently, that point was assumed to be the origin of our Cartesian system of coordinates. It can be seen that on average, whether the velocity was measured by LDA or PIV or numerically calculated by means of the CFD code, the longitudinal velocity distributions corresponding to twelve different geometry-flow configurations pass through the same point which is the origin of the system of coordinates $(0, 0, 0)$. This confirms the initial assumption that the two geometrically and kinematically similar jets impinge on each other at the symmetry plane between the nozzle outlets.

Besides the evolution of the mean longitudinal velocity on the jets centerline for the maximum jet to jet separation ($L^* = 20$) and the entire Reynolds number range, measured by PIV means, Figure 4.12 provides insight on the performance of two measurement techniques (LDA and PIV) and CFD while they are used to predict the velocity distribution corresponding to $\mathrm{Re} = 11000$. Even though the mean longitudinal velocity shows the same overall velocity decay,

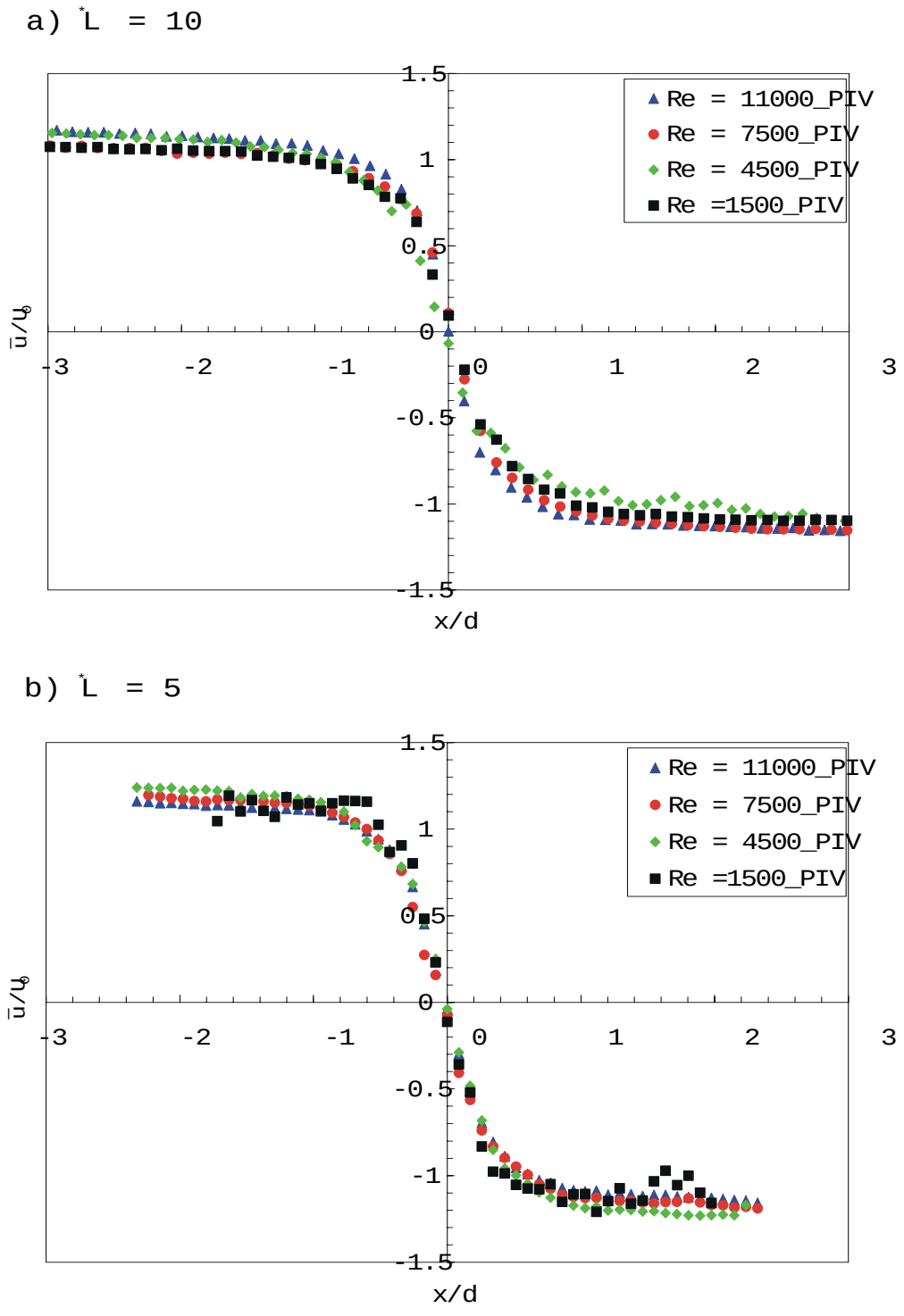

Figure 4.13: Turbulent opposed impinging jets - The effect of Reynolds number on the decay of mean longitudinal velocity on the jet centerline ($L^* = 10$, $L^* = 5$)

some disagreement between LDA and PIV data is seen on the portion of the graph within one nozzle diameter of the stagnation point (on either side of it). As discussed in section 2.6, there are several explanations for this fact. First, at the plane of impact, an adverse pressure gradient is generated, leading to the deceleration of the two opposed jets, this is then followed by a curved trajectory of the flow. Consequently, the pressure gradient would have a greater effect on the fairly large particles (larger than suggested by equation 2.12) used in PIV measurements (i.e. $50 - 250\ \mu m$) than on the natural particles of about $1\ \mu m$ used in LDA measurements. Furthermore, all particles are subject to drag which is a function of their dimensions, and again a greater influence is expected on the PIV data. The relatively small number of images (i.e. $250 - 1000$) used in the PIV technique to calculate mean velocity in comparison with 40960 instantaneous velocities used to determine the ensemble average velocity by the LDA technique may also contribute to this discrepancy. Even though little or no effect on data accuracy of the number of images used in PIV computations has been previously demonstrated (section 2.7.6) for the range of 250 to 1000 images, a number of images on the order of a few thousands to tens of thousands was not investigated but may matter.

Similar centerline mean longitudinal velocity decay is observed when comparing the LDA and CFD data. However, Figure 4.12 shows that the $k - \varepsilon$ CFD modeling does not yield any dependency of the decay of mean longitudinal velocity on the jet axis with Reynolds number. Failure of the CFD simulation to closely match the experimental data within the curvature zone of the flow could be attributed to the inability of the $k - \varepsilon$ model to account for the effects of streamline curvature on the flow. The constant time step assumed in the CFD simulation to resolve the transient fields toward the converged solution is perhaps responsible for the Re independent $\frac{\overline{u}}{U_0}$ distribution. A constant time step would lead to a limited or certain range of frequencies (wave numbers) captured by the solver.

The small differences between the results obtained when comparing the LDA and PIV techniques indicated the integrity of the PIV measurements in this flow configurations. Therefore, due to time efficiency and spatial mapping permitted by PIV, it was used for the remains of the results.

Each of the Figures 4.12 and 4.13 a), and b) shows the effect of Reynolds number and nozzle separation on the mean longitudinal velocity distribution for a given nozzle to nozzle separation distance L^*. In these representations, the distribution of centerline velocity can be seen as a composite of three regions: the free jet region, from $x/d > 2$ toward the nozzle, for $L^* = 20$ or from $x/d > 1.5$ for $L^* = \{5, 10\}$; the curved flow that links the initial axial jet with the impact zone, $x/d \in [0.5, 1.5]$ for $L^* = 20$ or $x/d \in [0.2, 1.5]$ for $L^* = 10$ or $x/d \in [0.25, 1.2]$ for $L^* = 5$; and the impingement region contained in between $-0.5 \leq x/d \leq 0.5$ for $L^* = 20$, or $-0.2 \leq x/d \leq 0.2$ for $L^* = 10$ or $-0.25 \leq x/d \leq 0.25$ for $L^* = 5$. Similar negative x/d intervals can be established for the second jet with regard to the free jet regime and the curved flow region. No particular Reynolds number effect is seen on the composition of the overall flow field. Even though similar centerline mean longitudinal velocity decay is observed for all Re numbers studied, slightly higher decay rates are noticed for lower Reynolds numbers when the separation distance is $L^* = 20$. For $L^* = 20$ and the four Reynolds number cases, $\frac{\overline{u}}{U_0}$ approached a near asymptotic distribution within the linear impingement region $1d$ wide. The $\frac{\overline{u}}{U_0}$ distribution for each Reynolds number within the impingement region can be represented fairly well by the linear expression:

$$\frac{\overline{u}}{U_0} = a_1 \frac{x}{d} + a_2 \tag{4.1}$$

The values of both coefficients a_1 and a_2 depend on the jet Reynolds number and nozzle to nozzle separation L^*. As an example for $L^* = 20$ and various Re numbers, a_1 and a_2 region take on the values provided in Table 4.1.

Table 4.1: Mean velocity distribution decay - model equation coefficients (L* = 20, slope α measured clockwise)

Re	11000	7500	4500	1500
a_1	-0.96204	-0.70723	-0.61640	-0.53139
$\alpha\,[^\circ]$	-43.89°	-35.269°	-31.649°	-27.985°
a_2	-0.000504	-0.000396	-0.001623	-0.003567

Parameter α represents the slope ($a_1 = \tan\alpha$) of the respective curves and is measured clockwise about x axis (e.g. see Figure 4.14 a) for $\alpha = -43.89^\circ$). As L^* decreases to 10 or 5, $\frac{\overline{u}}{U_0}$ exhibits an accentuated asymptotic tendency during the free jet condition while reaching an asymptotic slope of approximately -66.924° ($a_1 = -2.3472$, $a_2 = 0.0029544$) or -63.198° ($a_1 = -1.9795$, $a_2 = -0.0032577$) with respect to the x/d axis (measured counterclockwise) within the impingement region.

Therefore, it is evident that the Reynolds number affects not only the impingement region but the free jet region as well. It is the excess of momentum available at higher Re numbers, and related to this perhaps the specific stage in the jet development (jet spreading), that lead to such results.

Figures 4.14 a), b), c), and d) show the effect of separation distance, L^*, on the longitudinal velocity distribution for various Re numbers. An interesting evolution of $\frac{\overline{u}}{U_0}$ for Re = 11000 is shown in Figure 4.14 a), in that the velocity distributions corresponding to $L^* = \{5, 10\}$ are identical. A higher decay rate (about 70 %) is also noticed for lower L^* and with considerable differences in velocity magnitude between $\frac{\overline{u}}{U_0}$ distributions corresponding to $L^* = \{5, 10\}$ and $L^* = 20$ for the same Re number (Re = 11000).

As Reynolds number decreases below 7500, the $\frac{\overline{u}}{U_0}$ distributions corresponding to lower values separation distances $L^* = \{5, 10\}$, become individually visible while they are still closely grouped in the upper magnitude range. Moreover, the difference in magnitude between $\frac{\overline{u}}{U_0}$ for $L^* = 20$ and $L^* = \{5, 10\}$ remains about constant ($60 - 70$ %) while the Reynolds number influence is as previously discussed.

In conclusion, the effect of separation distance L^* on the flow field development can be summarized as follows: even though the three L^* have been chosen such that they satisfy a linear relationship of the form $L_i^* = 0.5L_{i-1}^*$, significant differences in the centerline mean velocity distributions are measured (between $33 - 50$ %) for $L^* = 20$ as compared to either one of the other two values of L^*. Small or no differences are found between $\frac{\overline{u}}{U_0}$ distributions corresponding to $L^* = 10$ and $L^* = 5$. A slight correlation of the results with Re number was also observed.

The measurements of the transverse velocity component are plotted in Figures 4.15 a, b, and c. There are large discrepancies between the LDA and PIV results as well as between the measured data and CFD predictions. The LDA data seems to the sign change in flow direction which is expected due to the opposed jets configuration. Similarly it seems to indicate the expected stagnation point even though its location this does not coincide with the origin of the coordinate system. The explanations must be related to the amount of both low and high frequencies the LDA system is able to resolve through its sampling rate (250 Hz) (high relative to PIV). The PIV data seems to be the most reliable since it demonstrates the radial

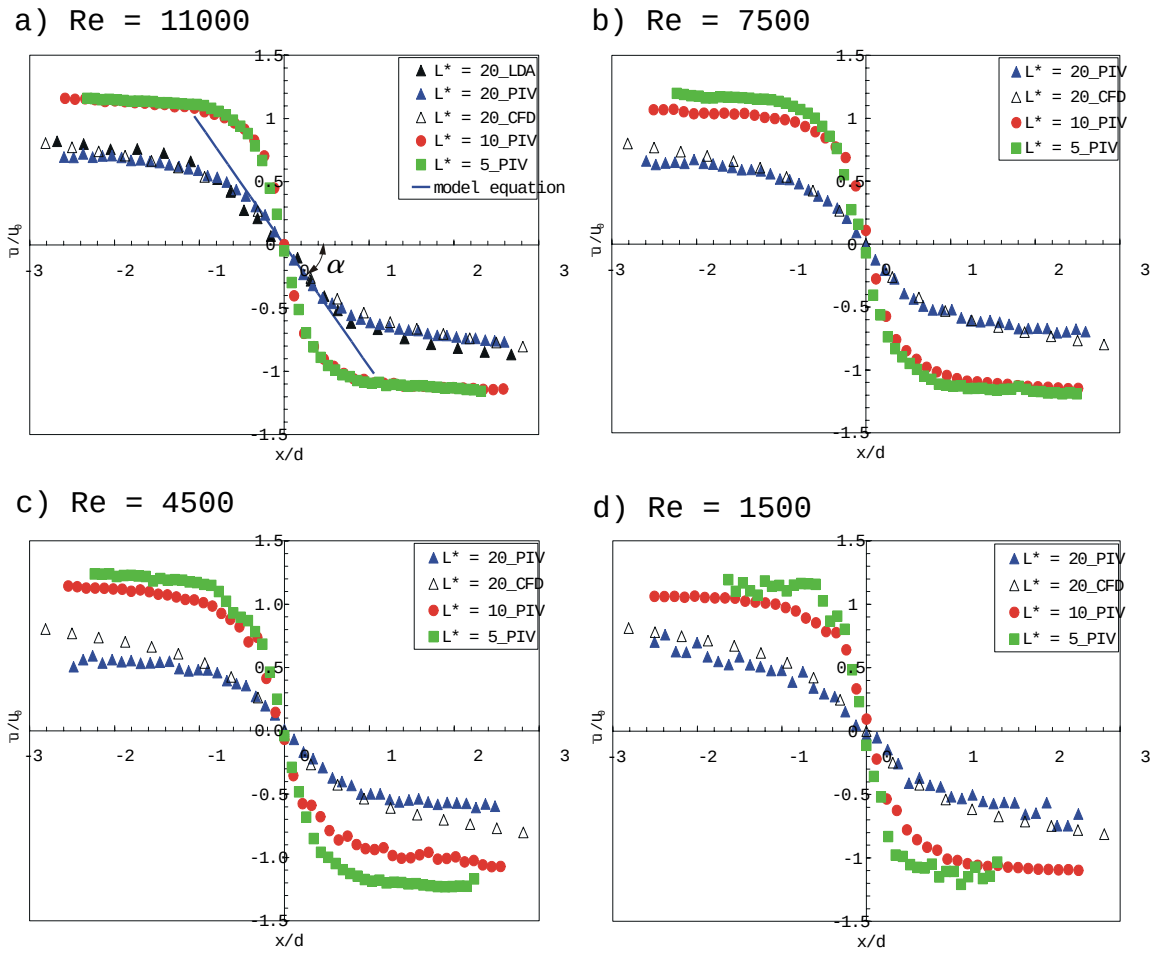

Figure 4.14: Turbulent opposed impinging jets - The effect of separation distance L^* on the decay of mean longitudinal velocity on the jet centerline

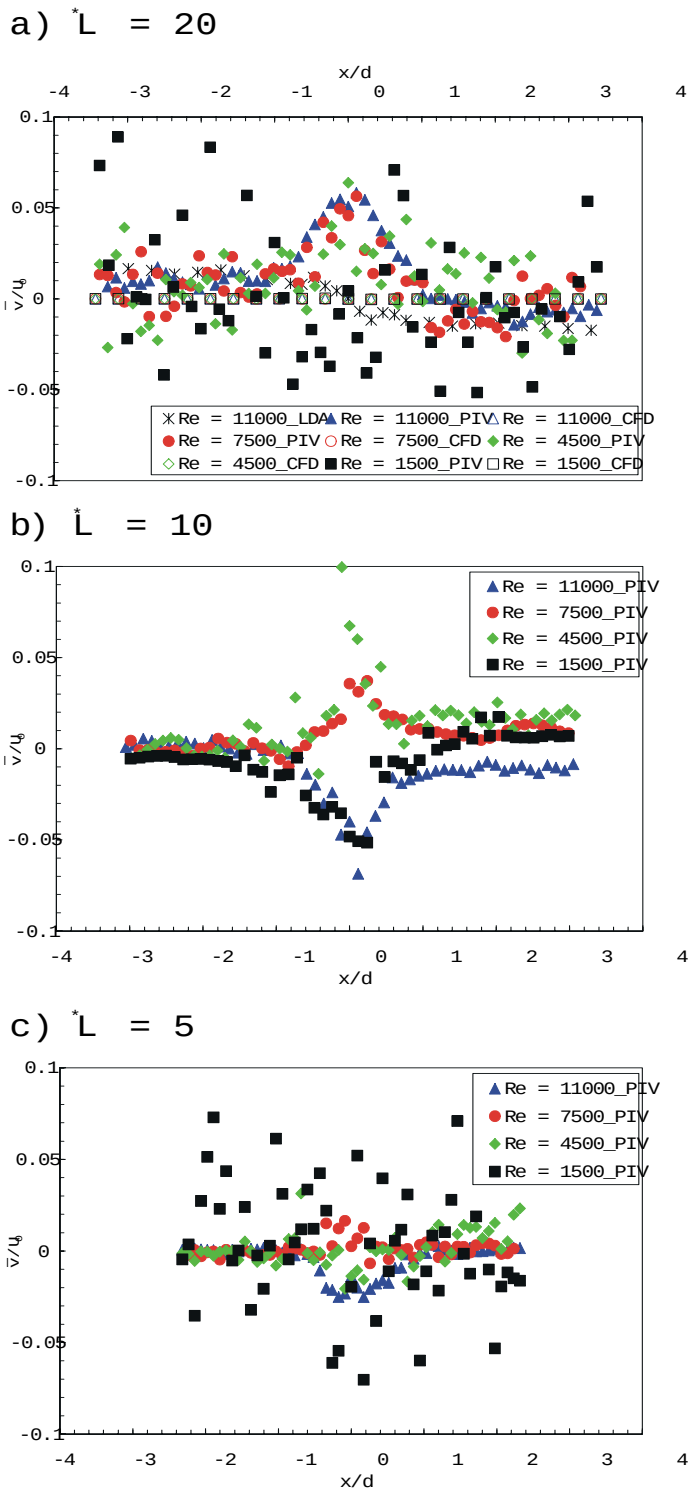

Figure 4.15: Turbulent opposed impinging jets - The evolution of mean transverse velocity on the jet centerline

jet formation with axial velocity which coincides with the transverse velocity component of the original jet flow. The PIV data sampled at 1 Hz and a variable illumination period (see Table 2.5) dictated by the flow speed exhibits Gaussian shape like $\frac{\overline{v}}{U_0}$ distributions with maxima corresponding to the stagnation point. As far as CFD data is concerned, the $\overline{v}$ velocity component is five to six orders of magnitude smaller than the average initial velocity and two to four orders of magnitude smaller than the measured transverse velocity. This explains why the graph in Figure 4.15 a), show a constant 0 mean transverse velocity along the jets axis. It is the axisymmetric geometry that is felt by the turbulence model through the gradient diffusion hypothesis which is responsible for such a low mean transverse velocity magnitude (the same results were obtained when checking $\frac{\overline{v}}{U_0}$ distribution in a plane perpendicular on $xy\,|_{z=0}$). Also there is no observable effect of the Re number on the $\frac{\overline{v}}{U_0}$ distribution.

In general, for all Reynolds numbers and separations studied, the component $\frac{\overline{v}}{U_0}$ is distributed in a symmetric manner about the centerline of the two initial jets (Figures 4.15 a, b, c). Exception to this rule are the flow fields corresponding to the lowest flow rate (Re = 1500) and the extreme nozzle to nozzle separations $L^* = \{5, 20\}$. In these cases, magnitudes of $\overline{v}$ component as high as 10 % of the mean initial velocity are possible. The acute instability manifested by this low momentum flow may be the cause of this state. For higher Reynolds numbers and up to the impingement region (within $0.5d$ to $1d$ on either side of the stagnation point), the mean transverse velocity components are two to three orders of magnitude smaller than the mean longitudinal components while within the impingement region its magnitude is similar to that of the mean radial velocity component of the radial jet. For the higher Reynolds number range, the occasional negative mean transverse velocities noticed may by associated with the entrainment of the surrounding fluid, whereas in the case of Re = 1500 this phenomenon can be explained by the severe unsteadiness of the corresponding flow.

Therefore, the overall flow and turbulence is mainly governed and created by the longitudinal velocity, u, for the axial flow field and by the v component for the radial jet flow.

4.2.4 Mean Velocities on the Radial Jet Axis

Through the " free radial jet" approach it was considered that on average a free radial jet is created when two opposed turbulent jets collide. Besides the vector plots previously discussed (Figures 4.8 - 4.10) where the overall appearance of the radial jet was revealed, Figure 4.16 demonstrates its existence through typical mean radial velocity distributions.

Essentially, the mean radial velocity distribution on the radial jet axis (Figures 4.16 a, b, c) resembles the mean dominant velocity variation in the radial wall jet excepting the fact that they are plotted on orthogonal axes with respect to each other. In other words the $\frac{\overline{v}}{U_0}$ of the free radial jet is represented against the radial jet axis while the dominant velocity distribution in a radial wall jet is plotted on a constant radius with respect to the stagnation point. In previous work [44] it was shown that when plotted at a constant radius ($1d$) about the stagnation point the mean radial velocity of free radial jet would exhibit a " Gaussian like" velocity profile. However, if the radial jet is instead viewed in a contrary manner, i.e. from its developing stage toward the stagnation point, then the resemblance to the radial wall jet is complete. In that case, the only difference between the present radial jet and the radial wall jet is the decaying velocity distribution exhibited by the radial jet beyond a certain distance as it advances from the stagnation point while a near constant distribution in that region is ensured by the nozzle proximity high momentum in the case of the radial wall jet. Furthermore, even though the collision of the two jets generates a stagnation point it is known that this phenomenon is not accompanied by a boundary layer flow along any impingement surface. This is in contradiction

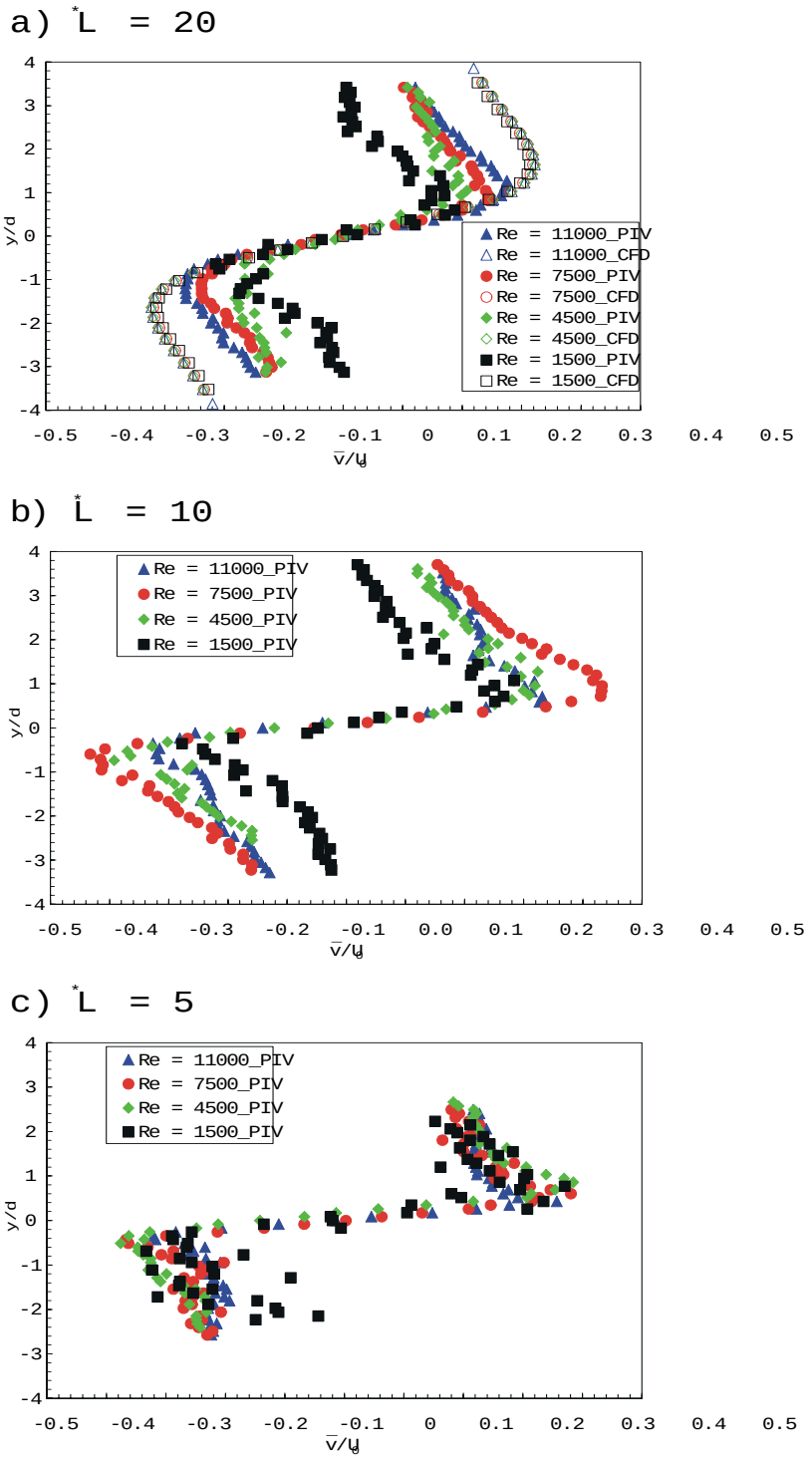

Figure 4.16: Turbulent opposed impinging jets - The effect of Reynolds number on the mean radial velocity distribution on the radial jet axis

with the radial wall jet where the boundary layer flow has an important contribution to the overall flow. Although no special features regarding the measurement or the computational grid are required in the impingement region (contrary to mesh agglomeration usually needed to solve a boundary layer flow near the wall) a fine mesh is utilized in the vicinity of the stagnation point in order to capture any low magnitudes in the velocity field.

These facts constitute enough arguments to totally separate the behavior of the free radial jet created by the impingement of two opposed jets from the radial wall jet concept. In fact, if regarded as an independent entity the radial jet has partially similar characteristics to free jet flow. What makes it different is its specific apparition from a sink/source. If viscous effects are neglected, which would be appropriate for our case since there is no wall boundary layer flow, the relatively low speed flow is irrotational (i.e. $\nabla \times \overrightarrow{v} = 0$) and a velocity potential exists. Therefore, the appearance of the free radial jet could be the result of a potential flow.

The impinging jet flow is more complicated where the resultant radial jet flow and the initial axisymmetric jet flows are coupled by means of a curved flow region accompanied by an adverse pressure gradient.

In this sense, the CFD mean radial velocity distribution shown in Figure 4.16 does not accurately predict the radial flow field due to the $k-\varepsilon$ model inability to solve curved flows and flows that are driven by anisotropic normal Reynolds stresses such as the impingement region in the present flow where the instantaneous dominant flow direction is suddenly changed (i.e. a sharp 90° deflection). This is mostly valid for the portion where the velocity distribution passes through a maximum to enter a decay condition, the linear velocity rise being well predicted. The assertions made in section 4.2.3 could be the explanations of the independent relative mean radial velocity distribution on the radial jet axis obtained with respect to the flow Re number.

In general the $\frac{\overline{v}}{U_0}$ distribution as plotted in Figures 4.16 a,b and c exhibits an almost linear rise (within about $1d$ region surrounding the stagnation point) followed by a decay portion. The radial acceleration exhibited by $\frac{\overline{v}}{U_0}$ on the rise portion is due to the strong adverse pressure gradient present in the impingement region. Passage from one velocity range to the other is sharply marked. For all Reynolds numbers an asymptotic $\frac{\overline{v}}{U_0}$ distribution is seen to characterize the flows corresponding to $L^* = \{10, 20\}$ (Figures 4.16 a, b). The maximum of the mean radial velocity is observed to change from 15 to 42 % of U_0 as a function of Reynolds number and L^*. For the maximum L^* studied ($L^* = 20$), an expected distribution of $\frac{\overline{v}}{U_0}$ with Re is illustrated in Figure4.16 a), in that the maximum value of $\frac{\overline{v}}{U_0}$ increased as Re increased. $\frac{\overline{v}}{U_0}$ distributions corresponding to $L^* = \{5, 10\}$ do not exhibit this behaviour. Instead, as L^* decreases, $\frac{\overline{v}}{U_0}$ distributions become more compact and the maximum value of $\frac{\overline{v}}{U_0}$ occurs toward the lower Reynolds numbers (Figures 4.16 b, c). The flow corresponding to Re = 1500 indicates a different trend. The maximum magnitude of $\frac{\overline{v}}{U_0}$ for $L^* = \{5, 10\}$ is constant and higher than the corresponding value for $L^* = 20$. Also, at $L^* = 5$, the decay portion of profile of $\frac{\overline{v}}{U_0}$ tends to approach a constant value.

A clearer dependence of $\frac{\overline{v}}{U_0}$ on separation L^* for various values of Re can be seen in Figures 4.17 a), b), c) and d). The conclusions are in agreement with those stated when Reynolds number effect was discussed. Comprehensive local $\frac{\overline{v}}{U_0}$ distributions are obtained for the extreme Re numbers while random variations are noticed for Re = $\{4500, 7500\}$. Thus, $\frac{\overline{v}}{U_0}$ exhibits a maximum for the smallest separation L^* and the overall mean radial velocity distribution follows an expected trend (i.e. as L^* increases $\frac{\overline{v}}{U_0}$ distribution move toward the radial jet axis) with small exceptions. In Re = 11000, there is an abnormal $\frac{\overline{v}}{U_0}$ decay for $L^* = 5$, and at Re = 1500, $\frac{\overline{v}}{U_0}$ decay appears unstable for $L^* = 5$. The maximum value of $\frac{\overline{v}}{U_0} = 0.42$ corresponds to $L^* = 5$, and Re = 7500.

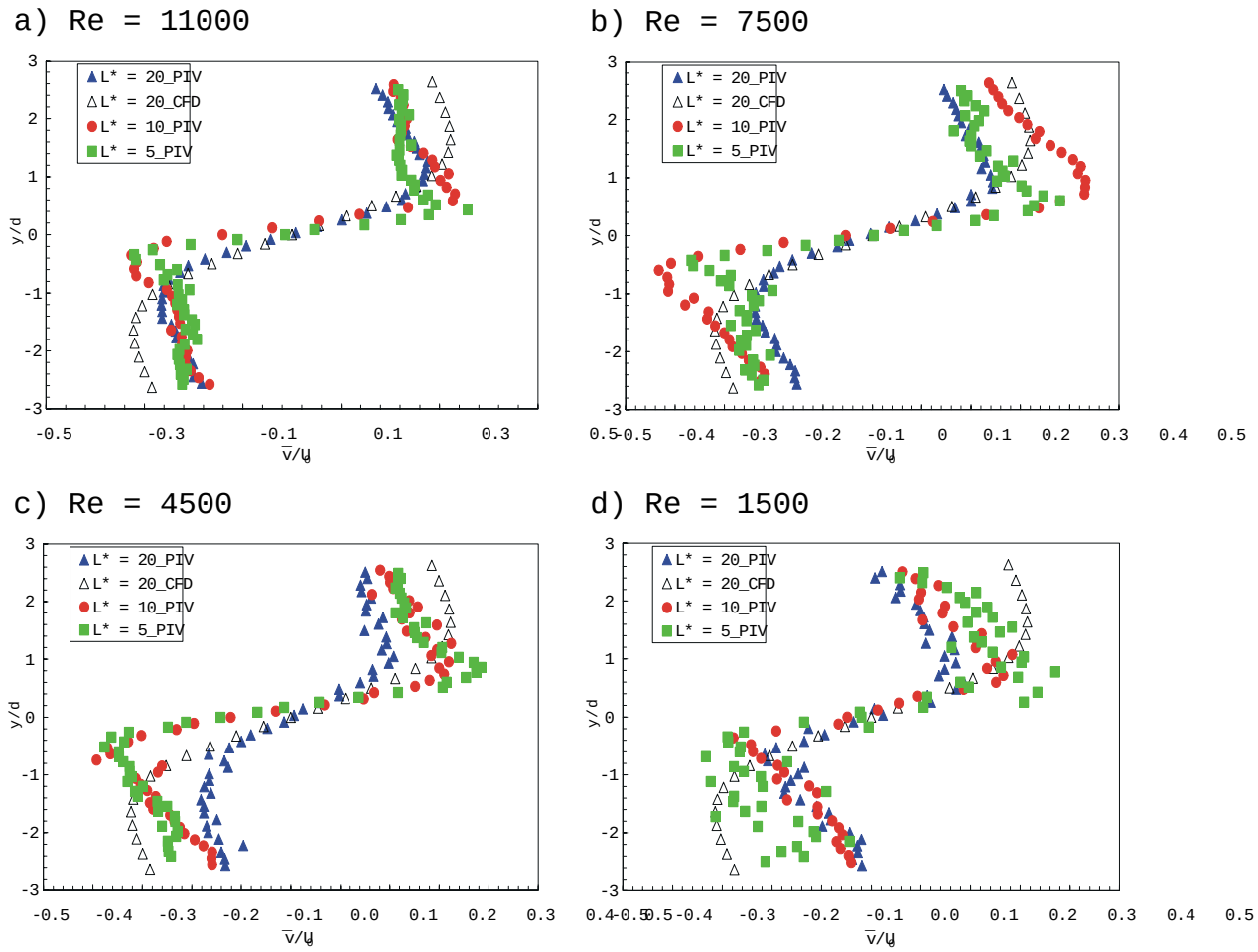

Figure 4.17: Turbulent opposed impinging jets - The effect of separation distance L^* on the mean radial velocity distribution on the radial jet axis

In a stable and stationary flow it is assumed that the above distributions would have led to more logical variation laws where the maximum magnitude of $\frac{\overline{v}}{U_0}$ would have corresponded to the most energetic flow (i.e. Re = 11000) and the smallest separation distance $L^* = 5$. However, due to the unstable and unsteady character of the impingement region (where the radial jet is created) this ideal state was not achieved.

Figures 4.18 a), b), c), provide an estimation of the mean transverse velocity distribution along the axis of the radial jet. Comparisons between the three study methods (LDA, PIV and CFD) presented in Figure 4.18 a) for Re = 11000 and $L^* = 20$, revealed an acceptable match between LDA and PIV data (the curves follow same trend within 0 to 50 % difference in magnitudes) while CFD values are at least two orders of magnitude smaller than any of the experimental data. Again, it is the flow curvature that is not properly solved by $k-\varepsilon$ modelling and in principal due to the weakness of the gradient diffusion hypothesis in evaluation of the normal Reynolds stresses, which is responsible for this disagreement. Similar to all the above velocity distributions, the CFD mean transverse velocity component variation on the radial jet axis is independent of the flow Reynolds number.

In general, the graphs in Figures 4.18 a), b), c) show no preferable trend in $\frac{\overline{u}}{U_0}$ distribution. For all Re numbers and L^* studied, the $\frac{\overline{u}}{U_0}$ distributions can be regarded as parabolic-Gaussian profiles exhibiting maxima in the immediate vicinity of the centerline of the opposed jets. The magnitude of these maxima is about the same (up to 40 % of U_0) as that of the mean radial velocity on the radial jet axis. Furthermore, these maxima belong to different regions ($-0.5 < y/d < 0.5$, on one side or the other of the line containing the stagnation point) which make the impingement region and the radial jet itself highly anisotropic and non-homogeneous. It is the unsteady and unstable flow motion observed to take place in this region which is the cause of this behavior.

Negative $\frac{\overline{u}}{U_0}$ values are also noticed at the periphery of these representations (usually $y/d > 2$ or $y/d < -2$ for any L^*) which would indicate the mixing of the surrounding fluid (entrainment) with the initial jet flow. Typical values of the entrainment velocity are in the range of 5 to 10 % of the initial mean velocity of the two jets.

In conclusion, the mean transverse velocity distribution in the radial jet plays a significant role in the dynamics of the impingement region and related to that in the mixing process between the two opposed jets and between the jets and the surrounding medium.

4.3 Turbulent Characteristics of the Opposed Impinging Jets Flow

This section intends to provide information regarding the turbulence aspects associated with the opposed impinging jets flow. The analysis is built around turbulent quantities derived from time traces of LDA and PIV data, such as longitudinal and transverse turbulence intensities (u_{rms}, v_{rms}). Numerical data such as turbulent kinetic energy and dissipation rate of turbulent kinetic energy are computed by using the CFD model. Aspects dealing with the turbulence distribution along the y axis for different stations within the flow field will be thoroughly discussed in the similarity analysis section. The overall flow field turbulence is emphasized in the present section. Symmetry about the axes of both axial and radial jets is assumed, so that only half of a distribution is usually discussed.

The absolute turbulent intensities were defined and evaluated as the *rms* of the measured velocities, i.e., the normal stress components in section 2.5. The calculation algorithm for

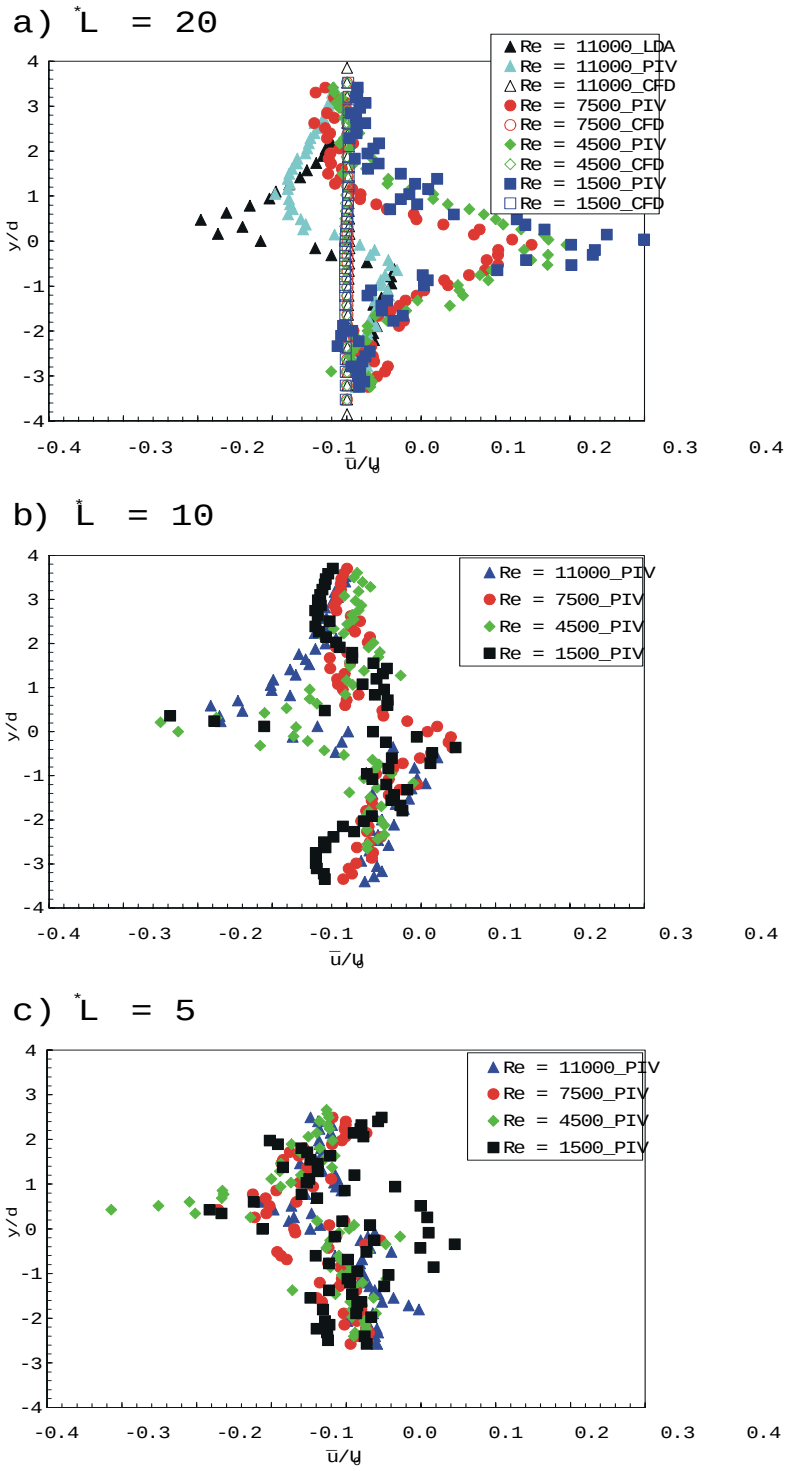

Figure 4.18: Turbulent opposed impinging jets - Mean transverse velocity distribution on the radial jet axis

related turbulent quantities such as turbulent kinetic energy, dissipation rate of turbulent kinetic energy, normalized correlation coefficients and turbulence time and length scales have also been described in section 2.5. Simultaneous collection of u and v data by LDA and PIV allow determination of u' and v' so that the Reynolds shear stress $\overline{u'v'}$ could be calculated at any point in the flow field. Point correlations are expected to provide valuable information about the level of production of turbulent kinetic energy at various locations within the flow field. From the CFD study, predicted values for k and ε were obtained for the fine computational mesh using a standard $k-\varepsilon$ turbulence model and UDS discretization scheme. CFD was employed for $L^* = 20$ only, over the entire spectrum of Re numbers. Comparisons between simulations and experimental data will be provided whenever appropriate .

It is well known that flow fields became turbulent when characteristic mean flow Re numbers become large. On the other hand flows characterized by very low turbulent Re numbers do not contain enough turbulent energy to support the wide spectrum of scales required in order to ensure isotropic dissipation. Consequently, the Reynolds number of the mean flow and nozzle to nozzle separation, L^*, are two key factors considered to significantly influence the structure of turbulence in the present flow. Higher levels of turbulent kinetic energy production are expected as mean flow Reynolds number increases and L^* decreases.

The turbulent intensities u_{rms}, v_{rms} defined as rms normal stresses provide an estimation of the turbulence magnitude in each of the three flow directions. In general, the largest values of rms normal stresses (u_{rms}, v_{rms}) and Reynolds stresses ($\overline{u'^2}$, $\overline{v'^2}$ and $\overline{u'v'}$) are found in the regions where the mean velocity gradient $\frac{\partial \overline{u}}{\partial y}$ is largest. This fact outlines the intimate connection between turbulence production and sheared mean flow. The measured turbulence quantities to be considered in this section correspond to mean velocity components ($\overline{u}$, $\overline{v}$) previously discussed (section 4.2). Since all measurements provided two dimensional data, only u_{rms} and v_{rms} were available. Assuming symmetry in the transverse plane (i.e. since the turbulence is a 3D process, the turbulent velocity profile on the third direction is assumed to be similar to the turbulent velocity profile in the y direction). Thus, the values of w_{rms} needed in turbulent kinetic energy calculations were estimated using v_{rms} data for the axial jet and u_{rms} data for the radial jet.

For purposes of data presentation and discussion, values of u_{rms} and v_{rms} were normalized by the mean velocity at the nozzle outlet, U_0, while the coordinates x and y were normalized by the nozzle wetted diameter d.

4.3.1 Turbulence Evolution Near the Nozzle

As illustrated in Figure 4.19 a), an expected trend is found for the variation of turbulence intensities u_{rms}, v_{rms} in the immediate vicinity of the nozzle. u_{rms} is low in magnitude, below 10 % of the initial U_0, in the central core of the jet while sharp increase (over 30 %) are measured at positions close to the jet ambient fluid interface. The transverse velocity fluctuations v_{rms} are of lower magnitude (below 5 %) through most of the flow, with higher values within the jet core region ($-0.2 < y/d < 0.2$). All this behavior is consistent with gradient regions in the dominant flow velocity, u, and partially accounts for nozzle edge shear layer prolongations (as far as the jet boundary spikes are concerned). The fact that the fluctuating velocity components are not equal, i.e. $u_{rms} \neq v_{rms}$, implies an anisotropic structure of the turbulence (u_{rms}/v_{rms} over 1.7 [46]).

The specific turbulent kinetic energy (i.e. k per unit mass) exhibits the same trend as u_{rms} (Figure 4.19 b). This graph shows the same trend as expected in a free jet in a stagnant ambient (or a very low co-flow stream), where k is higher in the central core of the jet, away from the centerline and decrease suddenly toward the outer edge of the jet, then continues with

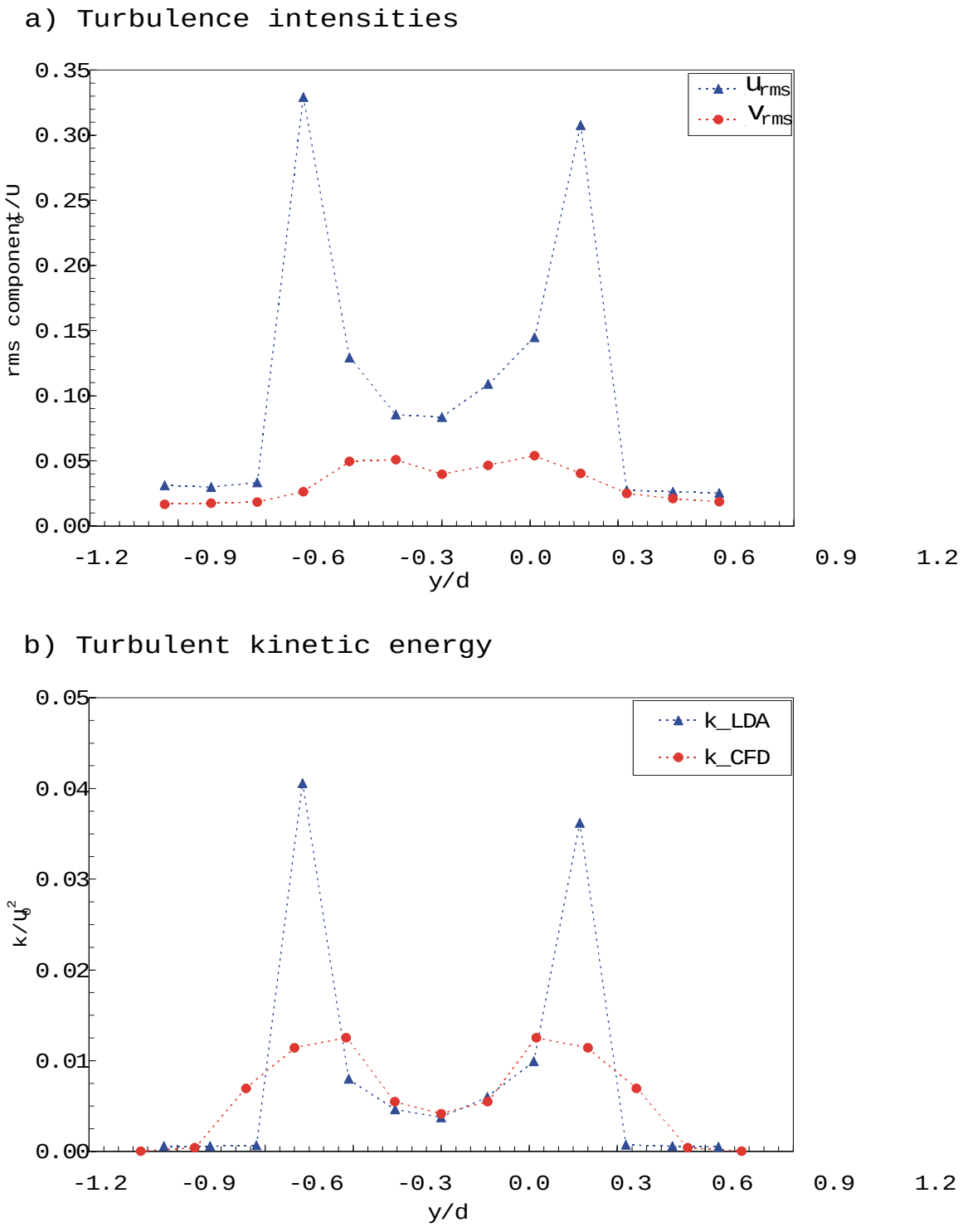

Figure 4.19: Turbulent intensity and specific turbulent kinetic energy profiles across the jet at $x/d = 0.3$ downstream of the nozzle exit plane ($L^* = 20$, Re = 11000; - - - suggested trend for visual purposes only)

a magnitude constant close to zero. The transverse component of the turbulent intensity v_{rms} accounts for about $10 - 12$ % of the total magnitude of k. Considering that a part of this value is due to measurement noise, the v_{rms} contribution to the overall turbulence evolution is expected to be even less significant. As expected and intuitively shown in Figure 4.19 a) and Table 4.2 the turbulent Reynolds shear stress $-\overline{u'v'}$ drops toward the centerline of the jet and changes sign there. Good agreement is noticed between LDA data and CFD prediction of turbulent kinetic energy in the region where the mean velocity gradient tends to zero, i.e. central core of the jet and in the outer flow. Since the underlying assumption of the $k - \varepsilon$ turbulence model is that the turbulent viscosity μ_t is isotropic, the lack of agreement shown in the regions corresponding to the jet boundary layer can be explained through limitations of the $k - \varepsilon$ turbulence model in predicting anisotropic flows (see Table 4.2).

Representations of the normalized velocity fluctuation correlations $R_{ii}(\tau)$ corresponding to each of the LDA measurement locations are provided in Figure 4.20. The autocorrelations in time give information regarding the degree of dependence in time between fluctuations of the flow. Positive values up to the first zero crossing or for $\tau < 0.2$ s are plotted so that the correlation curves do not clearly cross the axis. Instead they appear to decay in an exponential fashion with τ. The correlations do not appear to be an even function of the time separation as was anticipated. Instead both correlations corresponding to the measurement stations situated in the jet's central core region appear to be similar to those designated to isotropic turbulence with a wide spectrum of eddy sizes [46], [51]. The correlation coefficient $R_{ii}(\tau)$ decreases as the time interval τ increases; at large values of τ the signals are uncorrelated [49]. Since this could justify why some correlation curves have negative tails, however the complete shape of a correlation graph cannot be explained. It is reasonable to expect that the degree of correlation will decrease with increasing distance (about the centerline), and that beyond some finite distance this correlation will be practically zero [46]. A behavior closer to this supposition was noticed for $R_{ii}(\tau)$ corresponding to location $y = 2$ mm. As far as the jet's boundaries are concerned, for $y = 2$ mm and beyond the correlation coefficients decay to a constant non-zero value possibly suggesting the existence of a constant frequency superimposed to the flow's fundamental frequency. However, the correlation coefficients do not provide quantitative information regarding this frequency.

The evolution of integral and micro time and length scales initially defined in section 2.5 are presented in Figure 4.21. Figure 4.21 a) displays results obtained for the longitudinal and transverse integral and micro time scales while Figure 4.21 b) shows the variation of the corresponding length scales. Kolmogorov time and length scales for dissipation have also been included. Through its 250 Hz sampling frequency (can actually resolve 125 Hz), the LDA system used in these experiments is able to resolve time scales greater than 8 ms.

Mean longitudinal velocities, $\overline{u}$, at respective individual locations in the flow were used to calculate the length scales of the flow. It can be seen that the values of the scales (i.e. time or length) decrease approximately one order of magnitude between integral scales and Taylor microscales. This is reasonable since the Taylor microscale for time is a measure of the most rapid changes that occur in the fluctuations of u and v [21]. Within the jet's spreading area (approximate $0.5d$) the dominant length scale L_{11} is observed to be a strong function of the transverse coordinate y while independence about y is shown for the outer flow. The explanation of this behavior comes from the definition of L_{11} and also from the previously mentioned evolution of the time correlation coefficients. Consistent variations of the integral time scales are noticed (small time scale values for high mean longitudinal velocities). In general the longitudinal parameters are larger than the transverse ones. This fact strengthens the idea that the main flow and turbulence creation is dominated by the axial velocity component.

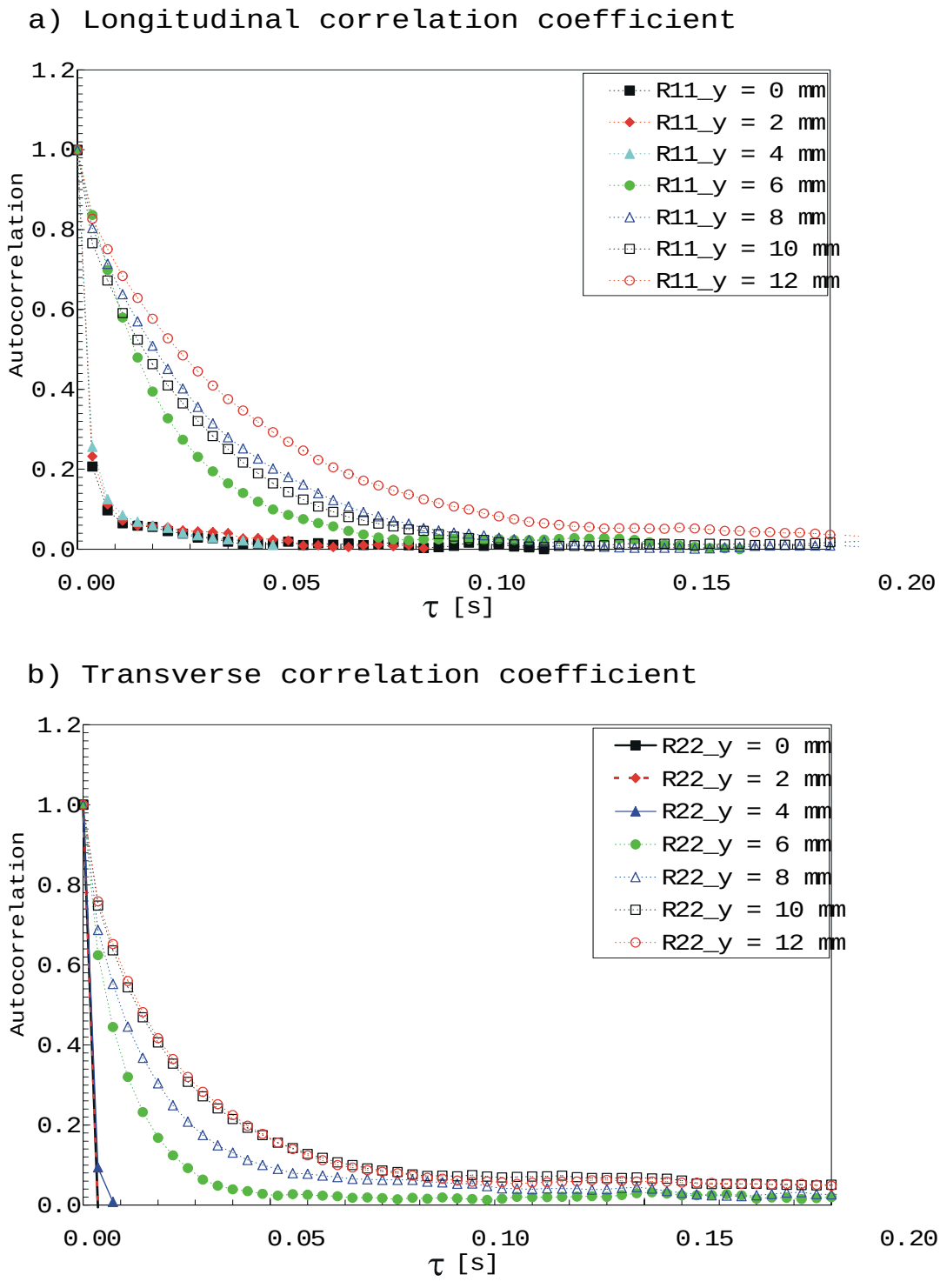

Figure 4.20: Longitudinal and transverse correlation degrees across the jet at $x/d = 0.3$ downstream of the nozzle exit plane ($L^* = 20$, Re = 11000)

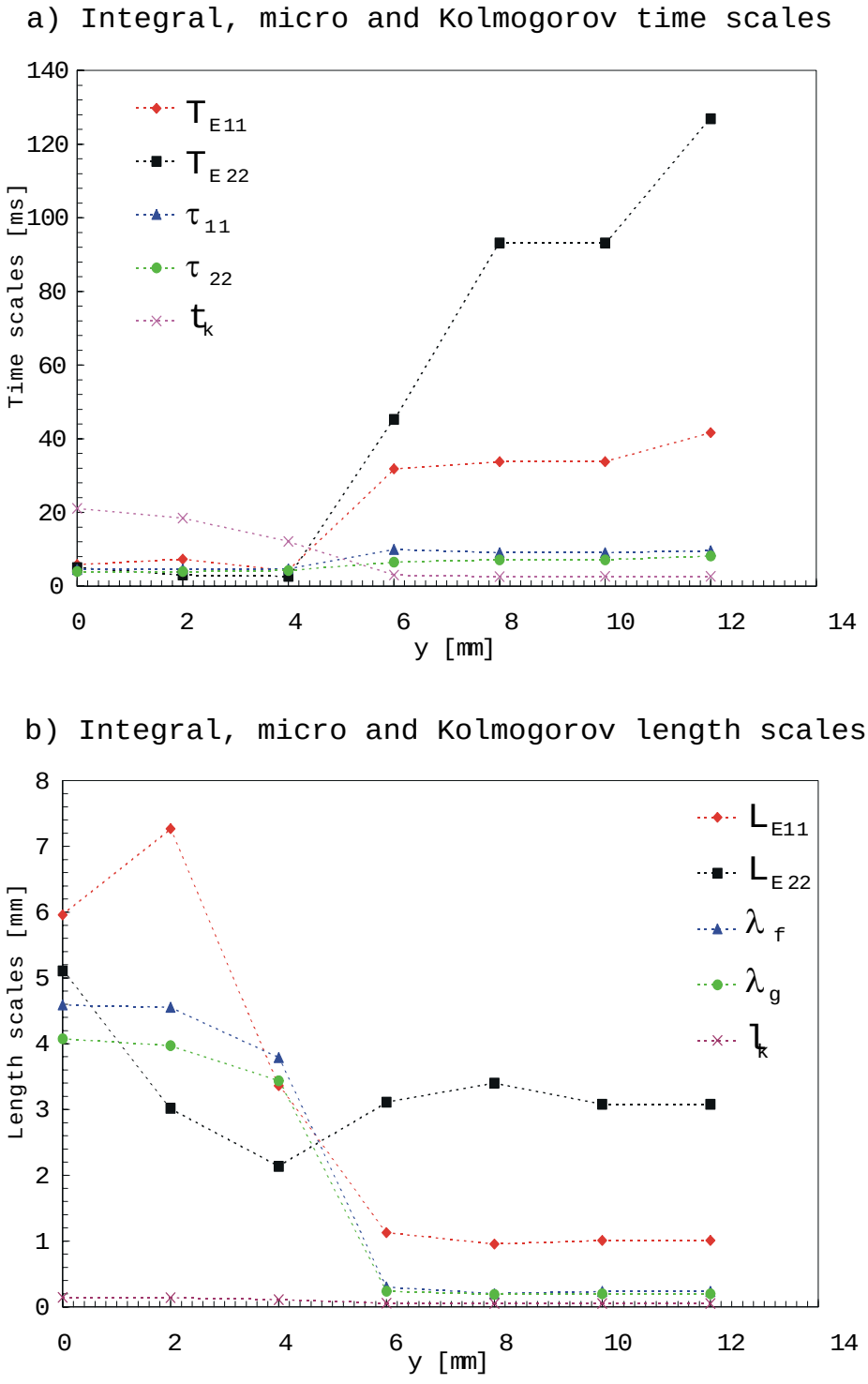

Figure 4.21: Distribution of longitudinal and transverse time and length scales across jet at $x/d = 0.3$ downstream of the nozzle exit plane ($L^* = 20$, Re = 11000; - - - suggested trend for visual purposes only)

The validity of the isotropic turbulence assumption, through which the longitudinal and transverse microscales should be related by a factor of $\sqrt{2}$, was further checked. Results are presented in Table 4.2, through the ratio $\lambda_g/\lambda_f = \frac{1}{\sqrt{2}}$.

Table 4.2: Flow near the nozzle - Turbulence isotropy evaluation and related data

$y\ [mm]$	$\overline{u'v'}_{LDA}\ [m^2/s^2]$	$\overline{u'v'}_{CFD}\ [m^2/s^2]$	λ_g/λ_f	$u_{rms}/\overline{u}$	$\mathrm{Re}_{\lambda_g\,LDA}$	Re_{tCFD}
0	$4.20E-05$	$3.90E-05$	0.887	0.0702	248	316
2	$-3.19E-06$	$-7.92E-01$	0.872	0.0738	269	302
4	$-1.41E-05$	$-3.65E-00$	0.906	0.1359	305	341
6	-6.22$E-06$	$-2.68E-00$	0.790	0.1007	6	150
8	$-5.88E-06$	$-1.56E-00$	0.962	0.7558	4	163
10	$-5.81E-06$	$-1.53E-02$	0.847	0.7924	5	18
12	$-5.81E-06$	$-5.06E-04$	0.847	1.0900	5	4

The calculated ratios λ_g/λ_f again indicate that no location strictly meets the isotropic turbulence condition. However, excepting the value corresponding to the steepest velocity gradient (i.e. $y = 8$), the turbulence field might be locally considered isotropic within $20 - 25$ % error. The relatively low level of turbulence intensity (between 3 to 8 %) shown in Figure 4.19 a) for the core of the jet is to good approximation consistent with Taylor's frozen hypothesis with its inherent limitations for high turbulence intensity non-homogeneous turbulence [46].Quantitatively this hypothesis requires that ratio $\frac{u_{\mathrm{rms}}}{\overline{u}} < 0.1$ [46]. Whereas numerical values in Table 4.2 indicate this applies in the region close to the axis of the jet, values derived at the outer jet measurement locations are inconsistent. Therefore, in the regions surrounding the centerline of the jet, up to the jet boundary, the isotropic (and so homogeneous) turbulence assumption is appropriate.

As Kolmogorov formulated his hypothesis [21], l_k and t_k are the dissipating scales where the turbulence is statistically in equilibrium and any change in the effective length and time scales of turbulence can only be a result of the effect of the dissipation rate of turbulent kinetic energy ε and the viscosity ν. This definition is consistent with the overall small and near constant magnitudes obtained for l_k and t_k.

It is known [46] that in order to obtain an equilibrium range in the intermediate scales the turbulent Reynolds number $\mathrm{Re}_{\lambda_g\,LDA}$ or Re_{tCFD} must be greater than 100. The turbulent Reynolds number for the CFD simulation has been computed as:

$$\mathrm{Re}_{tCFD} = \frac{\mu_t}{\mu C_\mu} \tag{4.2}$$

with the turbulent dynamic viscosity μ_t as defined in section 3.2.

Although both the experimental and computational data in Table 4.2 show consistency with this affirmation in the central core region, however CFD extends this agreement to the jet boundary too. This statement agrees well with the shape of the normalized fluctuation correlations being indicative of isotropic turbulence with a wide spectrum of scales. As mentioned above, the discrepancies between the experimental and computational data are mainly due to inability of $k - \varepsilon$ turbulence model to deal with anisotropic boundary flows.

Due to a large discrepancy between their magnitudes, the specific (per unit mass) production and dissipation rates of turbulent kinetic energy are plotted on a semi-logarithmic coordinate system (Figure 4.22 a). The velocity gradient used to evaluate the production of k

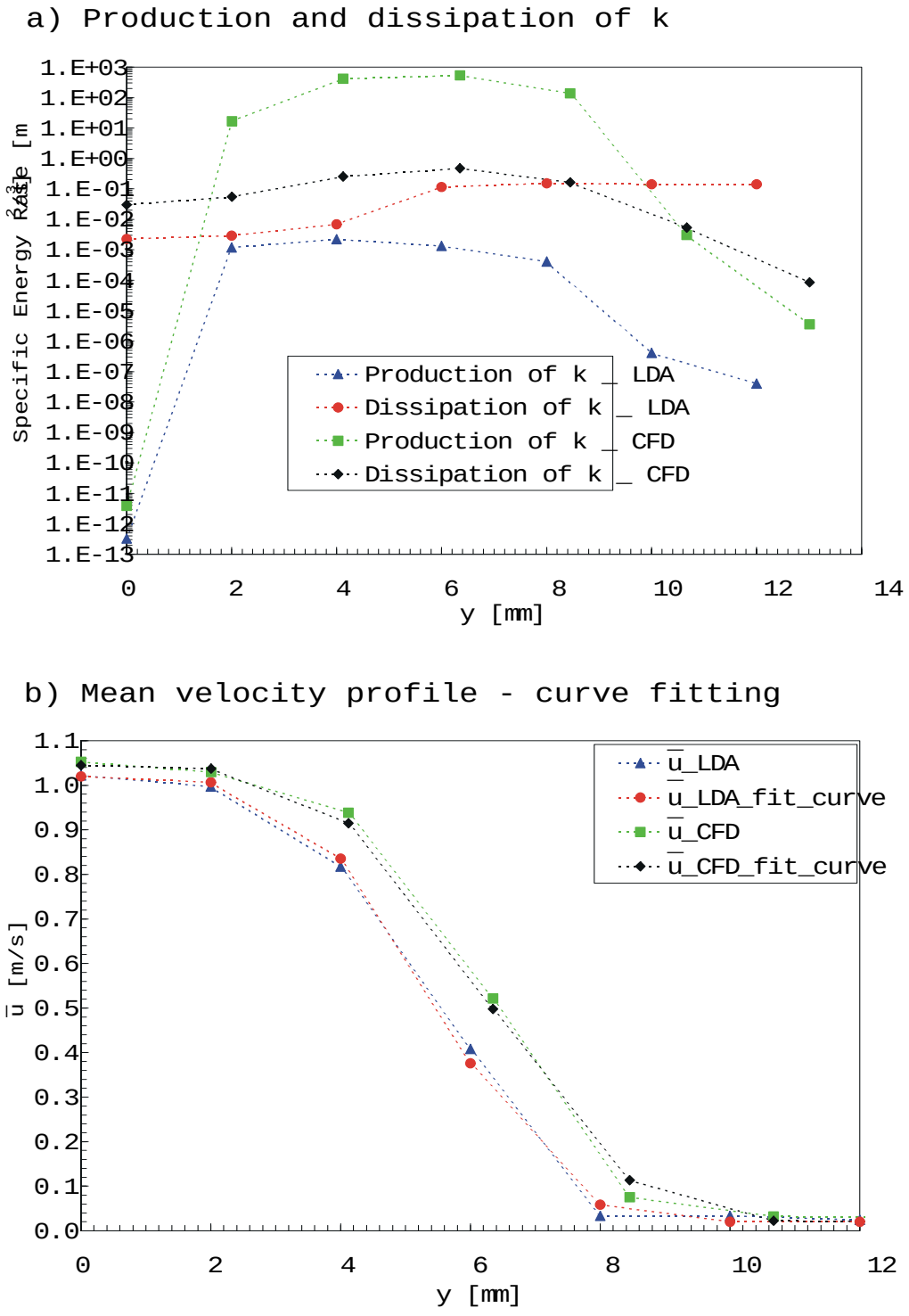

Figure 4.22: Variation of production and dissipation of turbulent kinetic energy across the jet at $x/d = 0.3$ downstream of the nozzle exit plane ($L^* = 20$, Re = 11000, - - - suggested trend for visual purposes only)

is calculated by fitting an exponential decay function to the mean velocity profile (Figure 4.22 b). The proposed function has the following form

$$\overline{u}\,(y) = (U_0 - \overline{u}_{\min})\, A \exp\left[-(\ln B)\left(\frac{y}{d}\right)^4\right] + \overline{u}_{\min} \tag{4.3}$$

where the constants A and B were determined in a spreadsheet through manual manipulation until the function fit the calculated mean velocity profile to a good approximation (maximum $2-3$ % deviation). $\{A,B\}_{\exp} = \left\{1.19, 10^9\right\}$ and $\{A,B\}_{CFD} = \left\{1.22, 2\cdot 10^5\right\}$ are the two sets of constants corresponding to experimental and CFD velocity profiles and $\overline{u}_{\min} = 0.2\ m/s$ is a minimum measured velocity which does not necessarily coincide with a co-flow velocity.

Significant information here includes the near constant nature of the dissipation profile relative to the production profile (Figure 4.22 a), and the large difference between the magnitudes of the two parameters in the favor of specific dissipation rate, 10^2 to 10^6 for experimental data. Contrary, the turbulent kinetic energy production overpower the dissipation for the CFD data. Although there is a large difference in production magnitude between experimental and CFD results (i.e. about 10^6 in the favor of CFD data), the two curves exhibits almost identical trends. As expected, the location of largest production corresponds to region of the most abrupt mean flow gradients ($y \in (2,6)\ mm$, the region out of the potential core and containing the boundary of the jet) for both experimental and CFD data. Although the dissipation is roughly constant relative to production, CFD and LDA results show that ε is maximum where production is maximum (region containing the jet boundary, more precisely $y = 6\ mm$). For the LDA results, whereas ε shows an increasing tendency toward the outer flow of the jet, the production has a contrary behaviour, i.e. decreasing is observed for locations situated beyond $y = 6\ mm$. Another important observation is that the small values of the experimental point correlations $\overline{u'v'}$ in Table 4.2 validate and emphasize the lack of turbulent kinetic energy production for the region close to the centerline of the jet ($y < 2\ mm$, Figure 4.22 a) and the high production rate existent from $y = 2\ mm$ toward the jet boundary. Also the location of the largest longitudinal scales do not thoroughly coincide with the region of highest k and P rates.

The high magnitude of dissipation in comparison with production in the region surrounding the centerline of the jet shows that the general assumption of turbulent equilibrium there is completely inadequate for this flow. A possible explanation for low production rates lies in the distance from the origin of the flow ($0.3d$ downstream of the nozzle) to the measurement location and because the flow is in its potential core region. However, turbulent equilibrium is satisfied to a good approximation for the region of the jet boundary ($y \in (2,4)\ mm$). Therefore, in this region the flow field can be considered isotropic and homogeneous. This is consistent with the magnitude of $\mathrm{Re}_{\lambda_g LDA}$ obtained for the flow corresponding to $y \in (2,4)\ mm$. Reasons that have already been discussed in section 3.2 led to the close link between CFD production and dissipation of k. Thus, the overpredicted level of turbulent kinetic energy production in the CFD results is expected.

4.3.2 Turbulence Evolution on the Jet Axis

Illustrated in Figures 4.23, 4.24, and 4.25 are the variation of longitudinal and transverse turbulence intensities u_{rms}, v_{rms} and distribution of k along the axis of the opposed jets. In order to investigate effects of Re number and L^* on turbulent flow structure, several separate groups of graphs separated by Re and L^* are displayed. A clear dependency of turbulence evolution on the jet axis as a function of flow Re and nozzle to nozzle separation $L^*$is evident. In general, as far as Reynolds number is concerned the largest values of rms normal stresses (u_{rms},

v_{rms}), and so those of normal and Reynolds shear stresses ($\overline{u'^2}$, $\overline{v'^2}$, and $\overline{u'v'}$) are found in the regions where the mean velocity gradient $\frac{\partial \overline{u}}{\partial y}$ is largest, i.e. the impingement region. However, two separate behaviors are noticed, namely: the low Reynolds number flows (Re = 1500) are characterized by the largest turbulence intensities (as high as 125 % of U_0) and therefore turbulent kinetic energy (Figures 4.23, 4.24, and 4.25 d), while the high Re number flows are characterized by lower and closely grouped values of rms velocities and k. The apparently large turbulence quantities exhibited by the flow at Re = 1500 might be explained through the highly unstable and unsteady character of this particular flow. Consequently the fluctuating velocities in the impingement region are not strictly an indication of the turbulent nature of the flow, instead they could be regarded as including turbulence fluctuations due to the jet development as well as fluctuations related to the flow oscillations (" false turbulence") that characterize the impingement region (i.e. including the radial jet). Possible methods of separating the two turbulence components would involve the study of a similar axisymmetric free jet, and therefore will not be discussed any further.

As far as the variation of maximum turbulent kinetic energy with nozzle to nozzle separation L^* is concerned four different behavior types could be distinguished (Table 4.3): a parabolic like variation of turbulence parameters with L^* corresponding to Re = 11000, a piece-wise linear distribution for Re = $\{7500, 4500\}$, and an almost exponential behavior corresponding to Re = 1500. If the same judgement in the case of maximum k variation with flow Re number is considered, a piece-wise linear dependency is found for $L^* = \{20, 5\}$ while a parabolic like behavior would characterize $L^* = 10$. These classifications are mainly concerning the maximum k values and do not have a general character. A summary of values supporting these conclusions is presented in Table 4.3.

Table 4.3: Distribution of maximum turbulent kinetic energy as a function of Re and L*

Parameters	$L^* = 20$	$L^* = 10$	$L^* = 5$
Re = 11000	10 %	24 %	10 %
Re = 7500	10 %	17 %	25 %
Re = 4500	10 %	25 %	25 %
Re = 1500	27 %	77 %	84 %

Although flow at Re = 1500 would provide the highest (about 90 % for $L^* = 5$) and most homogeneous (as far as the spreading along jet axis is concerned) turbulence levels (about 30 % magnitude) for all L^* values (see Figure 4.25 d), the above classification would recommend Re = $\{7500, 4500\}$ as the flow rates that will provide the most efficient turbulent mixing in the impingement region for $L^* = 20$ and similarly Re = 4500 for $L^* = 10$ (assuming that high values of k would indicate good mixing).

A shrinking impingement region width with decreasing L^* ($0.8d - 0.1d$ for $L^* = 20$ becomes $0.5d - 0.6d$ for $L^* = \{10, 5\}$) and independent of Re number is seen in Figures 4.25 a), b), c) and d). The level of longitudinal turbulence intensity u_{rms} is considerably affected by changing the dominant flow direction. The impingement region is characterized by higher u_{rms} and high turbulent kinetic energy, while a gradual influence on the distribution of transverse turbulent intensity is observed: little influence for $L^* = 5$ or no effect on $L^* = 20$ flow structure whereas there is a large influence on $L^* = 10$.

All the above observations combined can only explain the Reynolds number and L^* effects on k distribution on the radial jet axis illustrated in Figure 4.26. Little or no influence of various Re numbers on k distribution is observed. Exception to this rule is Re = 1500, for which the

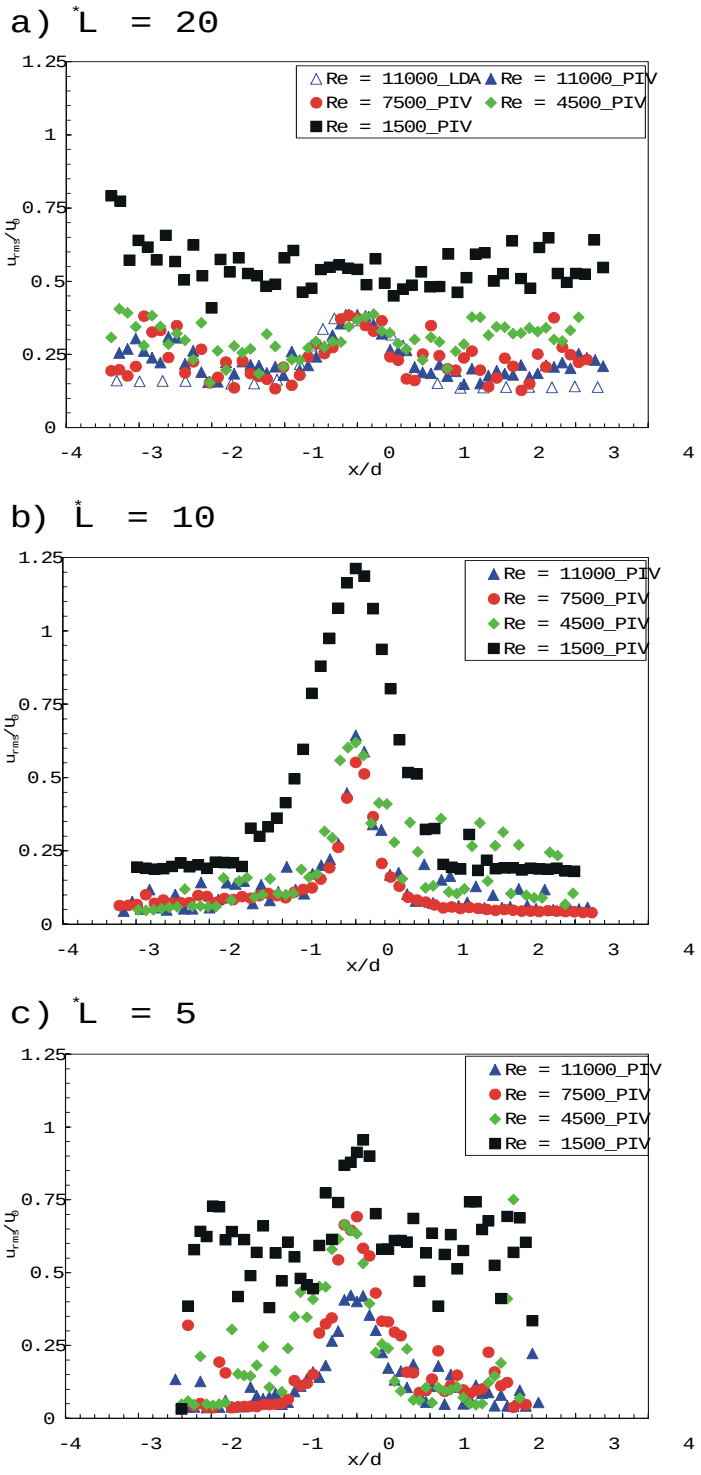

Figure 4.23: Reynolds number and L^*effects on longitudinal turbulent intensity distribution along opposed jets axis

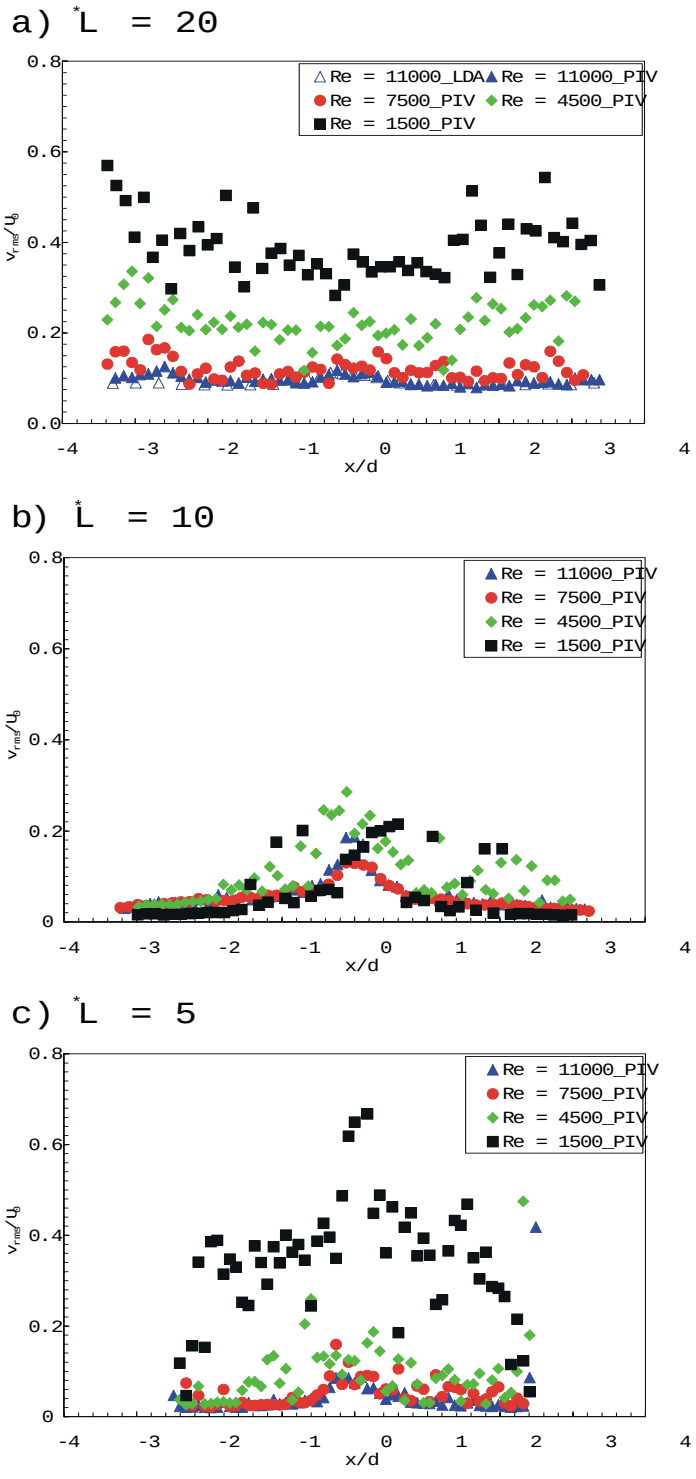

Figure 4.24: Reynolds number and L^*effects on transverse turbulent intensity distribution along opposed jets axis

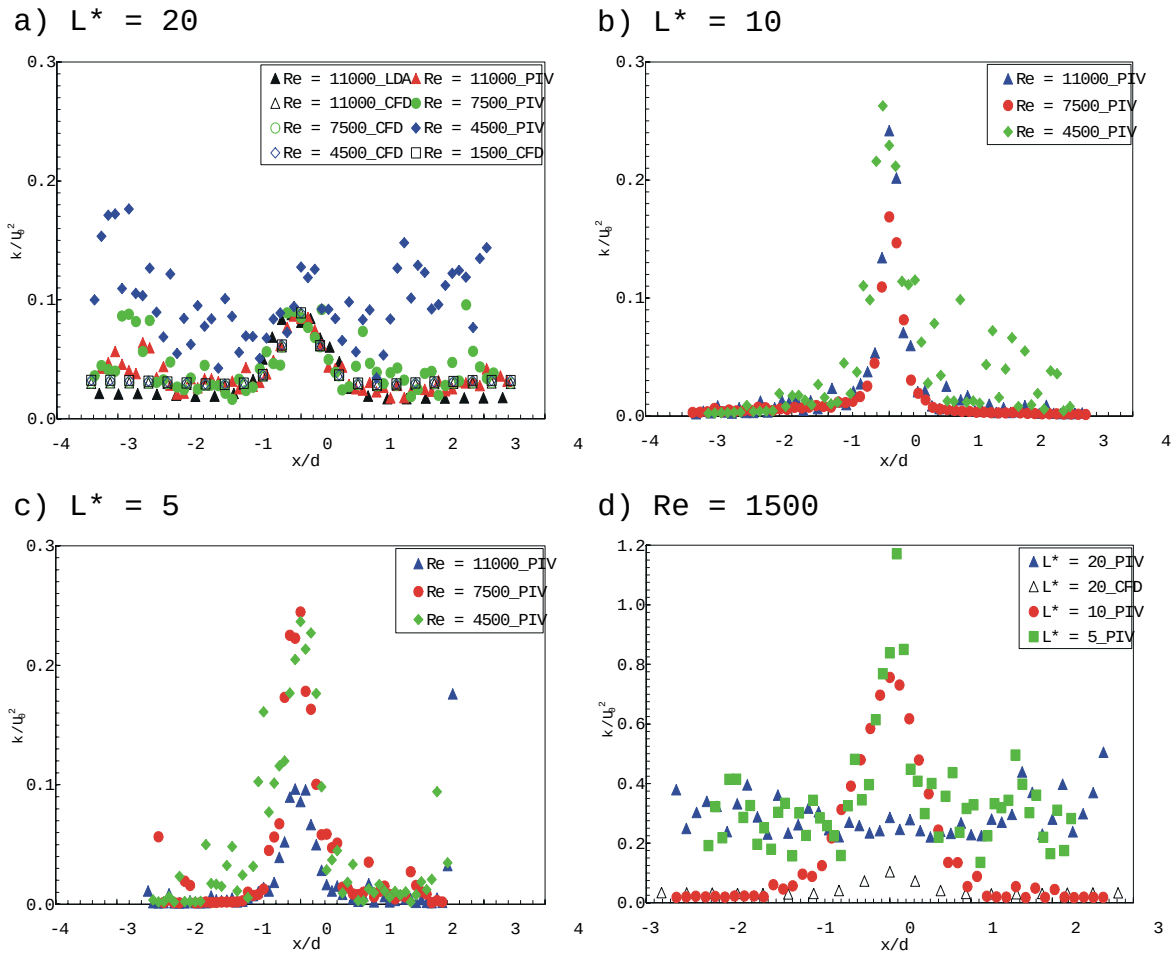

Figure 4.25: Reynolds number and L^*effects on turbulent kinetic energy distribution along opposed jets axis

largest k magnitude was always obtained independent of L^*. The reason may consist in the very sensitive oscillatory behaviour of the complex jet to jet impingement at Re = 1500. In this particular case (Re = 1500), it can be seen that the maximum level of k is obtained for $L^* = 10$ (Figure 4.26 b).

Although the plots in Figure 4.25 a) show good agreement between the experimental and computational magnitudes of k corresponding to $L^* = 20$ and Re = 11000, distributions of the CFD predicted turbulent kinetic energy data plotted in Figure 4.25 a) show no influence of Reynolds number on the turbulence flow structure. This fact could be explained through the isotropic turbulence the $k - \varepsilon$ model inherently assumes.

The relatively large number of measurement locations used to illustrate the variation of normalized velocity fluctuation correlations $R_{ii}(\tau)$ along the opposed jets' axis has led to separate charts for the longitudinal R_{11} (Figure 4.27 a) and transverse R_{22} (Figure 4.27 b) autocorrelations.

The general tendency in the results is the seeming exponential decay of the autocorrelations relative to the time separation. Exceptions to this rule are longitudinal $R_{ii}(\tau)$ distributions corresponding to measurement locations situated to the left (or right) of the impingement plane. For $x = \{2, 6, 10, 14, 18, 26\}\ mm$ the longitudinal correlation coefficients preserve a constant non-zero value which make us consider the existence of several constant frequencies superimposed to the dominant flow's fundamental frequency. However, quantitative information regarding these frequencies cannot be deduced from the graphs. Instead, all transverse autocorrelations appear to exhibit variations similar to those designated to isotropic turbulence with a wide spectrum of eddy sizes [46], [51]. As expected, due to the strong unsteady character of the flow under consideration which is seen more strongly within the impingement region, regardless of the correlation signal the degree of correlation increases with increasing distance from the stagnation point. This is more clearly observed in the case of transverse autocorrelation function (Figure 4.27 b).

The integral time scales displayed in Figure 4.28 a) exhibit variations consistent with distributions of the correlation coefficients along the jets axis. Since the value of T_{ii} is a rough measure of the interval over which $u_i^{'}(t)$ is correlated with itself, a constant variation of $R_{11}(\tau)$ would imply a linear distribution of the longitudinal integral time scale. For the measurement locations where the signal (u' or v') correlates with itself integral time scales measure the time interval over which u " remembers" its past history [49]. This behavior is consistent with the T_{22} and the portion of T_{11} profile beyond $x = 6\ mm$.

Consequently the dominant length scale L_{11} is observed to be a strong function of the axial coordinate x while L_{22} has an almost independent variation of x. Visible differences between the magnitude of the integral and micro time and length scales are also driven by the dominant axial velocity component or the radial velocity within the impingement region. Reasonable Taylor microscales for time and length are obtained within the free jet region due to the almost isotropic turbulent structure. However, discrepancies are noticed in the impingement region where the unsteady character of the flow leads to highly anisotropic and non-homogeneous turbulent structure.

The validity of the isotropic turbulence assumption on the centerline of the two opposed jets is illustrated in Table 4.4.

It is inferred from the values of λ_g/λ_f in Table 4.4 that the isotropic turbulence condition ($\lambda_g/\lambda_f = 0.707$) is locally satisfied at some points outside of the impingement region.

As already predicted by the k distribution for $L^* = 20$, and Re = 11000 this region seems to contain the flow within $\pm$ 8 mm away from the stagnation point. Taylor's frozen hypothesis which requires the ratio $u_{rms}/\overline{u} < 0.1$ is also in good approximation satisfied locally outside of the impingement region. The experimental data predicts equilibrium ($\mathrm{Re}_{\lambda_g LDA} > 100$) in the intermediate scales at all locations excepting the stagnation point, while the CFD

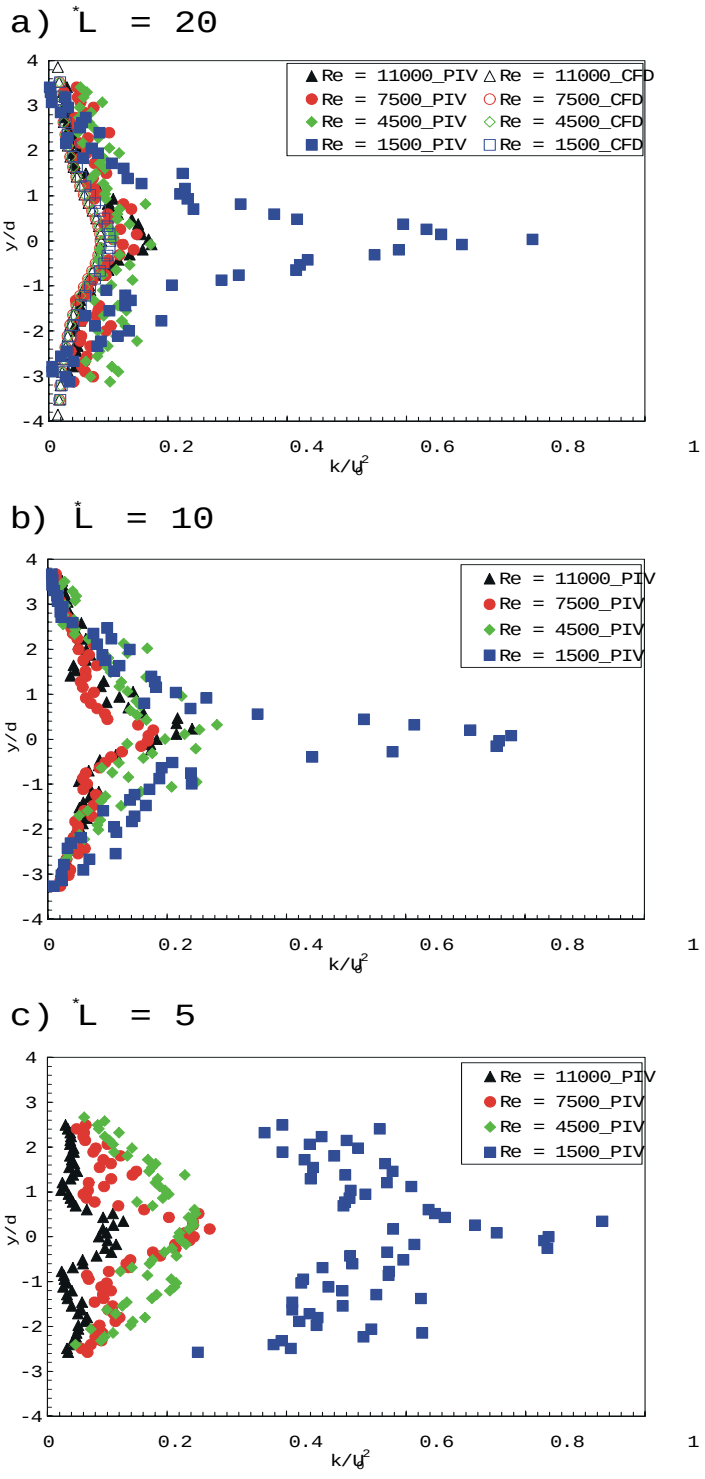

Figure 4.26: Reynolds number and L^*effects on turbulent kinetic energy distribution along the radial jet axis

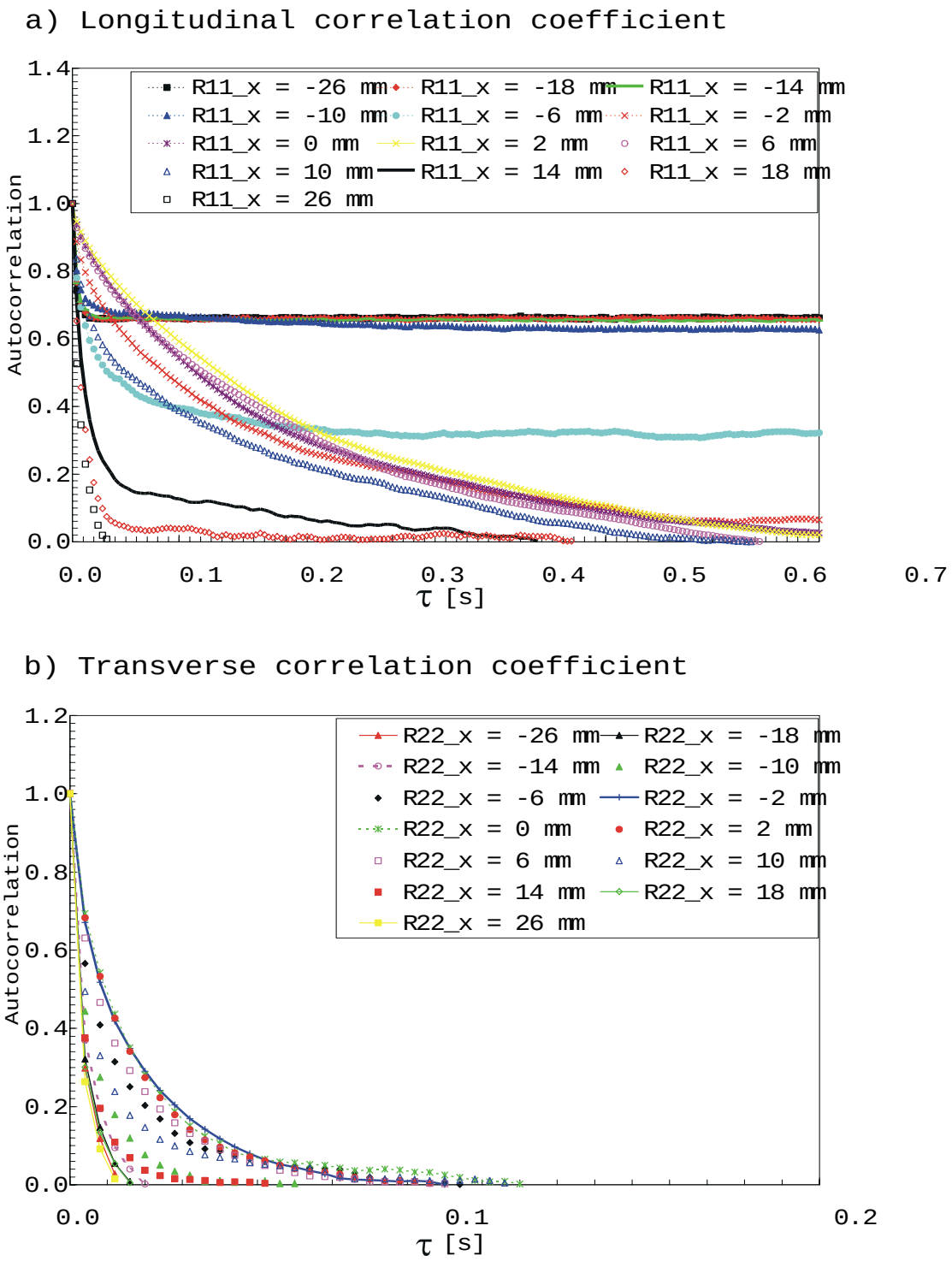

Figure 4.27: Longitudinal and transverse correlation coefficient variations on jet axis ($L^* = 20$, Re = 11000)

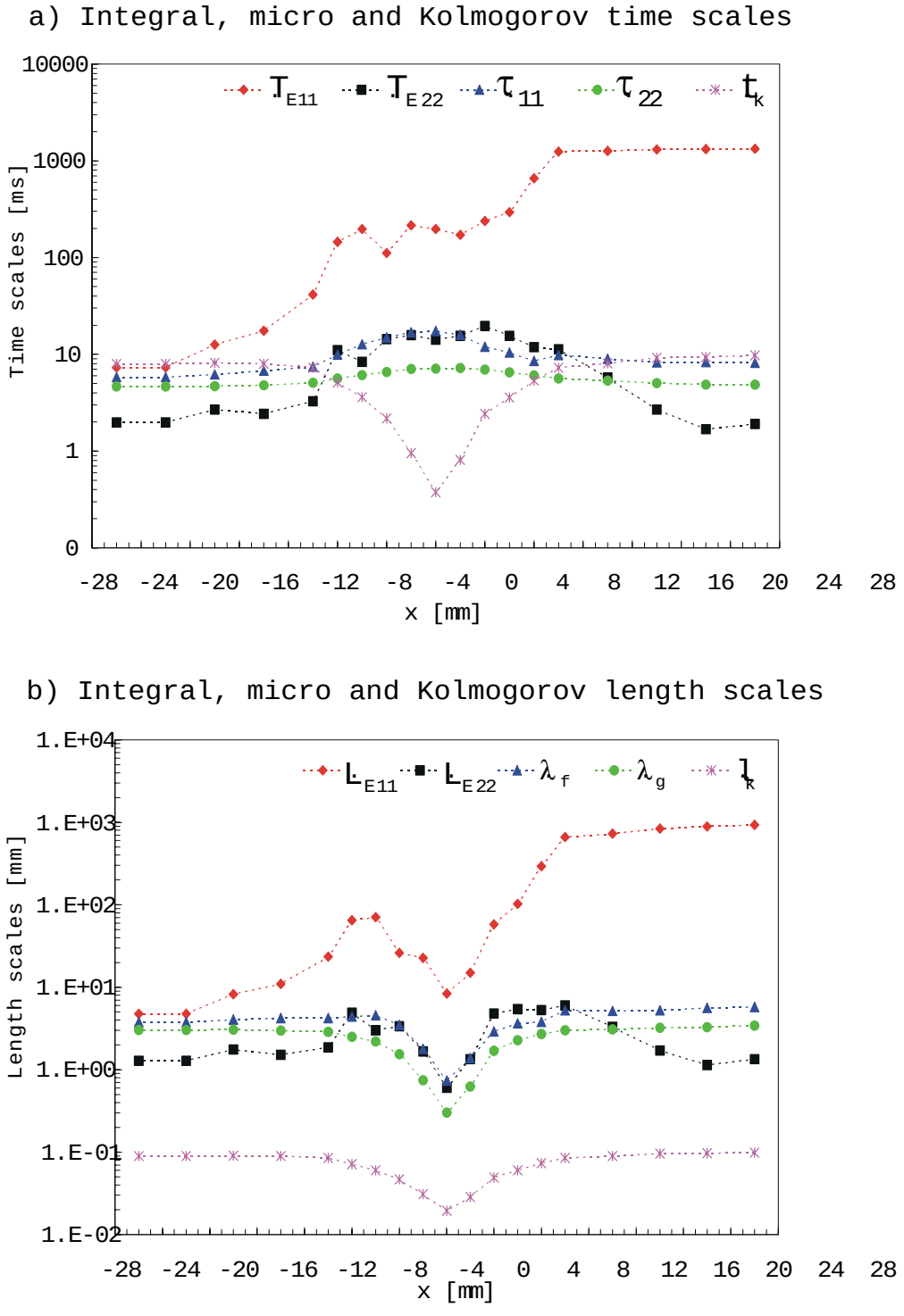

Figure 4.28: Distribution of longitudinal and transverse time and length scales on jet axis ($L^* = 20$, Re = 11000, - - - suggested trend for visual purposes only)

Table 4.4: Turbulence isotropy evaluation and related data on the jets axis (L* = 20, Re = 11000)

$x\ [mm]$	$\overline{u'v'}_{LDA}\ [m^2/s^2]$	$\overline{u'v'}_{CFD}\ [m^2/s^2]$	λ_g/λ_f	$u_{rms}/\overline{u}$	$\mathrm{Re}_{\lambda_g LDA}$	Re_{tCFD}
-16	$1.44E-04$	$-6.01E-05$	0.597	0.129	372	2006
-12	$-1.32E-04$	$-1.63E-04$	0.574	0.145	390	2152
-8	$-2.43E-04$	$-8.60E-05$	0.712	0.182	430	2566
-6	$-8.97E-04$	N/A	0.625	0.249	453	N/A
-4	$-9.91E-04$	$-3.50E-04$	0.583	0.374	375	3441
-2	$-1.27E-03$	N/A	0.454	1.110	153	N/A
0	$-1.35E-03$	$-5.92E-04$	0.410	2.218	77	4170
2	$-1.60E-03$	N/A	0.418	0.912	185	N/A
4	$-1.81E-03$	$-4.94E-04$	0.441	0.377	345	3441
6	$-1.28E-03$	N/A	0.479	0.239	419	N/A
8	$-3.56E-04$	$-3.71E-04$	0.569	0.179	388	2566
12	$-9.66E-05$	$-4.85E-04$	0.683	0.131	358	2152
16	$1.62E-04$	$-6.58E-04$	0.705	0.118	351	2006

calculated Re_{tCFD} (equation 4.2) is found to meet the equilibrium requirement even at the stagnation point. Moreover the Re_{tCFD} values are about one order of magnitude higher than the experimental findings. The differences noticed between point correlation experimental and numerical values indicate a lower level of P predicted by CFD results.

The excessively high magnitude of dissipation of k in the impingement region (see Figure 4.29) shows that the general assumption of turbulent equilibrium there is completely inadequate for this flow. As a consequence, distortions in the variations of Kolmogorov time and length scales are noticed. Due to the sinuous path of the mean longitudinal velocity on the jets' axis for which a derivative is hard to obtain, an evaluation of the turbulent kinetic energy production has not been attempted. The isotropic assumption for the calculation of the normal Reynolds stresses and so the gradient diffusion hypothesis in the CFD model and the experimental uncertainty in LDA are responsible for the inconsistency between the LDA and CFD results.

Based on this analysis similar discussions can be developed for the entire opposed impinging jets flow field as it was pictured by both experimental and computational means. However, due to their importance in mixing related issues two more sections will be discussed; they are concentrated on the results taken in the proximity of the impingement region boundaries at $1d$ upstream of the stagnation point in the axial direction and $1d$ downstream of the stagnation point in the radial direction.

4.3.3 Turbulence Evolution at Impingement Region Boundaries

As expected, the velocity fluctuation correlations associated with measurement locations situated across the axial and radial jets at $1d$ upstream and downstream of stagnation point (see Figure 4.1) and plotted in Figures 4.30 and 4.31 exhibit exactly opposite trends to each other.

The general tendency to notice is still the seemingly exponential decay of the autocorrelations relative to the time separation, however, constant non-zero distributions of the longitudinal correlations corresponding to the axial jet (Figure 4.30 a) and transverse correlations associated

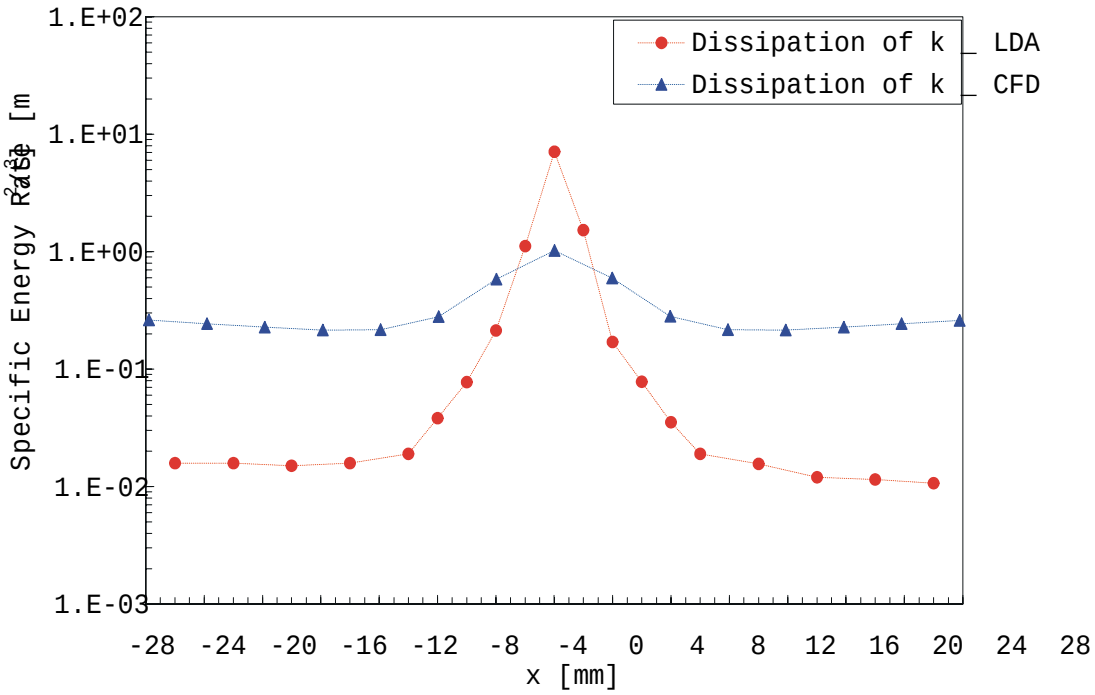

Figure 4.29: Variation of dissipation of turbulent kinetic energy on jets axis ($L^* = 20$, Re = 11000, - - - suggested trend for visual purposes only)

with the radial jet (Figure 4.31 b), can be noticed beyond certain time separation values. This behavior is certainly triggered by the change of the dominant flow direction with generation of an adverse pressure gradient within the impingement region. As previously stated, the variety of these constant $R_{ii}(\tau)$ values and the fact that they mostly correspond to locations closer to the jet axes make us consider the existence of several frequencies superimposed to the dominant flow's fundamental frequency. If in the vicinity of the nozzles a relatively high frequency (about 20 Hz) would have appeared as dominant (but this is not the case) it could have been associated with the resonant frequency of the electric pump (section 4.3.1). The differences noticed in R_{ii} magnitude for these specific locations make us associate the constant distributions of R_{11} for the axial jet and R_{22} for the radial jet with the visually observed random axial oscillations of the impingement region and radial oscillations of the radial jet periphery. However, quantitative information regarding these frequencies cannot be deducted from these plots. Instead R_{22} for the axial jet (Figure 4.30 b) and R_{11} for the radial jet (Figure 4.31 a) appear to exhibit variations similar to those designated to isotropic turbulence with a wide spectrum of eddy sizes [46], [51]. As expected, due to the strong unsteady character of the flow under inspection, which is seen more obviously within the impingement region, the degree of correlation decreases with increasing distance from axial jet centerline and increases with increasing distance from radial jet centerline.

Due to large discrepancies between various time and length scales semi-logarithmic representation charts have been used to better illustrate the results in Figures 4.32 a and b. In both cases the visible differences between the magnitude of the integral and micro time and length

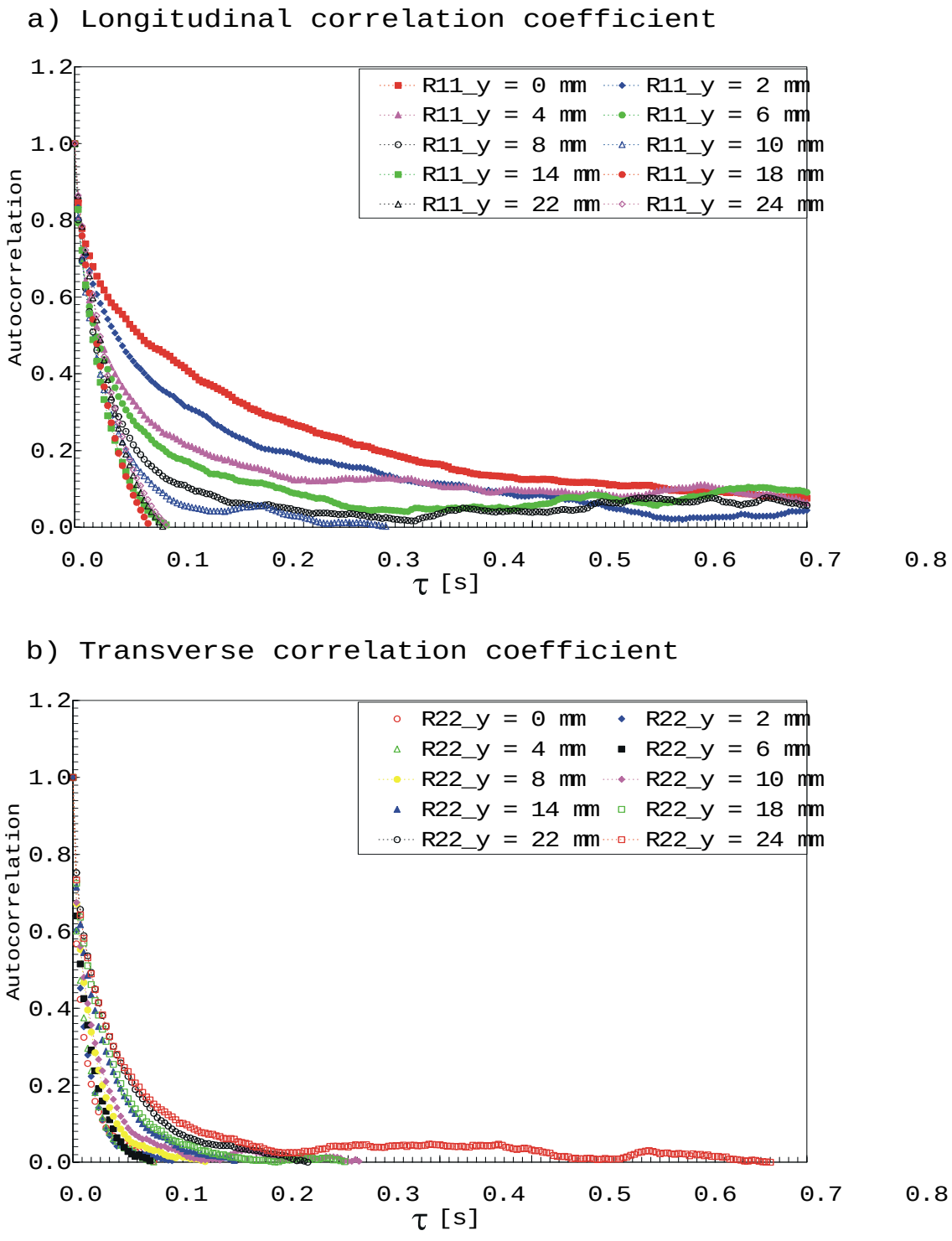

Figure 4.30: Longitudinal and transverse correlations across the axial jet at $1d$ upstream of the stagnation point ($L^* = 20$, Re $= 11000$)

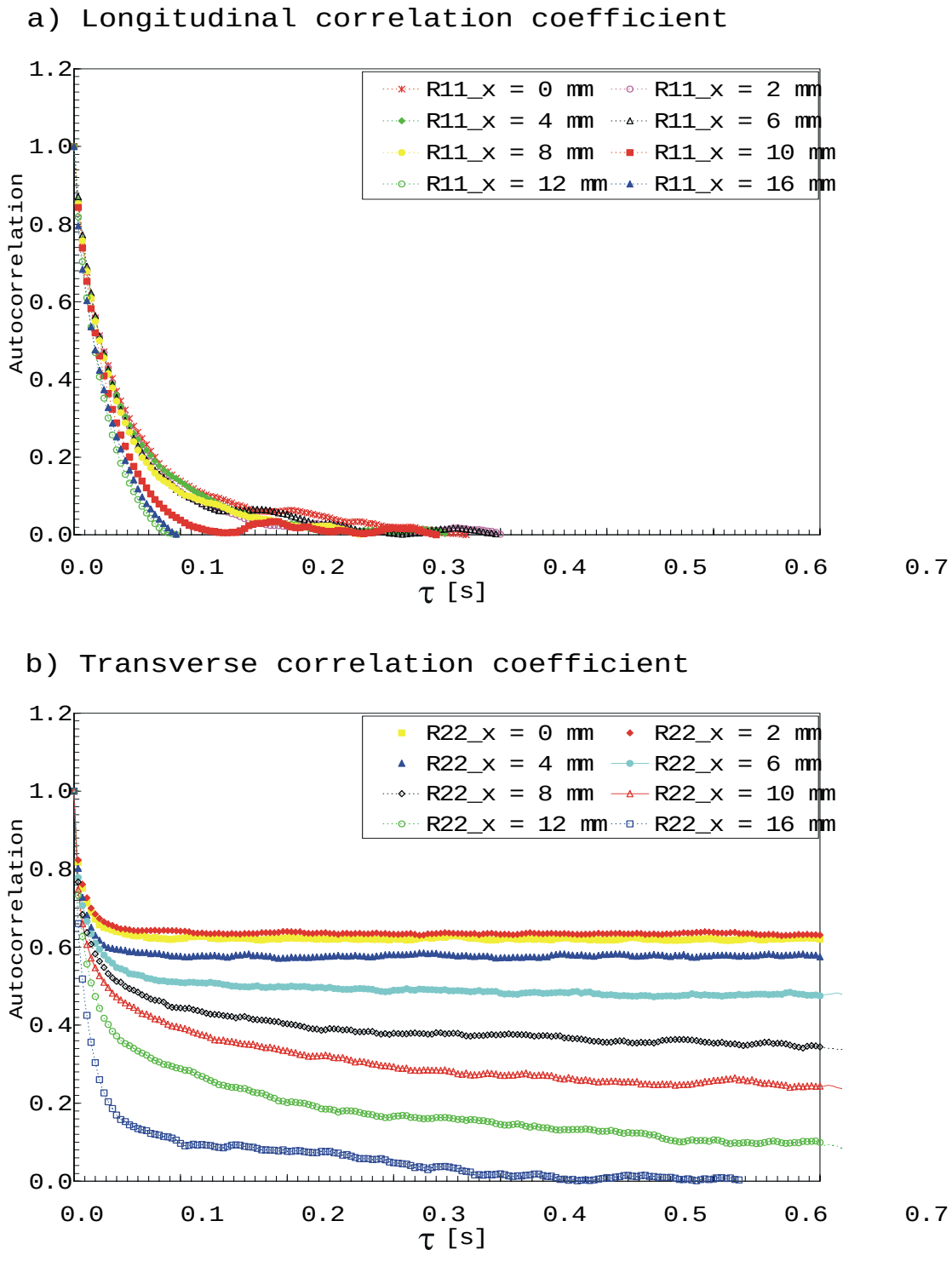

Figure 4.31: Longitudinal and transverse correlations across the radial jet at $1d$ downstream of the stagnation point ($L^* = 20$, Re $= 11000$)

a) Integral, micro and Kolmogorov time scales

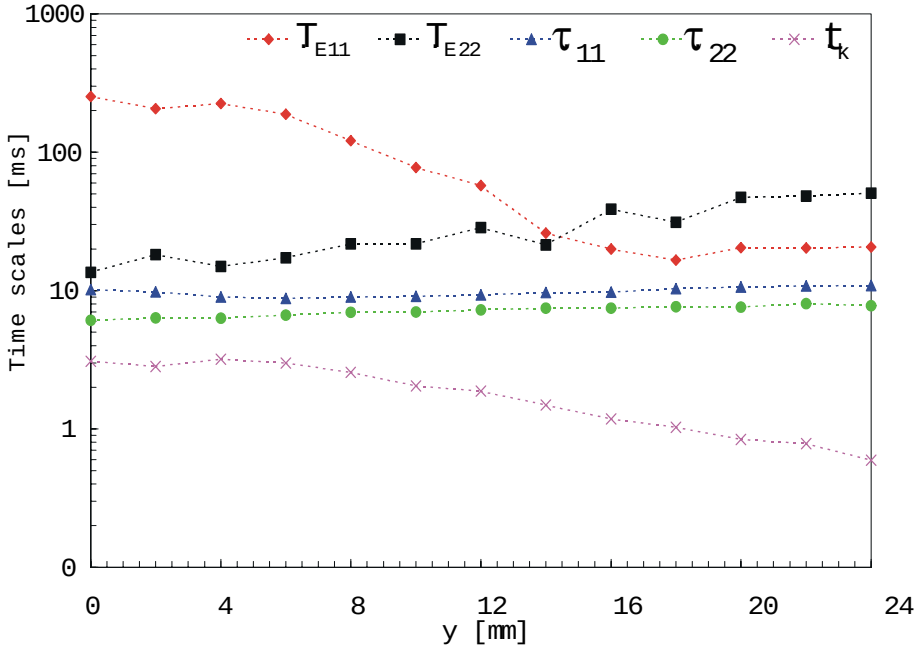

b) Integral, micro and Kolmogorov length scales

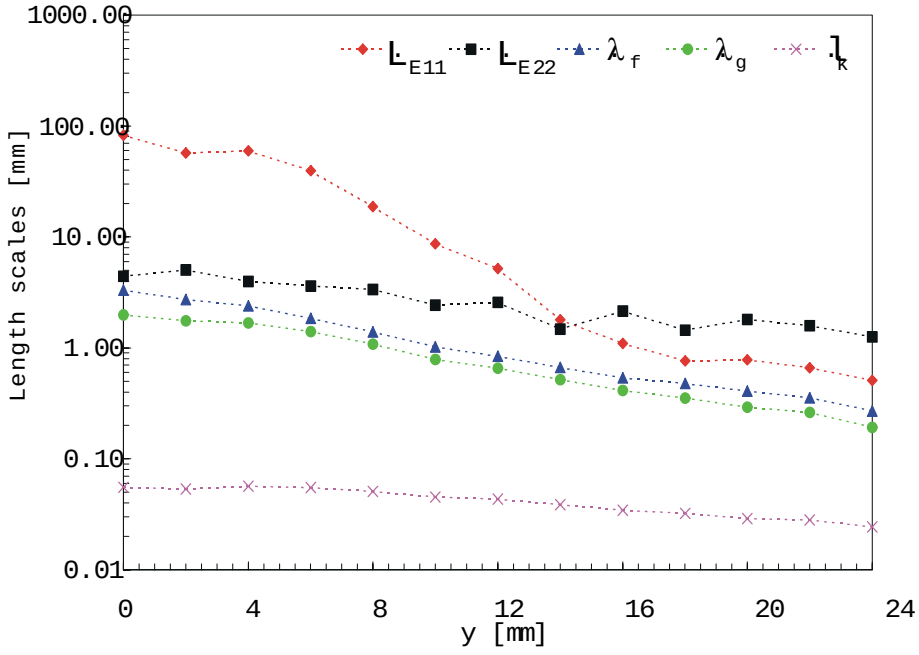

Figure 4.32: Distribution of longitudinal and transverse time and length scales across the axial jet at $1d$ upstream of stagnation point ($L^* = 20$, Re = 11000, - - - suggested trend for visual purposes only)

scales are driven by the dominant axial or radial velocity component within the impingement region. Reasonable Taylor microscales for time and length scales consistent with the most rapid changes that occur in the fluctuations of u and v or vice versa are found.

Plotted in Figures 4.32 a) and b), the integral time and length scales corresponding to locations $1d$ upstream of stagnation point across the axial jet present an interesting evolution. Whereas the longitudinal integral time scale is initially at least one order of magnitude greater than T_{22}, it continually decreases such that in the boundary layer region of the axial jet it becomes smaller than the transverse integral time scale. This is the influence of the strong entrainment in this region and its effect on the jet structure. Consequences of the entrainment are noticed in the variation of T_{22} which increases with increasing distance from jet centerline. Charts of the dominant length scale L_{11} and transverse integral scale L_{22} sustain this theory; beyond a certain y location where the flow structure is altered by the surrounding fluid entraining the jet boundary L_{22} overcomes L_{11}. Although L_{11} is seen to strongly depend on the transverse direction y, a large portion of the flow and turbulence structure is still dominated by the axial velocity component u. In general, due to the entrainment effect a relatively strong dependence with y is noticed at all length scale levels.

The validity of the isotropic turbulence and Taylor's " frozen hypothesis" assumptions at the impingement region boundaries in both axial and radial jets were examined. Results are summarized in Tables 4.5 and 4.6.

Table 4.5: Turbulence isotropy evaluation and related data at 1d upstream of stagnation point within the axial jet (L* = 20, Re = 11000)

$y\ [mm]$	$\overline{u'v'}_{LDA}\ [m^2/s^2]$	$\overline{u'v'}_{CFD}\ [m^2/s^2]$	λ_g/λ_f	$u_{rms}/\overline{u}$	$\mathrm{Re}_{\lambda_g LDA}$	Re_{tCFD}
0	$2.886E-04$	$-1.630E-04$	0.598	0.793	405	2152
2	$5.330E-04$	$1.592E+00$	0.646	0.896	345	2153
4	$3.248E-04$	$2.750E+00$	0.702	0.767	277	2156
6	$4.110E-04$	$3.315E+00$	0.758	0.841	205	2154
8	$2.623E-04$	$3.264E+00$	0.779	1.009	143	2130
10	$9.390E-05$	$2.722E+00$	0.769	1.261	95	2073
12	$1.801E-05$	$1.942E+00$	0.781	1.373	72	1979
14	$9.960E-05$	$1.120E+00$	0.775	1.761	57	1854
16	$2.350E-04$	$3.840E-01$	0.769	2.204	45	1710

The ratio λ_g/λ_f indicates that no location strictly meets the isotropic turbulence condition. However, the values are reasonable (within maximum 15 % difference) close to 0.707 so that we can assume to a good approximation that the isotropic turbulence supposition is valid for the axial jet flow structure at $1d$ upstream of the stagnation point. The excessively high level of turbulence intensity ($u_{rms}/\overline{u} \gg 0.1$) shown in Table 4.5 contradicts Taylor's frozen hypothesis with its inherent limitations for high intensity non-homogeneous turbulence. Although, the turbulent Reynolds number $\mathrm{Re}_{\lambda_g} > 100$ ensures an equilibrium range in the intermediate scales in the region close to the jet axis, the Re_{λ_g} obtained for the jet's boundary are lower than one would expect. These facts contradict the low level of turbulent kinetic energy production obtained for the measurement location situated on the jet axis and the isotropic turbulence assumption within the boundary region. However, the low Reynolds numbers are in accordance with the low level of turbulence production obtained (Figure 4.34) and the fact that at the edge of a free shear layer the entrainment process is nearly balanced by local diffusion. The

high level of Re_{λ_g} on the jet's axis is perhaps due to the " false" turbulence created by the impingement region oscillations.

As far as the time and length scale distributions at $1d$ downstream of the stagnation point across the radial jet are concerned, reasonable differences between the integral, micro and Kolmogorov scales are noticed in Figures 4.33 a), b). In general all time and length scales are more or less functions of y. One of the most important observations here is regarding the transverse integral time and length scales which overcome the longitudinal scales by at least an order of magnitude. This is explained by the fact that the transverse velocity has become the dominant direction of the flow and at this point there is a considerable discrepancy between the transverse and longitudinal velocity magnitudes. Although for most of the radial jet width the curves of L_{22} and L_{11} are found to follow the same trend, a change in the longitudinal integral length scale occurs towards the boundary layer of the jet signalizing the presence of weak entrainment.

Table 4.6: Turbulence isotropy evaluation and related data at 1d downstream of stagnation point within the radial jet (L* = 20, Re = 11000)

$y\ [mm]$	$\overline{u'v'}_{LDA}\ [m^2/s^2]$	$\overline{u'v'}_{CFD}\ [m^2/s^2]$	λ_g/λ_f	$u_{rms}/\overline{u}$	$\mathrm{Re}_{\lambda_g LDA}$	Re_{tCFD}
0	$3.546E-04$	$5.92E-02$	0.898	0.493	61	3514
2	$2.430E-05$	N/A	0.891	0.500	52	N/A
4	$6.993E-04$	$8.92E-02$	0.837	0.597	123	3028
6	$3.488E-03$	N/A	0.764	0.701	193	N/A
8	$4.132E-03$	$1.19E-01$	0.796	0.847	205	2342
10	$2.550E-03$	N/A	0.790	0.979	194	N/A
12	$3.001E-04$	$1.90E+00$	0.825	1.264	159	1981
14	$4.654E-07$	N/A	0.768	1.629	129	N/A
16	$1.863E-07$	$3.04E+00$	0.776	2.118	121	1866

Contrary to the axial jet behavior, locations situated closer to the radial jet's boundary reasonably meet the isotropic turbulence condition $\lambda_g/\lambda_f = 0.707$. The fact that the ratio λ_g/λ_f takes smaller values for the extreme locations indicates that these locations lie on or are close to the interface surface of the outer flow and jet where entrainment exists. An unexpected low turbulent Reynolds number is obtained for the locations situated on the radial jet axis while equilibrium in the intermediate scales is ensured for locations closer to the jet's boundary. Re_{λ_g} values are in good agreement with k production on the jet centerline whereas disagreement is found on the jet boundary. Furthermore, the excessively high level of turbulence intensity ($u_{rms}/\overline{u} \gg 0.1$) shown in Table 4.6 contradicts Taylor's frozen hypothesis with its inherent limitations for high intensity non-homogeneous turbulence.

Since the isotropic turbulence assumption constitutes the foundation of the $k-\varepsilon$ turbulence model it is not surprising that the CFD calculated turbulent Reynolds number satisfies the isotropy requirements for all locations across the axial or the radial jet.

All the above contradictions regarding either the axial or the radial jet are perhaps explained by the highly unstable and unsteady character of the impingement region flow.

The velocity gradients used to evaluate the production of k in Figures 4.34 a) and 4.35 a) are calculated by fitting an exponential decay function to the corresponding mean velocity profile (Figure 4.34 b or Figure 4.35 b). The proposed function has the following form

a) Integral, micro and Kolmogorov time scales

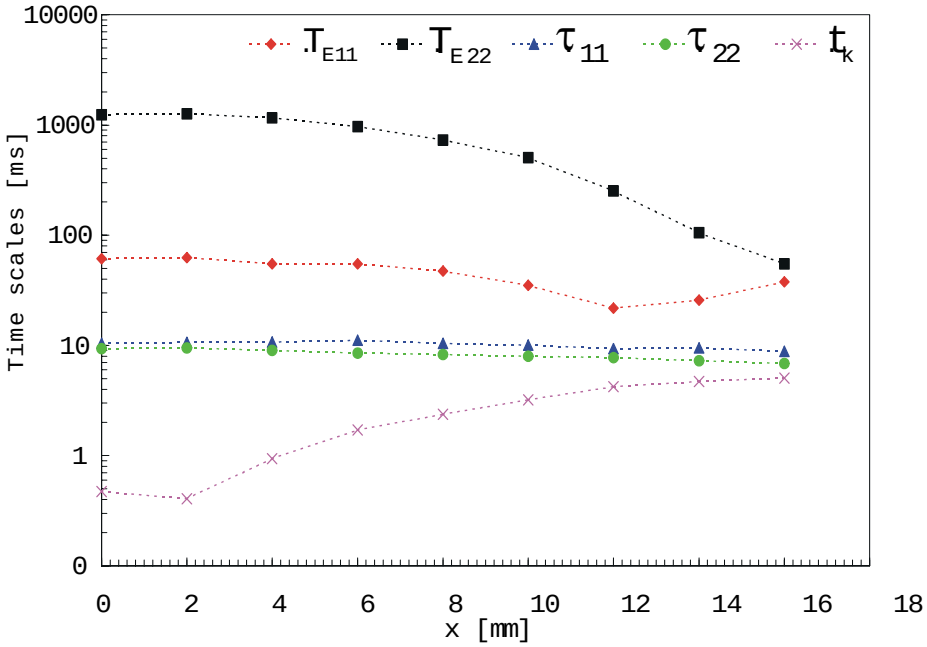

b) Integral, micro and Kolmogorov length scales

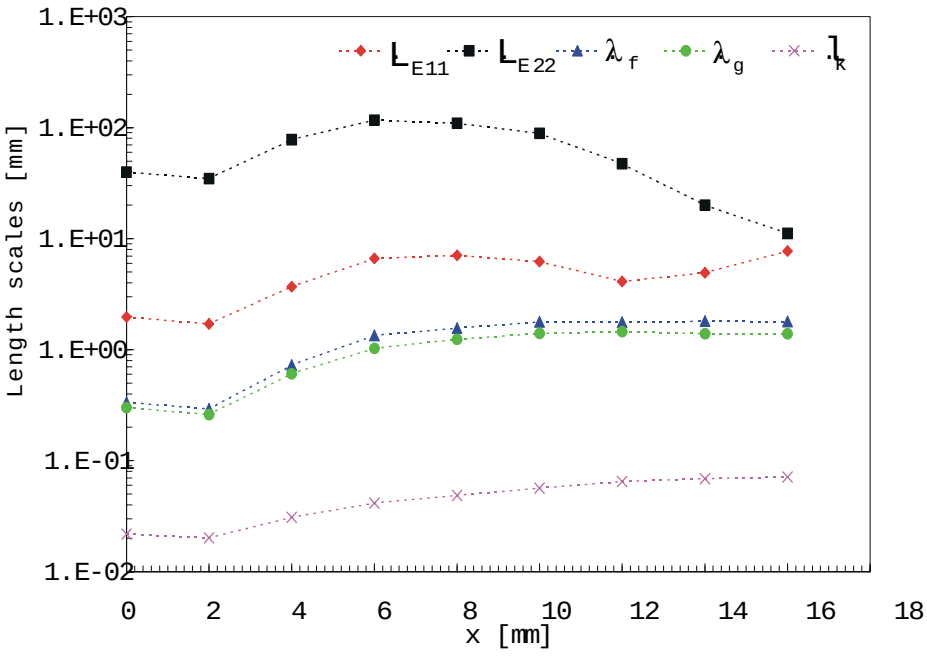

Figure 4.33: Distribution of longitudinal and transverse time and length scales across the radial jet at $1d$ downstream of the stagnation point ($L^* = 20$, Re $= 11000$, - - - suggested trend for visual purposes only)

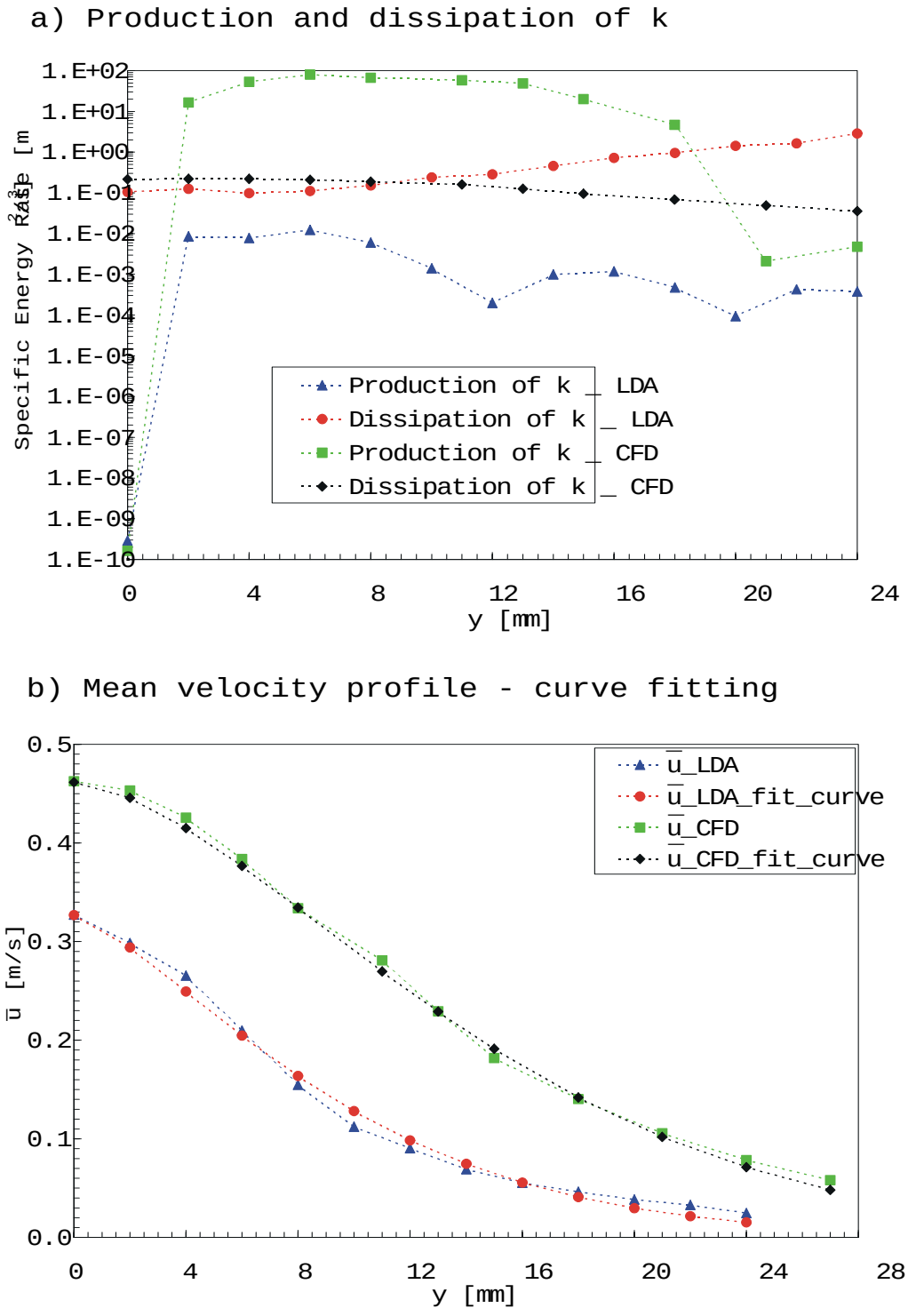

Figure 4.34: Variation of production and dissipation of turbulent kinetic energy across the axial jet at $1d$ downstream of stagnation plane ($L^* = 20$, Re $= 11000$, - - - suggested trend for visual purposes only)

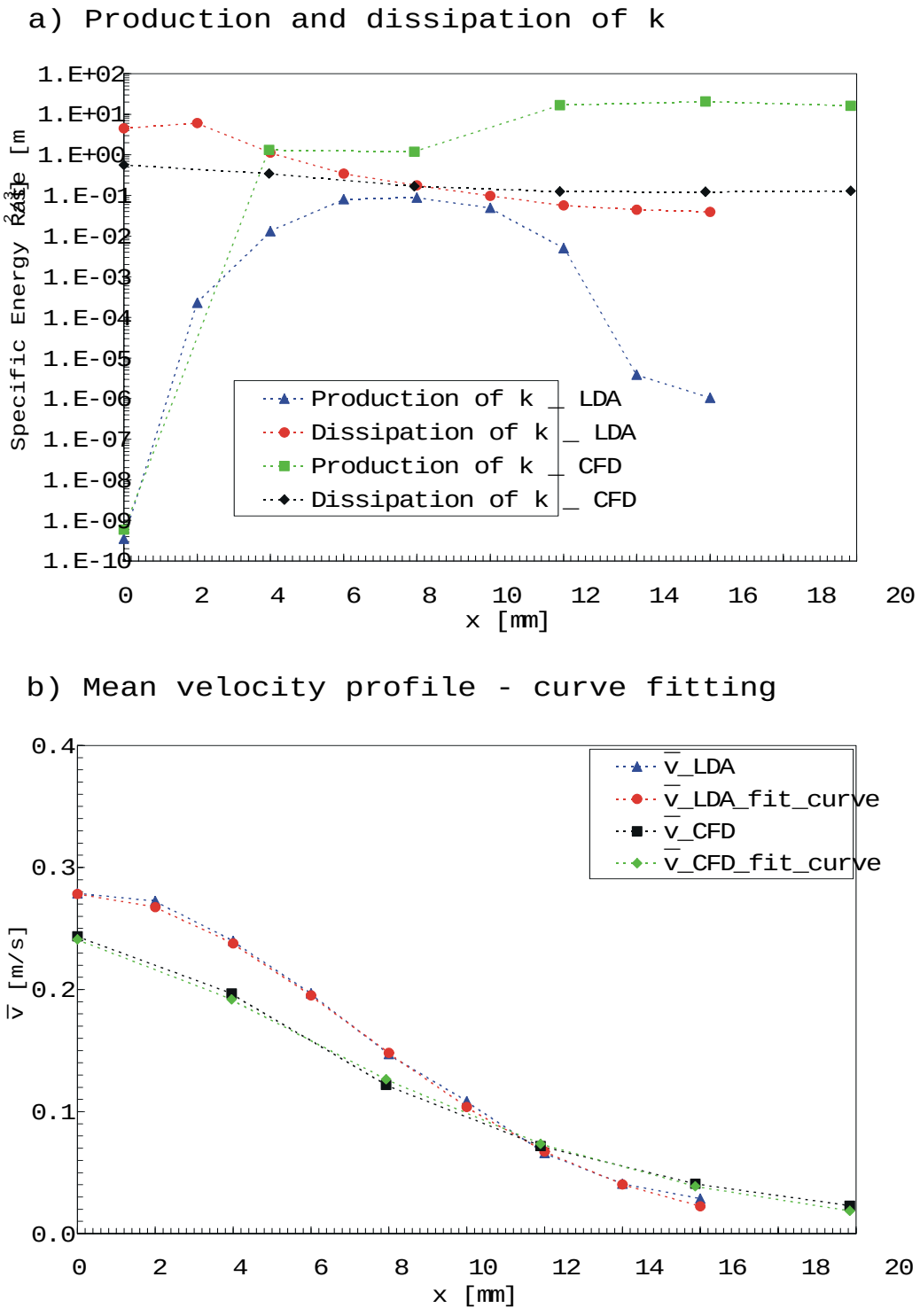

Figure 4.35: Variation of production and dissipation of turbulent kinetic energy across the radial jet at $1d$ downstream of stagnation plane ($L^* = 20$, Re $= 11000$, - - - suggested trend for visual purposes only)

$$\overline{u}\,(y) = U_{\max} A \exp\left[-(\ln B)\left(\frac{y}{d}\right)^{C}\right] \tag{4.4}$$

where the constants A and B were determined in a spreadsheet through manual manipulation until the function fit the calculated mean velocity profile in a good approximation (maximum $2-3$ % deviation) and $U_{\max}$ is the respective centerline velocity. The sets of fitting curve parameters corresponding to experimental and CFD velocity profiles are displayed in Table 4.7.

Table 4.7: Mean velocity profile - curve fitting parameters (L* = 20, Re = 11000)

Parameter	A	B	C	$U_{\max}$ $[m/s]$
LDA axial jet	$9.98E-01$	4.9	2	0.3272
CFD axial jet	$9.90E-01$	3.7	1.5	0.4624
LDA radial jet	$9.99E-01$	3.65	1.355	0.2788
CFD radial jet	$9.99E-01$	1.965	1.6	0.2436

Regardless of the flow direction, significant discrepancies between the experimental and CFD mean velocity profiles are generally observed. Exception makes the flow corresponding to the region $x \in (2,8)$ mm where a difference of about one order of magnitude between the two predictions with regard to the turbulent kinetic energy production is observed. It is the gradient diffusion hypothesis that is mainly responsible for these differences. As normal Reynolds stresses are defined by this theory, through their sign change (i.e. they are found to take either positive or negative values) they do favor increasing of the mean velocity of the dominant flow direction.

As expected, for all cases the location of largest production corresponds to a region in which the most abrupt mean flow gradients occur (closer to the jet axis ($y \in (2,8)$ mm for the axial jet due to the developing stage of the flow field and toward the jet boundary, i.e. $x \in (4,12)$ mm, for the radial jet since the investigated section of the flow is only a nozzle diameter away from the stagnation point, i.e. the point of the radial jet creation). Although the dissipation is roughly constant relative to production, we can observe that maximum ε do not correspond to maximum P for any of the experimental cases, axial jet section (Figure 4.34 a) or radial jet section (Figure 4.35 a). Instead the CFD generated ε and P have correspondent maxima for the axial jet but do not satisfy this condition for the radial jet. The experimental and CFD turbulence kinetic energy dissipations show similar magnitudes excepting the outer flow ($y > 13$ mm) for the axial jet and the inner flow (close to the jet centerline, $y < 3$ mm) for the radial jet. Opposite trends between the experimental and computational ε distributions are noticed in the axial jet case, whereas the same decreasing tendency with increasing y distance are found in the radial jet case (i.e. ε decreases as y increases). LDA data provides a maximum dissipation rate toward the boundary layer while a maximum dissipation rate in the vicinity of the axis is predicted by numerical data for the axial jet. In turn, both methods (experimental and numerical) predict maximum ε magnitudes in the proximity of radial jet centerline.

In both cases studied (axial and radial jet) the location of the largest dominant length scales (i.e. longitudinal or transverse) coincide with regions of maximum turbulent kinetic energy production rates ($2 < y < 8$ for the axial jet case and $5 < x < 11$ for the radial jet). Although the turbulence kinetic energy destruction and production rates have generally divergent trends, ε and P magnitudes are close (the difference magnitude is about 10^{-1} for the axial jet and even smaller for the radial jet). These conditions imply that in both cases the flow tends to approach turbulent equilibrium (points close to the axial jet centerline, i.e. $2 < y < 8$ for the axial jet case, and the boundary regions in the radial jet $5 < x < 11$). Based on these

affirmations we can conclude that the two jets proceed toward the fully turbulent stage of their development.

As far as CFD data is concerned, the turbulent equilibrium stage is approached for $5 < x < 8$ in the case of the radial jet, but never totally achieved. In general the production overpowers turbulent kinetic energy destruction for both cases. This arises mainly from the use of the gradient diffusion hypothesis to represent the normal Reynolds stresses. For a 2D case of an impinging jet on a flat plate Launder et. al. [11] demonstrated that close to the stagnation point the production of turbulent kinetic energy takes the form:

$$P \approx 2\nu_t \left(\frac{\partial \overline{u}}{\partial y}\right)^2 \tag{4.5}$$

where $\nu_t = C_\mu \frac{k^2}{\varepsilon}$ is the turbulent eddy viscosity as used in $k - \varepsilon$ turbulence model. This is explained through the fact that the mean longitudinal velocity decreases drastically as the stagnation point is approached and therefore $\partial\overline{u}/\partial y$ become very large. Consequently $(\partial\overline{u}/\partial y)^2$ becomes the dominant term in P and the k production increases as the stagnation point is approached. These observations along with the inability of the $k - \varepsilon$ turbulence model to handle anisotropic free shear boundary layer flows as well as the effect of turbulence on the streamline curvature may explain the above anomalies.

4.4 Probability Density Distribution

In a fluid dynamics experimental study the probability density function (PDF) could provide valuable information regarding the distribution of a specific quantity amplitude at a certain measurement point. Although researchers have mostly confined PDF usage to instantaneous velocity data and fluctuating flows that are statistically steady, its application is unlimited. Thus, based on a PDF study corrections can be applied to a certain artificial phenomenon (natural phenomena are difficult to adjust) such that its characteristic parameters will finally exhibit desirable amplitudes only.

In an attempt to cover a large spectrum of probability density of instantaneous velocities involved in the present study a few key examples of PDF distributions will be presented. They mainly describe the turbulent opposed impinging jets flow behavior corresponding to the configuration $L^* = 20$, Re = 11000 using LDA velocity measurements. Thus, the PDF distributions plotted in Figure 4.36 describe the velocity near the nozzle, within the impingement region on the axial and radial jet axes and at the stagnation point.

A close examination of these plots would reveal sufficient information in order to evaluate the mean dominant velocity of the flow. It is well known [21], [49] that the probability density of velocity amplitudes for isotropic turbulence is Gaussian in shape. Out of the four distributions displayed in Figure 4.36 it is only the graph corresponding to the flow near the nozzle (Figure 4.36 a) that satisfy this theory to a good approximation. Although the PDF charts associated with flows at $x/d = 1$ upstream of the stagnation point on axial jet axis and downstream of the stagnation point on radial jet axis (Figure 4.36 b, d) present a Gaussian like profile, they exhibit numerous deviations from an ideal Gaussian distribution. As a consequence a broader, non-uniform and non-centered instantaneous velocity range is observed. These features suggest a transverse spreading of the jet with increasing axial or radial distance combined with the unstable and unsteady character of the local flow field. Of course, on average the two PDF distributions are expected to exhibit profiles closer to the ideal Gaussian distribution.

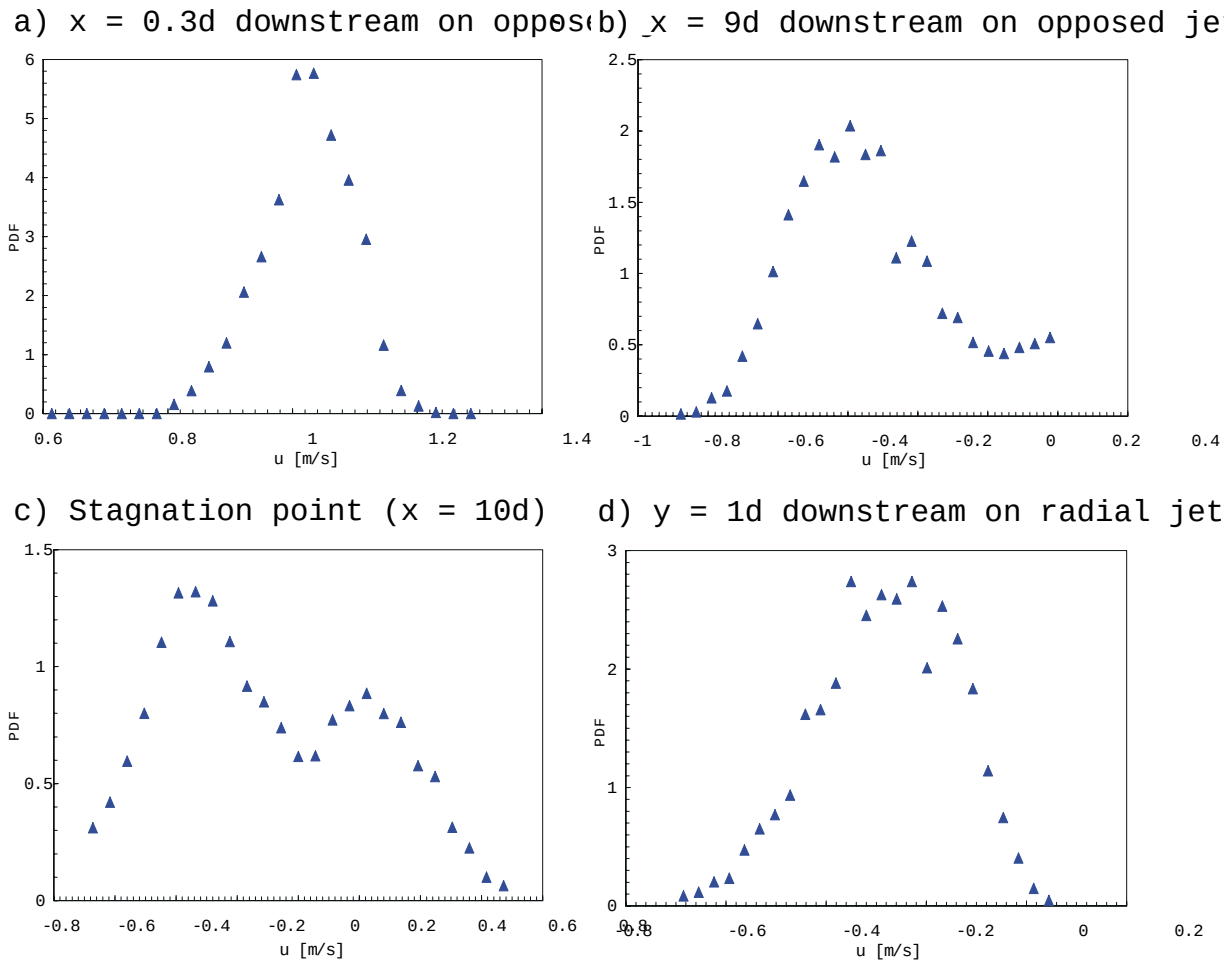

Figure 4.36: Probability density distribution for instantaneous velocity at four different locations in the opposed impinging jets flow field ($L^* = 20$, Re = 11000)

The irregular and wide probability density distribution at the stagnation point in Figure 4.36 c) confirms and strengths these conclusions. At this point, the bimodal PDF distribution suggests the existence of flow field oscillations through the bimodal ± velocity nature (i.e. flow in opposite directions; positive and negative velocities on one and the other sides of the stagnation point).

4.5 Similarity Analysis

As shown in subsection 4.2.2 both jets issue from the nozzles with a fully developed turbulent velocity profile. Also it was noticed that up to the impingement region (i.e. up to the radial jet development) the magnitude of mean longitudinal velocity component $\overline{u}$ of the two opposed jets is significantly larger than the mean transverse velocity $\overline{v}$. Considering a dynamically similar behavior of the two initial jets with respect to the impingement region, a single jet development is now discussed. Additionally, the radial jet structure created as a consequence of the jet to jet impingement is also discussed. In an attempt to evaluate the Reynolds number effects on the opposed impinging jets flow structure for the case $L^* = 20$, in previous work [44] it was concluded that as Re number increases the relative turbulence level decreases for both impinging jets and the radial jet as well. Longitudinal velocity fields corresponding to Re = 11000 alone were found to develop into a self-preserving state. In the case studied, turbulence intensity fields never become self-similar for any of the four Reynolds numbers considered. Thus, unlike the round free jet that maintains a self preserving shape of velocity profiles at about 20 diameters downstream regardless of Re [55], the opposed impinging jets become self similar at just 8 diameters downstream; this confirmed the faster fully turbulent development of the impinging jets and the role that the adverse pressure gradient within the impingement region plays in the mixing dynamics.

As a consequence, in order to avoid repetition and for efficiency in this section, the influence of nozzle to nozzle separation distance L^* is mainly discussed while the Re number effect is covered by considering the limit cases of Re = $\{1500, 11000\}$. In this manner, Figures 4.37 a), b) provide information regarding the distribution of mean longitudinal velocity across one of the two axial jets. The transverse coordinate y was normalized by the half width of the jet, b, corresponding to the location of half of the maximum velocity within a certain measurement section while mean longitudinal velocity was normalized by the maximum mean velocity within that section.

Indeed, visual inspection of the plots in Figures 4.37 a) and b) showed that self-similarity in the mean longitudinal velocity profile occurs by $x/d = 8$ for Re = 11000 and $L^* = 20$. Furthermore, good agreement is found between numerical and experimental data in all cases. For nozzle to nozzle separations smaller than $20d$ and Reynolds numbers below 11000 these profiles do not exhibit self-similarity in the range of x/d studied. However, regardless of the Re number or L^* values, an almost compact distribution of all data points about the Reichardt distribution of momentum in a plane or axisymmetric free jet [39] is noticed. In our case the Reichardt Gaussian distribution over the width of the jet can be represented by the formula:

$$\overline{u} = \overline{u}_m \exp\left[-A\,(y/b)^2\right] \tag{4.6}$$

where $\overline{u}_m$ is the maximum mean longitudinal velocity in a certain measurement set across the jet (for stationary flow it coincides with the mean longitudinal velocity on the jet axis) and $A = \ln 2$ is a constant largely unaffected by the Reynolds number orL^*.

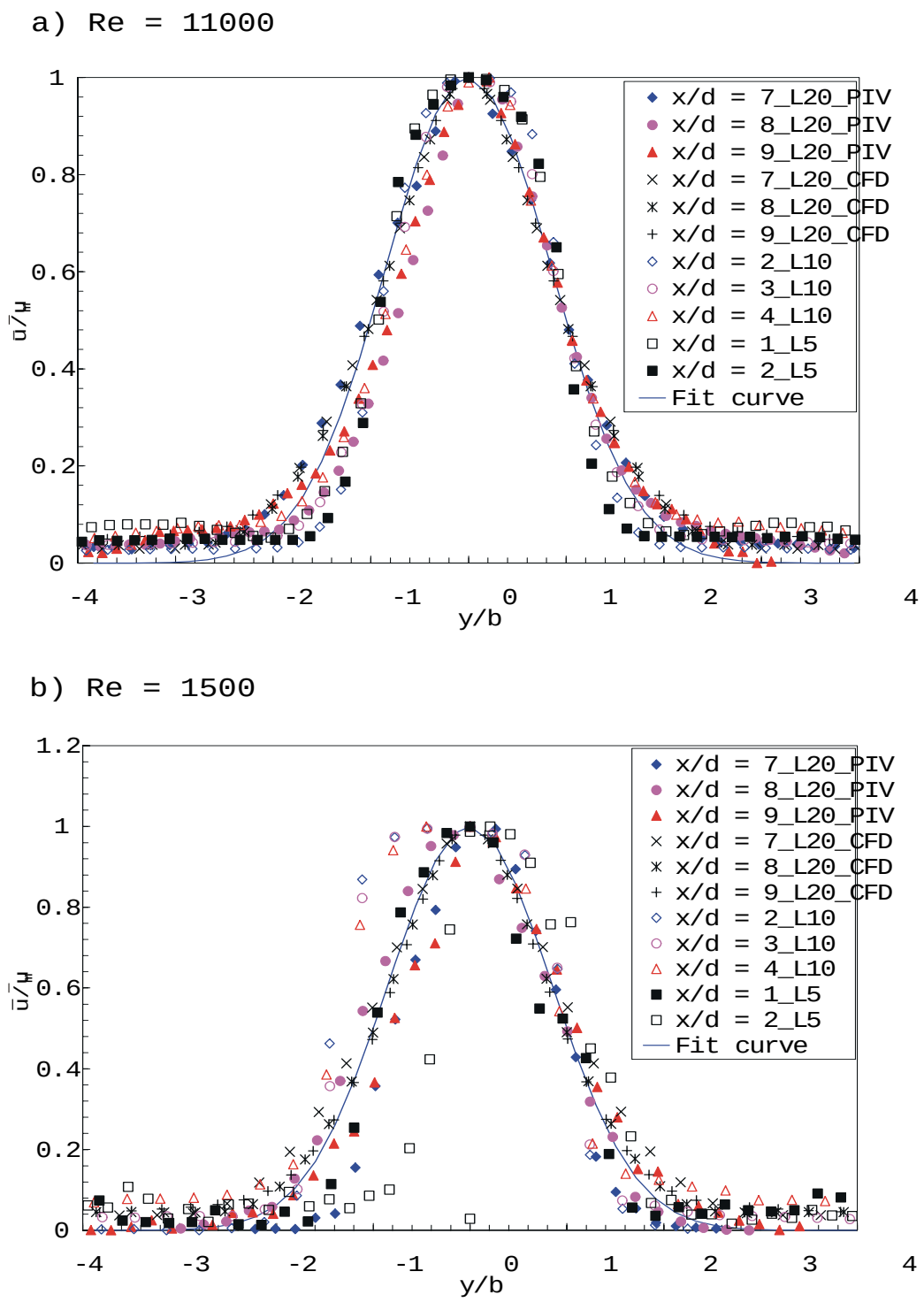

Figure 4.37: Axial jet - mean longitudinal velocity distributions. PIV and CFD data - verifying the approach to self-similarity (Fit curve = Reichardt momentum distribution in a free jet)

It must be mentioned that the self-preserving behavior was evaluated with regard to plot to plot match and not in comparison to Reichardt distribution in a free jet. Reichardt momentum distribution in a free jet does suggest a general velocity profile trend in the opposed impinging jets case, but matching this curve is not a self-similarity requirement).

It is perhaps the presence of the adverse pressure gradient within the impingement region that forces the development of the impinging jets such that the flow field reaches a fully turbulent stage earlier than expected.

Existing literature [55] mentions no certain range of x/d or Re numbers for which the turbulent quantities would present self-preserving behavior as far as the free jet flow is concerned (plane or round). As Figures 4.38 a) and b) show, it is evident that the relative longitudinal turbulence intensity profiles do not exhibit self-similarity for the range of x/d or Re numbers and L^* studied. While the relative turbulence intensity magnitudes toward the jet boundary layer were usually about $20-30$ %, maximum values are obtained within the region surrounding the centerline of the jet. At the same time unexpected high turbulence intensities (between 40 % and 80 %) were found as Re and L^* decrease and even on the jet axis itself. Again, it is perhaps the adverse pressure gradient created at the point of impact of the two jets which is responsible for this anomaly.

Illustrated in Figures 4.39 a) and b), downstream of the stagnation point in the radial direction, the flow begins to develop into the distinctive Gaussian type shape. Although for Re = 11000 and independent of L^* the mean radial velocity profiles seem to fairly well match the Reichardt distribution, none of them exhibit completely self-similar behavior for any of the control parameters (i.e. x/d, L^*, or Re =11000). The jet region, within $1d$ about the radial jet axis, is seen to display self-similarity in the mean radial velocity $\overline{v}$ for any of the control parameters (i.e. x/d, Re or L^*). In the CFD data, self-preserving behavior in the boundary region of the radial jet (i.e. the region outside of $1.5d$ to $2d$ away from the radial jet axis) occurs by $x/d = 2$ for Re = 11000 and $L^* = 10$ only. Since the boundary layer of the radial jet is the region where the entrainment occurs, a self-similar development in this region could signify dynamic turbulent equilibrium for Re = 11000 and $L^* = 10$. Furthermore, self-similarity of the turbulent radial intensities occurs by $x/d = 1$ for $L^* = 10$ and by $x/d = 2$ for $L^* = 20$ for the same region (boundary layer of the radial jet) and Reynolds number. This fact confirms the turbulent equilibrium theory in this region and so the early development to a fully turbulent flow field in the radial jet resulted as following the impingement of two turbulent opposed jets (in the case Re = 11000 and $L^* = 10$). For a sufficient small Re number (Re < 4500) the radial jet profile is considerably altered. This can be explained by the high unstable and unsteady character the flow manifests at these conditions. Given the always symmetric distributions CFD provides, half of the radial velocity profile has been plotted only. CFD results match the experimental data corresponding to the top part of the velocity profile for Re = 11000 and $x/d = 1$ surprisingly well while the base part of this distribution is overpredicted. No agreement is recorded in the cases associated with Re = 1500; given previous discussion, this is not surprising

It can be observed that both mean radial velocity and relative turbulent radial intensity exhibit maximum values in the vicinity of or on the radial jet axis itself. On average the centerline of radial jet becomes the line of vertical symmetry for the opposed impinging jets, which coincides with the average impinging surface location. Whereas for Re = 11000 the highest relative turbulent intensity levels (about $60-80$ %) are concentrated about the centerline of the radial jet (Figure 4.40 a), a relatively more uniform turbulent intensity (about 20 %) toward the lower limit of the Re numbers range is observed (Figure 4.40 b). For the control parameters considered in this study both the mean radial velocity profiles and turbulent radial intensity distributions become partially self-similar.

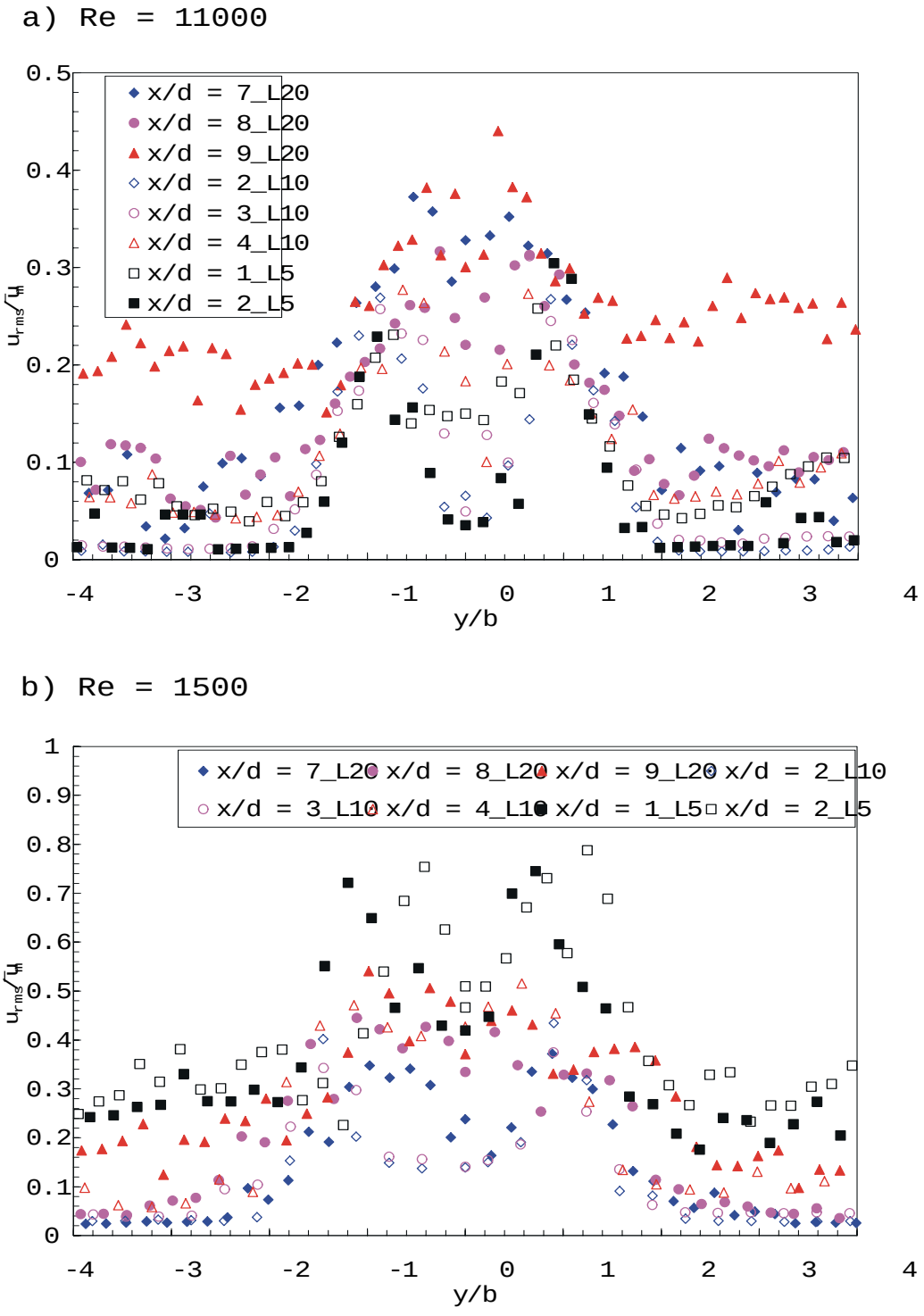

Figure 4.38: Axial jet - longitudinal turbulent intensity profiles. PIV data - illustrating the approach to self-similarity.

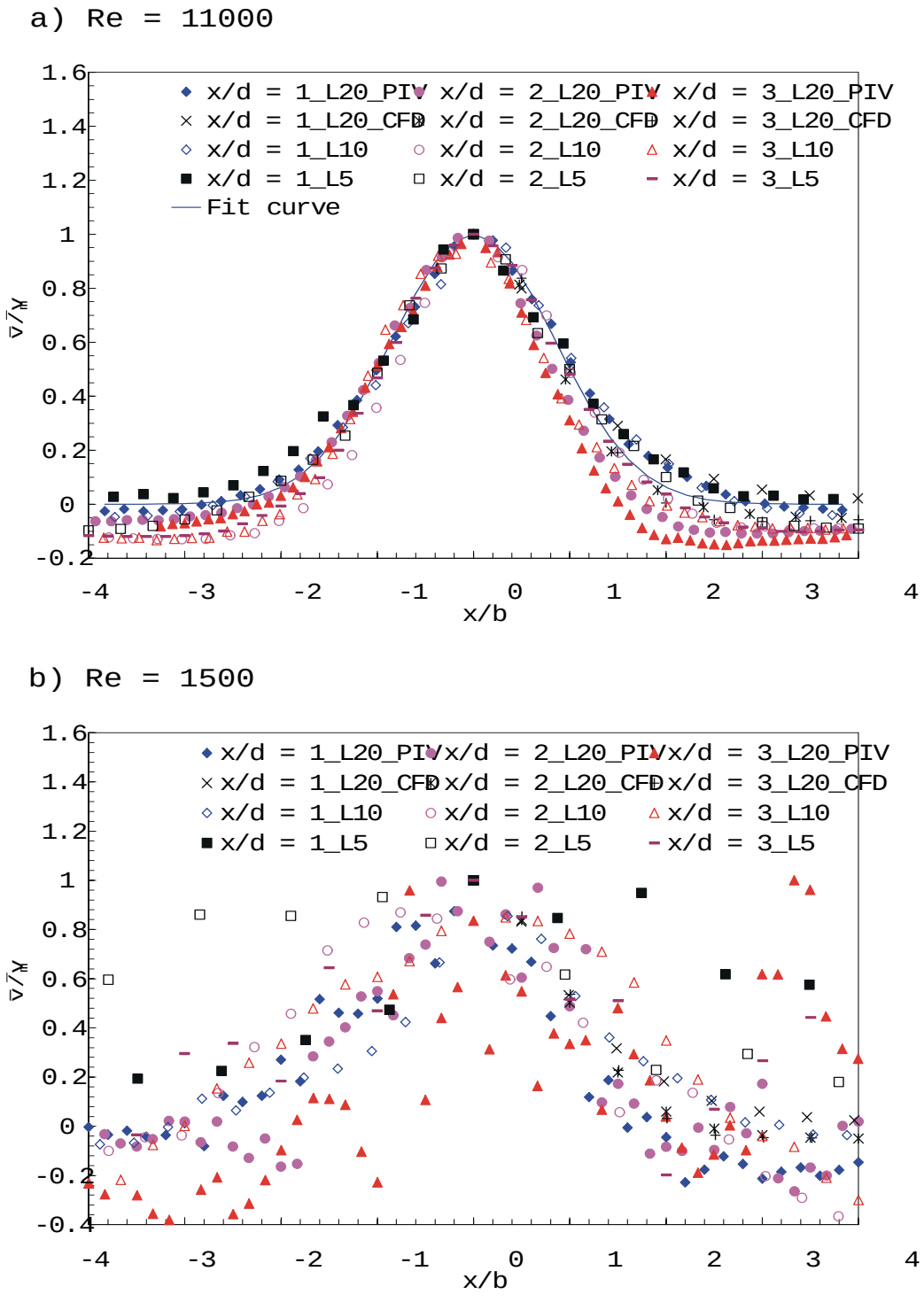

Figure 4.39: Radial jet - mean radial velocity distributions. PIV and CFD data - verifying the approach to self-similarity.

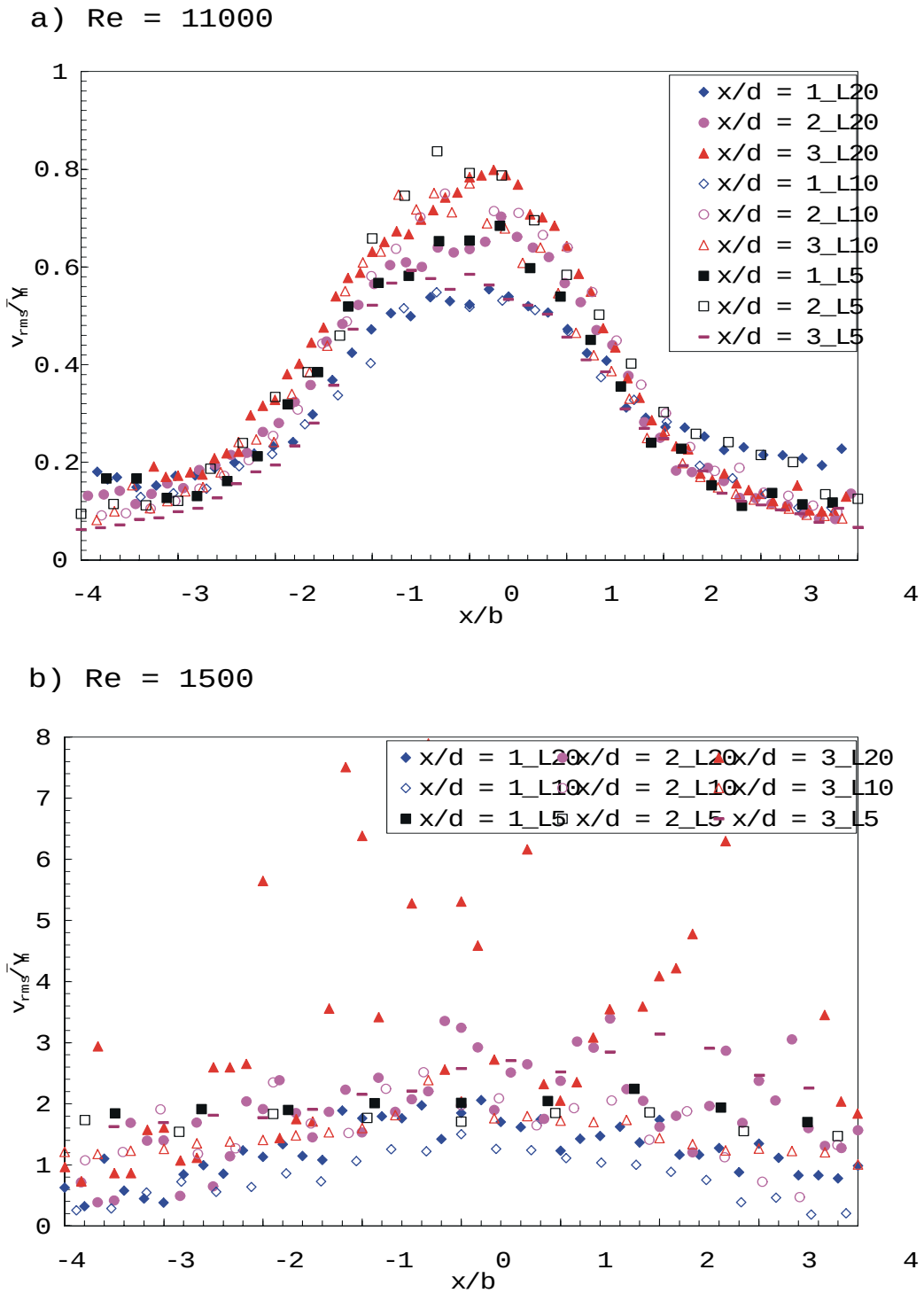

Figure 4.40: Radial jet - turbulent radial intensity distributions. PIV data - verifying the approach to self-similarity.

In general, the jet growth rate is evaluated by the change in the half with of the jet, b. In fact, this represents the distance from the jet axis to the point where the velocity becomes half of its maximum value within the respective cross section. Thus, data obtained from similarity analysis was used to determine the law of jet growth variation associated with each Reynolds number and nozzle to nozzle separation distance.

As illustrated in Figures 4.41 a), b), at least for the initial region (i.e. within $5d$ downstream of the nozzle for the axial jet and $5d$ downstream of the stagnation point for the radial jet) it was found that all the jets satisfy linear laws of growth, similar to those associated with free jet flows [31]. The general law of relative growth ($\frac{b}{d}$) variation as a function of the jet relative advancement ($\frac{x}{d}$) could be represented by

$$\frac{b}{d} = a_1 \frac{x}{d} + a_2 \tag{4.7}$$

where a_1 is the slope of the line and a_2 is an arbitrary constant. The values for a_1 and a_2 corresponding to both axial and radial jets are displayed in Table 4.8 and Table 4.9 respectively.

Table 4.8: Axial jet - Parameters of the growth rate variation law

		Re = 11000			Re = 1500		
Parameter		$L^* = 20$	$L^* = 10$	$L^* = 5$	$L^* = 20$	$L^* = 10$	$L^* = 5$
PIV	a_1	0.097	0.0055	0.010	0.003	0.002	0.054
	a_2	-0.078	0.527	0.457	0.518	0.351	0.305
CFD	a_1	0.126	N/A	N/A	0.177	N/A	N/A
	a_2	-0.193	N/A	N/A	-0.593	N/A	N/A

An unexpected variation of the experimental axial jet growth rate is shown in Figure 4.41 a. As Reynolds number increases the growth rate increases such that the maximum jet width would be achieved for Re = 11000 and $L^* = 20$; therefore the jet spreads out faster when Re increases. No additional benefit is seen when the nozzle to nozzle separation is increased. As expected for a constant Re, the growth rate increases as L^* increases. Literature describing free plane turbulent jet behavior shows the existence of a " natural" variation of jet growth with respect to Re variation. For example Otugen [31] determined that the value of a_1 decreases with increasing Re number. For a free plane turbulent jet he found $a_1 = 0.179$ for Re = 1000 and $a_1 = 0.098$ for Re = 6000. Instead, a contrary variation of a_1 was determined for the present flow (see Table 4.8). In this manner a_1 increased from 0.003 corresponding to Re = 1500 to the value 0.097 for Re = 11000. Interestingly, this last value almost coincides with Otugen's value for the free plane jet and Re = 6000. In conclusion, for the two jets initially separated by a distance $L = 20d$ and placed in a dynamic impingement configuration to reach a certain development stage, twice the momentum a free planar jet needs to reach the same growth rate is required. Furthermore, this distinctive evolution is amplified and maintained by the same pattern of the jet's growing rate with increasing separation L^* (i.e. as L^* increases the jet's growth rate increases). The explanation of such attitude may lie in the obstacle the axial jets meet through the adverse pressure gradient within the impact zone which forces the jet in a radial direction.

A similar kind of unexpected behavior is exhibited by the radial jet created when the two opposed jets impinge on each other. The values of a_1 corresponding to the radial jet are provided in Table 4.9.

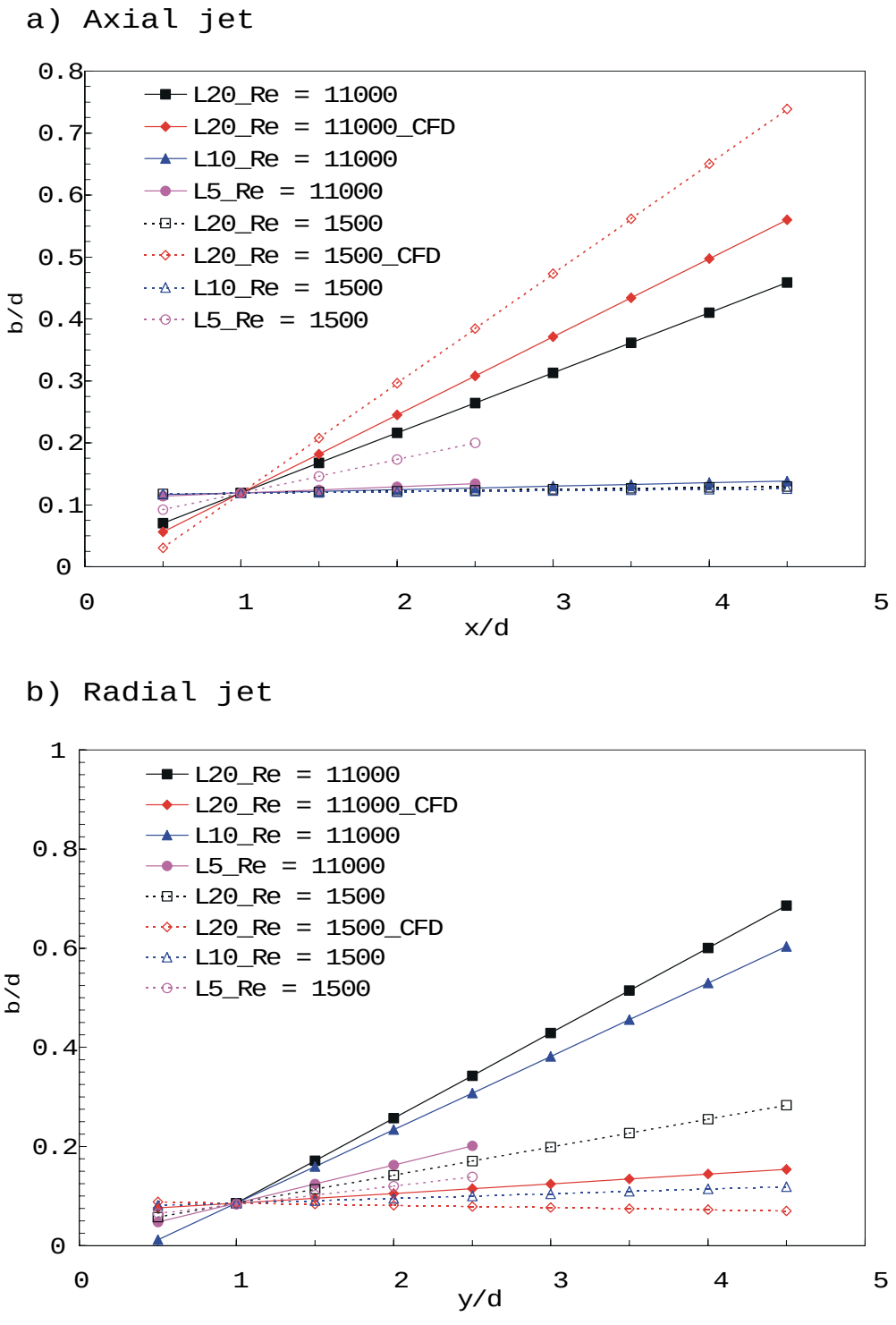

Figure 4.41: The effect of Reynolds number and nozzle to nozzle separation L^* on the growth rate of the jet (PIV and CFD data; - - - suggested trend for visual purposes only)

As far as the CFD solution is concerned, it predicts the evolution of a free jet flow but with different growth rates.

The entire evolution of the flow field generated by two opposed impinging jets is however consistent with the information provided from the flow visualization images presented and discussed at the beginning of this Chapter.

Table 4.9: Radial jet - Parameters of the growth rate variation law

		Re = 11000			Re = 1500		
Parameter		$L^* = 20$	$L^* = 10$	$L^* = 5$	$L^* = 20$	$L^* = 10$	$L^* = 5$
PIV	a_1	0.172	0.148	0.077	0.057	0.010	0.037
	a_2	-0.655	0.0403	0.167	0.187	0.319	0.046
CFD	a_1	0.020	N/A	N/A	-0.0045	N/A	N/A
	a_2	0.492	N/A	N/A	0.662	N/A	N/A

Chapter 5

Conclusions and Recommendations

5.1 Conclusions

In this research several experimental and computational techniques have been employed in an attempt to clarify some of the fundamental aspects of the complex flow created in the impingement region of two turbulent opposed jets. The study was performed by combining qualitative examination of the flow through visualization, with a classical analysis of measured and computed mean and turbulent velocity data. Various differences in flow and geometry configurations make direct comparisons between the results of this study and those provided by previous research (see Chapter 1) in this area impossible. The characteristics of the flow field generated by the impingement of two turbulent opposed jets as extracted from flow visualization data are given below.

- In principle, based on flow visualization considerations, the mechanism that governs the jet to jet interaction is observed to depend on the following parameters: nozzle to nozzle separation L^*, magnitude of Re number, fluctuations of the flow rate feeding the two nozzles and induced vibrations of any kind.
- In general, for all Re numbers and geometrical configurations examined the flow visualization study showed the formation of a composite flow field featured by the following distinct regions: a potential core, a developing jet region ("free jet region"), an impingement region and a free radial jet region. Further flow visualization investigations performed at limits of geometry and flow rate revealed that two identical opposed jets cease to impinge on each other for $L^* = 5$ and $\mathrm{Re} < 150$ while no deviation of the jets is observed for a high Reynolds number flow ($\mathrm{Re} = 142000$) and larger nozzle to nozzle spacing ($L^* = 20$), i.e. the impinging behavior is conserved. Therefore, the structure of the flow field is observed to be independent of Re number and nozzle to nozzle spacing for the range of $\mathrm{Re} \in [1500, 11000]$ and $L^* \in [5, 20]$.

- Both flow visualization and mean velocity vector plots illustrate no recirculation phenomena within the impingement region surroundings or in the flow fields close to the jets. However, the instantaneous flow field containing the impingement zone and a relatively large area surrounding it, manifested a significant alteration. Flow visualization images and PIV instantaneous vector plots demonstrated that the instantaneous flow field generated by the impingement of two coaxial opposed jets is not axisymmetric, nor stable and is highly unsteady. On average the impingement region becomes a steady radial jet. The impingement surface created at the point of impact is better defined and smoother as Re and L^* decrease. The entrainment process becomes more clearly visible when Re number as well as nozzle to nozzle separation increase.
- Even though the flow field still exhibits the general structure of a higher Re opposed jets impingement flow, special characteristics are observed when the Re drops to 1500. Up to the point of impingement, the jets have an almost laminar behavior in that their propagation is continuous and parallel to the jet axis, and the spread rate is almost nonexistent. The small area associated with the impingement region makes it resemble an impingement surface. These observations are consistent for all nozzle to nozzle separations L^*, the only difference arising in the flow field stability. The smaller the separation distance between nozzles at this Re, the more stable the associated flow field.
- Oscillations of the radial jet periphery in a plane perpendicular to the jet axis and of the entire impingement region along the opposed jets axis and in the vicinity of the stagnation point are clearly observed. They both depend on Re and L^* in the sense that the higher the Re number and the smaller the L^*, the higher the oscillation frequencies appeared. However, the examination of flow visualization images revealed non-repeatable and non-regular oscillations; a definite continuous measure of these frequencies could have not obtained.

LDA and PIV experimental data, as well as CFD numerical data, have been analyzed and compared within the context of classical turbulence theory. Although overall small disagreements were found between the mean dominant velocities obtained through the three different methods, great discrepancies were noticed between corresponding transverse velocity components and turbulent quantities. These were perhaps due to limited and different frequency sampling rates which have only partially resolved both the lowest and highest frequencies involved in the present flow. Since it offered by far a better flow statistics history, the majority of specific turbulent quantities were estimated from LDA data. As far as the CFD data is concerned, the formulation of the $k - \varepsilon$ turbulence model itself can explain its failure to predict this type of flow. The characteristics of the flow field generated by the impingement of the two turbulent opposed jets as revealed from measured and computed data are summarized below:

- The mean velocity vector plots obtained by any means sustain the theory of the free radial jet concept described in the introduction of this thesis. Consequently, a new radial jet symmetric about the vertical symmetry plane of the two axial jets is observed to develop.
- Reynolds number affects not only the impingement region but the free jet region as well; higher decay rates of the mean longitudinal velocity on the jets axis are noticed for lower Reynolds numbers. These influences are mostly correlated with the largest nozzle to nozzle separation distance. Mean longitudinal and transverse velocity variations on the radial jet axis as predicted by CFD are independent of the flow Reynolds number.
- Although the mean transverse velocity component of the axial jets can be neglected outside the impingement region, within the impingement region its magnitude is similar than that of the mean longitudinal velocity component of the axial jet (up to 40 % of U_0). Moreover, the maxima are noticed to belong to different regions which make the

impingement region and the radial jet itself highly anisotropic and non-homogeneous. It is the unsteady and unstable flow motion observed to take place in this region which is the cause of this behavior. For the higher Reynolds number range, occasional negative mean transverse velocities were noticed which may be associated with the entrainment of the surrounding fluid (in the range of 5 to 10 %). Therefore, the mean transverse velocity distribution in the axial and radial jet play a significant role in the dynamics of the impingement region, and related to that, in the mixing process between the two opposed jets and between jets and the surrounding medium.

- Variation of the longitudinal correlation coefficients on the jet axis, suggest the existence of several frequencies superimposed on the fundamental frequency of the dominant flow. However, quantitative information regarding these frequencies cannot be deduced from the data. Instead all transverse autocorrelations appear to exhibit variations similar to those designated to isotropic turbulence with a wide spectrum of eddy sizes.

- If regarded as an independent entity, the radial jet has similar characteristics to a free jet flow. What makes it different is its specific apparition from a sink-source.

- Although flow at Re = 1500 provides the highest (about 90 % for $L^* = 5$) and most homogeneous (as far as the spreading along jets' axis is concerned) turbulence levels (about 30 % magnitude) for all L^* values, Re = $\{7500, 4500\}$ were recommend as the flow rates that will provide the most efficient turbulent mixing in the impingement region for $L^* = 20$ and similarly Re = 4500 for $L^* = 10$. The excessively large turbulence quantities exhibited by flow at Re = 1500 are explained through the highly unstable and unsteady character of this particular flow regardless of L^*. The turbulence contribution due to the unsteadiness caused by oscillations of the global impingement region (including the radial jet) has been termed "false" turbulence. A general shrinking tendency as far as the impingement region width is concerned, with decreasing L^* ($0.8d - 0.1d$ for $L^* = 20$ becomes $0.5d - 0.6d$ for $L^* = \{10, 5\}$) and regardless of Re number is noticed.

- Variation of the axial jet dominant integral time scale at the boundary of the impingement region indicates strong entrainment in this region. The entrainment is found to increase in magnitude with increasing distance from the jet centerline. In the radial jet case, variation of the longitudinal integral length scale towards the boundary layer of the jet indicates the presence of weak entrainment.

- As in any classical investigation involving data derived from measurements, our first and most important assumption was concerning the homogeneous and isotropic character of the turbulence. Even though a 100 % isotropic (and therefore homogeneous) turbulent flow cannot be realized, it was demonstrated that isotropy was achieved in some limited sections of the flow. Whereas free jet behavior was observed for the flow near the nozzle with isotropic turbulence in the vicinity of the jet axis, in the impingement region near uniform (values of λ_g/λ_f ratio are within maximum 15 % deviation from $\sqrt{2}$) isotropic turbulence is noticed across the axial jet while weak tendencies toward isotropy are found for the outer boundary of the radial jet. Since the isotropic turbulence assumption constitutes the foundation of $k - \varepsilon$ turbulence model it is not surprising that the CFD calculated turbulent Reynolds number satisfies the isotropy requirements for all locations across the axial or the radial jet.

- A high turbulent Reynolds number as well as sometimes similar levels of turbulent kinetic energy production and dissipation characterize the impingement region. The high level of Re_{λ_g} on the jet axis is perhaps due to the "false" turbulence created by the impingement region oscillations. It is known that at high mean flow Reynolds number there is a

substantial degree of separation between the energy containing eddies and the dissipating ones. The microscale for time we have obtained, τ_ε , is with some exceptions greater than the Kolmogorov dissipation time scale a fact that implies a large mean flow Reynolds number and so an abundance of energy in the mean flow that is available to generate and sustain turbulence. In both cases studied (axial and radial jet) the location of the largest dominant length scales (i.e. longitudinal or transverse) coincide well with regions of maximum turbulent kinetic energy production. Although the turbulence kinetic energy destruction and production rates have divergent trends, ε and P magnitudes are close and at some points in the flow turbulent equilibrium is approached (at points close to the axial jet centerline and boundary regions in the radial jet). Based on these affirmations we can conclude that the two jets proceed toward the fully turbulent stage of their development.

- Unlike the round free jet that maintains a self preserving shape of mean velocity profiles at about 20 diameters downstream regardless of Re [55], the opposed impinging jets become self similar in the mean velocity at just 8 diameters downstream of the nozzles and for Re = 11000 and $L^* = 20$; this confirmed the faster fully turbulent development of the impinging jets and the role that the adverse pressure gradient within the impingement region plays in the mixing dynamics. Turbulence intensity profiles do not exhibit self-similarity for the range of x/d or Re numbers and L^* studied for the axial jets. While the relative turbulence intensity magnitudes toward the jet boundary layer were usually about $20 - 30$ %, maximum values are obtained within the region surrounding the centerline of the jet. At the same time unexpected high turbulence intensities (between 40 % and 80 %) were found as Re and L^* decrease and even on the jet axis itself. These surprisingly high magnitude of the turbulence quantities may be due to the highly oscillatory behaviour of the impinging jets flow.

- Although for Re = 11000 and independent of L^* the mean radial velocity profiles seem to fairly well match the Reichardt distribution for free jets, none of them exhibits a complete self-similar behavior for any of the control parameters (i.e. x/d, L^*, or Re =11000). However, if regarded in sections, both the mean radial velocity profiles and turbulent radial intensity distributions become partially self-similar. Of the radial jets it is the jet corresponding to Re = 11000 and $L^* = 10$ that satisfies the turbulent equilibrium theory in the boundary layer region of the radial jet (where the entrainment occurs). This fact confirms the early fully turbulent development of the radial jet resulted from the impingement of two turbulent opposed jets (in the case Re = 11000 and $L^* = 10$). For a sufficiently small Re number (Re < 4500) the mean and turbulent radial velocity profiles are considerably altered by the highly unstable and unsteady flow present at these conditions. CFD results match the experimental data corresponding to the top part of the velocity profiles for Re = 11000 and $x/d = 1$ surprisingly well while they overpredict the base part of this distribution. This is consistent with the theory of $k - \epsilon$ turbulence model. No agreement is recorded in the cases associated with Re = 1500.

- For the two jets initially separated by a distance $L = 20d$ and placed in a dynamic impingement configuration to reach a certain development stage, twice the momentum a free planar jet needs to reach the same growth rate is required. Furthermore, this distinctive evolution is amplified and maintained by the same pattern of the jet growth rate with increasing separation L^* (i.e. as L^* increases the jet growth rate increases). The explanation may lie in the obstacle the axial jets meet through the adverse pressure gradient within the impact zone which forces them to flow in a radial direction. Similar

unexpected behavior is exhibited by the radial jet created when the two opposed jets impinge upon each other.

At the end of this study a major conclusion makes sense; it is not the amount of time or the complicated mathematics involved in an experimental or CFD approach that make the difference between them but the uncertainty present in their outputs. While CFD results are always compared with corresponding experimental data and the codes are adjusted to these benchmarks there is nothing the experimental data can be compared with and nothing to tell which experimental data is good and which is erroneous. It is the researcher's experience and knowledge combined together that makes things work. This is the reason the experimental approach will never be abandoned.

5.2 Recommendations

Although this work represents a significant advance in the study and modeling of turbulent opposed impinging jets dynamics, more work remains to be done to thoroughly explain and extend it to practical applications. Some possibilities are given below.

- Due to the unstable and partially unsteady character of the composite impinging jets flow, classical turbulence analysis with its inherent assumptions has only been partially adequate for the flow considered in this thesis. Further work must be done in developing a strategy which can permit full analysis of the turbulent and unsteady flow.
- A comprehensive comparison between fundamental characteristics of turbulent opposed impinging jets flow structure and dynamics and those of the impinging jet on a flat plate as well as of the free jet would be useful. Following this combined study, the "natural" and "false" turbulence contributions in the opposed impinging jets flow unsteady turbulence could be separated.
- Future opposed jet impingement with the jets issuing in different symmetry planes (i.e. the centerline of one jet displaced at specific fractions of d from the centerline of the other jet) so that a tilted and larger impingement surface is obtained would be useful.
- Pressure measurements should be undertaken in order to explain the adverse pressure gradient generation and its role in the opposed impinging jets structure and dynamics evolution.
- The use of fundamental characteristics of turbulent opposed impinging jets to modify an existing turbulence model in order to achieve an accurate CFD solution would be also useful.

Appendix A

Errors in LDA

Laser Doppler anemometers are among the most accurate flow measurement devices. However, they are not immune to errors and, as with any other measurement method, it is important to know the sources of error when taking LDA measurements. Due to the large variety of relevant parameters, an estimation of the measurement uncertainty for a complex device such as the LDA is not trivial.

A.1 Noise in the LDA Signal

In general, the frequency of a LDA signal that is measured by a frequency detector is not equal to the Doppler frequency, it also accounts for the noise existent in that signal. The difference between measured frequency and Doppler frequency represents a mean error that increases with decreasing signal to noise ratio. The noise contribution in an LDA signal consists of two distinct terms: the background noise which includes all statistically steady noise sources such as the photomultiplier shot noise with all DC currents caused by constant background illumination [32] and electronic noise, and the pedestal shot noise associated with transient currents generated by the light scattered by a particle moving through the control volume.

High speed turbulent flows, such as the subject of this thesis, are not very susceptible to this noise due to high signal to noise ratio that can be easily realizable. However, appropriate electronic bandpass filters have been used to remove low-frequency components and frequencies that do not contain Doppler information prior to any frequency detection. Instead, noise appeared in the LDA time series overshooting the general fluctuation of the signal about the mean velocity. Consequently, filtering of the corrupted data has achieved through a simple technique already described in section 2.7.2.

A.2 LDA Measurement Uncertainty

In practice, it is not always possible to separate the systematic errors from the residual errors, so that the total error or the experimental uncertainty is usually expressed as a function of a bias error, B, and a random or precision error, S, [26]:

$$\epsilon_{_{0.95}} = \pm\sqrt{B^2 + (tS)^2} \tag{A.1}$$

where t is a multiplier for a 95 % confidence interval. For a sample number greater than 30, $t_{95} \simeq 2$ [33].

Mean and turbulent longitudinal velocity uncertainties are the subject of this section. Estimated from the most inaccurate measurements took throughout this experiments, the error calculations presented bellow, provide a maximum uncertainty level for the present research.

A.3 Bias Errors

Any error that will remain constant during an experiment and it passes along non-altered from an experiment to another is termed bias or fixed error. These are systematic errors and their provenience would be from tolerances of the instruments, calibration, data acquisition and data reduction processes, etc. The overall bias limit of a certain measurement is defined as the root sum-square combination of all the fixed error components [54]:

$$B = \sqrt{\sum_{i=1}^{n} B_i^2} \tag{A.2}$$

Values in Table A.1 and velocity data such as $\overline{u} \in (0.01, 1.021)\ m/s$, $\overline{v} \in (0.005, 0.3)\ m/s$, $u_{rms} \in (0.02, 0.33)\ m/s$, and $v_{rms} \in (0.01, 0.096)\ m/s$ will be used in future calculations.

Table A.1: LDA optical-counter processor parameters

Parameter	Green Beam (Vertical)	Blue Beam (Horizontal)
$\lambda\ [nm]$	514.5	488
$f\ [mm]$	600	600
$2\varphi\ [^\circ]$	6.81779 ± 0.15	6.61166 ± 0.15
$d_m\ [mm]$	0.06032	0.06359
$l_m\ [mm]$	1.01267	1.1009
$\Delta x\ [mm]$	4.32633×10^{-3}	4.23129×10^{-3}
N_{fr}	14	15
Optical Shift Frequency $[MHz]$	40	40
Doppler Shift Frequency $[MHz]$	1	1
Low Pass Filter $[KHz]$	2×10^3	2×10^3
High Pass Filter $[KHz]$	256	256

A.3.1 Seeding Errors

The bias errors introduced by seed particles can be classified as follows [33]: flow distortion bias caused by seed particles injection, seed particle lag bias caused by incapacity of certain seed particles to follow the flow and individual realization bias caused by counting preference in uniformly seeded flow.

Usually the flow distortion bias would become important if the seed injection velocity is different from the mean velocity of the flow. For the present measurements water's "natural" seeding has been used, therefore the flow distortion bias and the seed particle lag bias can be considered nonexistent or *negligible*.

The relatively high data rate indicated by the counters (in the average 300 to 800 validated particles) during the present measurements make us think of an uniformly seeded flow. In such a case proportionately more fast seed particles than slow seed particles are counted, thus causing the average velocity to be biased. For the present experiments, the constant sampling frequency (250 Hz) has continually shown to be much lower than the particle validation rate (in the average 11 to 17 KHz), a fact leading to negligible individual realization bias.

A.3.2 Laser Beam Geometrical Errors

In general, at least the following errors can be counted as sources of laser beam geometrical bias [33]: finite probe volume bias, positioning bias, fringe spacing uncertainty, negative velocity bias and incomplete signal bias.

Finite probe volume bias is usually influenced by the control volume's dimension and the existence of significant velocity gradients within the measurement control volume (mcv). The small control volume used in these measurements (see Table A.1) avoided high velocity gradients occurring within its perimeter therefore leading to *negligible* finite probe volume bias.

Positioning bias error consists of several distinct contributions: location bias, orientation bias and beam orthogonality bias [33]. The relative location bias for the mean velocity is defined as:

$$\frac{B_{Li}^{\overline{u}}}{\overline{u_i}} = \pm \frac{\partial \overline{u_i}}{\partial x_j} \frac{\Delta x_j}{\overline{u_i}} \tag{A.3}$$

For the velocity fluctuation this expression becomes:

$$\frac{B_{Li}^{u_{\mathrm{rms}}}}{u_{rms}^i} = \pm \frac{\partial \left(\frac{u_{\mathrm{rms}}^{\mathrm{i}}}{\overline{u_{\mathrm{i}}}} \right)}{\partial x_j} \Delta x_j \tag{A.4}$$

where $\overline{u_i}$ is the mean dominant velocity component, $u_{rms}^i = \left(\overline{u_i'^2} \right)^{1/2}$ is the turbulent intensity and Δx_j is the position uncertainty in the x_j direction. The mcv position uncertainty has the same order of magnitude with the LDA system traverse positioning and is observed to be approximately $\Delta x_j = 1\ mm$. As $B_{Li}^{\overline{u}}$ and $B_{Li}^{u_{\mathrm{rms}}}$ definitions show, these errors would exhibit maximums where mean and rms velocity gradients are maximum. The analysis in chapter 4 revealed two positions where mean longitudinal velocity component presents maximums gradients: near the nozzle on y direction and close to the stagnation point on x direction. In these regions, based on curve fitting procedures presented in chapter 4 estimated maximum values of these gradients are $\frac{\partial \overline{u}}{\partial y} = |-9.57|$ and $\frac{\partial \overline{u}}{\partial x} = |-5.43|$. Therefore the normalized location bias

in the mean longitudinal velocity is in the range $\pm 0.0271 \leq \frac{B_L^{\overline{u}}}{\overline{u}} \leq \pm 0.0319$. The largest of these errors (i.e. 3.19 %) corresponds to maximum velocity gradient near the edge of the nozzle. Similarly, the location bias in the turbulent velocity was evaluated to be in the range of $\pm 0.0725 \leq \frac{B_L^{u_{rms}}}{u_{rms}} \leq \pm 0.145$, and it corresponds to maximum turbulent velocity gradient near the nozzle.

The optimized alignment of the mcv with the mean flow direction can lead to *negligible* orientation bias. Errors generated by the intersection of two laser components (2 green beams intersecting 2 blue beams at an angle of 90°) represents the beam orthogonality bias. This error can be calculated as follows:

$$\frac{B_O^{\overline{uv}}}{U_{ref}^2} = \left(\frac{\overline{u^2}}{U_{ref}^2} - \frac{\overline{v^2}}{U_{ref}^2} \right) \sin |\Delta\alpha| \tag{A.5}$$

where U_{ref} is a reference velocity (measured at a fix point in the flow) against which the LDA setup is tested for each new set of measurements. In the present experiments this value was $U_{ref} = 1.021\ m/s$. $\Delta\alpha$ is the tolerance of the half angle from an orthogonal intersection of the two beams and presently it takes the value $\Delta\alpha = \pm 0.075°$. Thus, the beam orthogonality error is situated in the range $1.4 \cdot 10^{-6} \leq \frac{B_{45}^{\overline{uv}}}{U_{ref}^2} \leq 1.26 \cdot 10^{-3}$.

At these magnitudes, the location and beam orthogonality bias can be *neglected*.

The fringe spacing uncertainty is caused by uncertainty in beam intersection angle and non-parallel fringe patterns within mcv. The uncertainty in beam intersection angle is represented through the following relationships [33]:

$$\frac{B_{FS}^{\overline{u}}}{\overline{u}} = \pm \frac{|\Delta\varphi|}{\sin\varphi} \tag{A.6}$$

$$\frac{B_{FS}^{rms}}{u_{rms}} = \pm \frac{|\Delta\varphi|}{\sin\varphi} \tag{A.7}$$

where $\overline{u}$ is the velocity normal to the fringes and φ has the meaning and value in Table A.1 and $\Delta\varphi = 0.075°$and $\Delta\varphi$ is the tolerance of the half angle measurement. Substituting the beams' intersection angle and $\Delta\varphi$ (in radians) in the above equations yields $\pm 0.022 \leq \frac{B_{FS}^{\overline{u}}}{\overline{u}} = \frac{B_{FS}^{rms}}{u_{rms}} \leq \pm 0.0227$ for the uncertainty in beam intersection angle. Since the two laser beams were rigged by the manufacturer so that their waists coincide with the focal distance of the transmitting lens and so with the intersection point of the two laser beam, the uncertainty in the parallel fringe patterns were considered *negligible*.

Negative velocity bias occurs in highly turbulent and recirculating flows with small mean velocity magnitude if frequency shifting is not used. In the present experiments, the 55N10 frequency shifter provides a 40 MHz signal that controls a Bragg cell used to optically shift one of the beams by 40 MHz. This is to avoid directional ambiguity and to improve the signal to noise ratio. Therefore the negative velocity bias can be considered *negligible*.

Incomplete signal bias appears when the trajectory of a particle crossing the mcv is not perpendicular to the fringes. In this case the probability of detecting a particle crossing the mcv is defined as [33]:

$$P(\alpha) = \sqrt{1 - \left(\frac{\frac{M}{N_{fr}}}{\cos\alpha + \frac{V_f}{V_p}} \right)^2} \tag{A.8}$$

where M is the minimum number of fringes needed for a valid signal, N_{fr} is the number of fringes within mcv, α is the incident angle of the particle, V_f is the fringe velocity and V_p is the particle velocity. The Doppler shift frequency f_{ds} corresponds to the number of fringes per second passing a fixed spatial position (the fringe spacing) [18]. Therefore the fringes move at a constant velocity $V_f = f_{ds}\Delta x$. For the current setup $V_f = \{4.32633, 4.23129\}\ m/s$. For $M = 8$, an incidence angle of $\alpha = 15°$ and a usual $V_p = (0.2, 1.19)\ m/s$, the particle will be detected at least 99.4 % of the time. Thus, the incomplete signal bias can be *neglected*.

A.3.3 Processor Errors

The following errors can be mentioned as contributions to the uncertainty bias introduced by the counter processor [33]: clock synchronization error, quantizing error, threshold limit error and electronic noise induced error.

The clock synchronization bias is caused by the mismatch between the randomly occurring Doppler burst and the start of the clock cycle [33]. The following relationships can be used to determine such errors in the mean and turbulent velocities:

$$\frac{B_{CS}^{\overline{u}}}{\overline{u}} = \begin{cases} +\frac{f_D}{2Mf_c}\left(1 + \frac{\overline{u'^2}}{\overline{u}^2}\right) \\ -0 \end{cases} \tag{A.9}$$

$$\frac{B_{FS}^{rms}}{u_{rms}} = \begin{cases} +\frac{f_D}{2Mf_c}\left(1 - \frac{\overline{u'^2}}{\overline{u}^2}\right) \\ -0 \end{cases} \tag{A.10}$$

where f_D is the Doppler frequency, and f_c is the reference clock frequency (500 MHz). Using the above quantities (Table A.1) the clock synchronization bias become $1.425 \cdot 10^{-6} \leq \frac{B_{CS}^{\overline{u}}}{\overline{u}} \leq 3.03 \cdot 10^{-5}$ for the mean longitudinal velocity and $-6.161 \cdot 10^{-7} \leq \frac{B_{FS}^{rms}}{u_{rms}} \leq 3 \cdot 10^{-5}$ for rms respectively. At these magnitudes the clock synchronization errors are considered *negligible*.

Quantization errors arises from the determination of the frequency of the analog Doppler signal using a digital reference clock [33]. They can be calculated as follows:

$$\frac{B_Q^{\overline{u}}}{\overline{u}} = \pm\frac{1}{3}\left(\frac{f_D}{Mf_c}\right)^2\left(1 + 3\frac{\overline{u'^2}}{\overline{u}^2}\right) \tag{A.11}$$

for mean longitudinal velocity and

$$\frac{B_Q^{rms}}{u_{rms}} = \begin{cases} +\left[1 + \frac{1}{3}\left(\frac{f_D}{Mf_c}\right)^2 \frac{\overline{u}^2}{\overline{u'^2}}\right]^{1/2} - 1 \\ -0 \end{cases} \tag{A.12}$$

for the rms turbulent intensity. For the present LDA and counter processor setup the quantization errors are of the order of 10^{-9} and therefore they can be *neglected*.

The threshold limit error is defined as the bias introduced by using the nonzero volt Schmidt trigger to digitize Doppler bursts. These errors can be estimated using the following formulas [33]:

$$\frac{B_T^{\overline{u}}}{\overline{u}} = \begin{cases} +\frac{1}{12M} + \frac{1}{96M^2} \\ -0 \end{cases} \tag{A.13}$$

for mean longitudinal velocity and

$$\frac{B_T^{rms}}{u_{rms}} = \begin{cases} +0 \\ -\frac{1}{576M^2} \end{cases} \tag{A.14}$$

for rms turbulent intensity. For the present experimental setup $\frac{B_T^{\overline{u}}}{\overline{u}} = 0.01057$ and $\frac{B_T^{rms}}{u_{rms}} = 2.7126 \cdot 10^{-5}$.

In the spirit of the above philosophy (section A.1) the electronic noise mixed with the Doppler signal can cause important LDA bias errors if the signal to noise ratio is low. An estimation of these type of errors can be achieved using [33]

$$\log\left(\frac{B_{EN}^{\overline{u}}}{\overline{u}}\right) = 3.126 \log\left(\frac{23.32}{SN}\sqrt{\frac{f_U + f_L}{2f_D}}\right) - 4.0 \tag{A.15}$$

for the mean longitudinal velocity and,

$$\log\left(\frac{B_{EN}^{rms}}{u_{rms}}\right) = 5.67 \log\left(\frac{16.56}{SN}\sqrt{\frac{f_U + f_L}{2f_D}}\right) - 5.0 \tag{A.16}$$

for the rms turbulent intensity. In these relationships, SN is the signal to noise ratio and f_U and f_L are the upper and lower pass filter frequencies used in data acquisition (see Table A.1). For the present experiments $SN \in (5, 10)$ and therefore the following electronic noise induced errors resulted: $1.47 \cdot 10^{-3} \leq \frac{B_{EN}^{\overline{u}}}{\overline{u}} \leq 1.286 \cdot 10^{-2}$ in mean longitudinal velocity and $1.888 \cdot 10^{-4} \leq \frac{B_{EN}^{rms}}{u_{rms}} \leq 9.61 \cdot 10^{-3}$ in turbulent intensity.

A summary of the normalized bias errors in LDA measurements is provided in Table A.2.

A.4 Precision Errors

As previously mentioned (section 2.6) S is more often called the precision index of a measurement [26], and it represents a measure of measurement's random error. This can be estimated from the measured data only and is equal to its standard deviation. In a more complex situation, besides the standard deviation, variations in the measured value appear amongst repeated measurements, the precision index is calculated as:

Table A.2: Summary of bias errors in mean and turbulent longitudinal velocities

Bias error	Error in $\overline{u}$	Error in u_{rms}
Seeding	negligible	negligible
Positioning of mcv	$\pm 2.7 \cdot 10^{-2} \leq \frac{B_L^u}{\overline{u}} \leq \pm 3.2 \cdot 10^{-2}$	$\pm 7.2 \cdot 10^{-2} \leq \frac{B_L^{u\,rms}}{u_{rms}} \leq \pm 1.45 \cdot 10^{-1}$
Fringe spacing	$\pm 2.2 \cdot 10^{-2} \leq \frac{B_{FS}^{rms}}{u_{rms}} \leq \pm 2.27 \cdot 10^{-2}$	$\pm 2.2 \cdot 10^{-2} \leq \frac{B_{FS}^{rms}}{u_{rms}} \leq \pm 2.27 \cdot 10^{-2}$
Clock sincronization	$1.42 \cdot 10^{-6} \leq \frac{B_{CS}^u}{\overline{u}} \leq 3.03 \cdot 10^{-5}$	$-6.16 \cdot 10^{-7} \leq \frac{B_{FS}^{rms}}{u_{rms}} \leq 3 \cdot 10^{-5}$
Threshold limit	$\frac{B_T^u}{\overline{u}} = 1.057 \cdot 10^{-2}$	$\frac{B_T^{rms}}{u_{rms}} = 2.7126 \cdot 10^{-5}$
Electronic noise	$1.47 \cdot 10^{-3} \leq \frac{B_{EN}^u}{\overline{u}} \leq 1.28 \cdot 10^{-2}$	$1.88 \cdot 10^{-4} \leq \frac{B_{EN}^{rms}}{u_{rms}} \leq 9.6 \cdot 10^{-3}$
Total bias error	$\pm 0.0365 \leq \frac{B^u}{\overline{u}} \leq \pm 0.0425$	$\pm 0.0757 \geq \frac{B^{rms}}{u_{rms}} \leq \pm 0.147$

$$S = \sqrt{\sum_{i=1}^{n} S_i^2} \tag{A.17}$$

Sources of these variations would involve calibration, acquisition and data reduction.

The relative precision error in mean velocity can be determined using the following relationship [9]:

$$\frac{S_{\overline{u}}}{\overline{u}} = \frac{z_{\alpha/2}}{\sqrt{N}} \frac{\left(\overline{u'^2}\right)^{1/2}}{\overline{u}} \tag{A.18}$$

where $\overline{u}$ is the mean velocity, $\left(\overline{u'^2}\right)^{1/2}$ is the turbulent intensity (or u_{rms}), N is the number of samples, and $z_{\alpha/2}$ is the standard normal variable for a $(100 - \alpha)$ percent confidence interval. For a 95 percent confidence interval, $z_{\alpha/2} = 1.96$. In all experiments, $N = 40960$ instantaneous velocity samples were collected at a constant sampling frequency of 250 Hz and the relative turbulence intensity $u_{rms}/\overline{u}$ was in range of 15 % to 640 %. Thus, for the present measurements the relative precision error for the mean longitudinal velocity takes values in the interval $0.001452 \leq \frac{S_u}{\overline{u}} \leq 0.061$.

The relative precision error for the turbulent intensity is calculated as follows [9]:

$$\frac{S_{rms}}{u_{rms}} = \frac{z_{\alpha/2}}{\sqrt{2N}} \tag{A.19}$$

The result is independent of rms magnitude and depends on the number of instantaneous samples considered only, $\frac{S_{rms}}{u_{rms}} = 0.006847$.

Finally, the total experimental uncertainty for a 95 % confidence interval is summarized in Table A.3.

Table A.3: Summary of total uncertainty in mean and turbulent longitudinal velocities

Error	Error in $\overline{u}$	Error in u_{rms}
B [%]	±4.25	±14.7
S [%]	6.1	0.6847
$\epsilon_{0.95}$ [%]	±13.1	±14.76

Although both types of errors, bias and precision have the same weight in the case of mean longitudinal velocity uncertainty, however, the fluctuation component of the longitudinal velocity is mainly affected by bias errors. The larger bias error was due to position bias of mcv.

Bibliography

[1] Advances in Fluid Flow Diagnostics. TSI Inc. Fluid Mechanics Instrument Division, St. Paul, MN, U.S.A., 1997.

[2] G. N. Abramovich. *The Theory of Turbulent Jets*. The MIT Press, Cambridge, Massachusetts, 1963. Translation by Scripta Technica.

[3] R. J. Adrian. Particle-Imaging Techniques for Experimental Fluid Mechanics. *Annu. Rev. Fluid Mech.*, 23:261–304, 1991.

[4] AEA Technology. *TASCflow and CFX - Build: Theory Documentation*. Waterloo, Canada, January 1994.

[5] AIAA. Getting Down to the Fundamentals. *Aerospace America*, (5), May 2000.

[6] J. Anderson, G. Degrez, E. Dick, and R. Grundmann. *Computational Fluid Dynamics. An Introduction.* Springer-Verlag, Heidelberg, Germany, second edition, 1996.

[7] D. Bjorkquist. Particle Image Velocimetry for Determining Structures of Turbulent Flows. *Flow Lines. The Fluid Mechanics Magazine from TSI Incorporated.*, 6(1):3–8, 1991.

[8] R. Bracewell. *The Fast Fourier Transform and its Applications*. McGraw-Hill Kogakusha Ltd., Tokyo, second edition, 1978.

[9] I. Castro. *An Introduction to the Digital Analysis of Stationary Signals*. IOP Publishing Ltd., 1989.

[10] M. Champion and P. A. Libby. Reynolds Stress Description of Opposed and Impinging Turbulent Jets. Part I: Closely Spaced Opposed Jets. *Phys. Fluids*, A 5(1):203–216, January 1993.

[11] T. J. Craft, L. W. Graham, and B. E. Launder. Impinging Jet Studies for Turbulence Model Assessment - II. An Examination of the Performance of Four Turbulence Models. *Int. J. Heat Mass Transfer*, 36(10):2685–2697, 1993.

[12] DANTEC Documentation Department. *Dantec55X Modular Optics*, Denmark, 1983.

[13] DANTEC Documentation Department. *55N10 Frequency Shifter*, Denmark, 1985.

[14] DANTEC Documentation Department. *Dantec 55L90 Counter*, Denmark, February 1986.

[15] Dantec Measurement Technology. *FlowMap Particle Image Velocimetry Instrumentation. Installation User's Guide.*, Denmark, 1999.

[16] V. A. Denshchikov, V. N. Kondrat'ev, and A. N. Romashov. Interaction Between Two Opposed Jets. *Fluid Dynamics*, 6(924):924–926, 1978.

[17] V. A. Denshchikov, V. N. Kondrat'ev, A. N. Romashov, and V. M. Chubarov. Auto-Oscillations of Planar Colliding Jets. *Fluid Dynamics*, 3(460):460–463, 1983.

[18] T. Durani and C. Greated. *Laser Systems in Flow Measurement*. Plenum Press, New York, 1977.

[19] F. Durst, A. Melling, and J. H. Whitelaw. *Principles and Practice of Laser-Doppler Anemometry*. Academic Press Inc., New York, second edition, 1981.

[20] J. H. Ferziger and M. Peric. *Computational Methods for Fluid Dynamics*. Springer-Verlag, Germany, second edition, 1997.

[21] J. Hinze. *Turbulence*. McGraw-Hill, New York, 1975.

[22] G. Hitchman. *Data Acquisition and Processing For Laser Doppler Velocimetry in Mechanical Engineering*. University of Waterloo, Waterloo, Canada, 1995.

[23] F. S. Lien. *Finite Volume Methods for Fluid Flow and Heat Transfer Calculations - Course Notes*. University of Waterloo, Waterloo, Ontario, Canada, 1999.

[24] W. Merzkirch. *Flow Visualization*. Academic Press Inc., New York, second edition, 1987.

[25] S. J. Michell. *Fluid and Particle Mechanics*. Pergamon Press Ltd., first edition, 1970.

[26] R. J. Moffat. Describing the Uncertainties in Experimental Results. *Experimental Thermal and Fluid Science*, 1:3–17, 1988.

[27] N. S. Nosseir and S. Behar. Characteristics of jet impingement in a side-dump combustor. *AIAA*, 24(1752), 1986.

[28] N. Ogawa and H. Maki. Studies on Opposed Turbulent Jets (Influences of a Body on the Axis of Opposed Turbulent Jets). *Bulletin of JSME*, 29(255):2872–2877, September 1986.

[29] N. Ogawa, H. Maki, and K. Hijikata. Studies on Opposed Turbulent Jets (Impact Position and Turbulent Component in Jet Center). *JSME International Journal*, 35(2):205–211, 1992.

[30] K. Ohba, M. Sato, S. Sakaguchi, and A. Sakurai. Visualization and Measurement of Detailed Velocity Field in U-Bend and Branched Tube Using Laser Induced Fluorescence Method. *Applications of Laser Techniques to Fluid Mechanics*, (5th International Symposium), 9 - 12 July 1990.

[31] M. V. Otugen and I. Namer. In *The Effect of Reynolds Number on the Structure of Plane Turbulent Jets*, AIAA 24th Aerospace Sciences Meeting, Paper no. AIAA-86-0038, Reno, Nevada, USA, January 6 - 9 1986.

[32] P. Buchhave et al., editor. *The Accuracy of Flow Measurements by Laser Doppler Methods*. Proceedings LDA-Symposium Copenhagen 1975, Skovlundem Denmark, June 1976.

[33] W. P. Patrick. Error Sources in Laser Velocimeter Systems. Technical report, University of Connecticut, 1985.

[34] L. Prandtl and O. Tietjens. *Fundamentals of Hydro- and Aero-Mechanics*. New York, 1934.

[35] Proc. 5th Intl. Symp. on Appl. of Laser Techniques to Fluid Mechanics. *Particle Image Velocimetry Analysis System*, Lisbon, Portugal, 9 - 12 July 1990.

[36] R. J. Adrian et al., editor. *Applications of Laser Techniques to Fluid Mechanics*. Springer-Verlag, Heidelberbg, Germany, 1991.

[37] M. Raffel, C. Willert, and J. Kompenhans. *Particle Image Velocimetry - A Practical Guide*. Springer-Verlag, Gottingen, Germany, 1998.

[38] W. Rodi. *Turbulence Models and Their Application in Hydraulics - A State of the Art Review*. June 1980.

[39] H. Schlichting. *Boundary Layer Theory*. McGraw - Hill Series in Mechanical Engineering. McGraw - Hill Book Company, sixth edition, 1968.

[40] A. A. Shevtsov and N. M. Galin. The Effect of Flowrate on the Turbulence Characteristics of Countercurrent Coaxial Jets. *Thermal Engineering*, 39(6):332–335, 1992.

[41] L. M. Smith and W. C. Reynolds. On the Yakhot-Orszag Renormalization Group Method for Deriving Turbulence Statistics and Models. *Phys. Fluids*, A 4(2):364–390, February 1992.

[42] L. M. Smith and S. L. Woodruff. Renormalization-Group Analysis of Turbulence. *Annu. Rev. Fluid Mechanics*, (30):275–310, 1998.

[43] C. G. Speziale and S. Thangam. Analysis of an RNG Based Turbulence Model for Separated Flows. *Int. J. Engng. Sci*, 30(10):1379–1388, 1992.

[44] G. Stan and D. A. Johnson. In *Experimental Examination of Turbulent Opposed Impinging Jets*, ASME 2000 Fluids Engineering Division Summer Meeting, Paper no. FEDSM2000-11169, Boston, Massachusetts, June 2000.

[45] M. M. Stanisic. *The Mathematical Theory of Turbulence*. Springer-Verlag New York Inc., New York, 1985.

[46] A. B. Strong. *Turbulence - Course Notes*. University of Waterloo, Waterloo, Canada, 1996.

[47] G. D. Stubley. Derivation and Implementation of Strain Rate Sensitive Turbulence Model Coefficients. Technical report, Advanced Scientific Computing Ltd., Waterloo, Ontario, August 3 1995.

[48] G. D. Stubley. *Computational Fluid Dynamics - Course Notes*. University of Waterloo, Waterloo, Canada, 1998.

[49] H. Tennekes and L. J. Lumley. *A First Course in Turbulence*. MIT Press, Cambridge, MA, 1972.

[50] G. B. Thomas and R. L. Finney. *Calculus and Analytic Geometry*. Addison-Wesley Publishing Company, fifth edition, 1979.

[51] A. A. Townsend. *The Structure of Turbulent Shear Flow*. University Press, Cambridge, 1976.

[52] C. Tropea. *Measuring Techniques in Experimental Fluid Mechanics*. University of Waterloo, Waterloo, Canada, 1986.

[53] H. K. Versteeg and W. Malalasekera. *An Introduction to Computational Fluid Dynamics. The Finite Volume Method*. Longman Group Ltd., Essex, England, 1995.

[54] E. J. Weckman. *Experimental Methods in Thermo-Fluids - Course Notes*. University of Waterloo, Waterloo, Canada, 1998.

[55] F. M. White. *Viscous Fluid Flow*. McGraw-Hill, New York, 1991.

[56] F. A. Williams. Progress in knowledge of flamelet structure and extinction. *Progress in Energy and Combustion Sciences*, (26):657 – 682, 2000.

[57] P. Wood, A. Hrymak, R. Yeo, D. Johnson, and A. Tyagi. Experimental and computational studies of the fluid mechanics in an opposed jet mixing head. *Phy. Fluids A*, 3(1362), 1991.